Spring 2012

Electrokinetic Transport Phenomena in Nanofluidic Devices

Mingkan Zhang
Old Dominion University

ELECTROKINETIC TRANSPORT PHENOMENA IN NANOFLUIDIC DEVICES

by

Mingkan Zhang
B.S. June 2003, Zhejiang University, China
Ph.D. June 2008, Zhejiang University, China

A Dissertation Submitted to the Faculty of
Old Dominion University in Partial Fulfillment of the
Requirements for the Degree of

DOCTOR OF PHILOSOPHY

AEROSPACE ENGINEERING

OLD DOMINION UNIVERSITY
May 2012

Approved by:

Shizhi Qian (Co-Director)

Yan Peng (Co-Director)

Ali Beskok (Member)

Drew Landman (Member)

ABSTRACT

ELECTROKINETIC TRANSPORT PHENOMENA IN NANOFLUIDIC DEVICES

Mingkan Zhang
Old Dominion University, May 2012
Co-Directors: Dr. Shizhi Qian
Dr. Yan Peng

Nanofluidic devices have wide potential applications in biology, chemistry and medicine, and have been proven to be very valuable in sensing biological particles (e.g., DNA and proteins) due to their efficiency, sensitivity and portability. Electrokinetic control of ion, fluid, and particle transport by using only electric field is the most popular method employed in nanofluidic devices. A comprehensive understanding of the electrokinetic ion, fluid, and particle transport in nanofluidics is essential for developing nanofluidic devices for the detection of single molecules, such as the next generation nanopore-based DNA sequencing technology. This research explored numerical simulation of electrokinetic ion and fluid transport in both solid-state and soft nanopores, and also explored the electric field induced translocation of nanoparticles through solid-state and soft nanopores using a continuum based model.

In the first part of this dissertation, electrokinetic ion and fluid transport in two types of nanopores, charge-regulated solid-state and polyelectrolyte (PE)-modified soft nanopores, have been investigated for the first time using a continuum-based model, composed of the coupled Poisson-Nernst-Planck (PNP) equations for the ionic mass transport, and Stokes and Brinkman equations for the flow fields. Concentration polarization phenomenon, ionic conductance, potential drop inside the nanopore, and flow field as functions of the solution properties including pH and ionic strength, charge properties of the nanopore,

properties of the soft layer, and the electric field strength imposed were investigated. The results show that the electrokinetic ion and fluid transport in nanopore-based devices can be regulated by tuning pH and/or ionic strength and the properties of the polyelectrolyte layer grafted on the membrane wall. One could use the induced concentration polarization phenomenon to reduce the electric field inside the nanopore for slowing down nanoparticle translocation through the nanopore.

One major challenge in the nanopore-based DNA sequencing technology is to slow down DNA translocation for improving the read-out accuracy. Therefore, the second part of this thesis focused on numerical investigations of nanoparticle translocation through a nanopore. Three types of nanoparticles, which include soft nanoparticle consisting of a rigid core covered by a soft layer, DNA, and charge-regulated soft nanoparticle such as protein, in both solid-state and soft nanopores were considered. Based on the results, regulating DNA translocation by using the soft nanopore was proposed to simultaneously enhance the nanopore capture rate and slow down DNA translocation inside the nanopore. Versatile manipulations of charge-regulated nanoparticles, including separation, focusing, trapping and pro-concentration by using soft nanopores can be achieved by adjusting pH, background salt concentration, and the properties of the soft layer grafted on the nanopore wall. Regulation of DNA translocation by using a solid-state nanopore with a floating electrode coated on the inner surface of the nanopore was also proposed and investigated using numerical simulation.

ACKNOWLEDGMENTS

I would like to express my great gratitude to my advisors, Prof. Shizhi Qian and Prof. Yan Peng. Without their dedicated guidance, insightful comments and economic supporting, I could not have the opportunity to study nanofluidics in the United States and finished my sencond Ph.D in three years.

I also want to cordially thank my committee members, Prof. Ali Beskok and Prof. Drew Landman for reviewing my dissertation and providing helpful comments and suggestions.

I would like to express my gratefulness to Prof. Ali Beskok, Dr. Li-Hsien Yeh, Prof. Sang W. Joo (Yeungnam University, South Korea), Prof. Sharma (India), Prof. Jyh-Ping Hsu (National Taiwan University, R.O.C.) for the pleasant collaboration and many valuable scientific advices.

Finally, I would like to acknowledge my supportive family, in particlar, my wife, Ms. Yuning Xu and my parents.

TABLE OF CONTENTS

Page

LIST OF TABLES

LIST OF FIGURES

Figure Page

CHAPTER 1

INTRODUCTION

1.1. Nanofluidics

Over the recent decades, there has been a growing interest in developing nanofluidic devices, the characteristic dimension of which is below 100 nm. Fluids confined in these nanofluidic devices exhibit physical behaviors not observed in larger channels, such as those of micrometer dimensions and above, because the characteristic lengths of the fluid such as the Debye length very closely coincide with the dimensions of the nanofluidic channel itself. Significant advances in nanofabrication technology, such as the electron beam nanolithography[1] and nanoimprint lithography,[2-3] also enable the study and application of nanofluidics.

Different from microfluidics, ion transport in nanofluidics is surface-charge-governed, owing to the increasing surface-to-volume ratio.[4] This unique phenomenon offers a probability to selectively control the ion transport through nanopores for various applications. The charge selectivity becomes more significant when the characteristic length of the nanofluidic system becomes comparable to the Debye screening length.[5] Since the ions transport in nanofluidics is dominated by the surface charge, it is easy to control ionic transport by tuning the surface chemistry of the nanopore wall.[6-7] The adsorption of molecules onto the nanopore walls leads to the change of the surface charge on the nanopore wall and the ionic conductivity. Therefore, novel nanopore-based biosensors have been proposed and tested by monitoring the ion conductivity.[8-10] Nanofluidic diodes [11-13] and nanofluidic transistors[14-15] can also be fabricated by controlling the surface charge distribution on the nanopore wall. Nanofluidic resistors, diodes and transistors are new potential applications in nanofluidics and provide new opportunities to reach the goal of ionic integrated circuits. Owing to the unique ion-selectivity property, nanofluidics also provide potential applications in clean energy generation and water purification and desalination[16-17] and alternative energy sources, to meet the need of clean water and clean energy. In addition, the electrophoretic translocation of DNA molecules through a nanopore can be utilized to interrogate the

order of nucleotide bases in one single DNA molecule.[5] The nanopore-based DNA sequencing has emerged as one of the most promising approaches to achieve a high throughput and affordable DNA sequencing, which is the main focus of this thesis and thus is described in more details in the following subsection.

1.2. Nanopore-Based DNA Sequencing

The cost of DNA sequencing with the second-generation DNA sequencing technology is still too high for routine applications. For example, the estimated cost, including instrumentation, sample preparation and labor, for sequencing a haploid human genome ranges from $100,000 to $1,000,000.[18] The demand for sequence information also keeps increasing. A low-cost fast-sequencing method will thus not only change the future of medical fields dramatically but also offer a new tool for studying diverse biological functions and evolutions.

A voltage bias imposed across a nanopore merged in a salt solution, as schematically shown in Fig.1, generates an ionic current flowing through the nanopore, which can be measured using electrophysiological techniques. The resulting current is very sensitive to the properties, including surface charge, size and shape, of the nanopore and the nanoparticle translocating through the nanopore. Single bases or strands of DNA electrophoretically passing through the nanopore will induce a change in the ionic current.[19-20] Since the A, C, G, and T nucleotides on the DNA molecule carry different surface charges, each of them may obstruct the nanopore to a different characteristic degree, resulting in different magnitudes of current. The magnitude of the current at any given moment, therefore, varies depending on which of the four nucleotides blocks the nanopore as a DNA molecule passes through the nanopore. Therefore, the sequence of bases in DNA can be probed by monitoring the current modulations by using solid state nanopore [21-24] and modified nanopore[25-27], which has been reviewed by some investigators[28-30]. This method examines the electronic signals in contrast to the existing paradigms based on chemical techniques. The nanopore-based DNA sequencing thus does not require sample amplification; the sequencing time of nucleic acids is within a microsecond. In addition, the estimated cost of the nanopore-based sequencing of a

human genome would be on the order of $1,000, which meets the goals set by the NIH in 2004. This cost is believed to be sufficiently low to revolutionize genomic medicine.[18, 21-22, 28-29] All of these encouraging benefits of the nanopore-based DNA sequencing stimulated a fast-growing research area associated with nanopore analysis.[18, 20-22, 24-25, 27-35]

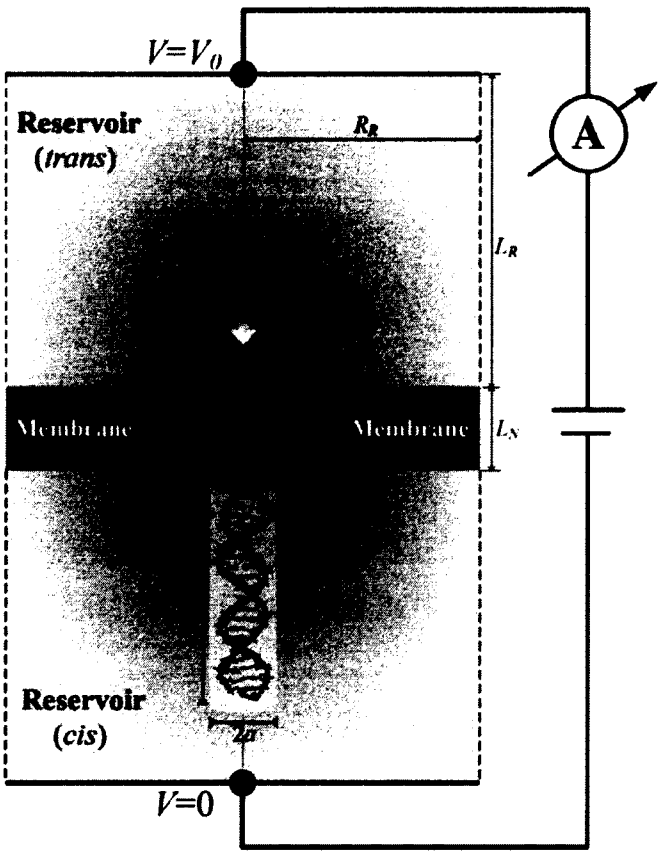

Figure 1.1. Schematic view of a dsDNA nanoparticle translocation through a nanopore.

The existing experimental studies demonstrated that the ionic current during DNA translocation depends on the voltage bias across the nanopore,[36] the length of the DNA molecule,[37-38] the length, size, and surface charge of the nanopore,[8, 38-40] and the electrolyte bulk concentration.[8, 38] When the solvent contains a high salt concentration (thin electric double layer), typically a "current blockade" is observed, which means that the ionic current of a nanopore with DNA particles inside is lower than the one without DNA particles.[33-34, 38, 41-42] The current enhancement means that the ionic current of a nanopore with DNA particles inside is greater than the one without DNA particles. When

the bulk ionic concentration is reduced, both current blockade and current enhancement are observed during a single molecule translocation.[43-44] When the bulk ionic concentration is low, current enhancement is often observed.[38, 45] One objective of this dissertation is to improve the understanding of these diverse phenomena through continuum simulations and to provide a predictive tool to estimate the effect of translocating molecules on ionic currents.

Since the size of fluid reservoirs is usually much larger than that of the nanopore, the local electric field within the nanopore is significantly higher than that in the fluid reservoir, resulting in slow particle motion within the fluid reservoir and high translocation velocity inside the nanopore. One of the major challenges in the nanopore-based technique is that DNA nanoparticles translocate through the nanopore too fast to be accurately detected. [22, 28, 41, 46-62] Although one can reduce the voltage bias applied across the nanopore to reduce the electric field inside the nanopore and consequently slow down the DNA translocation, lower voltage bias will simultaneously reduce the nanopore ability of capturing DNA into the it and the magnitude of the current change, leading to lower throughput and read-out accuracy. Therefore, a relatively high voltage bias is typically applied across the nanopore in the nanopore-based DNA sequencing applications. Additionally, several methods have been proposed to slow down the DNA translocation through the nanopore to achieve higher read-out accuracy.[41, 46-62] They include increasing the solvent viscosity to increase the viscous drag force on the particle,[50] lowering the fluid temperature to increase the fluid viscosity,[46] adjusting salt concentration and/or salt type to modify the charge property of the nanopore by chemical functionalization of the nanopore or by an ionic field effect transistor,[53, 63-66] imposing a salt concentration gradient[41, 49, 67-68], utilizing optical tweezers, conducting nanopores[56, 69], and bio-modified nanopore[55]. Such work has been reviewed by Keyser.[58] For example, Trepagnier et al.[70] used an expansive highly focused laser as optical tweezers to slow down the DNA translocation through a nanopore. Rincon-Restrepo et al.[55] slowed down the DNA translocation velocity by introducing positive charges into the lumen of the pore. Ai et al.[65] proposed to use nanofluidic field effect transistor to regulate DNA translocation through a nanopore. de Zoysa et al.[49] reported that the DNA translocation

velocity can be significantly reduced by using electrolyte solutions containing organic salts instead of the commonly used KCl solution.

Most of the aforementioned techniques simultaneously slow down the particle motion inside the nanopore and in the fluid reservoir. The latter reduces the capture rate and accordingly the throughput. Therefore, slowing down translocation inside the nanopore while enhancing particle motion inside the fluid reservoir are the main challenges in the nanopore-based DNA sequencing technique. To better understand the translocation process, the thesis theoretically investigated the phoretic motion of nanoparticles in nanopores, and successfully proposed regulation of nanoparticle translocation by using polyelectrolyte-modified nanopores (Chapter 4) and floating electrode (Chapter 5).

1.3. Fundamentals of Electrokinetics

Electrokinetics refers to the use of electric fields to exert electrostatic forces on charged or polarizable fluids and suspended particles, which in turn induce the motions of fluids and particles. In the nanopore-based DNA sequencing technology, the particle translocation and the ionic current flowing through the nanopore are generated by externally imposing an electric field across the nanopore. Therefore, electrokinetics becomes one of the most dominant effects in the translocation process. In the following, the basics of electrokinetics under DC electric field, including electrical double layer, electroosmosis, electrophoresis, and induced-charge electrokinetics are summarized.

1.3.1 Electrical Double Layer

Most solid surfaces obtain surface charges through adsorption or dissociation of functional groups when they are brought in contact with ionic solutions.[71-72] The charged surface attracts counter-ions and repels co-ionsresulting in a thin layer dominated by the counter-ions in the vicinity of the charged surface, which is called electrical double layer (EDL) and is schematically shown in Figure 1.2.

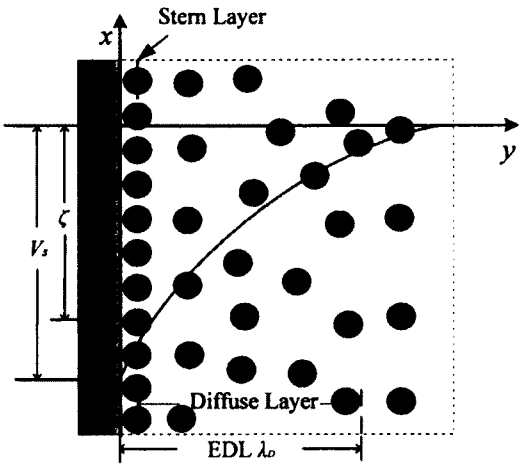

Figure 1.2. Schematic view of an EDL near a negatively charged surface.

The EDL consists of two layers, the Stern layer and the diffuse layer. The counter-ions in the Stern layer next to the charged surface are immobilized due to a very strong electrostatic force. However, the ions inside the diffuse layer are free to move under external field. Since the Stern layer is very thin, the detailed field within the Stern layer is usually neglected. Within the diffuse layer, the electric potential inside the electrolyte solution is described by the Poisson equation,

$$-\varepsilon_f \nabla^2 V = \sum_{i=1}^{N} F z_i c_i \,, \tag{1.1}$$

where ε_f is permittivity of the ionic solution, V is the electric potential, F is the Faraday constant, z_i and c_i are, respectively, the valence and molar concentration of the ith ionic species, and N denotes total number of the ionic species.

The ionic fluxes including the diffusive, electromigrative and convective flux densities are written as

$$\mathbf{N}_i = -D_i \nabla c_i - z_i \frac{D_i}{RT} F c_i \nabla V + \mathbf{u} c_i \,, \tag{1.2}$$

Where D_i is the diffusivity of the ith ionic species, R is the universal gas constant, T is the absolute temperature of the solution, and $\mathbf{u}$ is the fluid velocity vector.

Each ionic concentration, c_i, is governed by the following Nernst-Planck equation,

$$\frac{\partial c_i}{\partial t} + \nabla \cdot \mathbf{N}_i = 0 \,. \tag{1.3}$$

In the absence of the fluid motion and at steady-state, one-dimensional Eq. (1.3) leads to an analytical solution of the ionic concentration, which is known as the Boltzmann distribution

$$c_i = C_{i0} \exp(-z_i \frac{FV}{RT}), \tag{1.4}$$

where C_{i0} is the bulk concentration the ith species. Note that the far field boundary condition, V=dV/dy=0 and c_i=C_{i0} at y→∞, is required to derive the above Boltzmann distribution. One can easily obtain the Poisson-Boltzmann (PB) equation by substituting Eq. (1.4) into Eq. (1.1) under the assumption of binary, symmetric ionic solution in a one dimensional space.

$$\nabla^2\left(z\frac{FV}{RT}\right) = \frac{1}{\lambda_D^2}\sinh(z\frac{FV}{RT}), \tag{1.5}$$

where $z = |z_i|$ and $\lambda_D = \kappa^{-1} = \sqrt{\varepsilon_f RT \Big/ \sum_{i=1}^{2} F^2 z^2 C_0}$ is Debye length or EDL thickness. Clearly, the Debye length depends on the bulk salt concentration, C_0, and decreases as the salt concentration increases. Due to the use of the Boltzmann distribution, the above PB equation is valid when the EDL is at its equilibrium state in the absence of any disturbance from the external flow field and electric field and the EDL cannot interact with the other nearby EDLs (i.e., the EDLs are not overlapped). In nanofluidics, since the Debye length is on the same order of magnitude of the nanopore size, the PB equation is not valid.

When $V << RT/zF$, Eq. (1.5) can be linearized under the Debye–Hückel approximation [73] as

$$\nabla^2\left(z\frac{FV}{RT}\right) = \frac{1}{\lambda_D^2} z\frac{FV}{RT}. \tag{1.6}$$

Eq. (1.6) gives the electric potential as

$$V = \zeta \exp(-y/\lambda_D), \tag{1.7}$$

where ζ is the zeta potential, defined as the potential on the shear plane, which is the interface between the Stern layer and the diffuse layer, and y is the distance from the shear plane.

For an arbitrary surface potential, the Gouy-Chpman distribution [73] has been derived from Eq. (1.5)

$$V = \frac{4RT}{zF}\operatorname{atanh}\left(\tanh\left(\frac{zF\zeta}{4RT}\right)\exp(-y/\lambda_D)\right), \tag{1.8}$$

1.3.2 Electroosmosis

Under an external electric field applied parallel to a stationary charged surface, the accumulated counter-ions within the EDL of the charged surface migrate to the oppositely charged electrode, dragging the viscous fluid with them. The induced flow is called eletroosmosis flow (EOF), as shown in Figure 1.3.

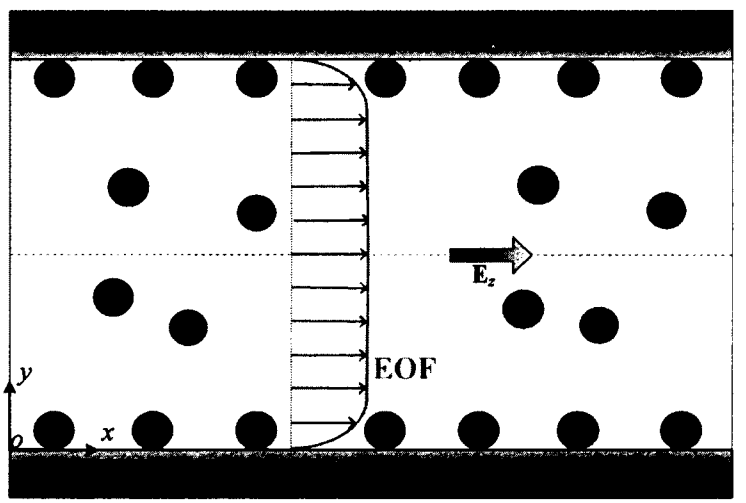

Figure 1.3. Schematic view of EOF in a slit channel with negatively charged surfaces.

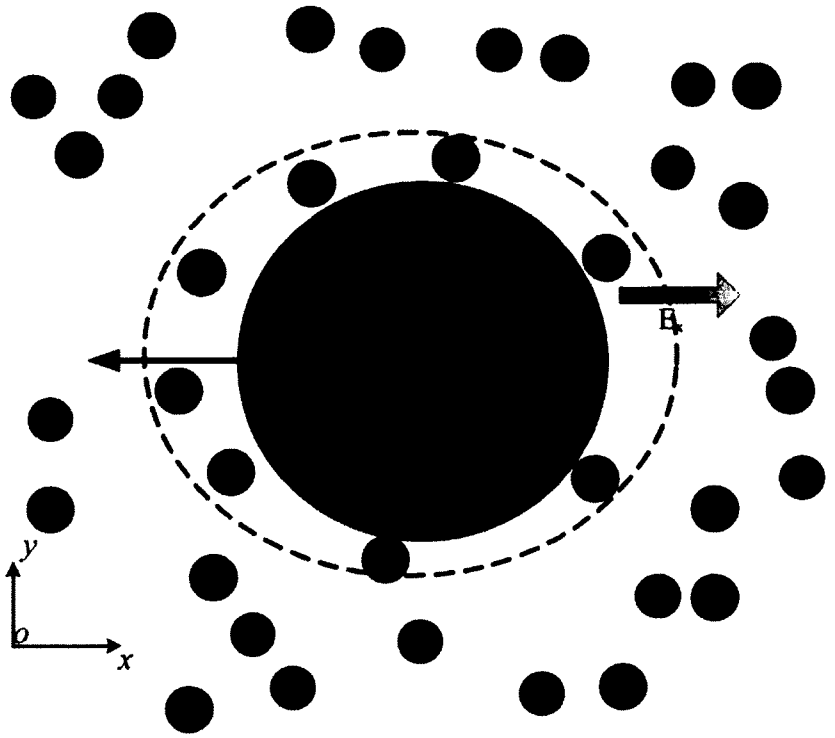

Figure 1.4. Schematic view of electrophoretic motion of a negatively charged particle.

The EOF of the incompressible electrolyte solution is governed by the modified Navier-Stokes (NS) equations by taking into account the electrostatic body force,[73]

$$\rho\left(\frac{\partial \mathbf{u}}{\partial t}+\mathbf{u}\cdot\nabla\mathbf{u}\right)=-\nabla p+\mu\nabla^2\mathbf{u}-\varepsilon_f\nabla^2V\mathbf{E}, \tag{1.9}$$

and the continuity equation

$$\nabla\cdot\mathbf{u}=0, \tag{1.10}$$

where ρ is the fluid density, p is the pressure, and μ is the fluid viscosity. The last term on the right-hand-side (RHS) of Equation (1.9) represents the electrostatic force arising from the electrostatic interaction between the net charge within the EDL and the applied electric field.

When the electric field induced by the surface charges on the solid surface is much stronger than the external applied one, the ionic concentration within the EDL is not distorted by the external field including both the applied electric field and the induced EOF. Therefore, the potential can be linearly decomposed into the potential stemming

from the charged surfaces and the external potential. For the fully developed EOF without external pressure gradient, Equations (1.9) and (1.10) can be simplified as

$$\mu \frac{d^2u}{dy^2} = \varepsilon_f \frac{d^2V}{dy^2}\mathbf{E}, \tag{1.11}$$

where u is the EOF velocity in the x direction, V denotes the potential arising from the charged surface, and $\mathbf{E}$ is the electric field externally imposed. Using the boundary conditions, $u(y = 0) = 0$, $du/dy(y \rightarrow \infty) = 0$, $V(y = 0) = \zeta$ and $dV/dy(y \rightarrow \infty) = 0$, one can easily obtain the velocity u by integrating Eq. (1.11),

$$u = \frac{\varepsilon_f \mathbf{E}}{\mu}\left(V(y) - \zeta\right), \tag{1.12}$$

where $V(y)$ is given by the Gouy-Chapman distribution given by Eq. (1.8). Equation 1.12 depicts that the velocity in the bulk region is a constant, $-\frac{\varepsilon_f \mathbf{E}\zeta}{\mu}$, where the electric potential induced by the charged surface decays to 0. The velocity in the bulk region is also known as the Smoluchowski velocity.[74] Note that the above EOF velocity is not appropriate in the DNA nanoparticle translocation process, where a strong electric field is imposed to achieve high throughput and the EDLs are also overlapped.

1.3.3 Electrophoresis

Electrophoresis refers to the motion of charged particles suspended in an aqueous solution under the influence of an external electric field, as schematically shown in Figure 1.4. Different from EOF in which the charged surfaces are stationary, the charged objects are free to move in electrophoresis.

At the quasi-steady state, the flow field, electric potential, and ionic concentrations can be described by [73]

$$-\nabla p + \mu \nabla^2 \mathbf{u} - \nabla V \sum_{i=1}^{N} F z_i c_i = 0, \tag{1.13}$$

$$\nabla \cdot \mathbf{u} = 0, \tag{1.14}$$

$$-\varepsilon_f \nabla^2 V = \sum_{i=1}^{N} F z_i c_i, \tag{1.15}$$

and

$$\nabla \cdot \mathbf{N}_i = \nabla \cdot \left(\mathbf{u}c_i - D_i \nabla c_i - z_i \frac{D_i}{RT} F c_i \nabla V \right) = 0 . \tag{1.16}$$

Since the Reynolds numbers of electrokinetic flows in nanofluidics are extremely low, the inertial terms in the Navier-Stokes (NS) equations are negligible and the NS equations can be simplified to the Stokes equations. At the quasi-steady state, the particle's electrophoretic velocity will be determined when net force acting on the particle vanishes. However, the equations (1.13)-(1.16) with the force balance equation are strongly coupled.

Under the conditions of the Debye–Hückel approximation and assuming the electric double layer is not distorted, the electrophoretic mobility of a spherical particle of radius a in an unbounded medium can be approximated by the Henry function [75],

$$\eta = \frac{2\varepsilon_f \zeta}{3\mu} f(\kappa a), \tag{1.17}$$

where

$$f(\kappa a) = 1 + \frac{1}{16}(\kappa a)^2 - \frac{5}{48}(\kappa a)^3 - \frac{1}{96}(\kappa a)^4$$
$$+ \frac{1}{96}(\kappa a)^5 + \frac{1}{8}(\kappa a)^4 e^{\kappa a} \left(1 - \frac{(\kappa a)^2}{12} \right) \int_{\kappa a}^{\infty} \left(\frac{e^{-t}}{t} \right) dt . \tag{1.18}$$

Note that the above approximation solution for the particle electrophoretic velocity is valid under the assumptions of low surface potential, weak electric field imposed, and no boundary effect (i.e., infinite fluid medium). During the nanoparticle translocation process, the conditions do not hold, therefore, one has to numerically solve Eq. (1.13)-(1.16).

1.3.4 Induced-Charge Electrokinetics

Recently, electrokinetic flows arising from the interaction between applied electric fields and ideally polarizable channels and particles (i.e. conducting channels and particles), referring to the induced-charged electrokinetics (ICEK), have attracted lots of attention in the micro/nano-fluidics community.[76-78] The main difference between the

conventional electrokinetics and ICEK is the origin of the surface charges. In conventional electrokinetics such as the EOF and electrophoresis described in the above two subsections, the surface charge is gained due to the adsorption or dissociation of specific chemical groups. However, the surface charge in ICEK arises from the polarization of materials. The induced surface charge of an ideally polarizable material is generally dipolar, as shown in Figure 1.5, in which the negative surface charge is induced near the anode while the positive surface charge is generated near the side of the cathode. However, the net induced surface charge is zero and the electric potential of the conducting material is a constant. The characteristic time scale of the induced surface charging is on the order of $a\lambda_D / D$, where a is the characteristic length of the ideally polarizable material and D is the ionic diffusivity. Figure 1.5 shows that the flow field around a circular conducting particle is a quadrupolar EOF, which moves toward the particle along the field axis and then leaves the particle radically. The induced zeta potential is not a constant, however, varies along the surface with an order of aE_∞. Therefore, the electroosmotic slip velocity of ICEK is proportional to the square of the electric field strength, $u \propto -\varepsilon_0 \varepsilon_f a E_\infty^2 / \mu$. Obviously, ICEK is a non-linear electrokinetic phenomenon. As the induced zeta potential is tunable through the externally applied electric field and the geometry, ICEK-based microfluidics holds more versatile and sophisticated manipulations of fluids and suspended particles. So far, ICEK has been successfully utilized to generate circulating flows for fluid stirring and mixing in microfluidics. [79-82] Very recently, particle enrichment and trapping have also been experimentally demonstrated using the ICEK technique.[83-85] Chapter 5 reviews the propose use of ICEK on a floating electrode coated on the inner surface of the nanopore to control nanoparticle translocation.

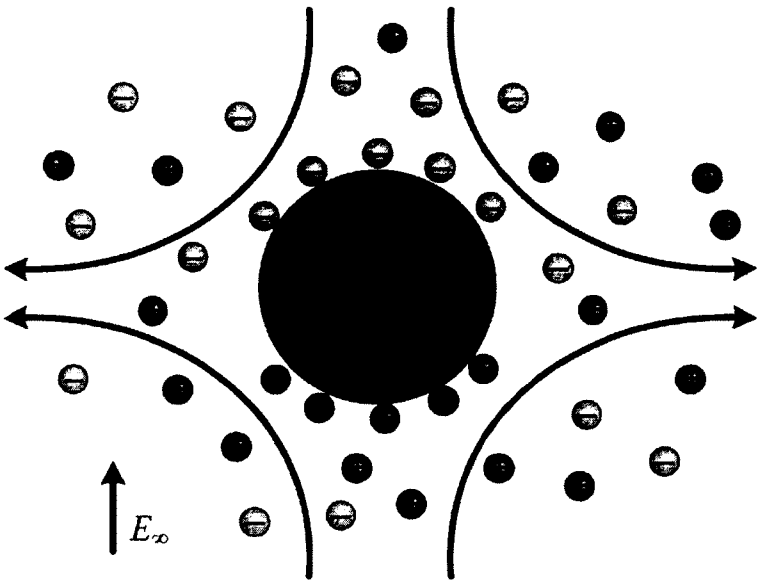

Figure 1.5. Schematics of induced-charge electroosmosis around a conducting particle.

1.4. Organization of the Dissertation

A comprehensive understanding of the electrokinetic fluid and particle transport in nanofluidics is crucial to the development of the next generation nanopore-based DNA sequencing technology. Therefore, this dissertation research consisted of comprehensive numerical studies of electrokinetic flow and particle transport in nanofluidics. Chapter 1 briefly discusses nanofluidics and its applications with the focus on the DNA translocation through a nanopore. This chapter also briefly reviews the basic theories of electrokinetics. The rest of this dissertation can be divided into two parts, electrokinetic ions and fluid transport in nanofluidics (Chapter 2 and Chapter 3), and electrokinetic particles transport in nanofluidics (Chapter 4-8). Chapter 2 investigates electrokinetic flow and ion transport in a nanopore functionalized by polyelectrolyte. Chapter 3 investigates electrokinetic flow and ion transport in a charge–regulated nanopore. Chapter 4 investigates electrophoretic motion of a soft nanoparticle in a nanopore using numerical simulation. Based on the knowledge obtained from Chapter 2, a novel soft nanopore comprising a solid-state nanopore and a functionalized soft layer is proposed to regulate the DNA electrokinetic translocation, which is described in Chapter 5.

Regulation of DNA translocation by a floating electrode coated on the inner nanopore wall is described in Chapter 6. Chapter 7 investigates the local permittivity environment effect on the DNA electrokinetic translocation through a nanopore. Chapter 8 studies translocation of a charged-regulated protein through a soft nanopore. The last chapter is Chapter 9, which concludes the thesis and provides future work related to this thesis.

CHAPTER 2

ELECTROKINETIC ION AND FLUID TRANSPORT IN POLYELECTROLYTE BRUSHES-FUNCTIONALIZED NANOPORES

Abstract

Chemically functionalized nanopores in solid-state membranes have recently emerged as versatile tools for regulating ion transport and sensing single biomolecules. In this chapter, we theoretically studied the importance of the bulk salt concentration, the geometries of the nanopore, and the thickness and fixed charges of the polyelectrolyte (PE) brushes layer on the electrokinetic ion and fluid transport in two types of PE modified nanopores: the PE layer is end-grafted to the overall wall surface of the membrane (system I) and it is only end-grafted to the inner wall surface of the nanopore (system II). Due to more significant ion concentration polarization (CP) occurring in the system II, the variations of the enhanced local electric field, the conductance and the electroosmotic flow (EOF) velocity in the system II are remarkably larger than those in the system I. In the system I, in addition to a significantly enhanced EOF occurring inside the nanopore, the flow field near both openings of the nanopore is opposite to the EOF inside the nanopore. The flow field in the system I can be further used to regulate the electrokinetic translocation of biomolecules through them.

2.1. Introduction

Electrokinetic transport of ions and fluid in nanoscale pores or channels plays an important role in modern biophysics and biochemistry due to the growing desires and interests to understand the real physiological process in living organisms and to develop them for engineering applications.[86-87] In nanofluidic devices whose characteristic length is comparable to the thickness of the electric double layer (EDL), several fascinating features, such as ion selectivity,[88] ion concentration polarization (CP),[89-90] and ionic current rectification (ICR),[91-93] were observed experimentally. Potential applications based on these electric-field-induced ion and fluid transport phenomena include energy

conservation,[94] desalination of seawater,[95] concentration and separation of biomolecules,[96] and nanofluidic diodes,[12] to name a few. Fundamental understanding the electrokinetic flow and ion transport inside the nanopores promotes to develop novel nanofluidic devices, such as the next generation nanopore-based DNA sequencing platform.

Inspired by nature, in recent years polyelectrolyte (PE) brushes-functionalized nanopores, synthetic nanopores chemically modified by synthetic[97-102] or biological polyelectrolytes,[34, 42-43, 103-105] have attracted considerable attentions in using them as a versatile tool to rectify ionic transport[97-104] as well as to detect and analyze individual biomacromolecules[34, 42-43, 105]. All of these applications are based on the variation of the resistive ionic current pluses when a potential bias is applied across the nanopore. Comparing to the large number of experimental studies,[34, 42-43, 97-105] a comprehensive theoretical analysis on electrokinetic ion transport in PE brushes-functionalized nanopores is still very limited.

Typically the electrokinetic flow in a microchannel can be analyzed based on the Poisson-Boltzmann (PB) equation,[106-107] where the distribution of the ionic concentrations follows the Boltzmann distribution. However, the PB model, based on the assumptions of equilibrium EDL, electroneutrality existing far away from the charged surface, and non-overlapping EDLs,[108] fails to describe the fascinating features aforementioned due to the significant overlapping of EDLs and the non-equilibrium EDLs resulting in uneven distributions of coions and counterions inside the nanopore.[86-87] Recently, a continuum model based on the Poisson-Nernst-Planck (PNP) equations has been developed and widely used to describe the ionic mass transport phenomena in nanopores or nanochannels.[14, 109-116] A remarkable agreement between the theoretical predictions obtained from the PNP model and the existing experimental results suggests that the PNP model is capable of capturing and elucidating the essential physics of the electrokinetic ion transport phenomena in nanopores with radii larger than 3 nm.[114-117] It was also demonstrated by Corry et al.[118] that in channels with radii larger than 1 nm, the results based on the PNP model agree well with those of Brownian dynamic simulations.

In this chapter, a continuum-based model, composed of the coupled PNP equations for the ionic mass transport and the Stokes and Brinkman equations for the flow fields in the

exterior and interior of the PE layer, is developed to comprehensively investigate for the first time the electric field induced electrokinetic ion and fluid transport in PE brushes-functionalized nanopores. The effects of several important factors, including the coverage of the PE layer on the membrane wall surface, the bulk salt concentration, the geometry of the nanopore, and the thickness and fixed charge of the PE layer, on the resulting electrokinetic ion and fluid transport are investigated. The results show that the conductance and EOF are distinctly different for the PE layers coated on the overall membrane wall surface and only coated on the inner wall surface of the nanopore.

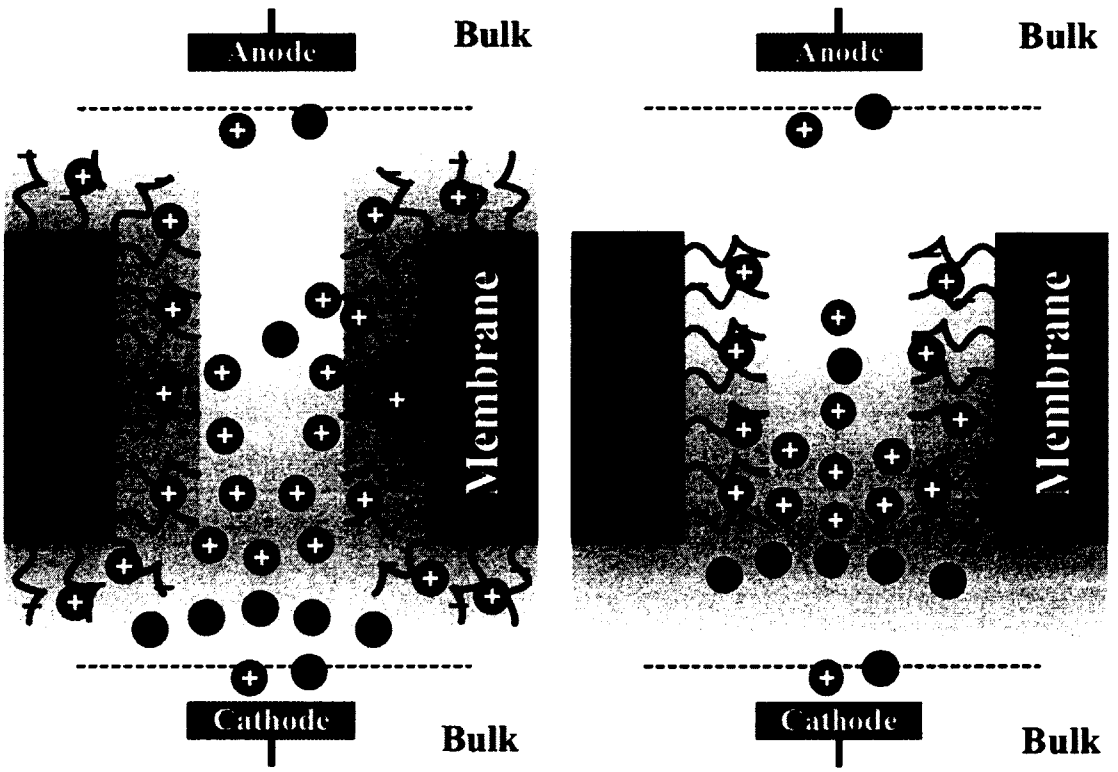

Figure 2.1. Schematic illustrations of ion CP phenomenon in PE modified nanopores. The overall wall surface of the membrane (a) and only the inner wall surface of the membrane (b) are modified with negatively charged PE brushes.

2.2. Theoretical Modeling

As schematically shown in Figure 2.1, two types of PE brushes-functionalized nanopore are considered in this chapter. System I (Fig.1a) consists of a rigid, cylindrical nanopore

of length L_N and radius R_N connected to two large, identical reservoirs on either side, and the PE layer, is end-grafted to the whole wall surface of the membrane. In contrast, the PE layer is only end-grafted on the inner wall surface of the nanopore so there are no PE layer on the side wall of the membrane in system II (Figure 2.1b). For simplicity, we assume the PE layer is ion-penetrable, homogeneously structured, highly charged (non-regulated), and of uniform thickness R_s, which yields a fixed charge $\rho_{fix} \cong (eZ\sigma_s / R_s)$ density with e, Z, and σ_s being the elementary charge, the valance of the dissociable groups per PE chain, and the PE chain surface density grafted to the membrane, respectively. In addition, the possible molecular morphology deformation of the PE brushes[119-120] is neglected. The value of σ_{PE} typically ranges from 0.1 to 0.6 nm^{-2}.[119-121] The nanopore and two reservoirs are filled with an aqueous binary electrolyte solution (i.e., KCl electrolyte solution). Due to the symmetric nature of the present problems, the cylindrical coordinate (r, z) with the origin fixed at the center of the nanopore is adopted. A verified continuum-based model[109, 117, 122] is employed to describe the electrokinetic ion transport and flow field in the present problems:

(i) Poisson-Nernst-Planck (PNP) equations for the potential distribution and ionic mass transport:[109, 117, 122]

$$-\nabla^2 V = \frac{h\rho_{fix} + \rho_e}{\varepsilon_f},\ h=0 \text{ or } 1, \tag{2.1}$$

$$\mathbf{N}_j = \mathbf{u}c_j - D_j \nabla c_j - z_j \frac{D_j}{RT} F c_j \nabla V, \tag{2.2}$$

$$\nabla \cdot \mathbf{N}_j = 0. \tag{2.3}$$

Here, V is the electric potential; $\mathbf{u} = u\mathbf{e}_r + v\mathbf{e}_z$ is the fluid velocity with $\mathbf{e}_r$ and $\mathbf{e}_z$ being, respectively, the unit vectors in the r- and z-directions; $\rho_e = \sum_j F z_j c_j$ is the space charge density of the mobile ions; $\mathbf{N}_j$, c_j, D_j, and z_j are the flux density, concentration, diffusivity, and valence of the j^{th} ionic species, respectively, (j=1 for cations, and 2 for anions), ε_f, F, R, and T are the fluid permittivity, the Faraday constant, the universal gas constant, and the absolute temperature, respectively. h is a unit region function (h=0, the region outside the PE layer; h=1, inside the PE layer). Note that the first, second, and

third terms on the right-hand side of Eq. (2.2) denote contributions from the convective, diffusional, and migrational flux densities, respectively.[123]

(ii) Modified Stokes and Brinkman equations for the flow field of the incompressible fluid:[117, 124-125]

$$-\nabla p + \mu\nabla^2\mathbf{u} - \rho_e\nabla V - h\gamma\mathbf{u} = 0 \ , \tag{2.4}$$

$$\nabla\cdot\mathbf{u} = 0, \tag{2.5}$$

where p, μ, and γ are the hydrodynamic pressure, the fluid viscosity, and the hydrodynamic frictional coefficient of the PE layer, respectively.

To specify the boundary equations associated with Eqs (2.1), (2.3), (2.4), and (2.5), we assume the following. (i) The rigid surface of the membrane is non-slip ($\mathbf{u} = \mathbf{0}$), ion-impenetrable ($\mathbf{n}\cdot\mathbf{N}_j = 0$) and uncharged ($-\varepsilon_f\mathbf{n}\cdot\nabla V = \sigma_w = 0$), where σ_w is the surface charge density on the membrane wall and $\mathbf{n}$ is the unit outer normal vector. (ii) The ionic concentrations at both ends of the two large reservoirs are maintained at their bulk values, $c_j = C_{j0} = C_0$, and the electric potential there are $V(cathode) = 0$ and $V(anode) = V_0$. A normal flow without external pressure gradient is specified at the ends of the two big reservoirs.[52] (iii) The electric potential and field, ionic concentrations, and flow field are all continuous on the PE layer/liquid interface.[124-125] Moreover, slip boundary condition for the flow field, insulation boundary condition for the potential, and zero normal ionic fluxes are imposed at the side boundaries of the two reservoirs, which are far away from the nanopore. Symmetric boundary condition is specified along the axis of the nanopore.

The cross-sectional averaged EOF velocity, $\bar{v}$, and conductance, G, through the nanopore are, respectively, evaluated by

$$\bar{v} = \int_S \mathbf{u}\cdot\mathbf{n}dS \Big/ \pi R_N^{\,2} \ , \tag{2.6}$$

$$G = I/V_0 = \int_S F(\sum_{j=1}^{2} z_j\mathbf{N}_j)\cdot\mathbf{n}dS \Big/ V_0 \ . \tag{2.7}$$

Here, I is the ionic current flowing through the nanopore, and S denotes either end of the reservoirs due to the conservation of the ionic current.

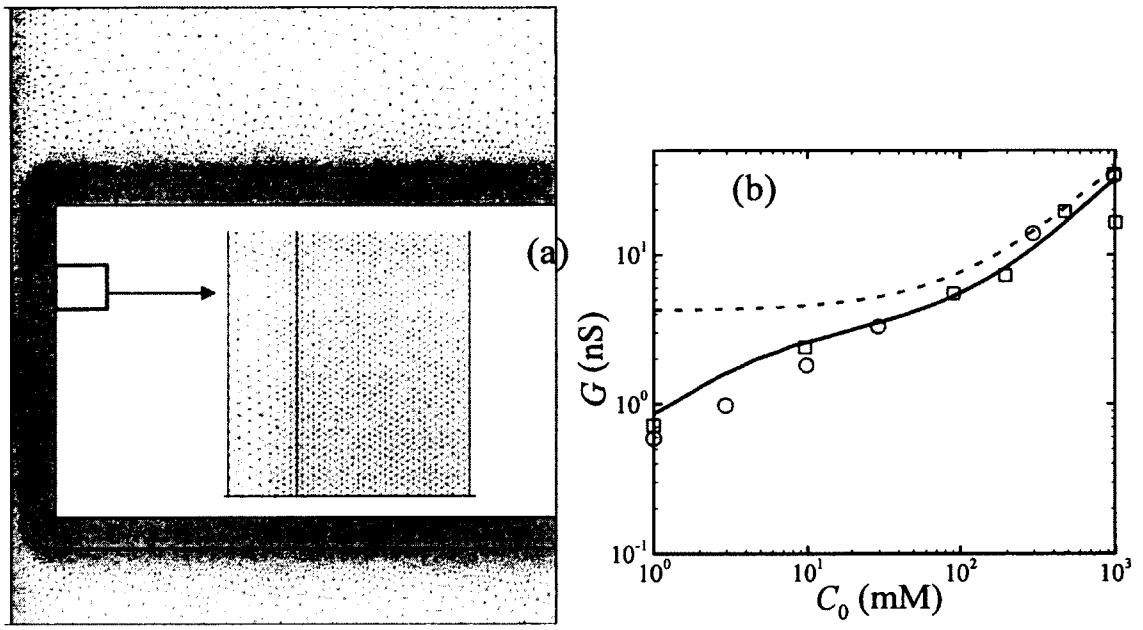

Figure 2.2. (a): the meshes used in the simulation with enlarged finer mesh in the PE layer. (b): the dependence of conductance in a silica nanopore on the bulk salt concentration. Solid line represents the present numerical result for $R_N = 5.5\,\text{nm}$ and surface charge density of the nanopore $\sigma_w = -60\,\text{mC/m}^2$. Dashed line denotes analytical result of Eq. (2.8), and discrete symbols correspond to the experiment data of Smeets et al.[38]

2.3. Results and Discussion

2.3.1 Numerical Method and Code Validation

The strongly coupled non-linear equations, (2.1), (2.3), (2.4), and (2.5), and the associated boundary conditions are numerically solved by the commercial finite element package, COMSOL Multiphysics (version 3.5a, www.comsol.com) operating in a high-performance cluster. The computational domain is discretized into quadratic triangular elements. Nonuniform elements are employed with larger numbers of elements assigned locally as necessary. Typically the total number of elements for system I and II are approximately 210,000 and 100,000, respectively, with finer mesh in the PE layer to capture the EDL as shown in Figure 2.2(a). Lagrange – Quadratic elements are used for solving PNP equations, while Lagrange – P_2P_1 elements are for the Stokes and Brinkman

equations. The ionic current through the nanopore is obtained by using the weak constrain in COMSOL specially developed for an accurate calculation of flux. Rigorous mesh-refinement tests have been performed to ensure that the solutions obtained are convergent and grid independent. A maximum tolerance of 0.1% is imposed on the relative difference $(|I_a| - |I_c|)/|I_a|$, where I_a and I_c are respectively the current entering (anode) and leaving (cathode) the nanopore. The numerical scheme has been validated to be sufficiently efficient and accurate for solving similar electrokinetic problems, such as the electrokinetic ion transport in a solid-state nanopore[14, 109-113] and the electrokinetic rigid and soft nanoparticle translocation through a nanopore.[52, 115-117, 122, 126]

To further verify the applicability of the present numerical model, it is first used to predict the conductance of a silica solid-state nanopore with L_N=34 nm and $R_N = 5 \pm 1\,\text{nm}$ at the potential bias $V_0 = 200\,\text{mV}$, and its results are compared to the experimental data of Smeets et al.[38] To simulate the solid-state nanopore, we specify $\gamma = 0$ and consider the surface charge on the nanopore stemming only from the surface charge density, σ_w. Figure 2.2(b) depicts the nanopore conductance as a function of the bulk salt concentration, C_0. For comparison, we also present the corresponding approximate result of Smeets et al[38] (dashed line in Figure 2.2(b)),

$$G = \frac{\pi R_N^2}{L_N}\left[(\mu_1 + \mu_2)C_0 F + \mu_1 \frac{2|\sigma_w|}{R_N}\right], \tag{2.8}$$

where $\mu_1(\text{K}^+) = 7.571\times10^{-8}\ \text{m}^2/\text{sV}$ and $\mu_2(\text{Cl}^-) = 7.861\times10^{-8}\ \text{m}^2/\text{sV}$ are, respectively, the electrophoretic mobilities of cations and anions based on the fluid temperature T=300 K. The first and second terms in the square bracket on the right-hand side (RHS) of Eq. (2.8) denote the contributions from the bulk electrolyte solution and the surface charge density of the nanopore, respectively. In general, if the salt concentration is high the nanopore conductance is dominated by the first term in the square bracket on the RHS of Eq. (2.8), while the nanopore conductance is influenced by the second term if the salt concentration is sufficiently low. Figure 2.2(b) clearly shows that the result of the present numerical model (solid line) with the parameters, $R_N = 5.5\,\text{nm}$ and $\sigma_w = -60\,\text{mC/m}^2$, are in good agreement with the experimental data (discrete symbols). However, the analytical result based on Eq. (2.8) (dashed line) fails to describe the general trend of the nanopore

conductance, especially when the salt concentration is relatively low. The behavior at low salt concentration can be attributed to the CP effect since the EDL overlapping becomes significant, as will be explained in detail later. It should be pointed out that the estimated value of $\sigma_w = -60\ \mathrm{mC/m^2}$ matches very well with the typical value of the silica nanopore reported in the literature.[127] The present analysis is capable of providing a sound interpretation of the general electrokinetic ion transport behavior of the nanopore that is essential to the design of relevant nanofluidic devices.

In subsequent discussions, the influences of some key parameters, including the coverage of the PE layer on the membrane wall surface (the systems I and II), the bulk salt concentration (C_0), the geometry of the nanopore (L_N and R_N), and the thickness and fixed charge of the PE layer (ρ_{fix}), on the electrokinetic ion and fluid transport phenomena are investigated in detail. The physical parameters used in the simulations are $\varepsilon_f = 7.08\times10^{-10}$ F/m, $\eta = 1\times10^{-3}$ Pa·s, F=96490 C/mol, R=8.314 $\mathrm{JK^{-1}mol^{-1}}$, T=300K, $Z = -2$, $D_1(\mathrm{K^+}) = 1.957\times10^{-9}\ \mathrm{m^2/s}$, and $D_2(\mathrm{Cl^-}) = 2.032\times10^{-9}\ \mathrm{m^2/s}$. Although the softness degree of the PE layer, $\lambda^{-1} = (\eta/\gamma)^{1/2}$,[128] affects the hydrodynamic field inside the nanopore, the ionic current is not affected significantly by the flow field.[56, 117] Therefore, we fix $\lambda^{-1} = 1\,\mathrm{nm}$, corresponding to the typical values of PEs (ca. 0.1~10 nm)[124, 129], in this chapter. The potential bias, $V_0 = 200\,\mathrm{mV}$ [38], is applied across the nanopore.

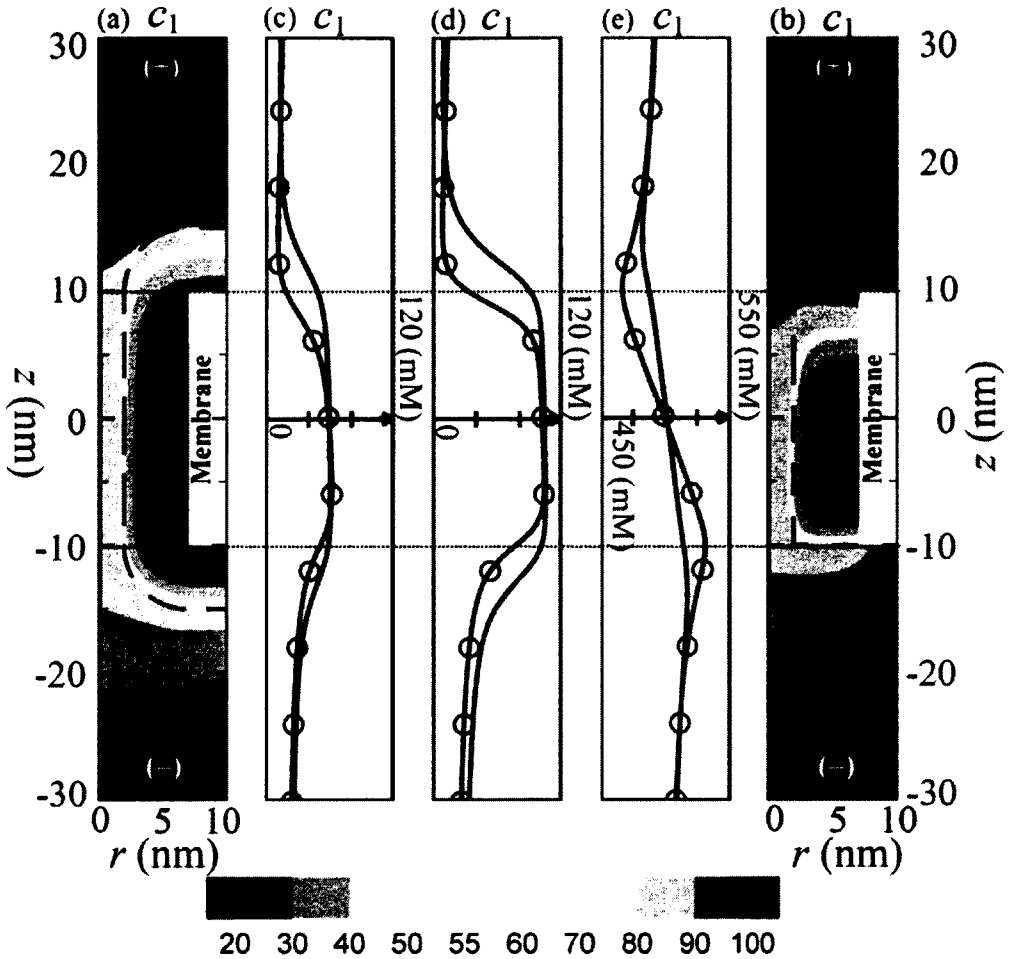

Figure 2.3. Spatial distribution of the concentration of cations, c_1, in the systems I (a) and II (b) for $\rho_{fix} = -0.91 \times 10^7$ C/m^3 and $C_0 = 20$ mM. The dashed lines in (a) and (b) denote the outer boundary of the PE layer. Distribution of c_1 along the axis of the nanopore for $\rho_{fix} = -0.91 \times 10^7$ C/m^3 and $C_0 = 20$ mM (c), $\rho_{fix} = -2.73 \times 10^7$ C/m^3 and $C_0 = 20$ mM (d), $\rho_{fix} = -0.91 \times 10^7$ C/m^3 and $C_0 = 500$ mM (e). Lines and lines with symbols represent the results of the system I and II, respectively.

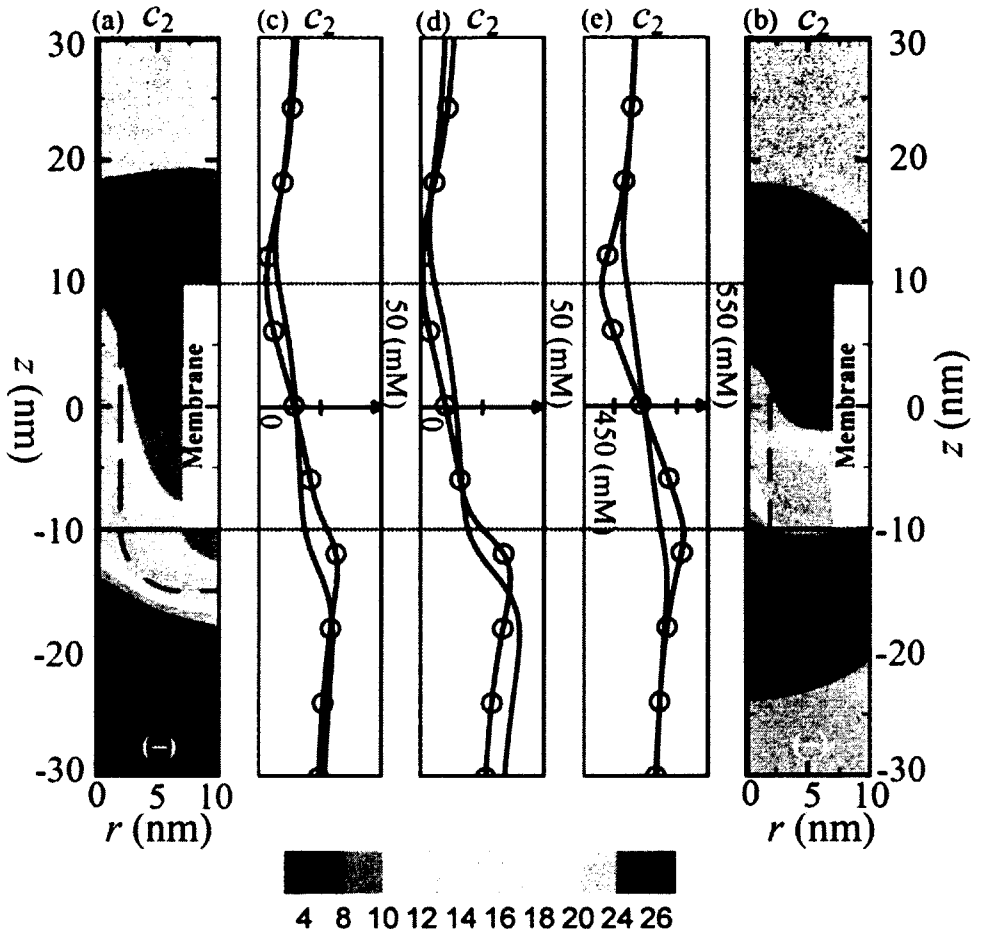

Figure 2.4. Distributions of the concentration of anions, c_2, in the systems I (a) and II (b). Lines and lines with circles in (c)-(e) represent the results for the systems I and II, respectively. The conditions are the same as those in Figure 2.3.

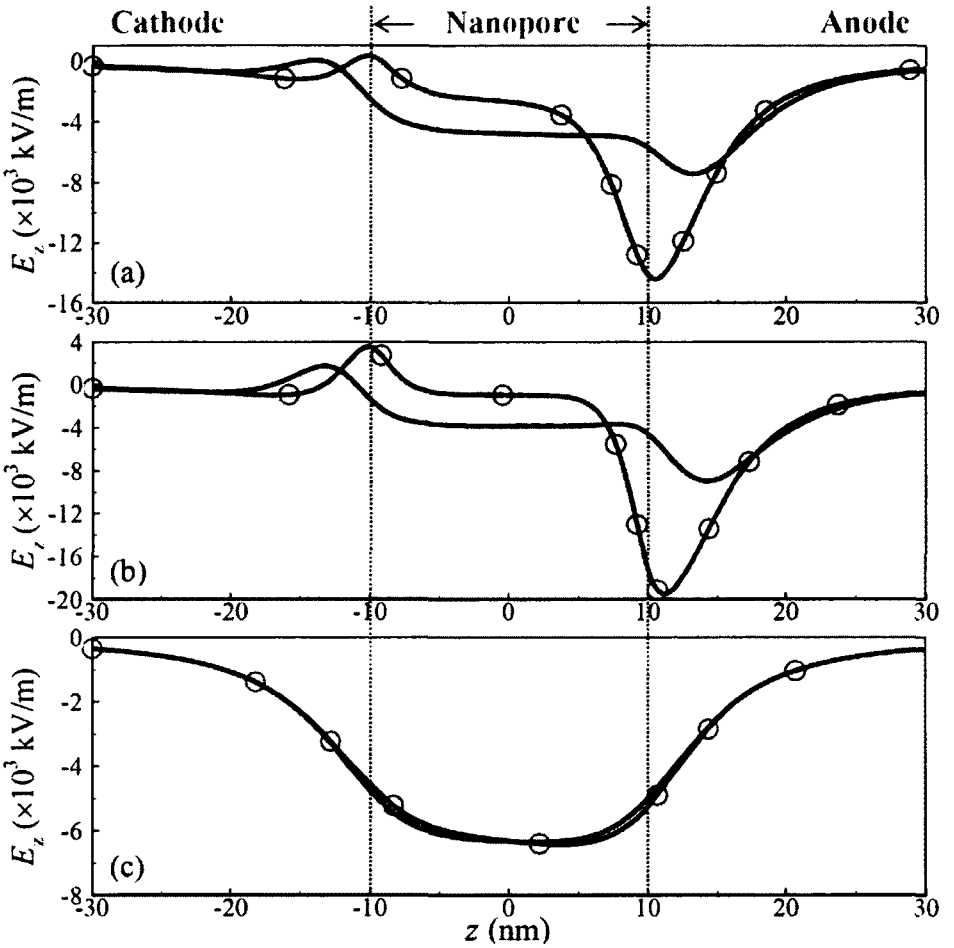

Figure 2.5. Axial electric field along the axis of the nanopore, $E_z = -\partial V(0,z)/\partial z$, for the corresponding cases of Figires 2.3(c)-(e). Lines and lines with circles represent the results of the systems I and II, respectively.

2.3.1 Ion Concentration Polarization (CP) and Local Axial Electric Field

When an external electric field is applied through the nanopore, cations (anions) migrate from the anode (cathode) side toward the cathode (anode) side, resulting in ion CP phenomenon occurring near both openings of the nanopore. Both cations and anions are enriched (depleted) near the opening of the cathode (anode) side, as schematically shown in Fig.1. It is generally accepted that the ion CP arises mainly from the selective transport of ions inside the nanopore due to the overlapping of EDLs.[123] To comprehensively understand the ion CP phenomena in various PE brushes-functionalized

nanopores, Figures 2.3 and 2.4 depict, respectively, the spatial distributions of the concentrations of cations and anions in the systems I (a) and II (b). Solid lines without and with circles in (c)-(e) of Figures 2.3 and 2.4 represent, respectively, the variations of the ionic concentrations of the cations (Figure 2.3) and anions (Figure 2.4) along the axis of the nanopore in the systems I and II. Since the fixed charge density of the PE layer is negative, more counterions (i.e. cations) are electrostatically attracted into the nanopore, whereas coions (i.e. anions) are repelled out. Therefore, the magnitude of the transport flux of the cations (anions) inside the nanopore is significantly larger (smaller) than those in both reservoirs at the cathode and anode sides, resulting in enrichment (depletion) of concentrations of cations and anions at the cathode (anode) side of the nanopore. These two figures also show that the degree of the ion CP, quantified by the difference of the concentrations of cations (or anions) at both openings of the nanopore, in the system II is more significant than that in the system I, yielding more enriched (depleted) ions at the cathode (anode) opening of the nanopore. The concentration differences of the cations, $\Delta c_1 = c_1(0,-L_N/2) - c_1(0,L_N/2)$, and the anions, $\Delta c_2 = c_2(0,-L_N/2) - c_2(0,L_N/2)$, at the openings of the nanopore for the cases of Figures 2.3(c)-2.3(e) and 2.4(c)-2.4(e) are summarized in Table 1. In general, the Δc_j in the system II is remarkably higher than that in the system I, implying more significant ion CP phenomenon in the system II. This interesting phenomenon can be attributed to stronger equilibrium electric field stemming from the charged PE layer in the system I, which captures more counterions inside the PE layer.

To explain the influences of the bulk salt concentration C_0 and the fixed charge density of the PE layer, ρ_{fix}, on the ion CP in the PE-modified nanopores, we define a factor, $\Delta c_j / C_0$, and summarize their results for the cases of Figures 2.3(c)-2.3(e) and 2.4(c)-2.4(e) in Table 1. Degree of the ion CP becomes more significant with higher value of $\Delta c_j / C_0$. We find that the larger the ρ_{fix} and/or the smaller the C_0, the more significant the ion CP is. The former is expected because the concentration of counterions gathered inside the nanopore increases with increasing ρ_{fix}. The latter arises from the fact that the thickness of EDL increases with decreasing C_0, yielding more significant EDL

overlapping. It should be pointed out that the induced ion CP behavior plays an essential role in the study of the electrokinetic ion transport in nanopores. Not only the local ionic concentrations but also the local electric and flow fields near the openings of the nanopore can be affected by the ion CP, which will be discussed later.

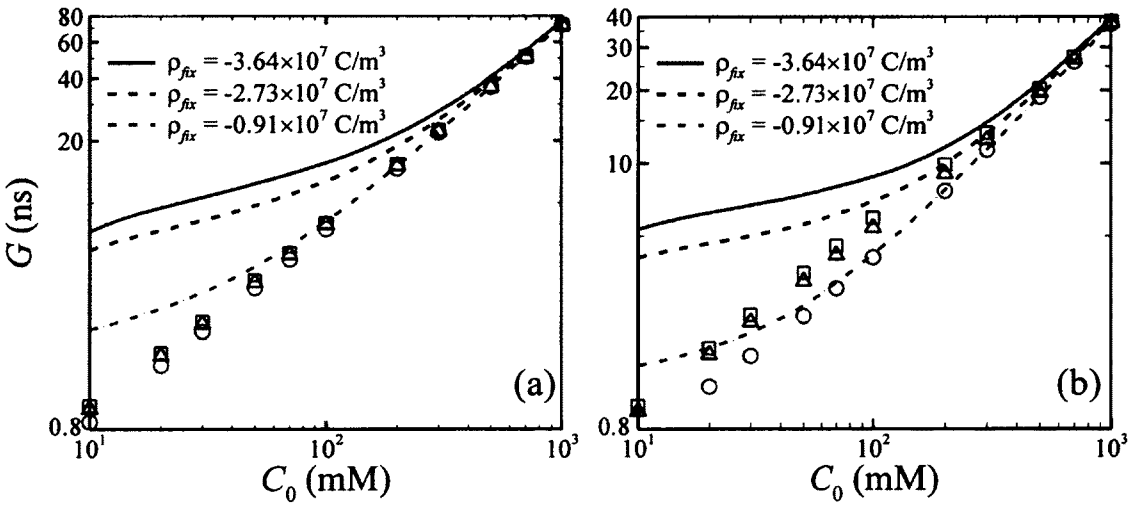

Figure 2.6. Conductance as a function of the bulk salt concentration, C_0, at various fixed charge density, ρ_{fix}, when the pore length $L_N = 20$ nm (a) and 50 nm (b), R_N=7 nm, and R_s=5 nm. Lines represent the results of the system I. squares, triangles, and circles represent the results in the system II with $\rho_{fix} = -3.64$, -2.73, and -0.91×10^7 C/m^3, respectively.

Figure 2.5 shows the influences of both C_0 and ρ_{fix} on the axial electric field along the axis of the nanopore, $E_z = \partial V(0,z)/\partial z$, in the systems I (solid lines) and II (solid lines with circles). These figures depict that the variation of the local electric field in the system II is more significant than that in the system I due to stronger ion CP occurring in the system II. When the bulk salt concentration, C_0, is relatively low (a) and (b), the axial electric field inside the nanopore for the system II is lower than that for the system I. In both systems, a positive local electric field occurs near the cathode side of the nanopore, while the local electric field near the anode side of the nanopore is significantly enhanced. The amplified local electric field near the anode side has been experimentally observed

by Kim et al.,[130] and they attributed this to the significant depletion of ions at that region. Due to mismatch of the cross-sectional areas of the nanopore and the fluid reservoirs, typically the local electric field inside the nanopore is much higher than that inside the reservoirs, which has been experimentally observed[86, 131]. The momentarily positive local electric field occurring at the cathode side of the nanopore has not been reported in the literature, and we believe it is attributed to the enriched ions at the cathode side of the nanopore. The enriched (depleted) ions at the cathode (anode) side of the nanopore generate an electric field opposite to the externally imposed one. The induced electric field increases as the degree of ion CP increases. Since the ion CP in the system II is more significant than that in the system I, resulting in higher induced electric field and accordingly lower net electric field inside the nanopore of the system II. Due to the significantly enriched ions at the cathode side, the magnitude of the induced electric field is even larger than the applied one, leading to the momentarily positive local electric field in that region. The local electric field inside the nanopore is highly asymmetric, as shown in Figures 2.5a and 2.5b, due to the significant CP effect occurring near the nanopore openings, suggesting that using the Poisson-Boltzmann equation usually adopted in the literatures [127, 132-134] to simulate the electrokinetic ion transport phenomena in nanofluidics is inapplicable. The induced ion CP becomes insignificant when the bulk concentration C_0 is sufficiently high due to thin EDL and accordingly no EDL overlapping, under this condition the momentarily positive electric field at the cathode side and the significantly enhanced electric field at the anode side vanish, as shown in Figure 2.5c. The electric fields in the systems I and II are almost identical, and the local electric field inside the nanopore is larger than that in the fluid reservoir mainly due to the mismatch of the cross-sectional areas. Comparing 2.5a and 2.5c, the local electric field at the center of the nanopore for C_0=500 mM is much higher than that for C_0=20 mM, which is attributed to the insignificant ion CP and the induced opposite electric field by the ion CP for C_0=500 mM is much lower than that for C_0=20 mM. Comparison between 2.5a and 2.5b shows that the magnitudes of the momentarily positive electric field at the cathode side and the enhanced electric field at the anode side for ρ_{fix}=−2.73×10^7 C/m^3 are higher than those for ρ_{fix}=−0.91×10^7 C/m^3 due to more significant ion CP at higher fixed charge density of the PE layer.

2.3.2 Nanopore Conductance

Figure 2.6 depicts the conductance in PE brushes-functionalized nanopores as a function of bulk salt concentration C_0 at various fixed charge density of the PE layer ρ_{fix} when the nanopore length L_N=20 nm (a) and 50 nm (b). Lines and symbols denote the results for the systems I and II, respectively. As expected, the nanopore conductance increases with increasing C_0 in both systems. The dependence of the conductance on the fixed charge density ρ_{fix} is insignificant in the system II especially in a short nanopore as shown in Fig.6a, while ρ_{fix} significantly affects the conductance of the system I. In addition, if C_0 is relatively low the conductance for the system I decreases nonlinearly with the decrease in C_0 due to the increase in the contribution of the accumulated counterions inside the nanopore; however, this nonlinear behavior vanishes in the system II. Comparing to the system I, the ability of concentrating counterions inside the nanopore of the system II is weaker due to lower equilibrium electric field stemming from the charged PE layer. Therefore, the contribution of the nanopore's charge to the conductance of the PE-modified nanopore in the system II is weaker, especially when the nanopore is very short, as shown in Fig.6a. Comparisons between the results for L_N=20 nM and 50 nM in the system II show that the dependence of the conductance on ρ_{fix} for L_N= 50 nM is more significant than that for L_N=20 nM, which is attributed to the increase in the concentrated counterions inside a longer nanopore. Figure 2.6 also reveals that the conductance for the system I (lines) is remarkably higher than that for the system II (symbols). This is because the induced ion CP in the system I is less significant than that in the system II, as shown in Figures 2.3 and 2.4, resulting in more counterions accumulated inside the nanopore of the system I.

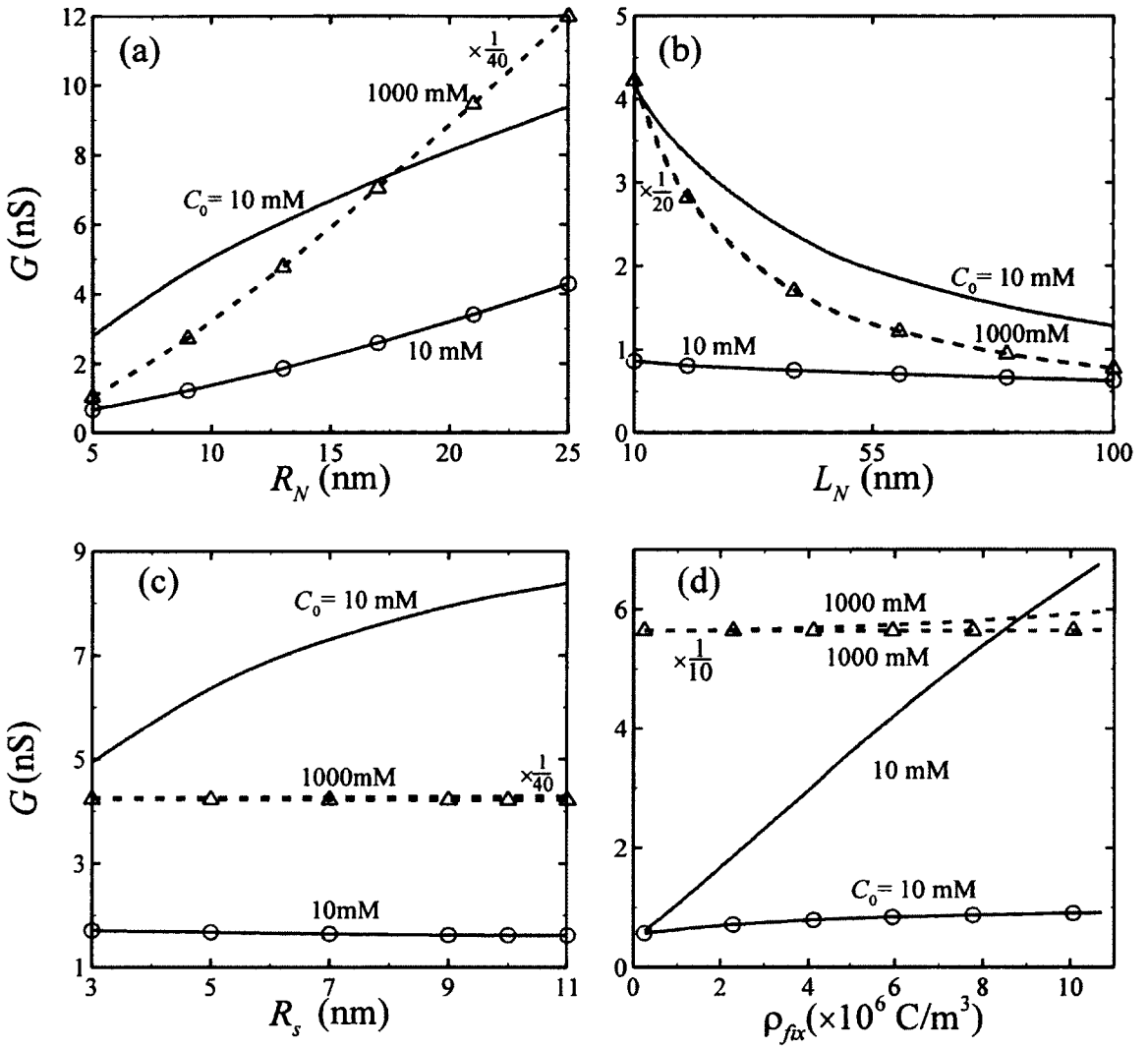

Figure 2.7. Conductance as a function of the nanopore radius R_N (a), the nanopore length L_N (b), the thickness of the PE layer R_S (c), and the fixed charge density of the PE layer ρ_{fix} (d) when C_0=10 mM (solid lines) and 1000 mM (dashed lines). (a): ρ_{fix}= -1.82×10^{7}C/m^3, L_N = 20 nm, and R_s = 4 nm; (b): ρ_{fix}= -1.82×10^{7}C/m^3, R_N= 6 nm, and R_s = 4 nm; (c): ρ_{fix}= -1.82×10^{7}C/m^3, L_N = 20 nm and R_N= 12 nm; (d) L_N = 20 nm, R_N= 6 nm, and R_s = 4 nm. Lines and lines with circles represent the results of the systems I and II, respectively. A scale of 1/40, 1/20, 1/40, and 1/10 are applied to the lines with circles in (a), (b), (c), and (d), repectivly.

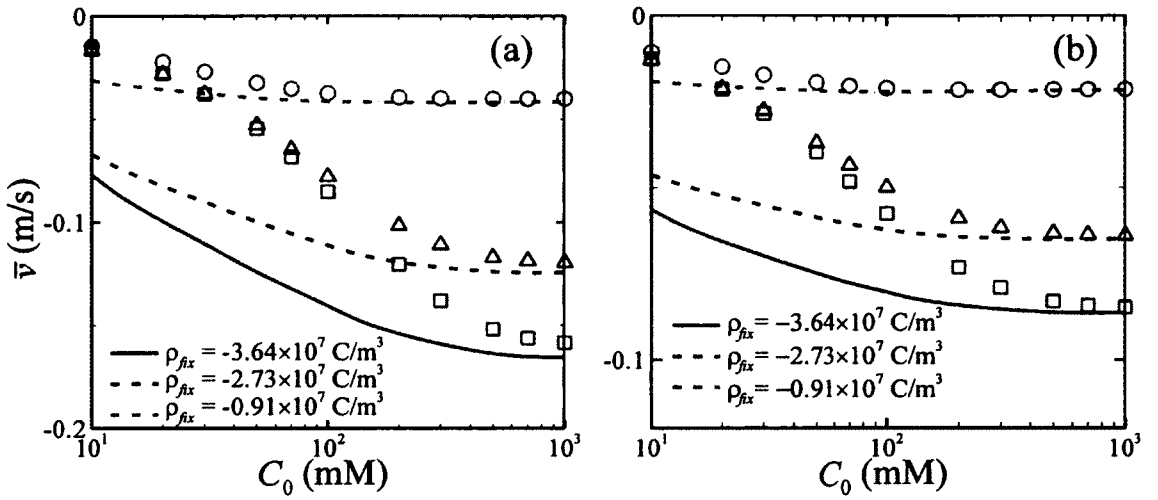

Figure 2.8. Cross sectionally averaged EOF velocity at the cross section z=0 as a function of the bulk salt concentration C_0 at various fixed charge density ρ_{fix} when $L_N = 20$ nm (a) and 50 nm (b). Other conditions are the same as those in Figure 2.6. Lines and lines with symbols represent the results of the system I and II, respectively.

The influences of the nanopore radius R_N, nanopore length L_N, PE layer thickness R_s, and fixed charge density ρ_{fix} on the conductance in PE brushes-functionalized nanopores for two levels of C_0 are shown in Figure 2.7. Lines without and with circles denote the results for the systems I and II, respectively. The general behaviors of the nanopore conductance observed in Figure 2.7 can be explained by Eq. (2.8). The conductance increases with increasing R_N(a), R_s(c), and ρ_{fix} (d), and decreases with increasing L_N(b). Note that larger thickness of the PE layer (R_s) also represents higher surface charge on the nanopore. Figure 2.7 also reveals that if C_0 is relatively low (i.e. 10 mM), the conductance in the system II is remarkably lower than that in the system I due to more significant ion CP occurring in the system II; however, the conductance between the systems I and II are nearly identical if C_0 is sufficiently high (i.e. 1000 mM) due to thin EDL and weak ion CP. If C_0 is relatively low, the influences of R_N, L_N, R_s, and ρ_{fix} on the nanopore conductance are insignificant in the system II; otherwise, these influences

become significant in the system I due to less significant ion CP and accordingly more counterions accumulated inside the nanopore in the system I.

2.3.3 Electrokinetic Fluid Flow

Figure 2.8 depicts the cross sectionally averaged EOF velocity, $\bar{v}$, at the cross section z=0 as a function of the bulk salt concentration C_0 at various fixed charge densities of the PE layer ρ_{fix} when L_N=20 nm (a) and 50 nm (b). Lines and symbols denote the results of the systems I and II, respectively. Due to the negative charge density in the PE layer, the fluid is pumped from the anode reservoir toward the cathode reservoir. The averaged EOF velocity, $\bar{v}$, increases with increasing $|\rho_{fix}|$ and C_0. The former is because the larger the $|\rho_{fix}|$ the more counterions accumulated inside the nanopore. The latter is unexpected and can be attributed to the significant ion CP effect. In general, the ion CP becomes more significant as the bulk salt concentration C_0 decreases, leading to two major effects occurring inside the nanopore: (i) less amount of counterions as shown in Figure 2.3 and (ii) lower axial electric field as shown in Figure 2.5. As a result, the electroosmotic flow inside the PE-modified nanopore decreases as C_0 decreases. Under the same conditions, since the induced ion CP in the system I is weaker than that in the system II, the magnitude of the EOF velocity in the system I is higher than that in the system II, especially for high $|\rho_{fix}|$ and low C_0 under which strong ion CP occurs. If C_0 is sufficiently high, the EOF velocities in both systems are very close due to insignificant ion CP at high bulk concentration. Similarly, the EOF velocities in both systems are almost the same for low $|\rho_{fix}|$ except when the bulk concentration is relatively low. In general, the difference between the EOF velocities in both systems increases as C_0 decreases and $|\rho_{fix}|$ increases due to increase in the degree of ion CP.

The influences of R_N, L_N, R_s, and ρ_{fix} on the averaged EOF velocity, $\bar{v}$, for two levels of C_0 are shown in Figure 2.9. Similar to the results in Figure 2.8, the magnitude of $\bar{v}$ in the system I (lines) is consistently higher than that in the system II (lines with

circles), especially for the case of C_0=10 mM due to more significant ion CP. The driving force for the EOF is the product of the charge density of the mobile ions, ρ_e, and the local electric field (i.e., the 3rd term in the left hand side of Eq. (2.4)). As discussed in section 3.1, the induced ion CP reduces both ρ_e and the local electric field inside the nanopore, thus reduces the EOF inside the nanopore. Fig.9a depicts that the magnitude of $\bar{v}$ for C_0= 10 mM initially increases as the nanopore radius R_N increases, attains a local maximum, and then decreases as R_N further increases. However, for C_0=1000 mM the EOF velocity remains almost a constant when R_N is relatively small, and decreases with increasing R_N when the latter exceeds a critical value. In general, the electric field inside the nanopore and accordingly the EOF velocity increase as the nanopore radius R_N decreases. Meanwhile, the induced ion CP becomes more significant as the degree of the EDL overlapping, quantified by the ratio of R_N to the EDL thickness, increases. As R_N decreases, the enhanced ion CP induces stronger electric field opposite to the applied one, leading to the decrease in the net electric field and accordingly EOF velocity inside the nanopore. The behavior of the EOF velocity versus R_N shown in Fig.9a arises from the competition of the above two opposite effects. Figure 2.9b shows that the magnitude of $\bar{v}$ increases with decreasing L_N. Since the imposed potential bias V_0 is fixed and most potential drop falls within the nanopore,[57] the decrease in the nanopore length results in an increase in the electric field inside the nanopore, and accordingly an increase in the EOF. Figure 2.9c shows that $|\bar{v}|$ increases with decreasing R_s if C_0 is relatively low (i.e., 10 mM), while decreases as R_s decreases if C_0 is relatively high (i.e., 1000 mM). Since the fluid velocity inside the PE layer is much lower than that outside of the PE layer due to the hydrodynamic friction force within the PE brushes (i.e., the last term in the left-hand-side of Eq. (2.4)), the averaged velocity decreases as the thickness of the PE layer increases. However, the total volumetric charge within the PE layer, which is the product of the fixed charge density and the volume of the PE layer, increases with increasing R_s, resulting in more counterions accumulated inside the nanopore, which leads to an increase in the charge density of the mobile ions inside the nanopore, ρ_e, and accordingly an increase in the EOF velocity. As R_s increases, the degree of EDL overlapping also increases, resulting in an increase in the ion CP and accordingly a decrease in the fluid

velocity. The behavior of the EOF velocity versus R_s shown in Fig.9c is the net result of the above competing factors. Except for the case of C_0=10 nM in the system II Fig.9d shows that the EOF velocity increases with increasing $|\rho_{fix}|$ due to an increase in the accumulated counterions and accordingly the charge density, ρ_e, inside the nanopore. Due to significant ion CP occurring for C_0=10 nM in the system II, the EOF velocity initially increases with increasing $|\rho_{fix}|$, and reaches a plateau once $|\rho_{fix}|$ exceeds a certain threshold value. As $|\rho_{fix}|$ increases, more couterions are attracted inside the nanopore, resulting in an increase in the EOF velocity. Meanwhile, the degree of ion CP and the induced electric field opposite to the externally imposed one also increase as $|\rho_{fix}|$ increases, resulting in the decrease in the net electric field and accordingly EOF inside the nanopore. The saturation of the EOF velocity for sufficiently high $|\rho_{fix}|$ is the competition of the above opposite effects. When the ion CP is insignificant, EOF velocity increases with $|\rho_{fix}|$ mainly due to the increase in the accumulated counterions inside the nanopore.

To further understand the influences of ρ_{fix} and C_0, two important controlled parameters in the experiments, on the electrokinetic fluid flow inside the PE-functionalized nanopores, the flow fields near the nanopore (Figures 2.10a and 2.10b) and the axial fluid velocity along the axis of the nanopore (Figures 2.10c-e) are shown in Figure 2.10. Lines and lines with circles in Figures 2.10(c)-(e) denote the results for the systems I and II, respectively. As expected, the fluid velocity inside the nanopore of the system I is higher than that in the system II due to more significant ion CP. In the system II, the flow field in the anode reservoir converges into the nanopore and then diverges into the cathode reservoir. Due to the presence of PE layer on the side walls of the membrane, in the anode reservoir fluid flows along the side wall of the membrane, and part of it enters the nanopore while the rest flows toward the end of the anode reservoir. Fluid flows through the nanopore into the cathode reservoir. Inside the cathode reservoir, fluid flows from the end of the reservoir toward the nanopore entrance and merges with the fluid coming from the nanopore to flow along the side wall of the membrane. In

addition to the enhanced EOF inside the nanopore, the flow inside the two reservoirs is opposite to the EOF inside the nanopore. During the next generation nanopore-based DNA sequencing technology, negatively charged DNA suspended inside the cathode reservoir is electrophoretically translocated through the nanopore, and resulting in a current change during the translocation process. Two main challenges in the technology include decreasing DNA translocation inside the nanopore to improve the read-out accuracy and increasing the capture rate of the nanopore to increase throughput. The generated flow pattern in the system I can be used to simultaneously resolve the aforementioned challenges.[117] The flow field toward the nanopore entrance inside the cathode reservoir facilitates to drag DNA from the cathode reservoir to the nanopore entrance, leading to an increase in the capture rate. The enhanced EOF inside the nanopore is opposite to the particle translocation, thus retards the DNA translocation process inside the nanopore. Figures 2.10 (c)-(e) show that the axial EOF velocity along the axis of the nanopore increases with increasing $|\rho_{fix}|$ but decreases with increasing C_0. The former is expected because the concentration of counterions inside the nanopore increases with increasing $|\rho_{fix}|$. The latter is a unique behavior in the PE-functionalized nanopore, that is, the salt concentration dependence of the electrokinetic fluid velocity inside the PE layer of the nanopore is distinctly different to that outside the PE layer.[117] We attribute this interesting behavior to the development of EDL inside a PE-functionalized nanopore, which affects the distribution of its fluid velocity profile appreciably.

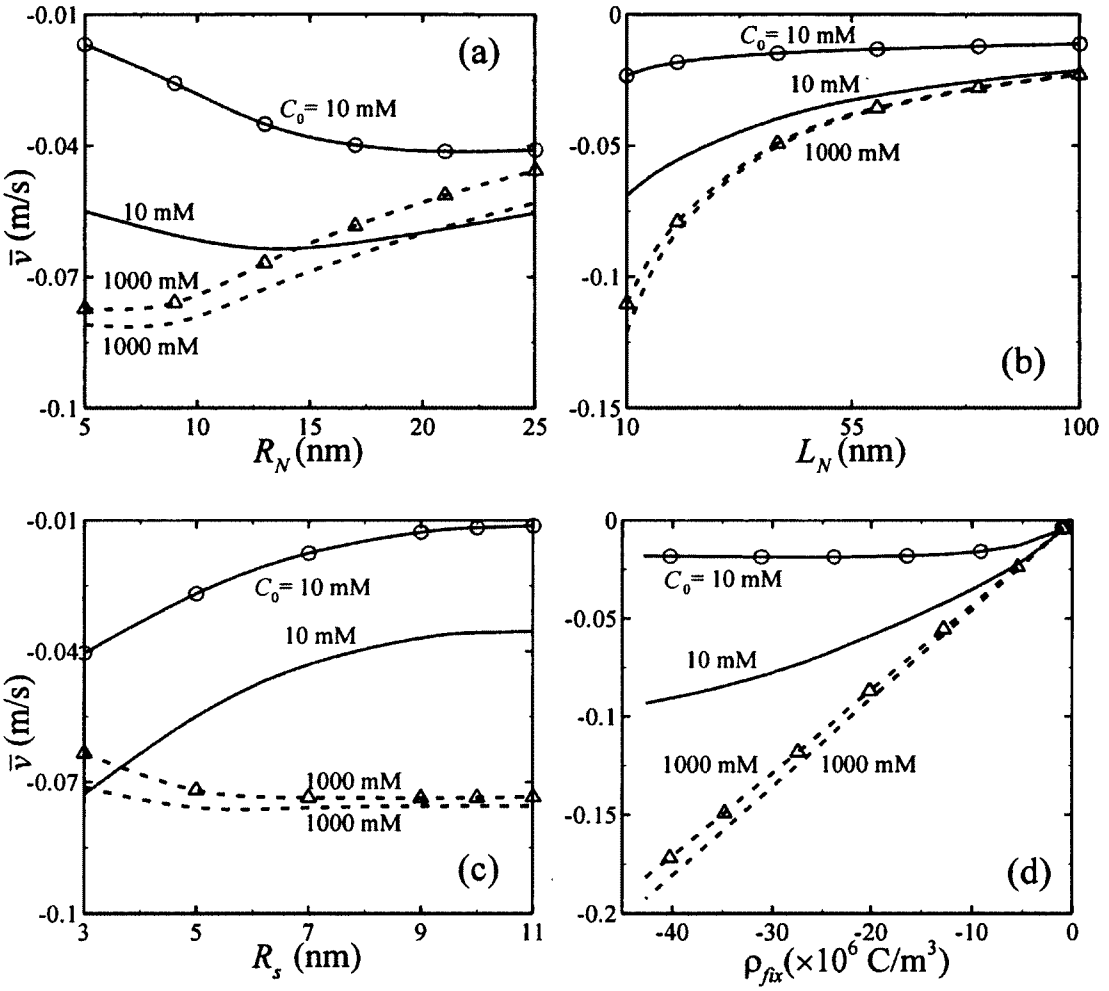

Figure 2.9. Cross sectionally averaged EOF velocity as a function of the nanopore radius R_N (a), the nanopore length L_N (b), the thickness of the PE layer R_s (c), and the fixed charge density of the PE layer ρ_{fix} (d) when C_0=10 mM (solid lines) and 1000 mM (dashed lines). Other conditions are the same as those in Figure 2.7. Lines and lines with circles represent the results of the systems I and II, respectively.

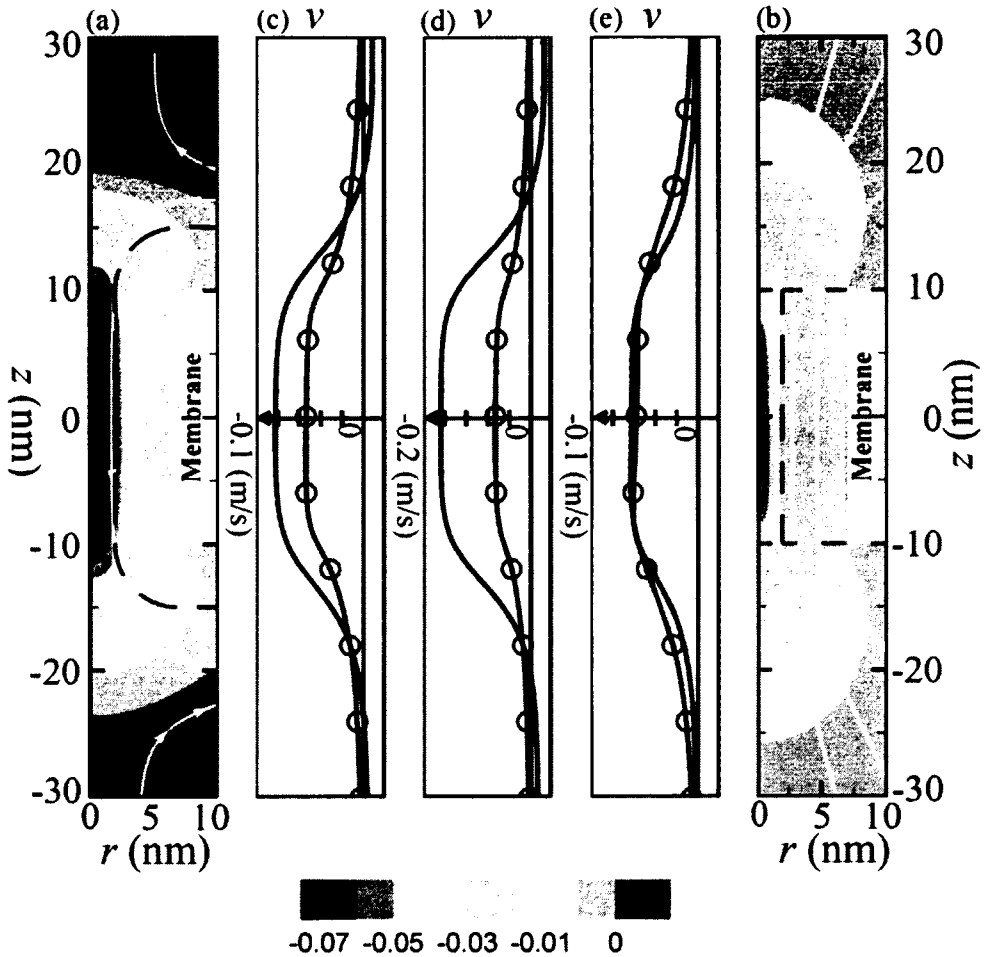

Figure 2.10. Flow field near the nanopore (a and b), and the axial velocity along the axis of the nanopore (c-e) under the same conditions of Figure 2.3. Color bars in (a) and (b)denote the axial fluid velocity and streamlines with arrows denote the fluid velocity vector. Lines and lines with circles in (c)-(e) represent the results in the systems I and II, respectively.

2.4. Conclusions

Effects of the presence of a floating electrode in the form of a conducting metal coating along the inner surface of a nanopore on the DNA translocation through a nanopore has been studied using a continuum model. The model includes coupled PNP equations for the ionic mass transport and the modified Stokes equations for the flow field. The ideally polarizable floating electrode interacting with the applied electric field induces a non-

uniform charge density on its surface. Two main factors, induced-charged eletroosmosis (ICEO) and particle-floating electrode electrostatic interaction, could significantly affect the DNA translocation through a nanopore. The ICEO effect exists under both thin and thick EDLs and is proportional to the square of the applied electric field. As a result, the ICEO is negligible under a relatively low electric field and becomes significant under a relatively high electric field. The ICEO retards the DNA translocation when it approaches the floating electrode, however, facilitates the DNA translocation when it moves away from the floating electrode. It has been predicted that the particle could be trapped near the floating electrode when the applied electric field is relatively high and the EDLs are relatively thin. On the other hand, the particle-floating electrode electrostatic interaction is only pronounced when the EDLs of the particle and floating electrode are overlapped. An attractive (or repulsive) particle-floating electrode electrostatic interaction is generated when the polarity of the particle's surface charge is opposite (identical) to that of the local floating electrode. In general, the particle-floating electrode electrostatic interaction facilitates the DNA translocation at the two ending regions of the floating electrode and retards the DNA translocation in the middle region of the floating electrode. Thus, the floating electrode technique might be helpful for attracting DNA from the reservoir into the nanopore and slowing down its motion inside the nanopore during sequence sensing. A longer floating electrode implies a higher surface charge is induced on the floating electrode, which in turn induces a more significant effect on the DNA translocation. The present of the floating electrode attracts more ions inside the nanopore resulting in an increase in the ionic current flowing through the nanopore, and exhibits a minor effect on the ionic current deviation.

Table 2.1. Difference of the concentration of cations, Δc_1, and anions, Δc_2, between two openings of the nanopore, and their percentage ratios, $\Delta c_1 / C_0$ and $\Delta c_2 / C_0$, for the cases of the systems I and II in the Figures 2.3(c)-2.3(e) and 2.4(c)-2.4(e).

System I	Δc_1 (mM)	$\Delta c_1 / C_0$ (%)	**System II**	Δc_1 (mM)	$\Delta c_1 / C_0$ (%)
Figure 2.3(c)	10.1	50.5	Figure 2.3(c)	31.3	156.5
Figure 2.3(d)	10.2	51	Figure 2.3(d)	41.6	208
Figure 2.3(e)	26.9	5.38	Figure 2.3(e)	64.6	12.92
System I	Δc_2 (mM)	$\Delta c_2 / C_0$ (%)	**System II**	Δc_2 (mM)	$\Delta c_2 / C_0$ (%)
Figure 2.4(c)	10.8	54	Figure 2.4(c)	24.5	122.5
Figure 2.4(d)	13.8	69	Figure 2.4(d)	24.7	123.5
Figure 2.4(e)	27.1	5.42	Figure 2.4(e)	65	13

CHAPTER 3

ELECTROKINETIC ION NAD FLUID TRANSPORT IN A CHARGE-REGULATED NANOPORE

Abstract

Solid-State nanopores have emerged as powerful tools for the study of ion transport and single molecules such as DNA and RNA, in which the surface charge density of the nanopore plays a crucial role. However, some of these solid-state nanopores are charge regulated, and their surface charge densities stemming from the reactive groups at the solid-liquid interface of the nanopores depend on pH and ionic strength. In contrast to most existing studies on electrokinetic ion and fluid transport in a nanopore, which is assumed to bear a pre-specified constant surface charge density regardless of the values of pH and ionic strength, this chapter, for the first time, investigated electrokinetic ion and fluid transport in a solid-state nanopore using the Poisson-Nernst-Planck equations for the ionic mass transport, the Navier-Stokes equations for the flow field, and the protonation/deprotonation surface reactions for the charge regulation. The model without considering the charge regulation failed to explain the ionic transport in a nanopore such as the nanopore conductance when the salt concentration is relatively low, while the predictions of the present model considering the charge regulation agree with the experimental results obtained from the literature. The obtained results demonstrate that the solution properties including pH and background salt concentration significantly affect the surface charge density of the nanopore, which in turn affects the conductance, electroosmotic flow, and ion selectivity of the nanopore.

3.1. Introduction

With recent advances in nanofabrication techniques, nanopores have emerged as promising tools for the study of individual (bio)nanoparticles, such as RNA,[21, 135] DNA,[21, 33, 37-38, 61, 131, 136-137] proteins,[31, 42, 138-139] polystyrenes,[115-116, 126] and single-wall carbon nanotubes,[140] over the past decades. In these applications, a voltage bias is applied across

the nanopore connecting two fluid reservoirs on either side, as schematically shown in Figure 3.1 Charged nanoparticles suspended in the cathode reservoir are electrophoretically driven through the nanopore, resulting in an ionic current change. One aim is to characterize the translocating nanoparticle, such as DNA sequences in the next generation nanopore-based DNA sequencing technology, based on the recorded detectable changes in the ionic current signals.[141-142]

Since the electrical double layer thickness is on the same order of magnitude of the nanopore size, only counter-ions are able to pass through the nanopore while co-ions are rejected. The resulting ionic current flowing through the nanopore is mainly carried by the enriched counterions inside the nanopore due to the ion selectivity.[86, 123] Many theoretical and experimental studies have demonstrated that the electric-field-induced ion transport in solid-state nanopores is governed by the nanopore's surface charge,[98, 102, 110, 143] therefore one can control the ionic mass transport and ionic current by tuning the surface charge density of the nanopore wall.[144] Many experimental results demonstrated that the surface charge densities of most solid-state nanopores made of oxides such as silica and alumina depend on the properties of the electrolyte solution, such as pH and salt concentration,[93, 97, 99, 127, 145] implying that the nanopore is charge regulated and its surface charge density is governed by the surface reactions of the reactive groups at the solid-liquid interface of the nanopores. However, most existing theoretical studies on ionic mass transport, electrokinetic fluid and particle transport in solid-state nanopores used a pre-specified, constant surface charge density,[98, 110] that is valid only when the nanopore wall is highly charged and is not appropriate for charge-regulated nanopores, such as the widely used nanopores made of silica and alumina. Very recently, Hsu's group numerically investigated electrophoretic motion of charge-regulated spherical particles (i.e., SiO_2 particles) suspended in an unbounded liquid mediua[146-148]Yeh et al.[107] derived an approximation solution of the fully developed electroosmotic flow in a charge-regulated nano-slit when the electric double layers are not overlapped and double layer polarization is also neglected. The results show that the electroosmotic flow in a charge-regulated nanochannel and the electrophoretic behaviors of charge-regulated particles depend on both pH and the background salt concentration. The actual nanopore-based nanofluidic devices consist of a nanopore connecting two fluid reservoirs on either side.

Under an electric field imposed, both counter-ions and co-ions are enriched at the opening of the nanopore in the cathode fluid reservoir, while both counter-ions and co-ions are depleted at the opening of the nanopore in the anode fluid reservoir, as schematically shown in Figure 3.1. This important phenomenon is referred to as ionic concentration polarization, which also plays a critical role on ions, fluid and particle transport in nanopore-based devices. Note that the effects of the fluid reservoirs and the induced ionic concentration polarization occurring at the interface of the reservoir and nanopore are not considered in the aforementioned studies.

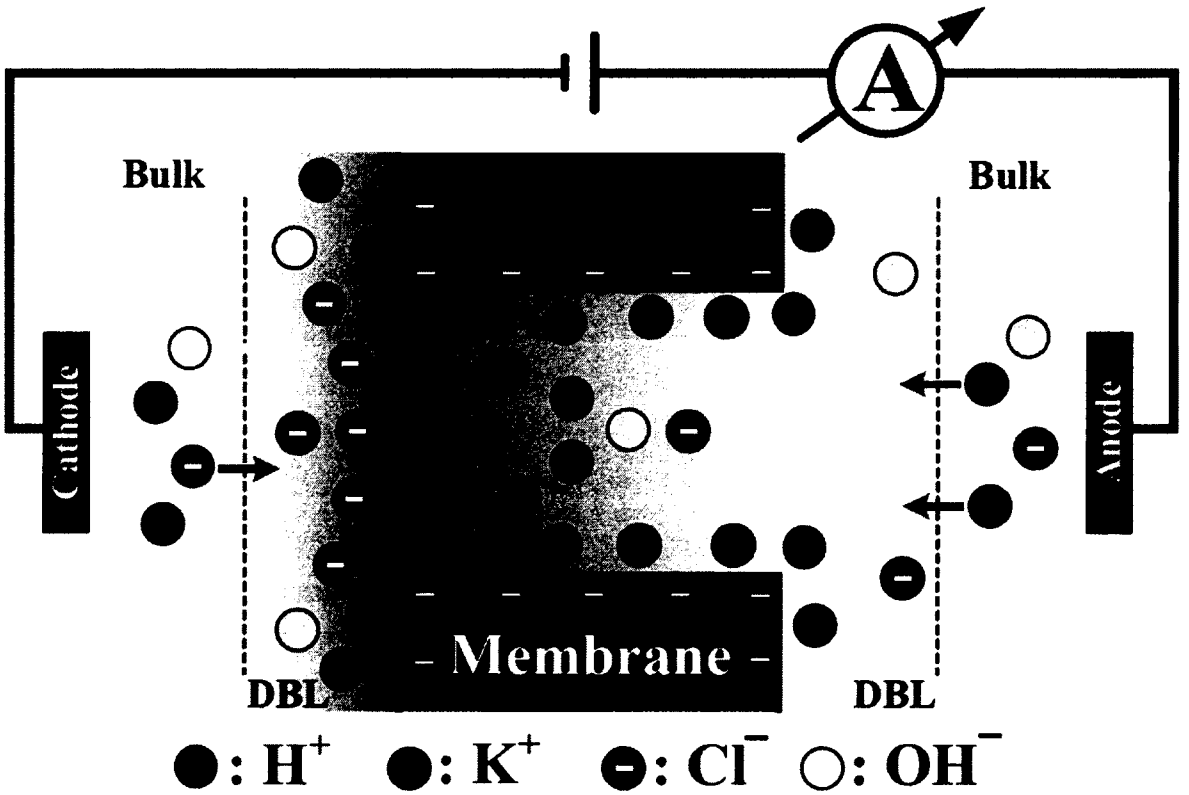

Figure 3.1. Schematic illustration of multi-ions concentration polarization (CP) phenomenon in a charge-regulated nanopore. Concentrations of cations and anions are enriched at the cathode side and depleted at the anode side of the nanopore, leading to a gradient of salt concentration, the so-called diffusion boundary layer (DBL) on both openings of the nanopore.[123]

In the this chapter, we consider a more realistic nanofluidic device consisting of a silica nanopore connecting two fluid reservoirs on either side, and numerically investigate the electrokinetic fluid flow and ion transport using a continuum model, comprising of the Poisson-Nernst-Planck (PNP) equations for the ionic mass transport, the modified Stokes equations for the flow field, and the protonation/deprotonation surface reactions for the charge regulation. Due to the confinement of the geometry and the presence of the reservoirs, both boundary effect and the effect arising from the induced ionic concentration polarization occurring at both ends of the nanopore are considered. Different from the existing studies using a pre-specified constant surface charge density on the nanopore wall,[98, 110] surface charge density of the nanopore wall is part of the solution in the present model. We first validate the present model by comparing its predictions of the nanopore conductance as a function of the salt concentration to the experimental data obtained from the literature. Subsequently, the verified model is used to elucidate the effects of the solution properties (i.e., pH and background salt concentration) on the nanopore surface charge density, ionic concentration polarization, potential drop within the nanopore, nanopore conductance, and electrokinetic flow.

3.2. Mathematic Model

We consider a cylindrical nanopore of length L_N and radius R_N connected to two large, identical fluid reservoirs filled with an electrolyte solution containing N types of ionic species, as schematically shown in Figure 3.1. The axial length, L_R, and radius, R_R, of the reservoirs are large enough so that the concentration of each ionic species at places far away from the nanopore maintains its bulk ionic concentration, C_{j0} (j=1,..., N). A potential bias V_0 is applied between two electrodes positioned far away from the nanopore inside the two fluid reservoirs, resulting in a negative axial electric field, **E**, which induces electroosmotic flow and simultaneously generates an ionic current through the nanopore. Due to the axial symmetric, the cylindrical coordinates (r, z) with the origin at the center of the nanopore is adopted.

A continuum-based mathematical model, composed of the Poisson-Nernst-Planck (PNP) and the modified Stokes equations, is employed to describe the ionic mass transport and

induced electroosmotic flow in the charge-regulated nanopore. The ionic mass transport in the electrolyte solution is governed by the PNP equations:

$$-\nabla^2 V = \frac{\rho_e}{\varepsilon_f} = \frac{\sum_{j=1}^{N} F z_j c_j}{\varepsilon_f}, \tag{3.1}$$

$$\mathbf{N}_j = \mathbf{u} c_j - D_j \nabla c_j - z_j \frac{D_j}{RT} F c_j \nabla V, \tag{3.2}$$

and

$$\nabla \cdot \mathbf{N}_j = 0. \tag{3.3}$$

In the above, V is the electric potential; $\mathbf{u} = u\mathbf{e}_r + v\mathbf{e}_z$ is the fluid velocity with $\mathbf{e}_r$ and $\mathbf{e}_z$ being, respectively, the unit vectors in the r- and z-directions; $\rho_e = \sum_{j=1}^{N} F z_j c_j$ is the space charge density of mobile ions; $\mathbf{N}_j$, c_j, D_j, and z_j are the flux density, concentration, diffusivity, and valence of the j^{th} ionic species, respectively; ε_f, F, R, and T are the fluid permittivity, the Faraday constant, the universal gas constant, and the absolute temperature, respectively. Note that the first, second, and third terms on the right-hand side of Eq. (3.2) denote contributions from the convective, diffusive, and migrative fluxes, respectively.

Since the Reynolds number of the electrokinetic flow in nanopores is extremely small (i.e. Re<<1), the steady-state flow field can be described by the continuity and the modified Stokes equations:[52, 149]

$$\nabla \cdot \mathbf{u} = 0, \tag{3.4}$$

$$-\nabla p + \mu \nabla^2 \mathbf{u} - \rho_e \nabla V = \mathbf{0}, \tag{3.5}$$

where p and μ are the hydrodynamic pressure and the fluid viscosity, respectively.

To solve the above coupled governing equations (3.1)-(3.5), appropriate boundary conditions are required. We assume that the ionic concentrations at the ends of the two reservoirs are maintained at their bulk values, $c_j = C_{j0}$, and the electric potentials are $V(cathode) = 0$ and $V(anode) = V_0$. A normal flow with no external pressure gradient (i.e. p=0) is applied at the ends of the two big reservoirs. The fixed wall surface of the membrane is non-slip, ion-impenetrable and bears a surface charge density, yielding

$\mathbf{u}=\mathbf{0}$, $\mathbf{n}\cdot\mathbf{N}_j=0$ and $-\mathbf{n}\cdot\nabla V=\sigma_w/\varepsilon_f$, where $\mathbf{n}$ is the unit outer normal vector and σ_w is the surface charge density of the membrane wall. A symmetric boundary condition is specified along the axis of the nanopore. The slip boundary condition for the flow field, insulation boundary condition for the potential ($-\mathbf{n}\cdot\nabla V=0$), and zero normal ionic fluxes ($\mathbf{n}\cdot\mathbf{N}_j=0$) are applied at the side boundaries of the two reservoirs, which are far away from the nanopore.

Due to the protonation/deprotonation surface reactions often occurring on the dissociably functional groups of the solid/liquid interface, the dielectric material of the membrane surface typically reveals a charge-regulated nature when it is in contact with an aqueous solution. Therefore, the surface charge property of the nanopore, which significantly affects the electrokinetic transport phenomena inside it, highly depends on the solution properties such as solution pH and its ionic strength. The surface charge density of the charge-regulated membrane wall, σ_w, is determined by the following protonation/deprotonation surface reactions with equilibrium constants K_A and K_B:[107]

$$\mathrm{AOH}\leftrightarrow\mathrm{AO^-}+\mathrm{H^+}, \tag{3.6}$$

and

$$\mathrm{AOH}+\mathrm{H^+}\leftrightarrow\mathrm{AOH_2^+}. \tag{3.7}$$

Under equilibrium, $K_A=n_{\mathrm{AO^-}}[\mathrm{H^+}]_s/n_{\mathrm{AOH}}$ and $K_B=n_{\mathrm{AOH_2^+}}/n_{\mathrm{AOH}}[\mathrm{H^+}]_s$, where n_{AOH}, $n_{\mathrm{AO^-}}$, and $n_{\mathrm{AOH_2^+}}$ are the surface site densities of AOH, $\mathrm{AO^-}$, and $\mathrm{AOH_2^+}$, respectively, and $[\mathrm{H^+}]_s$ is the molar concentration of $\mathrm{H^+}$ ions at that membrane wall/liquid interface. The total surface site density on the nanopore/liquid interface is $N_{\mathrm{total}}=n_{\mathrm{AOH}}+n_{\mathrm{AO^-}}+n_{\mathrm{AOH_2^+}}$, and the resulting surface charge density is

$$\sigma_w=-F(n_{\mathrm{AO^-}}-n_{\mathrm{AOH_2^+}})=-FN_{total}\left\{\frac{K_A-K_B([\mathrm{H^+}]_s)^2}{K_A+[\mathrm{H^+}]_s+K_B([\mathrm{H^+}]_s)^2}\right\}. \tag{3.8}$$

Eq. (3.8) shows that the surface charge density depends on the concentration of the $\mathrm{H^+}$ ions on the membrane wall, and is a part of the solution instead of externally specified.

The resulting volumetric flow rate, Q_{flow}, and conductance, G, through the nanopore are, respectively, evaluated by

$$Q_{\text{flow}} = \int_S \mathbf{u} \cdot \mathbf{n} dS \ , \tag{3.9}$$

$$G = I / V_0 = \int_S F(\sum_{j=1}^{N} z_j \mathbf{N}_j) \cdot \mathbf{n} dS \Big/ V_0 \ . \tag{3.10}$$

Here, I is the ionic current flowing through the nanopore, and S denotes either end of the reservoirs due to the conservations of mass and ionic current.

3.3. Results and Discussion

3.3.1 Numerical Method and Code Validation

The above fully coupled model is numerically solved using the commercial finite-element package, COMSOL (version 3.5a, www.comsol.com), operating in a high-performance cluster. The computational domain is discretized into quadratic triangular elements. Nonuniform elements are employed with larger numbers of elements assigned locally as necessary. Typically, the total number of the mesh is around 130,000, with finer mesh on the nanopore wall to capture the EDL and surface charge variation as shown in Figure 3.2a. Lagrange – Quadratic elements are used for solving PNP equations, while Lagrange – P_2P_1 elements are for the Stokes equation. The ionic current through the nanopore is obtained by using the weak constrain in COMSOL specially developed for an accurate calculation of flux. Rigorous mesh-refinement tests have been performed to ensure that the solutions obtained are convergent and grid independent. The relative tolerance is set as 10^{-6} in all the cases of this chapter. A maximum tolerance of 0.1% is imposed on the relative difference $(|I_a| - |I_c|)/|I_a|$, where I_a and I_c are respectively the current entering (anode) and leaving (cathode) the nanopore. The numerical scheme has been validated to be sufficiently efficient and accurate for solving similar electrokinetic problems, such as the electrokinetic ion transport in a solid-state nanopore[14, 109-113] and the electrokinetic rigid and soft nanoparticle translocation through a nanopore.[52, 115-117, 122, 126]

We assume that the background electrolyte is made of KCl with concentration C_{KCl}, and the solution's pH is adjusted by KOH and HCl. Therefore, four major ionic species (i.e., N=4), H^+, K^+, Cl^-, and OH^-, are considered, and their bulk concentrations are,

respectively, C_{10}, C_{20}, C_{30}, and C_{40}(in the unit of mM). Due to electroneutrality, the bulk concentrations are $C_{10}=10^{(-\mathrm{pH}+3)}$, $C_{20}=C_{\mathrm{KCl}}$, $C_{30}=C_{\mathrm{KCl}}+10^{(-\mathrm{pH}+3)}-10^{-(\mathrm{pK}_w-\mathrm{pH})+3}$, and $C_{40}=10^{-(\mathrm{pK}_w-\mathrm{pH})+3}$ if $\mathrm{pH}\le \mathrm{pK}_w/2$; and $C_{10}=10^{-\mathrm{pH}+3}$, $C_{20}=C_{\mathrm{KCl}}-10^{-\mathrm{pH}+3}+10^{-(\mathrm{pK}_w-\mathrm{pH})+3}$, $C_{30}=C_{\mathrm{KCl}}$, and $C_{40}=10^{-(\mathrm{pK}_w-\mathrm{pH})+3}$ if $\mathrm{pH}>\mathrm{pK}_w/2$.[147-148] Here, $\mathrm{pH}=-\log([\mathrm{H}^+]_0)=-\log(C_{10}/1000)$ and $\mathrm{pK}_w=-\log(\mathrm{K}_w)=14$ with $[\mathrm{H}^+]_0$ and K_w being the bulk molar concentration of H^+ ions (in the unit of M) and the dissociation constant of water, respectively.

In subsequent discussions, the influences of the solution properties (pH and background salt concentration, C_{KCl}) on the conductance, the electroosmotic flow, and the relevant electrokinetic ion transport phenomena through a silica nanopore are investigated. Unless otherwise specified, the potential bias $V_0=500$ mV is applied between the two electrodes, and the length and radius of the nanopore are assumed to be L_N=70 nm and R_N=5 nm, respectively. It should be pointed out that for the radius of the nanopore considered it has been validated that the continuum model is sufficient to capture and elucidate their essential physics.[47, 56, 117, 150] The size of the reservoirs are $L_R=200$ nm and $R_R=200$ nm. The diffusivities of ions H^+, K^+, Cl^-, and OH^- are 9.31×10^{-9}, 1.96×10^{-9}, 2.03×10^{-9}, and 5.30×10^{-9} m^2/s, respectively. The other physical parameters used in the simulations are $\varepsilon_f=7.08\times10^{-10}$ F/m, R = 8.31 J/(K·mol), F=96490 C/mol, $\mu=1\times10^{-3}$ Pa·s, and T = 300K.

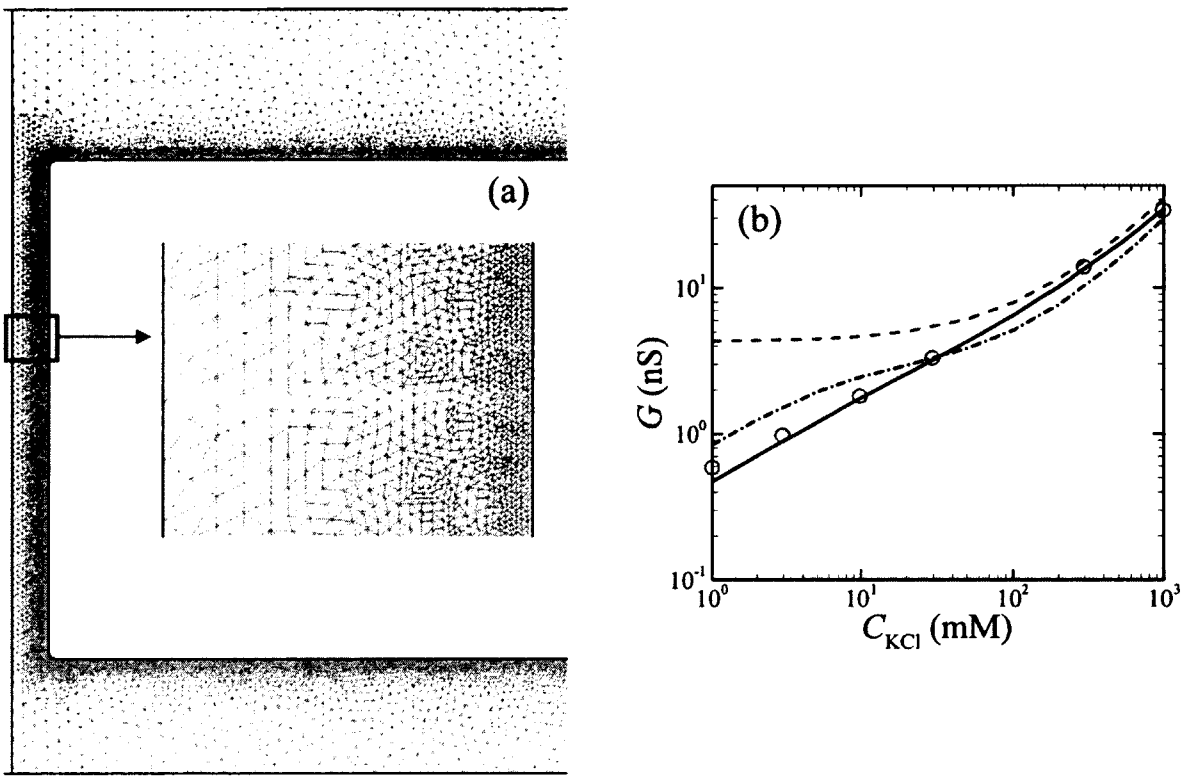

Figure 3.2. (a): the meshes used in the simulation with enlarged finer on the nanopore wall. (b): the dependence of the background salt concentration C_{KCl} on the nanopore conductance at pH $= 7.5$ and the potential bias $V_0 = 200$ mV. Solid line: numerical result based on the present charge-regulated model with $pK_A = 7$, $pK_B = 1.9$, and $N_{total} = 8 \times 10^{-6}$ mol/m^2; dash-dotted line: numerical result based on a constant surface charge density $\sigma_w = -60$ mC/m^2; dashed line: analytical result of Smeets et al.[38] based on $\sigma_w = -60$ mC/m^2; circles: experimental data of Smeets et al.[38]

To validate the applicability of the present numerical model, it is first used to predict the conductance of a silica nanopore with L_N=34 nm and $R_N = 5 \pm 1$ nm at pH=7.5 and $V_0 = 200$ mV, and the conditions are the same as the experimental setup of Smeets et al.[38] Figure 3.2b depicts the nanopore conductance as a function of the background salt concentration C_{KCl}. For comparison, the corresponding numerical result (dash-dotted line) and analytical result of Smeets et al.[38] (dashed line) based on a constant surface charge

density, $\sigma_w = -60\ \mathrm{mC/m^2}$, typical value of a silica nanopore used in the literatures,[38, 127] are also included. Figure 3.2b shows that the result of the present charge-regulated model (solid line) with the following parameters, $R_N = 5\ \mathrm{nm}$, $\mathrm{p}K_A = -\log K_A = 7$, $\mathrm{p}K_B = -\log K_B = 1.9$, and $N_{total} = 8\times10^{-6}\ \mathrm{mol/m^2}$, are in very good agreement with the experiment data (circles in Figure 3.2b of Smeets et al.[38]), while both the analytical and numerical results based on a constant surface charge density significantly deviate from the experiment results. This is expected because the surface charge density of the silica nanopore is not a constant and highly depends on the solution properties (pH and background salt concentration), which will be shown later. The estimated values of $\mathrm{p}K_A$, $\mathrm{p}K_B$, and N_{total} also reasonably correspond to the dielectric layer of the membrane made of silicon dioxide in the literatures.[127, 151] Therefore, we use the aforementioned values of $\mathrm{p}K_A$, $\mathrm{p}K_B$, and N_{total} in the following simulations.

3.3.2 Effect of Solution Properties on Nanopore Surface Charge Density

Figure 3.3 depicts the average surface charge density on the nanopore wall, $\bar{\sigma}_w = \int_\Gamma \sigma_w d\Gamma / L_N$ with Γ denoting the nanopore wall, as a function of the background salt concentration, C_{KCl}, for various pH values (Figure 3.3a) and as a function of the pH value for various background ionic strengths (Figure 3.3b). The solid, dashed and dash-dotted lines in Figure 3.3a represent, respectively, the results under pH = 9, 6 and 4, while the solid, dashed and dash-dotted lines in Figure 3.3b denote, respectively, the results for C_{KCl} = 100mM, 4 mM and 1 mM. Obviously, the surface charge density is not a constant and highly depends on background ionic strength and pH.

Figure 3.3 shows that the $\bar{\sigma}_w$ increases with increasing C_{KCl} and solution pH. The former is expected because the higher the C_{KCl} results in the thinner thickness of electric double layer (EDL), so is the surface charge density on the nanopore. This behavior was also observed by Yeh et al in the field effect control of surface charge properties in a silica nanochannel.[107] The latter arises because the higher the pH (the lower concentration of H^+ ions in the solution) the more negatively charged surface site groups AO^- dissociated on the nanopore surface (refer to eq. 3.6) and, therefore, the higher is the $\bar{\sigma}_w$.

Note that the isoelectric point (PI) of the silica nanopore wall considered is 2.55. This is why the $\bar{\sigma}_w$ is very small when pH is sufficiently low (i.e. pH<5).

Under the same background salt concentration, the magnitude of the surface charge density increases with increasing pH, which qualitatively agrees with the experimental results. [152] For pH increasing from 4 to 9, the increase in the surface charge density for C_{KCl}=100 mM is higher than that for C_{KCl}=4 mM, which is higher than that for C_{KCl}=1 mM. Therefore, it is more sensitive to tune the surface charge density of silica nanopore through pH when the background salt concentration is relatively high. As pH increases, the concentration of H^+ ions inside the nanopore decreases, which in turn promotes the surface reaction (3.6) leading to more negative surface sites AO^- and higher negative surface charge density.

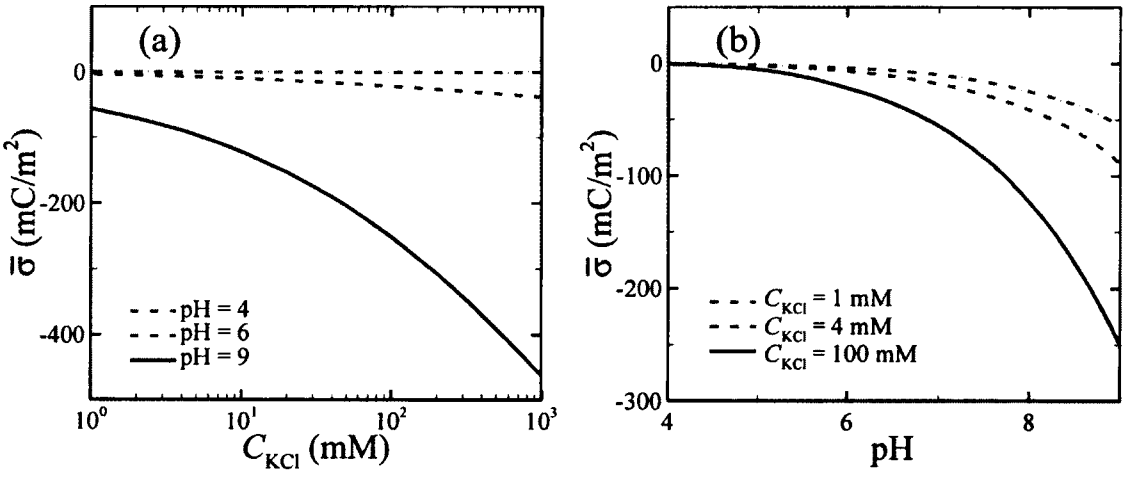

Figure 3.3. Average surface charge density of the nanopore as a function of the background salt concentration C_{KCl} at various solution pH (a) and as a function of pH at various C_{KCl} (b).

3.3.3 Effect of Solution Properties on Ions Distribution

Since the ion transport in a nanopore is governed by its surface charge, which highly depends on the pH and salt concentration, the ionic concentrations inside the nanopore are thus dependent on the solution properties. Figure 3.4 depicts axial variation of the normalized concentrations of cations, $(c_1 + c_2)/C_{KCl}$ (a) and (c), and anions, $(c_3 + c_4)/C_{KCl}$

(b) and (d), for various background salt concentration C_{KCl} at pH=4 (a and b) and 9 (c and d). For C_{KCl}=1 mM (dash-dotted lines) and 4 mM (dashed lines), the concentrations of the cations and anions near the opening of the nanopore in the cathode side (i.e., the left side in Figure 3.4) are obviously higher than those at the other opening in the anode side (i.e., the right side in Figure 3.4), which is called the ion concentration polarization, as schematically shown in Figure 3.1. The concentration polarization, arising mainly from the uneven magnitudes of the electromigrative fluxes of the cations and anions inside the nanopore due to the ion selectivity, becomes significant when electrical double layers are overlapped and the surface charge density is relatively high.[123] Concentration polarization is not significant for C_{KCl} = 100 mM at pH=4 due to relatively thin EDL and especially low surface charge density as shown in Figure 3.3. Therefore, the normalized concentrations of both cations and anions are almost equal to 1 along the axis of the nanopore. However, the solid line in Figure 3.4d shows that an obvious concentration polarization occurs for C_{KCl} = 100 mM at pH=9. Since the scale in the y-axis of Figure 3.4c is very large, the induced concentration polarization is not clearly shown in Figure 3.4c. But we indeed check that the cations are enriched at the cathode opening and depleted at the anode opening of the nanopore by reducing the scale of the y-axis. The appearance of the concentration polarization at pH=9 is due to the resulting high surface charge density at pH=9, as shown in Figure 3.3. Although the double layers are not overlapped for C_{KCl} =100 mM, the resulting high negative surface for pH=9 strongly excludes anions out of the negatively charged nanopore, and anions migrating from the cathode reservoir toward the anode reservoir could not enter the nanopore and are accumulated near the left opening of the nanopore in the cathode side. As a result, anions are enriched (depleted) near the opening in the cathode (anode) side of the nanopore, as shown in the solid line in Figure 3.4d. At the same pH, Figure 3.4 also shows that the concentration polarization becomes weaker as the salt concentration increases due to the decrease in the degree of double layer overlapping.

To further show the important concentration polarization phenomenon which affects electrokinetic ion and fluid in nanofluidics,[123] Figure 3.5 depicts the spatial concentration distributions of the ions H^+ (c_1), K^+ (c_2), Cl^- (c_3), and OH^- (c_4) in the nanopore region for C_{KCl} = 1 mM at pH = 4 (a-d) and 9 (e-h). Since the bulk concentration of OH^- is much

lower than that of Cl^-, the concentration of OH^- inside the nanopore is also much lower than that of Cl^-. Due to the extremely low surface charge density as shown by the dash-dotted line in Figure 3.3a, the nanopore is occupied by both cations including H^+ and K^+ and anions predominantly by Cl^-. The concentration of the cations is a little bit higher than that of anions since the nanopore wall bears a low negative surface charge. Figure 3.5a also shows that the ionic concentrations of both H^+ and K^+ inside the nanopore are not spatially uniform, and their maxima occur at about z=–20 nm on the nanopore wall instead of at z=0 due to the electromigration under the negative axial electric field. The nonuniform distribution of ions H^+ generates a pH gradient inside the nanopore, and the signs of the induced pH gradient at both openings of the nanopore are opposite. Figures 3.5a-d also show that the ionic concentration polarization since the concentrations of both cations and anions at the left opening (cathode side) are higher than those at the right opening (anode side), and the ions are enriched (depleted) at the opening of the cathode (anode) side. Since the surface charge density at pH=4 is very low, the regions of the ion enrichment and depletion are small and occur near both openings of the nanopore. On the other hand, the surface charge density on the nanopore wall is very high if the pH is sufficiently high (i.e. pH=9 in Figure 3.5e-h). In this case, more counterions (cations) are electrostatic concentrated inside the nanopore while the coions (anions) are repelled out the nanopore, leading to a significant equilibrium electric field (normal to the direction of the applied electric field). As a result, the CP effect at higher pH is less significant than that at lower pH. Note that at pH=9 the concentration of H^+ ions is significantly lower than the background electrolyte ions (K^+ and Cl^-) and the significantly electrostatic effect, resulting in the concentration of K^+ inside the nanopore is obviously higher than the other concentrations of ions.

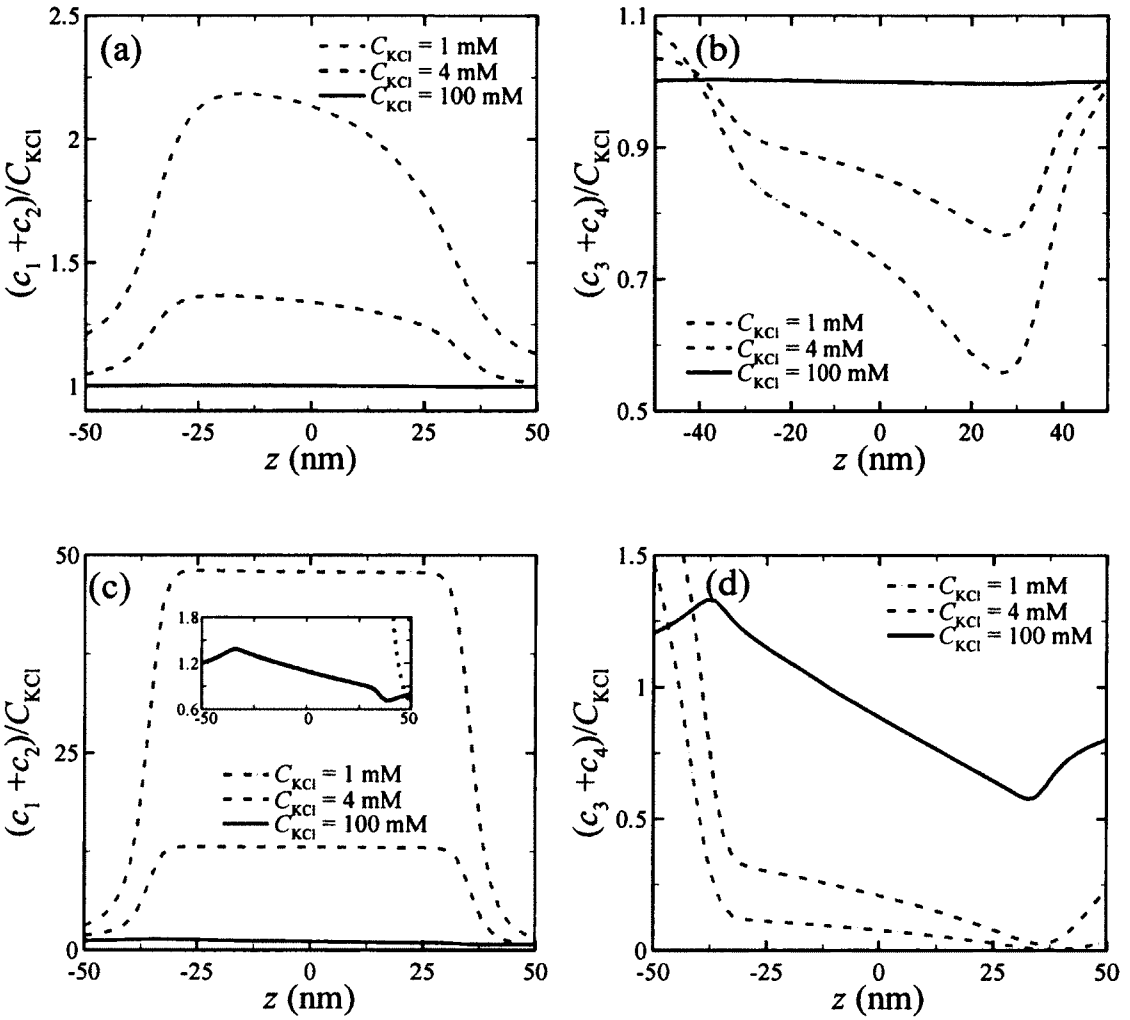

Figure 3.4. Axial variation of the concentrations of cations (c_1+c_2), (a) and (c), and cations (c_3+c_4), (b) and (d), in a silica nanopore for various background salt concentration C_{KCl} at the solution pH=4, (a) and (b), and 9, (c) and (d). Inset of (c): enlarge view of (c) for $(c_1-c_2)/C_{KCl}$ from 0.6 to1.8.

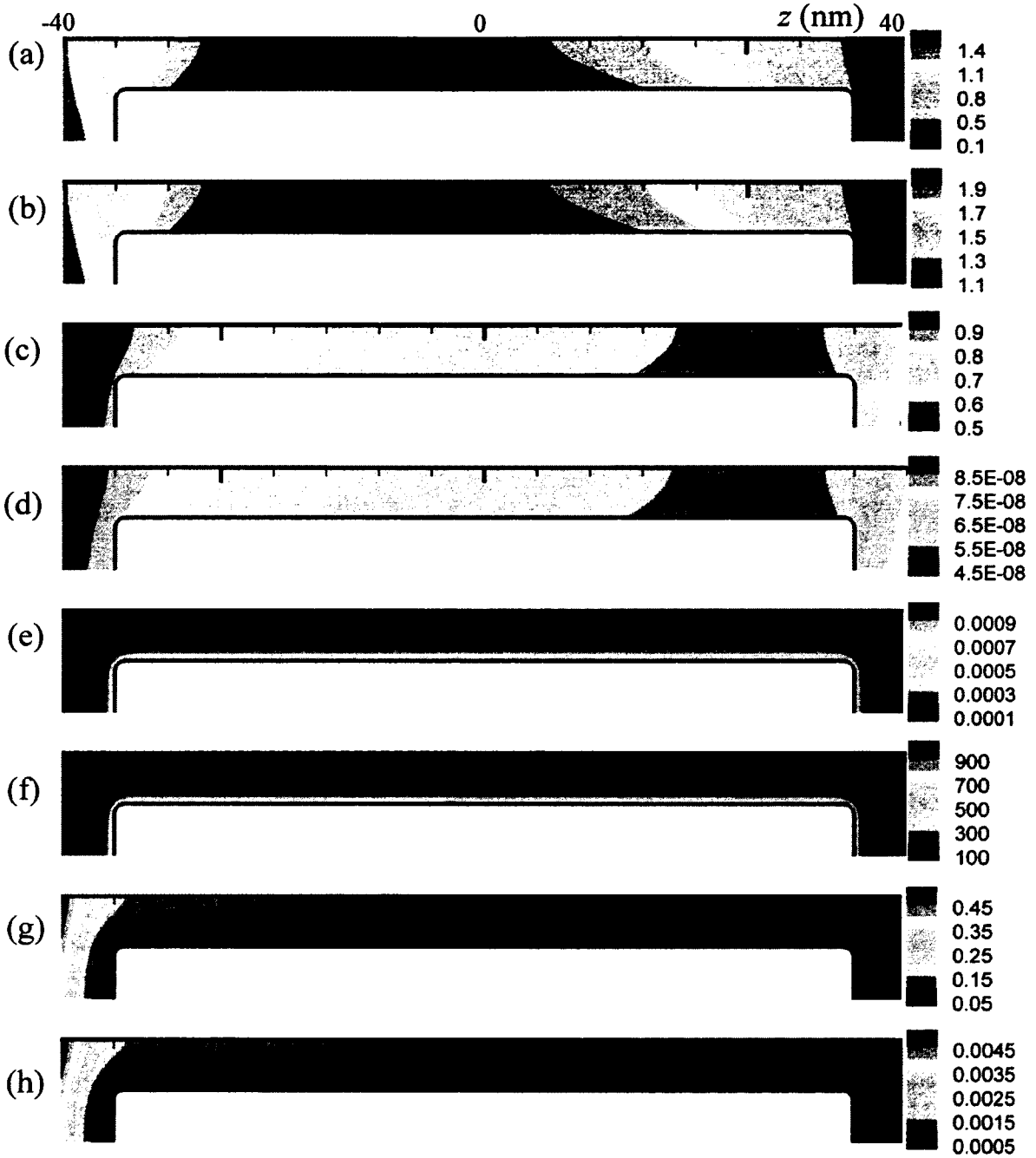

Figure 3.5. Illustrating contours of the concentration of in a silica nanopore for the case of Figure 4 at $C_{KCl} = 1$ mM. (a)-(d): pH=4; (e)-(h): pH=9. (a) and (e): c_1; (b) and (f): c_2; (c) and (g): c_3; (d) and (h): c_4.

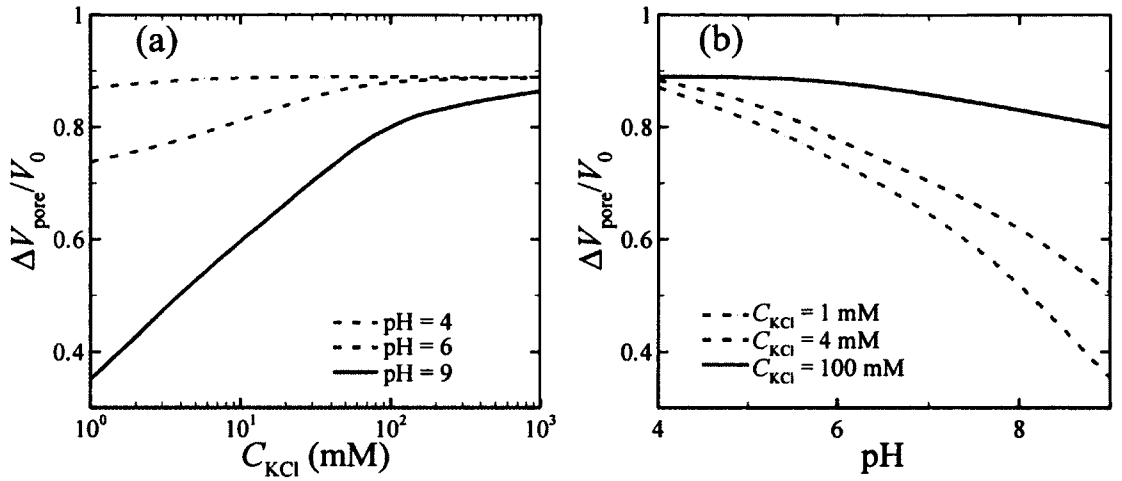

Figure 3.6. Potential drop within the nanopore $\Delta V_{pore}/V_0$ as a function of the background salt concentration C_{KCl} at various solution pH (a) and as a function of pH at various C_{KCl} (b).

3.3.4 Effect of Solution Properties on the Nanopore Potential Drop

One of the main challenges in the nanopore-based DNA sequencing technology is that DNA translocates through the nanopore too fast. One hopes to slow down DNA translocation through the nanopore to improve the read-out performance. Since the DNA electrophoretic velocity is proportional to the electric field inside the nanopore, which can be roughly estimated as the potential drop within the nanopore over the nanopore length. For a fixed nanopore length, one expects to achieve lower translocation speed with lower potential drop inside the nanopore. Figure 3.6 depicts the potential drop within the nanopore normalized by the voltage bias imposed, $\Delta V_{pore}/V_0$, as a function of the background salt concentration at various pH (a) and as a function of pH at various ion strength, C_{KCl} (b). The potential drop inside the nanopore is defined as the potential difference between both openings of the nanopore on the nanopore axis, $\Delta V_{pore} = V(0, L_N/2) - V(0, -L_N/2)$. Due to the potential drops in the two fluid reservoirs, $\Delta V_{pore}/V_0<1$.

At fixed pH, the potential drop initially increases with the ionic strength when the salt concentration is relatively low. When the salt concentration is above a critical value, the potential drop inside the nanopore reaches a plateau. At pH=4, the effect of C_{KCl} on the potential drop is insignificant due to the low surface charge density of the nanopore wall,

as shown in Figure 3.3a. The effect of C_{KCl} on the potential drop within the nanopore increases with increasing pH due to the increased surface charge density. The maximum potential drops for pH=4 and 6 are the same, which are larger than that for pH=9. For a salt concentration below than the critical value, the potential drop for pH=9 is lower than that for pH=6, which is lower than that at pH=4. The dependence of the potential drop on both salt concentration and pH is attributed to the dependence of the induced concentration polarization on the solution properties. The induced concentration polarization with enriched (depleted) ions at the opening of the cathode (anode) side induces an electric field opposite to that externally imposed. The induced opposite electric field increases with the increase in the degree of the concentration polarization, which becomes more significant with the increase in the surface charge density and the degree of double layer overlap, as described in section 3.3.2. The concentration polarization is insignificant due to the low surface charge density at pH=4, therefore, the potential drop does not significantly vary with the ionic strength. Due to the resulting high surface charge density at pH=6 and 9, the induced concentration polarization increases as C_{KCl} decreases owing to the increase in the degree of double layer overlap, resulting in an increase in the induced electric field opposite to the applied one, which in turn decreases the potential drop inside the nanopore. Concentration polarization also becomes insignificant when the salt concentration exceeds the critical one since the thin double layers are not overlapped, resulting in the saturation of the potential drop as the salt concentration further increases. Figure 3.6b shows that the potential drop inside the nanopore decreases as the pH increases, which is mainly due to the increase in the surface charge density and accordingly the concentration polarization. Therefore, one can utilize the induced concentration polarization through adjusting the solution properties to control the potential drop inside the nanopore, which in turn controls the electrokinetic motions of both fluid and particle inside the nanopore.

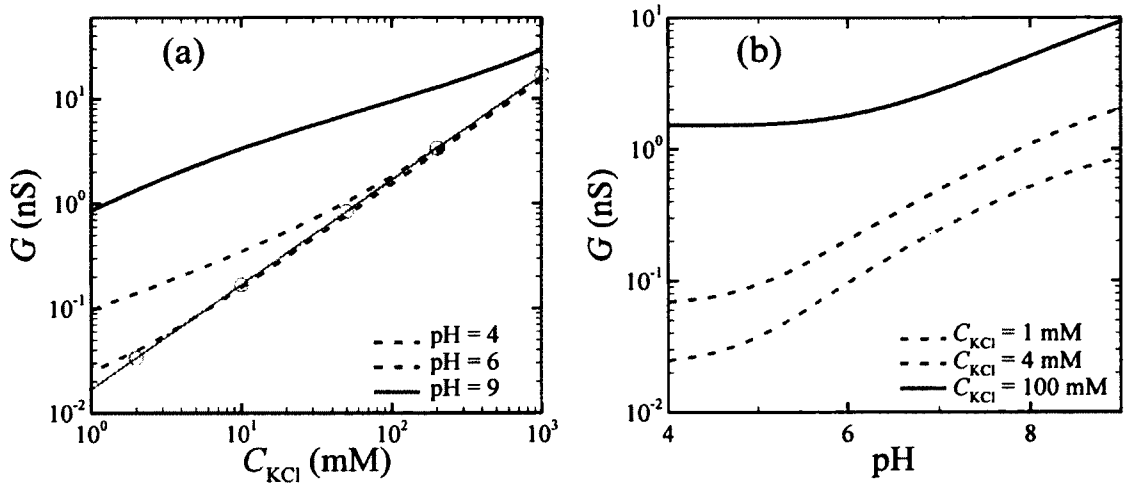

Figure 3.7. Conductance as a function of the background salt concentration C_{KCl} at various solution pH (a) and as a function of pH at various C_{KCl} (b). The solid line with circle in Figure 3.7a indicates the bulk conductance of the nanopore.

3.3.5 Effect of Solution Properties on the Nanopore Conductance

The nanopore conductance depends on the concentrations of both cations and anions confined inside the nanopore, which are governed by the surface charge of the nanopore. Due to the significant dependence of the surface charge density on pH and ionic strength, the solution properties including pH and background salt concentration significantly affect the conductance, as shown in Figure 3.7.

Figure 3.7a shows that the nanopore conductance increases with increasing the background salt concentration. The bulk conductance of the nanopore, $G_{bulk} \cong \pi R_N^2 F(v_1 C_{10} + v_2 C_{20} + v_3 C_{30} + v_4 C_{40})/(L_N + 2R_s)$, is also shown by the solid line with circles. Here, $v_1(H^+) = 3.62\times10^{-7}\,m^2/sV$, $v_2(K^+) = 7.616\times10^{-8}\,m^2/sV$, $v_3(Cl^-) = 7.909\times10^{-8}\,m^2/sV$, and $v_3(OH^-) = 2.06\times10^{-7}\,m^2/sV$ are the electrophoretic mobilities of H^+, K^+, Cl^- and OH^-, respectively. Obviously, the bulk conductance is linearly proportional to the background salt concentration, C_{KCl}, due to the increase in the concentrations of both K^+ and Cl^- inside the nanopore. Since the surface charge density of the nanopore at pH=4 is relatively low and remains almost a constant during 1 mM$\leq C_{KCl} \leq$1 M, as shown in Figure 3.3a, the nanopore conductance at pH=4 agrees with the bulk conductance when

C_{KCl} is above 10 mM. The nanopore conductance is slightly larger than the bulk conductance when C_{KCl} is below 10 mM due to the double layer overlap, resulting in more cations accumulated inside the nanopore. Since the surface charge density at pH=6 is higher than that at pH=4, more cations are attracted into the nanopore resulting in higher conductance than the bulk conductance. Due to very high surface charge at pH=9, the nanopore is predominately occupied by ions K^+, as shown in Figure 3.5f. The nanopore conductance is mainly contributed by the significantly enriched K^+ ions, and its conductance is much higher than the bulk conductance. As C_{KCl} decreases, double layer thickness and the degree of double layer overlap increase, resulting in more cations enriched inside the nanopore, which in turn increases the deviation between the nanopore conductance and the bulk conductance.

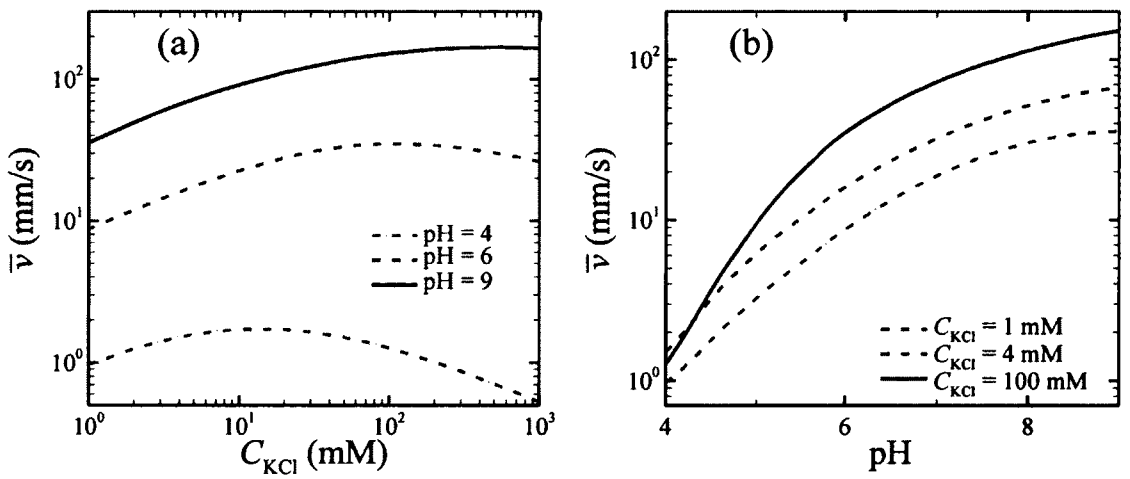

Figure 3.8. Cross-sectional surface-averaged electroosmotic flow velocity $\bar{v}$ as a function of the background salt concentration C_{KCl} at various solution pH (a) and as a function of pH at various C_{KCl} (b).

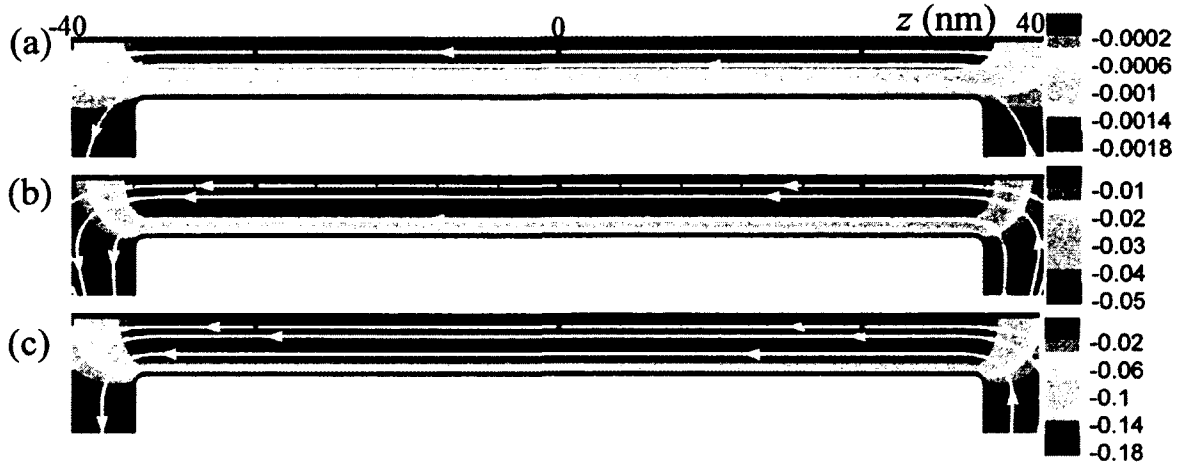

Figure 3.9. Flow field near the silica nanopore for various combinations of the solution pH and the background salt concentration C_{KCl}. (a): pH=4, C_{KCl}=1 mM; (b): pH=9, C_{KCl} =1 mM; (c): pH=9, C_{KCl}=100 mM. Color bars denote the fluid velocity in the z-direction and streamlines with arrows denote fluid velocity vector.

Figure 3.7b depicts the nanopore conductance as a function of pH for different salt concentrations. When the salt concentration is relatively low and the resulting double layers are overlapped (i.e., C_{KCl}=1 mM and 4 mM), the conductance increases with the increasing pH due to the increase in the surface charge density, as shown in Figure 3.3b. For C_{KCl}=100 mM and pH<5, the conductance reaches the bulk conductance and is nearly independent of pH, which is attributed to low surface charge density as shown in Figure 3.3b and double layers are not overlapped. In the range of pH>5, the conductance increases with pH due to significant increase of the surface charge density as shown in Figure 3.3b.

3.3.6 Effect of Solution Properties on the Electroosmotic Flow

The solution properties affect both the ion concentration distributions and the potential drop inside the nanopore, which in turn affects the electrostatic driving force (i.e., the third term in the left hand side of equation (3.5)) and accordingly the electroosmotic flow. Figure 3.8 depicts the cross-sectionally averaged electroosmotic flow velocity, $\bar{v}$, as a function of the bulk salt concentration for various pH (Figure 3.8a) and as a function of

pH for various ionic strengths (Figure 3.8b). Figure 3.9 shows the flow field near the silica nanopore for various combinations of pH and C_{KCl}. Since the nanopore is negatively charged, the induced electroosmotic flow is directed from the anode reservoir toward the cathode reservoir. By comparing Figure 3.9a, b and c, one can easily find that the electroosmotic flow enhances by the increasing pH and background concentration.

As the ionic concentration increases, the potential drop inside the nanopore (Figure 3.6a) increases, leading to an increase in the fluid velocity. The surface charge density also increases with the salt concentration (Figure 3.3a), which attracts more cations inside the nanopore resulting in an increase in the net charge density ρ_e and accordingly the driving force for the electroosmotic flow. However, as the salt concentration increases the double layer thickness decreases, leading to the decrease in the net charge density inside the nanopore and accordingly a decrease in the driving force. The electroosmotic flow velocity versus the salt concentration is the competition of the above three factors. For pH=9, the first two factors dominate when the salt concentration is relatively low and the resulting double layers are overlapped, leading to the fluid velocity increases with an increase in the salt concentration. The third factor also becomes important when the salt concentration is relatively high. Due to the competition among the three factors, the fluid velocity for pH=9 reaches a plateau when the salt concentration is relatively high and the double layers are not overlapped. For pH=4, the effect of the second factor is negligible since the surface charge density is nearly a constant for C_{KCl} varying from 1 mM to 1 M, as shown in Figure 3a. When the salt concentration is relatively low, the potential drop inside the nanopore slightly increases as the salt concentration increases, leading to a slight increase in the fluid velocity. However, the potential drop inside the nanopore reaches a plateau as C_{KCl} further increases. Therefore, as the salt concentration further increases, the third factor becomes dominant. As a result, the fluid velocity reaches the maximum and then decreases as the salt concentration further increases. For pH=6, the particle velocity increases with the salt strength when the latter is low, which is attributed to the first and second factors, and attains a maximum and then decreases as salt concentration further increases due to the saturation of the potential drop inside the nanopore (Figure 3.6a) and the third factor. Since the critical salt concentration at which the potential drop inside the nanopore reaching the plateau for pH=6 is higher than that

for pH=4, the salt concentration at which the maximum fluid velocity occurs for pH=6 is higher than that for pH=4. At the same salt concentration, the electroosmotic flow velocity increases with pH when the latter is low, and the increase in the flow field becomes insignificant when pH is relatively high. As pH increases, the potential drop inside the nanopore decreases (Figure 3.6b), while the surface charge density increases (Figure 3.3b). The variation of the fluid velocity as a function of pH arises from the competition between the aforementioned two opposite effects.

3.4. Conclusions

Charge regulation has been considered for the first time to explore the electric-field-induced ion and fluid transport in a silica nanopore connecting two reservoirs at each end. Different from the existing studies using a pre-specified constant surface charge density, the surface charge density is part of the solution in the present model and highly depends on both pH and the background salt concentration. The prediction of the nanopore conductance by the existing model using a constant surface charge density significantly deviates from the experimental data obtained from the literature, while the present model taking into account the charge regulation successfully captures the physics of the dependence of the nanopore conductance on the salt concentration and favorably agrees with the experimental data. The results show that both pH and ionic strength significantly affect the nanopore surface charge density, which governs the electrokinetic ion and fluid transport, especially when the double layers overlap. Therefore, one can control the ion and fluid transport by tuning pH and/or the ionic strength. pH and salt concentration also significantly affect the concentration polarization with enriched (depleted) counter- and co-ions occurring at the opening of the cathode (anode) side. The induced concentration polarization creates a concentration gradient across the nanopore, which induces an electric field opposite to the externally imposed one, and accordingly reduces the potential drop or electric field inside the nanopore. One can use the dependence of the electric field inside the nanopore on the solution properties to control ekectrokinetic fluid and particle transport inside the nanopore, which highly depend on the electric field inside the nanpopre. For example, one can control the induced concentration polarization

by tuning pH and/or ionic strength to reduce the electric field inside the nanopore for slowing down DNA translocation in the next generation nanopore-based DNA sequencing technology. One can also control pH and/or salt concentration to tune the surface charge density of the nanopore wall, which in turn controls the nanopore conductance and electroosmotic flow.

CHAPTER 4

ELECTROPHORETIC MOTION OF A SOFT SPHERICAL PARTICAL IN A NANOPORE

Abstract

Many biocolloids, biological cells and micro-organisms are soft particles, consisting of a rigid inner core covered by an ion-penetrable porous membrane layer. The electrophoretic motion of a soft spherical nanoparticle in a nanopore filled with an electrolyte solution, has been investigated using a continuum mathematical model, which consists of the Poisson-Nernst-Planck (PNP) equations for the ionic mass transport, and the modified Stokes and Brinkman equations for the hydrodynamic field outside and inside the porous membrane layer, respectively. The effects of the "softness" of the nanoparticle on its electrophoretic velocity along the axis of a nanopore are examined with changes in the ratio of the radius of the rigid core to the double layer thickness, the ratio of the thickness of the porous membrane layer to the radius of the rigid core, the friction coefficient of the porous membrane layer, the fixed charge inside the porous membrane layer of the particle and the ratio of the radius of the nanopore to that of the rigid core. The presence of the soft membrane layer significantly affects the particle electrophoretic mobility.

4.1. Introduction

When a particle bearing a charge immersed in an electrolyte solution is subjected to an external electric field, a relative motion between the particle and the electrolyte solution is induced. This phenomenon is referred to as electrophoresis, which has been widely utilized to characterize, separate, and purify colloidal particles and macromolecules,[71-73] and propel particles in micro/naofluidic systems.[29, 137, 153-158] For example, the electrophoretic translocation of DNA nanoparticles through a nanopore could result in a change of the ionic current through the nanopore. Through the particle's effect on the

ionic current, one hopes to detect the presence of the particle inside the nanopore as well as obtain information on the nanoparticle's characteristics, such as the sequence of nucleotide bases in DNA nanoparticles. This nanopore-based DNA sequencing method has the potential to revolutionize genomic medicine.[29, 137]

Electrophoretic motions of rigid particles in both unbounded and confined media have been studied extensively,[153-173] In nature, a large amount of particles including biological cells such as human erythrocytes,[174] bacteria,[175-176] environmental colloids such as humic substances, [177] and colloidal particles covered with charged polyelectrolyte layer [178-183] are soft particles, consisting of a rigid core covered by a porous membrane layer. The presence of the charged porous membrane layer will affect both the electrostatic and the hydrodynamic forces acting on the particle as well as the ionic concentration distributions inside and outside the membrane layer, and accordingly will have a significant influence on the electrophoretic motion of a soft particle, which makes its theoretical analysis more complicated than that of rigid particles. Comparing to the study of electrophoresis of rigid particles, comprehensive understandings of the electrophoretic motion of a soft particle, especially a soft nanoparticle in a nanopore, are currently very limited, which is the objective of this chapter.

Previous investigations on the electrophoresis of a soft particle are subject to several restrictions. For example, Ohshima [125, 184-187] derived approximation solutions for the electrophoretic mobility for a variety of soft particles without considering the double layer polarization (DLP) and relaxation effects; while Duval's group investigated the electrokinetics of diffuse soft interface and electrophoresis of diffuse soft particle with non-uniformly distributed polymer segments without considering the DLP.[180-181, 188-191] Saville,[192] Hill et al.,[193] Hill,[194] Hill and Saville,[195] and Lopez-Garcia et al.[196] investigated the electrophoretic motion of soft particles in an unbounded medium taking into account the polarization and relaxation effects, and found that DLP effect is very important when the fixed charge inside the membrane layer is relatively high. However, the boundary effect is not considered in the aforementioned studies. In the practical applications of electrophoresis in micro/nanofluidic systems,[29, 137, 153-158] the particle is not isolated and its electrophoretic motion is affected by the rigid boundaries such as the channel walls. Comparing to the numerous studies on the influence of the boundary on the

electrophoretic motion of rigid particles, the study on the boundary effect on soft particle's electrophoretic behavior is still very limited so far. Only recently, Hsu's group[197-198] adopted the linearized Poisson-Boltzmann model to theoretically investigate electrophoresis of a soft particle along the axis of a cylindrical pore under the conditions of lower surface potential (or charge) and weak applied electric field. Lee et al.,[199] Huang et al.,[200] and Cheng et al.[201] theoretically investigated the electrophoresis of a soft particle in a spherical cavity, in a cylindrical pore, and normal to a planar surface, respectively, under the condition of a weak electric field imposed. In the present study, electrophoresis of a soft nanoparticle along the axis of a nanopore is investigated using the Poisson-Nernst-Planck (PNP) model, which takes into account the full interactions of particle, fluid, electric field, and ionic mass transport, with no assumption made concerning the level of charge inside the membrane, the electrical double layer (EDL) thickness, and the magnitude of the electric field applied, which will overcome the limits of the Poisson-Boltzmann model. Double layer polarization, relaxation, and compression due to the nanopore wall are also considered in the current study.

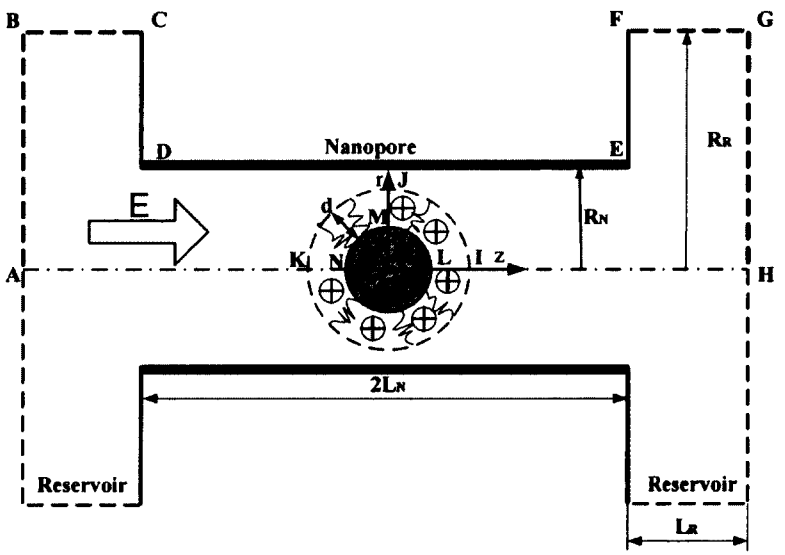

Figure 4.1. Schematics of a nanopore of length $2L_N$ and radius R_N connecting two identical reservoirs on either side. A charged soft spherical particle, consisting of a rigid spherical core of radius a covered by an ion-penetrable porous membrane layer of thickness d, is positioned in the center of the nanopore. An electric field, $\boldsymbol{E}$, is externally

imposed parallel to the axis of the nanopore, resulting in the particle electrophoretic motion.

4.2. Mathematical Model

We consider a soft spherical nanoparticle of radius (a + d), consisting of a rigid spherical core of radius a covered by an ion-penetrable porous membrane layer of thickness d, positioned in the center of a nanopore with length $2L_N$ and radius R_N, which is filled with a binary electrolyte solution supplied by two identical reservoirs at each end. Considering the axial symmetry of the geometry and physical fields, we use a cylindrical coordinate system (r, z) with the origin fixed at the center of the nanopore, as shown in Figure 4.1. The nanoparticle is observed when its center coincides with the origin for convenience, so that the axisymmetric flow is studied by considering the region I, surrounded by the boundary ABCDEFGH, the symmetric line HI, the particle's outer surface IJK, and the symmetric line KA, and the region II in the porous membrane layer of the particle bounded by the particle's inner rigid surface LMN and outer surface IJK. The dashed line segments AB, BC, FG, and GH represent the regions in the reservoirs. The length and radius of the reservoirs are, respectively, L_R and R_R, which are sufficiently large to maintain the electrochemical properties at the locations of AB, BC, FG, and GH unaffected by the charged nanoparticle and nanopore wall. We assume that the walls of the two reservoirs (line segments CD and EF) are electrically neutral surfaces, the nanopore wall (the segment DE) carries a uniform surface charge density of σ_w, and the ion-penetrable membrane layer has a fixed charge density ρ_{fix}. The porous membrane layer of the particle resembles a packed bed with friction coefficient γ. Although the surface charge on the nanopore wall plays an important role in electrophoretic motion of particles, to emphasis the influence of the soft layer on the particle electrophoretic motion, the surface charge density on the nanopore σ_w in the present study is set to zero. A potential difference, ϕ_0, is applied across AB and GH to introduce an axial electric field across the nanopore, and there is no pressure and concentration gradient imposed across AB and GH. Due to the applied electric field, the particle electrophoretically translates

along the axis of the nanopore with a velocity $\mathbf{U}_p$. Hereafter, bold letters represent vectors.

A continuum model, consisting of the PNP equations for the ionic mass transport and the modified Stokes equations for the flow field, has recently been used to investigate the electroosmotic, electrophoretic, diffusioosmotic, and diffusiophoretic flows in a nanopore, and the numerical results are in qualitative agreement with experimental data available from the literature and the predictions from the molecular dynamics simulations [53, 68, 164-167, 202-205]. In this study, we extend the verified continuum model, by taking into account the ionic mass transport and fluid flow within the porous membrane layer, to investigate the electrophoretic motion of a soft nanoparticle in a nanopore. The extended model reduces to the existing one for a rigid particle of radius a if the porous membrane layer vanishes (i.e., $d = 0$). The model takes into account the DLP by the imposed electric field, and the induced fluid and particle motions without any assumption made concerning the EDL thickness and the magnitude of the imposed electric field.

4.2.1 Mathematical Model for the Fluid Motion

Since a typical Reynolds number for the electrokinetic flow in a nanopore is extremely small, the inertial terms in the Navier-Stokes equations are neglected and the hydrodynamics is described by the modified Stokes equations in the free-flow region I and the Brinkman equations in the porous region II. For a binary, incompressible electrolyte solution with viscosity μ and valences z_1 and z_2, respectively, for the positive and negative ions, the conservation laws for mass and momentum are written as

$$\nabla \bullet \mathbf{u} = 0, \qquad \text{in regions I and II} \tag{4.1}$$

$$-\nabla p + \mu \nabla^2 \mathbf{u} - F\left(z_1 c_1 + z_2 c_2\right)\nabla V = 0, \text{ in region I} \tag{4.2}$$

and

$$-\nabla p + \mu \nabla^2 \mathbf{u} - F\left(z_1 c_1 + z_2 c_2\right)\nabla V - \gamma\left(\mathbf{u} - \mathbf{U}_p\right) = 0, \text{ in region II} \tag{4.3}$$

where $\mathbf{u} = u_r \mathbf{e}_r + u_z \mathbf{e}_z$ is the fluid velocity vector, in terms of the radial and axial unit base vector $\mathbf{e}_r$ and $\mathbf{e}_z$, p is the hydrostatic pressure, F is the Faraday constant, c_1 and c_2 are, respectively, the molar concentrations of the positive and negative ions, and V is the

electric potential in the electrolyte solution. The third term on the left hand side (LHS) of the momentum Eq. (4.2) and Eq. (4.3) represents the electrostatic force through the interaction between the electric field, $\mathbf{E} = -\nabla V$, and the net charge density, $\rho_e = F\left(z_1 c_1 + z_2 c_2\right)$, in the electrolyte solution. Eq. (4.3) is the modified Brinkman equations (by taking into account the electrostatic body force) that describe the fluid flow in a porous medium, and the last term on the LHS of Eq. 4.(3) represents the viscous drag exerted on the interstitial fluid inside the membrane layer. From some previous work [206-208], the Brinkman model without considering the deformation of the soft layer, which we used in this chapter, can provide results with great agreement to the experimental data.

A non-slip boundary condition (i.e., $u_r = u_z = 0$) is specified at the fixed, solid walls of the nanopore and the reservoirs (line segments CD, DE, and EF in Figure 4.1). On the planes AB and GH of the reservoirs which are far away from the nanopore, normal flow with pressure p = 0 is used. Symmetric boundary condition is used along the lines of symmetry, HIL and AKN. Slip or symmetric boundary conditions are used on the segments BC and FG, which are in the bulk electrolyte reservoirs and far away from the entrances of the nanopore. Along the outer surface of the particle (arc segment IJK in Figure 4.1), continuous flow boundary condition is applied (e.g., the fluid velocity and both the normal and tangential viscous stresses are continuous). Finally, along the inner surface of the particle (arc segment LMN in Figure 4.1) translating with an electrokinetic velocity $\mathbf{U}_p$, we neglect the thickness of the adjacent Stern layer, and impose the non-slip boundary condition as

$$\mathbf{u}(r,\ z) = \mathbf{U}_p = u_p \mathbf{e}_z \text{, on LMN.} \tag{4.4}$$

The particle's electrokinetic velocity u_p is determined by requiring the total force in the z direction (F_T) acting on the particle

$$F_T = F_E + F_D = 0, \tag{4.5}$$

where

$$F_E = \int_S (\mathbf{T}^E \bullet \mathbf{n}) \bullet \mathbf{e}_z dS \tag{4.6}$$

and

$$F_D = \int_S (\mathbf{T}^D \bullet \mathbf{n}) \bullet \mathbf{e}_z dS \tag{4.7}$$

are, respectively, the electrostatic and hydrodynamic forces acting on the particle. S is the particle's outer surface IJK; $\mathbf{T}^E = \varepsilon_f \mathbf{E}\mathbf{E} - \frac{1}{2}\varepsilon_f (\mathbf{E} \bullet \mathbf{E})\mathbf{I}$ and $\mathbf{T}^D = -p\mathbf{I} + \mu\left(\nabla \mathbf{u} + \nabla \mathbf{u}^T\right)$ are, the Maxwell stress tensor and the hydrodynamic stress tensor, respectively; ε is the permittivity of the electrolyte solution; and $\mathbf{I}$ is the unit tensor.

4.2.2 Mathematical Model for the Ionic Mass Transport

The flux density vector for each aqueous species due to convection, diffusion, and migration is given by the Nernst-Planck equation [159]:

$$\mathbf{N}_k = \mathbf{u}\, c_k - D_k \nabla c_k - z_k \frac{D_k}{RT} F c_k \nabla V \qquad (k=1, 2), \tag{4.8}$$

where D_k is the diffusion coefficient of the k^{th} ionic species, R is the universal gas constant, and T is the absolute temperature of the electrolyte solution. Under steady-state conditions, the concentration of each species in both regions I and II is governed by the steady ionic mass conservation equations:

$$\nabla \bullet \mathbf{N}_k = 0 \qquad (k=1, 2). \tag{4.9}$$

The electric potential in the electrolyte solution is governed by the Poisson equation:

$$-\varepsilon_f \nabla^2 V = F\left(z_1 c_1 + z_2 c_2\right), \quad \text{in region I} \tag{4.10}$$

and

$$-\varepsilon_f \nabla^2 V = F\left(z_1 c_1 + z_2 c_2\right) + \rho_{fix}, \quad \text{in region II.} \tag{4.11}$$

Note that the fixed charge density inside the soft layer, ρ_{fix}, is spatially dependent to take into account the non-uniformly distributed polymer segments [180-181, 188-191]. To simplify the complicated but important problem, the current study assumes the soft particle has uniformly distributed charge density inside the soft layer, and ρ_{fix} is a constant within the region II.

On the planes AB and GH, which are sufficiently far away from the nanopore, the ionic concentrations are the same as the bulk concentration of the electrolyte solution present in the fluid reservoirs:

$$c_1 = c_2 = C_0, \qquad \text{on AB and GH} \tag{4.12}$$

At the walls of the reservoirs (line segments CD and EF) and the wall of the nanopore (line segment DE), which are impervious to ions, the net ionic fluxes normal to the rigid walls are zero:

$$\mathbf{n} \bullet \mathbf{N}_1 = \mathbf{n} \bullet \mathbf{N}_2 = 0, \quad \text{on CD, DE, and EF.} \tag{4.13}$$

In the above, $\mathbf{n}$ is the unit vector normal to the corresponding surface. Along the inner surface of the nanoparticle (arc segment LMN), which is impervious to ions and translating with a velocity $\mathbf{U}_p$ in Eq. (4.4), the normal ionic fluxes satisfy [159]

$$\mathbf{n} \bullet \mathbf{N}_k = \mathbf{n} \bullet (\mathbf{u} c_k), \qquad k = 1 \text{ and } 2. \tag{4.14}$$

Note that the coordinate is fixed to the stationary nanopore wall and the particle moves according to Eq. (4.4), the net ionic flux normal to the particle's inner surface, which is impervious to ions, thus exclusively includes the convective term.

Zero normal flux is used along the segments BC and FG, which are in the bulk electrolyte reservoirs:

$$\mathbf{n} \bullet \mathbf{N}_1 = \mathbf{n} \bullet \mathbf{N}_2 = 0, \text{ on BC and FG.} \tag{4.15}$$

Along the segments HIL and AKN, symmetric boundary condition is used for the ionic concentrations:

$$\mathbf{n} \bullet \mathbf{N}_1 = \mathbf{n} \bullet \mathbf{N}_2 = 0, \text{ on HIL and AKN.} \tag{4.16}$$

Along the outer surface of the particle (arc segment IJK), the concentrations and normal fluxes of the positive and negative ions are continuous.

Symmetric boundary condition for the electric potential is used on the planes HIL and AKN:

$$\mathbf{n} \bullet \nabla V = 0, \text{ on HIL and AKN.} \tag{4.17}$$

An external potential, ϕ_0, is applied along the plane AB (anode):

$$V = \phi_0, \text{ on AB.} \tag{4.18}$$

Along the plane GH (cathode), the boundary condition for the electric potential is

$$V = 0, \text{ on GH.} \tag{4.19}$$

Since the surfaces of BC and FG are far away from the nanopore and are in the bulk electrolyte reservoirs, no charge boundary condition for the potential is used:

$$\mathbf{n}\bullet\left(-\varepsilon_f\nabla V\right)=0\,,\ \text{on BC and FG.} \tag{4.20}$$

Since the walls of the reservoirs (planes CD and EF) do not carry fixed charge, we use

$$\mathbf{n}\bullet\left(-\varepsilon_f\nabla V\right)=0\,,\ \text{on CD and EF.} \tag{4.21}$$

Along the nanopore wall (line segment DE), zero surface charge boundary condition is used:

$$\mathbf{n}\bullet\left(-\varepsilon_f\nabla V\right)=0\,,\ \text{on DE,} \tag{4.22}$$

Along the particle's inner surface (arc segment LMN), we assume it is not charged, thus zero surface charge boundary condition is used:

$$\mathbf{n}\bullet\left(-\varepsilon_f\nabla V\right)=0\,,\ \text{on LMN.} \tag{4.23}$$

Along the particle's outer surface (arc segment IJK), continuous boundary condition for the potential and normal electric field is used.

4.2.3 Dimensionless Form of the Models

We use the bulk electrolyte concentration in the fluid reservoir, C_0, as the ion concentration scale; RT/F as the potential scale; the radius of the nanoparticle's rigid core, a, as the length scale; $U_0=\varepsilon_f R^2T^2/\left(\mu aF^2\right)$ as the velocity scale; and U_0/a as the pressure scale. The dimensionless governing equations of the above models for the fluid motion and ionic mass transport are:

$$\nabla^*\bullet\mathbf{u}^*=0,\ \text{in regions I and II,} \tag{4.24}$$

$$-\nabla^* p^*+\nabla^{*2}\mathbf{u}^*-\frac{1}{2}(\kappa a)^2\left(z_1c_1^*+z_2c_2^*\right)\nabla^*V^*=0,\ \text{in region I} \tag{4.25}$$

$$-\nabla^* p^*+\nabla^{*2}\mathbf{u}^*-\frac{1}{2}(\kappa a)^2\left(z_1c_1^*+z_2c_2^*\right)\nabla^*V^*-(\lambda a)^2\left(\mathbf{u}^*-\mathbf{U}_p^*\right)=0,\ \text{in region II} \tag{4.26}$$

$$\nabla^*\bullet\mathbf{N}_i^*=0,\ \text{in regions I and II} \tag{4.27}$$

$$-\nabla^{*2}V^*=\frac{1}{2}(\kappa a)^2\left(z_1c_1^*+z_2c_2^*\right),\ \text{in region I} \tag{4.28}$$

$$-\nabla^{*2}V^*=\frac{1}{2}(\kappa a)^2\left(z_1c_1^*+z_2c_2^*\right)+Q,\ \text{in region II} \tag{4.29}$$

In the above, variables with superscript * are dimensionless. $\kappa^{-1} = \lambda_D = \sqrt{\varepsilon_f RT/2F^2C_0}$ is the dimensional EDL thickness. $\lambda a = \sqrt{\gamma a^2/\mu}$ is the dimensionless friction coefficient of the porous membrane layer [197]. $Q = \rho_{fix} a^2 F/(\varepsilon_f RT)$ is the dimensionless fixed charge in the soft membrane layer. The reciprocal of λ is called "screening length", which is on the order of several nanometers [200]. For example, the value of λ for poly hydrogel layers around latex particles ranges from 8.3×10^8 m^{-1} to 1.1×10^9 m^{-1}, while that for the microbial cell surface of a collection of four pseudomonas syringae strains ranges from 0.67×10^9 m^{-1} to 0.26×10^9 m^{-1} [175]. Therefore, λa = 1 means the screening length is identical to the nanoparticle radius.

The dimensionless flux density normalized by U_0C_0 is

$$\mathbf{N}_i^* = \mathbf{u}^* c_i^* - (D_i/D_0)\nabla^* c_i^* - z_i (D_i/D_0) c_i^* \nabla^* V^*, \tag{4.30}$$

with $D_0 = \varepsilon_f R^2T^2/(\mu F^2)$.

The dimensionless particle velocity u_p* is determined by the zero net force acting on the particle,

$$F_E^* + F_D^* = 0, \tag{4.31}$$

with

$$F_E^* = \int_{S^*} \left[\frac{\partial V^*}{\partial r^*}\frac{\partial V^*}{\partial z^*} n_r + \frac{1}{2}\left[\left(\frac{\partial V^*}{\partial z^*}\right)^2 - \left(\frac{\partial V^*}{\partial r^*}\right)^2 \right] n_z \right] ds^*, \tag{4.32}$$

and

$$F_D^* = \int_{S^*} \left[\left(\frac{\partial u_r^*}{\partial z^*} + \frac{\partial u_z^*}{\partial r^*}\right) n_r + \left(-p^* + 2\frac{\partial u_z^*}{\partial z^*}\right) n_z \right] ds^*. \tag{4.33}$$

u^* and v^* are, respectively, the r- and z- components of the dimensionless velocity $\mathbf{u}^*$. n_r and n_z are, respectively, the r- and z- components of the unit vector $\mathbf{n}$ which is normally directed outward the particle's center of mass, and s^* is the outer surface of the nanoparticle (the arc segment IJK in Figure 4.1).

4.3. Results and Discussion

4.3.1 Numerical Method and Code Validation

The commercial package COMSOL version 3.5a (www.comsol.com), installed in a high-performance cluster, is used to directly solve the coupled system with finite-element method. In contrast to the previous study [200] where perturbation approach is used and is limited to relatively low electric field imposed so that the EDL is only slightly distorted from its equilibrium state by the external field, there is no assumption concerning the magnitude of the imposed electric field is made in the current study.

Quadratic triangular elements with variable sizes are used to accommodate finer resolutions inside the charged porous membrane layer. A total of 150 thousand elements are employed in the simulation, while inside the porous membrane layer the maximum element size is only $0.01a$. We use p2-p1 Lagrange elements for modified Stokes and Brinkman equations and Lagrange quadratic elements for the rest equations, respectively. No specific stabilization method is introduced to solve the modified Stokes and Brinkman equations. The relative tolerance is set as 10^{-6} in all the cases of this chapter. Solution convergence is guaranteed through mesh-refinement tests on the conservation laws. The mathematical model and its implementation with COMSOL have been validated by comparing its results of electroosmotic, electrophoretic, and diffusioosmotic flows in nanopores with the corresponding approximate analytical solution and experimental results obtained from the literatures [53, 164-167, 202-205]. We also compared our numerical results of the electrophoretic mobility of a soft particle with the corresponding approximate solution [187]:

$$\eta^* = \frac{u_p^*}{E_\infty^*} = \frac{Q}{(\lambda a)^2}\left[1+\frac{2}{3}\left(\frac{\lambda}{\kappa}\right)^2\left(\frac{1+\lambda/2\kappa}{1+\lambda/\kappa}\right)\left(1+\frac{a^3}{2(a+d)^3}\right)\right], \qquad (4.34)$$

where E_∞^* represents the dimensionless electric field imposed far away from the particle, and η^* is the dimensionless electrophoretic mobility. Note that the above approximation solution is valid under the conditions of $\kappa a \gg 1$, $\lambda a \gg 1$, $\kappa d \gg 1$, $\lambda d \gg 1$, and $Q \ll (\kappa a)^2/2$. The last one is required to satisfy the assumption of $\rho_{fix}/FC_0 \ll 1$ in the Ohshima's work [187]. Figure 4.2a depicts the dimensionless electrophoretic mobility as a function of λa when $\kappa a = 20$, $d/a = 1$, $Q = 1$, and $R_N/(a+d) = 20$. Our numerical results

(circles) are in good agreement with the approximation solution (solid line). Figure 4.2b depicts the dimensionless electrophoretic mobility as a function of the dimensionless charge within the porous medium layer when $\kappa a = 20$, $d/a = 1$, $\lambda a = 10$, and $R_N/(a+d) = 20$. Our numerical results (circles) are in good agreement with the approximation solution (solid line) for small Q ($Q << (\kappa a)^2/2$). The approximation solution is valid only for small Q, thus overpredicts the mobility for $Q > (\kappa a)^2/2 = 200$ under the considered conditions.

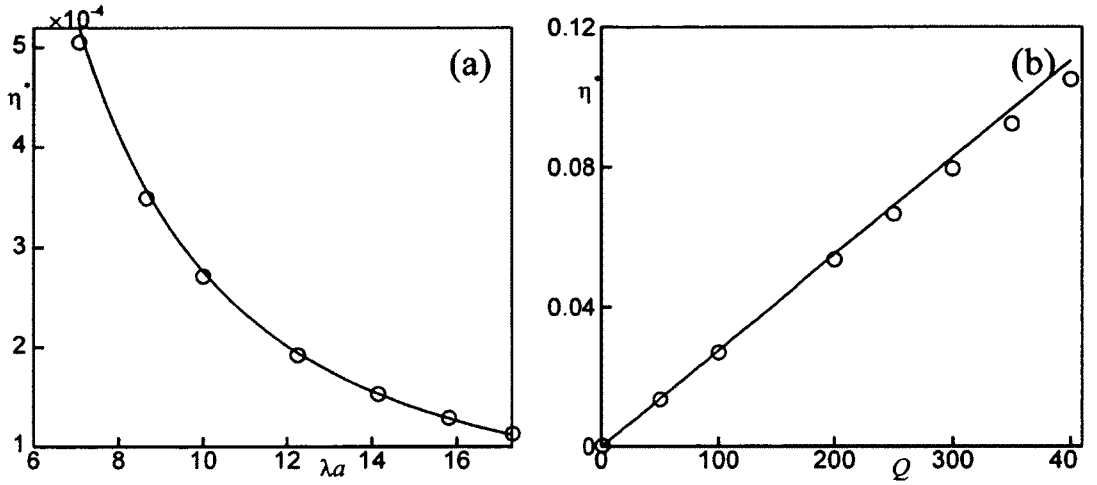

Figure 4.2. Dimensionless electrophoretic mobility as a function of λa (a) and Q (b). (a): $\kappa a = 20$, $Q = 1$, and $d/a = 1$; (b): $\kappa a = 20$, $d/a = 1$, and $\lambda a = 10$. Circles and lines represent, respectively, our numerical results and Ohshima's approximation solutions.

In this section, we present a few numerical results of the electrophoretic motion of a spherical soft nanoparticle along the axis of a nanopore under various conditions. We focus on the electrophoretic motion of a soft particle as functions of the ratio of the radius of the rigid core to the EDL thickness, κa, the ratio of the membrane layer thickness to the radius of the rigid core, d/a, the friction coefficient in the porous medium layer, λa, the homogeneous fixed charge within the soft layer, Q, and the ratio of the radius of the nanopore to that of the rigid core, R_N/a. A representative case of the numerical simulation corresponds to a nanopore with length $2L_N$ = 0.6 μm connecting two fluid reservoirs of L_R = 0.2 μm and R_R = 0.2 μm, the radius of the rigid core is a = 10 nm, and the imposed potential difference is V_0 = 0.6 V. The choice of the reservoir lengths is to ensure the electrochemical properties at AB and GH are not affected by the charged nanoparticle

and nanopore. The temperature of the electrolyte solution in the reservoirs and the nanopore is $T = 300$ K. The electrolyte solution is *KCl*, and the diffusion coefficients of the ions K^+ and Cl^- are, respectively, 1.95×10^{-9} m^2/s and 2.03×10^{-9} m^2/s [73].

4.3.2 The Effect of κa, Ratio of the Radius of the Rigid Core to the EDL Thickness

Figure 4.3 depicts the dimensionless particle velocity as a function of κa for $Q = 20$ (a) and 50 (b) when $\lambda a = 0$ (solid lines), 1 (dash lines), and 10 (dash-dotted lines) in a nanopore. When λa is relatively small (i.e., $\lambda a = 0$ and 1), the particle velocity increases with increasing κa when the latter is relatively small. Once κa reaches a certain value, which is about 1, the particle velocity peaks and then decreases as κa further increases. When λa is relatively large (i.e., $\lambda a = 10$), the particle velocity monotonically decreases as κa increases. The particle velocity for $\lambda a = 0$ is higher than that for $\lambda a = 1$, which is higher than that for $\lambda a = 10$ when the other conditions remain identical. The larger λa represents larger viscous drag on the particle arising from the porous membrane layer, which in turn retards the particle motion. Comparing Figure 4.3a to Figure 4.3b, it is found that the particle velocity for $Q = 50$ is higher than that for $Q = 20$ under the same other conditions. The increasing fixed charge in the membrane layer leads to an increase in the electrostatic force arising from the interaction between the particle's fixed charge inside the soft layer and the imposed electric field, F_E, leading to an increase in the particle electrophoretic velocity. The effects of Q on the particle electrophoretic velocity will be elaborated in details later. Ennis and Anderson [161] investigated the electrophoretic motion of rigid particles with relatively thick EDLs and found that the velocity of a particle with a fixed zeta potential increases as κa increases. Similarly, Huang et al. [200] found that the velocity of a soft particle with a fixed zeta potential on the surface of the rigid core generally increases as κa increases. However, the zeta potential of a rigid particle with a fixed surface charge density decreases as κa increases [171]. Accordingly, the particle velocity decreases as κa increases, confirmed by a previous study [165]. Similar to a rigid particle, the zeta potential of a soft particle with a fixed charge in the membrane layer also decreases as κa increases (results are not shown here). As a result, the particle velocity, in general, decreases as κa increases, as shown in Figure 4.3. However, the particle velocity exhibits a local maximum value around $\kappa a = 1$ when λa is relatively

small (i.e., λa = 0 and 1), which is attributed to the DLP effect. In the absence of any external disturbance, the EDL is symmetric with respect to the center of the spherical particle. However, the external fields including the imposed electric field, the induced fluid and particle motion may significantly disturb the EDL, resulting in a non-uniform ionic concentration distribution around the particle and accordingly the DLP effect. The equilibrium ionic concentration without external disturbance is defined as $\overline{c_i}$ (i=1 and 2), which are obtained by solving the equations (27)-(29) without external electric field, fluid and particle motions. $\delta c_i = c_i - \overline{c_i}$ (i=1 and 2) represents the distorted ionic concentration by the external fields. Since the ionic concentration scale C_0 varies with κa, it is more reasonable to discuss the DLP effect by comparing the dimensional disturbed concentration difference $\delta(c_1 - c_2)$ for different κa. Figure 4.4 depicts $\delta(c_1 - c_2)$ for Q = 50, λa = 1, d/a = 0.5, and R_N/a = 5 when κa = 0.5 (a), 1 (b) and 2.5 (c), which corresponds to the dashed line in Figure 4.3b. When λa = 1 and κa is small (i.e., κa = 0.5 and 1), more negative (positive) ions induced by the external fields accumulate near the upper (lower) hemisphere (Figs. 4a and 4b), indicating a significant DLP. Consequently, an extra electric field in the same direction of the applied one is induced to enhance the particle velocity. Comparing Figs. 4a to 4b, the region of $\delta(c_1 - c_2)>0$ near the lower hemisphere for κa = 1 is larger than that for κa = 0.5, implying that the DLP for κa = 1 is more significant than that for κa = 0.5, resulting in an increase in the particle velocity with increasing κa in the range of $\kappa a \leq 1$. When κa >1, as κa further increases, the magnitude of $\delta(c_1 - c_2)$ and accordingly the degree of DLP decreases. For example, Figure 4.4c depicts $\delta(c_1 - c_2)$ for κa = 2.5 and its magnitude is much lower than that for κa = 1. Therefore, as κa further increases, the DLP effect becomes insignificant resulting in the particle velocity deceases as κa increases.

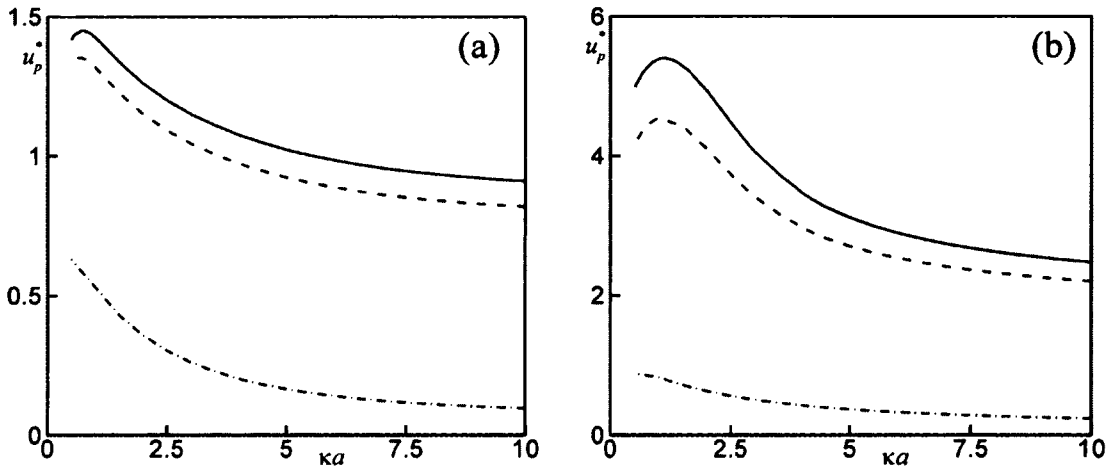

Figure 4.3. Dimensionless particle velocity as a function of κa for $Q = 20$ (a) and $Q = 50$ (b) when $\lambda a = 0$ (solid lines), 1 (dash lines), and 10 (dash-dotted lines), $d/a = 0.5$, and $R_N/a = 5$.

Note that the DLP effect in general retards the particle electrophoretic motion, as observed by Huang et al. [200]. In contrast, our results show that the DLP enhances the electrophoretic mobility under the considered conditions. Recently, Hsu and Tai [146] found that there are two types of DLP in electrophoresis of rigid particles. One is type I DLP which occurs inside the double layer and reduces the particle motion, and the other is type II DLP occurring immediately outside the double layer and raising the mobility. Our results imply that the type II DLP, which induces an extra electric field in the same direction of the applied one, dominants over the type I DLP under the considered conditions in the current study.

4.3.3 The Effect of d/a, Ratio of the Soft Layer Thickness to the Radius of the Rigid Core

Figure 4.5 depicts the dimensionless particle velocity in a nanopore as a function of the ratio, d/a, when $Q = 25$ and $R_N/a = 5$. Since the particle velocity for $\lambda a = 50$ (dash-dotted and dash-double-dotted lines) is very small compared to that for $\lambda a = 1$ (solid and dashed lines), it is multiplied by a factor of 10 to enhance visibility. For $\lambda a = 1$ (solid and dashed lines), the particle velocity monotonically increases as the ratio, d/a, increases for both $\kappa a = 0.5$ (solid line) and 10 (dashed line). When λa is relatively small, Huang et al. [200] also

obtained similar results. For λa = 50 (dash-dotted and dash-double-dotted lines), the particle velocity increases as the ratio, d/a, increases when the latter is relatively small. Once the ratio, d/a, reaches a critical value, the particle velocity peaks and then decreases as the ratio, d/a, further increases.

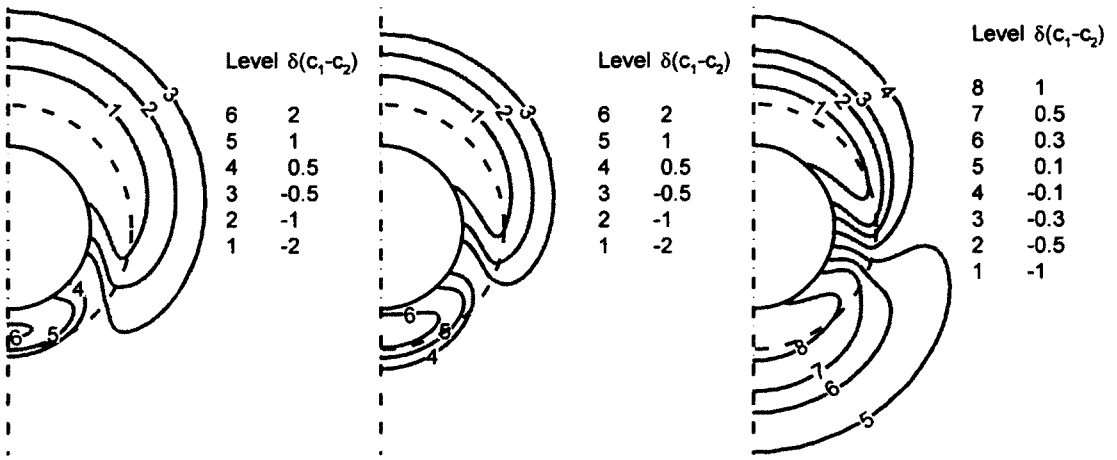

Figure 4.4. Dimensional disturbed concentration difference for Q = 50, λa = 1, d/a = 0.5, and R_N/a = 5 when κa = 0.5 (a), 1 (b) and 2.5 (c), which corresponds to the dashed line in Figure 4.3. The solid and dashed lines represent the inner and outer surfaces of the soft particle.

Obviously, the thickness of the porous membrane layer increases as the ratio, d/a, increases, which leads to an increase in the total amount of fixed charge inside the porous membrane layer and consequently the electrostatic force, F_E, acting on the particle. The increase in the electrostatic force, F_E, in turn leads to an increase in the particle velocity. However, the increase of the ratio, d/a, also increases the fluid-membrane interaction inside the porous membrane layer, leading to an increase in the viscous force, F_D, arising from the membrane layer. The increasing F_D, however, reduces the particle velocity. For a relatively small λa (i.e., λa = 1), the fluid-membrane interaction is relatively weak, the increase in F_D is unable to compete the increase in F_E as d/a increases, resulting in a monotonic increase in the particle velocity with the increasing d/a. For a relatively large λa (i.e., λa = 50 in Figure 4.5), the increase in F_E with the increasing ratio, d/a, dominates

over that of F_D, resulting in an increase in the particle velocity with increasing d/a when the ratio d/a is relatively small. However, the viscous drag arising from the porous membrane layer is proportional to $(\lambda a)^2$, as shown in Eq. (4.26). Therefore, once the ratio, d/a, reaches a critical value, the increase in F_D dominates over that of F_E, resulting in a local maximum of the particle velocity and a monotonic decreases as the ratio d/a further increases.

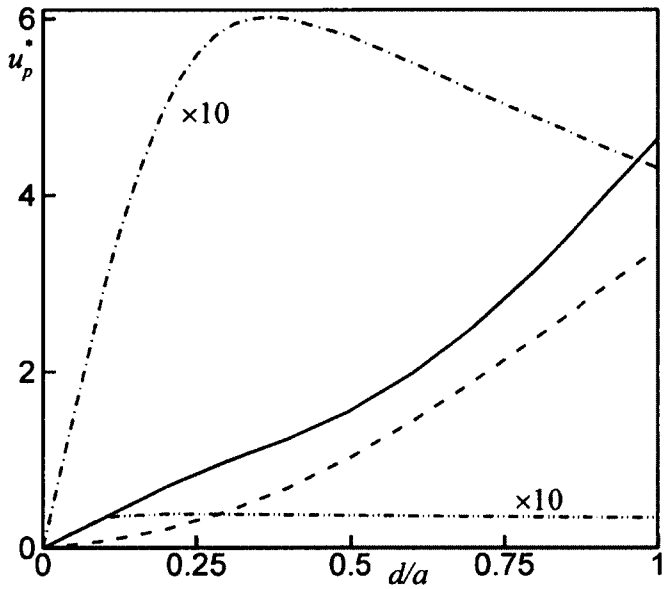

Figure 4.5. Dimensionless particle velocity as a function of d/a when $\lambda a = 1$ and $\kappa a = 0.5$ (solid line), $\lambda a = 1$ and $\kappa a = 10$ (dashed line), $\lambda a = 50$ and $\kappa a = 0.5$ (dash-dotted line), and $\lambda a = 50$ and $\kappa a = 10$ (dash-double-dotted line) for $Q = 25$ and $R_N/a = 5$.

Figure 4.6 depicts the dimensionless particle velocity as a function of κa when $d/a = 1$ (dashed line), 0.5 (solid line), and 0.2 (dash-dotted line), for $Q = 20$, $\lambda a = 1$, and $R_N/a = 5$. When d/a is relatively small (i.e., $d/a = 0.2$), the particle velocity deceases monotonically as κa increases. As explained in section 3.1, this is attributed to the decreasing zeta potential with increasing κa, which results in a decrease in F_E and thus a monotonic decrease in the particle velocity. Based on the spatial distribution of $\delta(c_1 - c_2)$ for various values of d/a (results are not shown here), the degree of DLP generally increases with increasing d/a. When d/a is relatively large (i.e., $d/a = 0.5$ and 1), owing to the DLP effect discussed in section 3.1, the particle velocity increases with increasing κa when the

latter is relatively small; once κa reaches a critical value, it peaks and then declines as κa further increases.

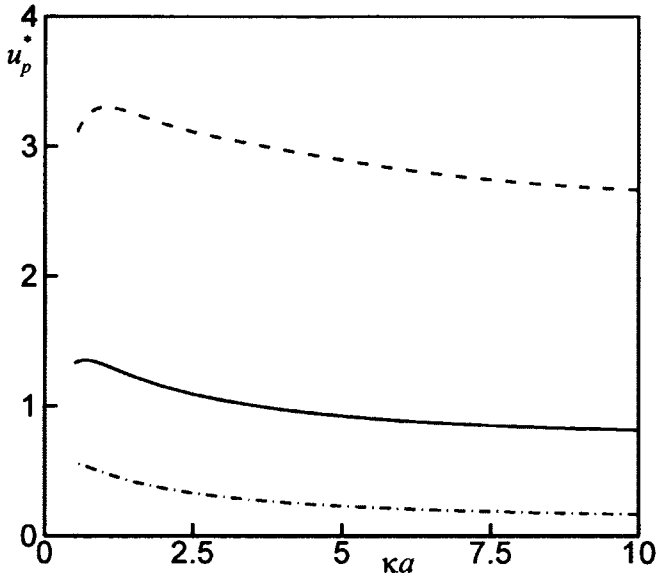

Figure 4.6. Dimensionless particle velocity as a function of κa when d/a = 1 (dashed line), 0.5 (solid line), and 0.2 (dash-dotted line) for Q = 20, λa = 1, and R_N/a = 5.

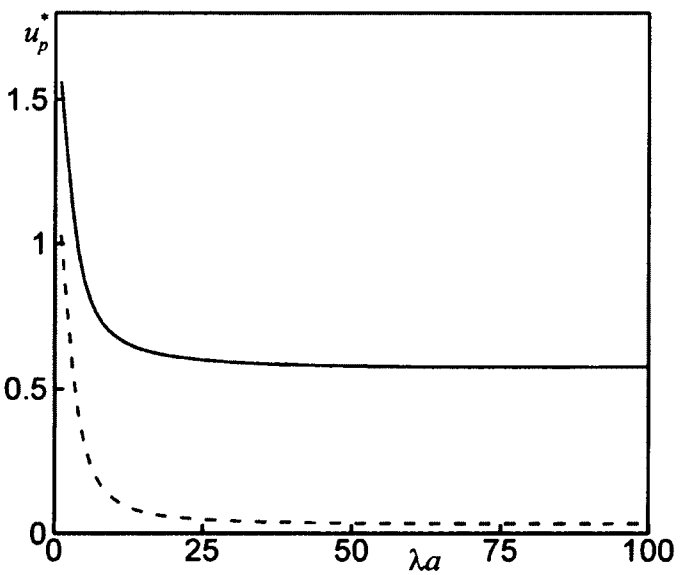

Figure 4.7. Dimensionless particle velocity as a function of λa when κa = 0.5 (solid line) and 10 (dashed line) for Q = 25, d/a = 0.5, and R_N/a = 5.

4.3.4 The Effect of λa, Friction Coefficient of the Porous Medium

Figure 4.7 depicts the dimensionless particle velocity as a function of λa, the friction coefficient of the porous medium layer, for κa = 0.5 (solid line) and 10 (dashed line) when Q = 25, d/a = 0.5, and R_N/a = 5. Different from a rigid particle, the porous membrane layer generates an extra viscous drag force characterized by the dimensionless friction coefficient, λa. When λa is very low (i.e., $\lambda a \rightarrow 0$), the fluid-membrane interaction becomes negligible, and the soft particle is equivalent to a rigid particle of radius a. When λa is very high (i.e., $\lambda a \rightarrow \infty$), the fluid velocity inside the membrane layer is identical to the particle velocity. Hence, the soft particle is equivalent to a rigid particle of radius of $(a + d)$ when λa is very high. In general, a larger particle has a lower electrophoretic velocity due to the boundary effect [161]. Therefore, the particle velocity decreases and eventually approaches a constant as λa increases. The reason that the particle velocity for κa = 0.5 is larger than that for κa = 10 has been explained in section 4.3.1.

4.3.5 The Effect of Q, Fixed Charge in the Soft Membrane Layer

Figure 4.8 depicts the particle velocity in a nanopore as a function of Q for λa = 1 (solid and dashed lines) and λa = 50 (dash-dotted and dash-double-dotted lines) when κa = 0.5 and 10. The velocities for λa = 50 are multiplied by a factor of 5 to enhance visibility. The magnitude of the particle velocity, in general, increases as the magnitude of the fixed charge, $|Q|$, increases, which is attributed to the electrostatic driving force, F_E, increasing with the amount of fixed charge in the membrane layer of the particle and has been confirmed by the Huang et al. [200]. As expected, the positively (negatively) charged particle electrophoretically migrates toward cathode (anode) with positive (negative) particle velocity. It is revealed that the particle velocity is almost linearly proportional to Q when the EDL is relatively thin (i.e., κa = 10) and becomes nonlinear for a relatively thick EDL (i.e., κa = 0.5), which arises from the effect of the DLP.

Figure 4.9 depicts the dimensional disturbed concentration difference $\delta(c_1 - c_2)$ for κa = 0.5, λa = 1, d/a = 0.5, and R_N/a = 5 when Q = 5 (a), 25 (b) and 50 (c). When κa = 0.5 and Q is relatively small (i.e., Q = 5), more negative (positive) ions are accumulated near the lower (upper) surface of the inner core as shown in Figure 4.9a, which induces an extra

electric field opposite to the applied one and accordingly decreases F_E. However, for relatively large Q (i.e., $Q = 25$ and 50), more negative (positive) ions accumulate near the upper (lower) surface, which induces an electric field in the same direction of the applied one and accordingly enhances the particle velocity. The type I (II) DLP dominants over the other when the magnitude of the fixed charge inside the soft layer is relatively small (large), resulting in the decrease (increase) in the particle mobility. When κa is relatively large (i.e., κa = 10), the ionic concentration distribution around the particle is almost symmetric with respect to the center of the particle indicating an insignificant DLP. As a result, the particle velocity for κa =10 is linearly proportional to the fixed charge Q inside the porous membrane layer.

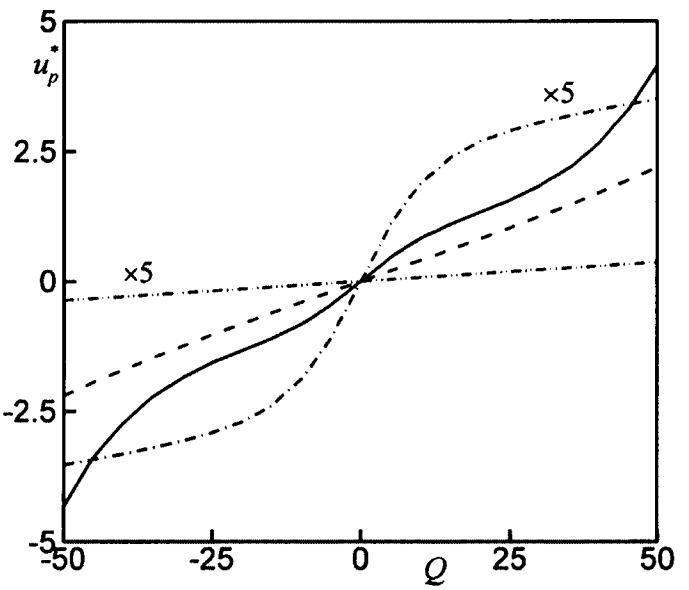

Figure 4.8. Dimensionless particle velocity as a function of the fixed charge, Q, when λa = 1 and κa = 0.5 (solid line), λa = 1 and κa = 10 (dashed line), λa = 50 and κa = 0.5 (dash-dotted line), and λa = 50 and κa = 10 (dash-double-dotted line) for d/a = 0.5 and R_N/a = 5.

4.3.6 The Effect of R_N/a, Ratio of the Radius of the Nanopore to That of the Rigid Core

Figure 4.10 depicts the particle velocity in a nanpore as a function of R_N/a when Q = 25 and d/a = 0.5. The particle velocities for λa = 50, κa = 0.5 (dash-dotted line) and 10 (dash-double-dotted line) are multiplied by a factor of 2.5. The particle velocity for λa =

1 is higher than that for $\lambda a = 50$ due to the friction effect arising from the membrane layer when the other conditions are identical. The gap distance between the particle's surface and the nanopore wall increases as the ratio, R_N/a, increases. For $\kappa a = 0.5$ (solid and dash-dotted lines), the particle velocity rapidly increases with increasing R_N/a if the latter is small, and saturates when R_N/a exceeds a certain value. Similarly, the particle velocity for $\kappa a = 10$ (dashed and dash-double-dotted lines) also increases with increasing R_N/a if the latter is very small, and gradually becomes almost insensitive to R_N/a once the latter exceeds a certain value. However, the variation of the particle velocity with the gap distance becomes much smaller, compared to the particle velocity for $\kappa a = 0.5$.

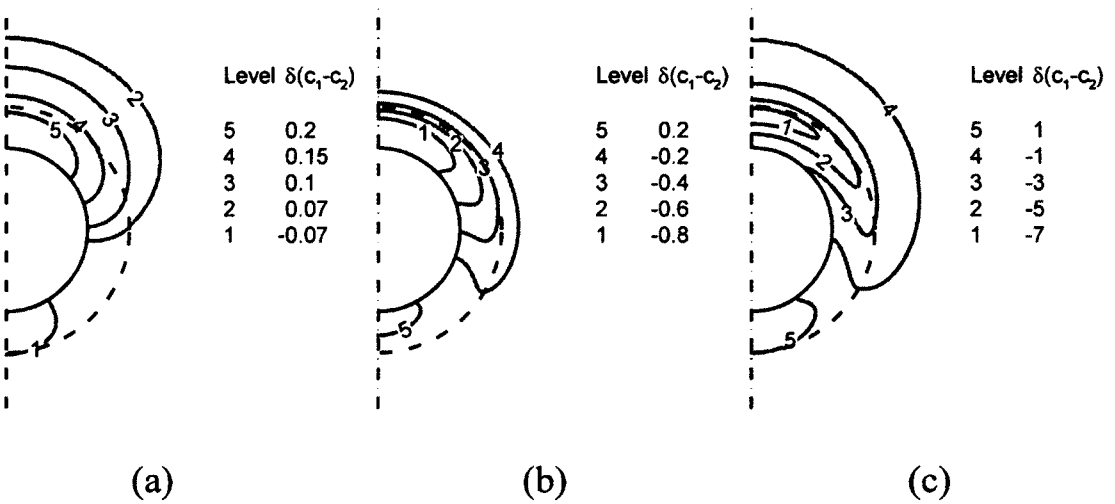

Figure 4.9. Dimensional disturbed concentration difference for $\kappa a = 0.5$, $\lambda a = 1$, $d/a = 0.5$, and $R_N/a = 5$ when $Q = 5$ (a), 25 (b) and 50 (c), which corresponds to the solid line in Figure 4.8. The solid and dashed lines represent the inner and outer surfaces of the soft particle.

As the gap distance increases, the hydrodynamic retardation stemming from the stationary nanopore wall decreases, which leads to an enhancement to the particle motion. Meanwhile, the electric field in the gap also decreases due to the increase in the cross-sectional area as the gap distance increases, resulting in a decrease in the electrostatic force, F_E. If the EDL thickness exceeds the gap distance, the EDL will be compressed by the nanopore wall and eventually increases the hydrodynamic retardation. The effect of the ratio, R_N/a, on the particle motion arises from the competition among the above three

factors. When κa = 0.5 (solid and dash-dotted lines), the EDL surrounding the particle is relatively thick and compressed by the nanopore wall if R_N/a < 3.5, under which the degree of EDL compression by the nanopore wall decreases as the gap distance increases. As a result, the decrease in hydrodynamic retardation force leads to a rapid increase in the particle velocity. When R_N/a > 3.5, the EDL detaches from the nanopore wall. As the ratio further increases, the increase of the particle velocity with the gap distance mainly arises from the decrease in the hydrodynamic retardation and the degree of DLP due to the nearby nanopore wall. When the ratio, R_N/a, exceeds a certain value, the boundary effect becomes insignificant, therefore the particle velocity is almost independent of the ratio, R_N/a.

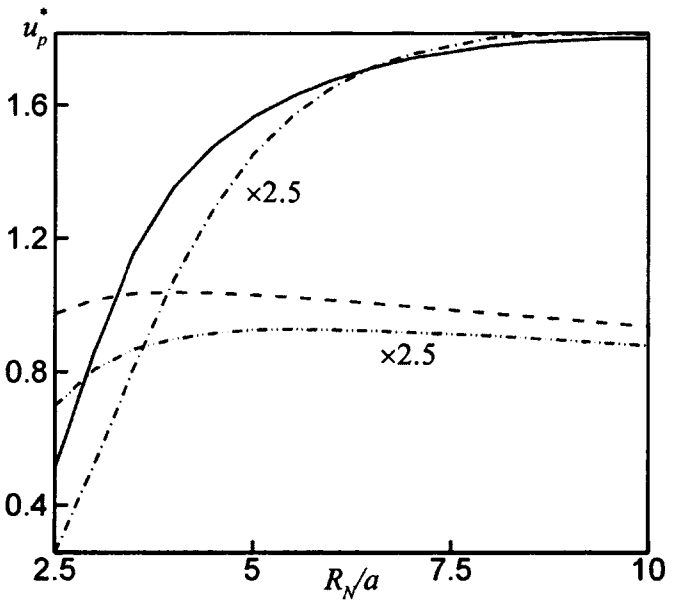

Figure 4.10. Dimensionless particle velocity as a function of R_N/a when λa = 1 and κa = 0.5 (solid line), λa = 1 and κa = 10 (dashed line), λa = 50 and κa = 0.5 (dash-dotted line), and λa = 50 and κa = 10 (dash-double-dotted line) for Q = 25 and d/a = 0.5.

When the EDL is relatively thin (i.e., κa = 10), under which the gap distance is much larger than the EDL thickness. When R_N/a is small, the slight increase in the particle velocity with increasing R_N/a mainly arises from the decrease in the hydrodynamic retardation due to the nanopore wall. Once the wall is far away from the particle, the

boundary effect becomes insignificant so that the particle velocity becomes insensitive to the increase in the gap distance. The particle velocity slightly decreases as R_N/a increases further, mainly arising from the decrease in the electric field in the gap that accordingly decreases the electrostatic driving force. When $R_N/a \to \infty$, the particle velocity approaches to a constant, which can be estimated by the approximation solution Eq. (4.34) if $\kappa a \gg 1$, $\lambda a \gg 1$, $\kappa d \gg 1$, and $\lambda d \gg 1$.

4.4. Conclusions

The electrophoretic motion of a soft spherical particle, consisting of a rigid core covered by a charged porous membrane layer, along the axis of a nanopore has been numerically investigated using a continuum-based mathematical model. The model includes PNP equations for the ionic mass transport, Stokes equations and modified Brinkman equations for the hydrodynamic field outside and inside the porous membrane layer, respectively. The model considers the DLP by the imposed electric field and the induced fluid and particle motions with no assumptions made concerning the EDL thickness and the magnitudes of the imposed electric field and fixed charge inside the membrane layer. The particle motion is determined by balancing the electrical force on the fixed charge inside the membrane layer and the hydrodynamic force arising from the fluid flow.

In general, the resulting particle velocity decreases as κa increases, mainly arising from the decrease in the zeta potential of the particle with a fixed charge inside the porous membrane layer. If the friction coefficient, λa, is small, the particle electrophoretic velocity monotonically increases with the increasing ratio of the membrane layer thickness to the particle size, d/a, primarily due to the increase in the amount of fixed charge and accordingly the electrostatic driving force. If λa is relatively large, the viscous drag force by the membrane layer also comes into play, which increases as d/a increases due to the increase in the fluid-membrane interaction. The effect of d/a on the resulting particle velocity is the result of the competition between the increasing electrostatic force and viscous friction force. The electrophoretic particle velocity increases with increasing d/a if the latter is small. Once d/a exceeds a certain critical value, the particle velocity

peaks and then decreases as d/a further increases. If λa is small, the particle velocity decrease as λa increases. Once λa exceeds a certain critical value, the particle velocity becomes independent of the friction coefficient, λa. At a relatively large κa, the electrophoretic velocity linearly increases with the magnitude of the fixed charge inside the porous membrane layer due to an insignificant DLP effect and the increasing electrostatic force. At a relatively low κa (i.e., $\kappa a \approx 1$), the particle velocity nonlinearly increases with the fixed charge arising from the significant DLP effect. Two types of DLP are observed, which has not been reported previously in the study of electrophoresis of soft particle. When the magnitude of the fixed charge inside the soft layer is relatively low (large), the effect of type I DLP is more (less) significant than that of the type II DLP, leading to the decrease (increase) in the particle mobility. As the ratio of the nanopore size to the particle size increases, the electrophoretic velocity increases due to the decrease in the degree of DLP arising from the EDL compression and hydrodynamic retardation by the nanopore wall, and the particle velocity reaches a plateau if the gap distance is sufficiently large.

CHAPTER 5

REGULATING DNA TRANSLOCATION THROUGH FUNCTIONALIZED SOFT NANOPORES

Abstract

Nanopores have emerged as promising next-generation devices for DNA sequencing technology. The two major challenges in such devices are: (i) find an efficient way to raise the DNA capture rate prior to funneling a nanopore, and (ii) reduce its translocation velocity inside it so that single base resolution can be attained efficiently. To achieve these, a novel soft nanopore comprising a solid-state nanopore and a functionalized soft layer is proposed to regulate the DNA electrokinetic translocation. We show that, in addition to the presence of an electroosmotic flow (EOF), which reduces the DNA translocation velocity, counterions concentration polarization (CP) occurs near the entrance of the nanopore. The latter establishes an enrichment of the counterions concentration field, thereby electrostatically enhancing the capture rate. The dependence of the ionic current on the bulk salt concentration, the soft layer properties, and the length of the nanopore are investigated. We show that if the salt concentration is low, the ionic current depends largely upon the length of the nanopore, and the density of the fixed charge of the soft layer, but not upon its softness degree. On the other hand, if it is high, ionic current blockade always occurs, regardless of the levels of the other parameters. The proposed soft nanopore is capable of enhancing the performance of DNA translocation while maintaining its basic signature of the ionic current at high salt concentration. The results gathered provide necessary information for designing the devices used in DNA sequencing.

5.1. Introduction

Since the sensing single-stranded DNA (ssDNA) and ssRNA were first demonstrated by using α-hemolysin protein pore within a lipid bilayer,[21, 209] nano-sized pores have emerged as promising platforms for both detection and sequencing of individual

biopolymers.[20, 29, 141-142] In the nanopore-based sensing techniques, charged nanoparticles are electrophoretically driven through a nanopore, yielding detectable changes in ionic current so that the label-free single-molecule translocation can be probed by the ionic current signals.[20, 29, 141-142] Among various applications, nanopore-based DNA sequencing technique[29] is one of the most attractive ones because it has high prospective potentials to identify the sequence of nucleotide bases by discriminating the ionic current signatures at high throughout and low cost.[18, 29, 33, 35, 210] However, two crucial challenges still remain to be resolved at the present stage, namely, to facilitate DNA capture at the nanopore mouth (capture stage),[41, 57] and to reduce its translocation velocity inside the nanopore[56, 65] so that single base resolution at high speed can be achieved. Several attempts have been made recently to solve relevant problems. These include, for example, exerting extra mechanical drag by optical tweezers,[211-212] adopting chemically functionalized nanopores,[35, 213] adjusting the physiochemical properties of the liquid phase,[41, 46, 64] and utilizing the nanopores embedded with gated field effect transistors (FET)[56-57, 65] and polarizable floating electrode.[59] However, an effective way, which is capable of completing simultaneously both challenges, has yet to be devised.

As illustrated in Figure 5.1a, we propose using a solid-state nanopore coated with a functionalized soft layer (i.e., polyelectrolyte-modified nanopore[120]), referred to as soft nanopore, to regulate the translocation of a double-stranded DNA (dsDNA) through it. Although similar concepts were realized experimentally by coating hairpin-loop (HPL) DNA,[43, 105] tail-modified DNA,[34] and fluid lipid bilayer[42] on synthetic nanopores to enhance both detecting resolution and selectivity for single biomolecule, there lacks a thorough theoretical analysis on the DNA electrokinetic translocation through such soft layer-functionalized nanopores. Adopting a continuum-based model comprising Poisson-Nernst-Planck (PNP) equations for the ionic transport, and Stokes and Brinkman equations[125] for the fluid flow, we theoretically investigate the DNA electrokinetic translocation through a soft nanopore for the first time. The PNP equations have been verified to successfully capture the essential physics of the DNA translocation process.[65, 149] Note that using the simplified model based on the Poisson-Boltzmann equation is inappropriate in this chapter due to extremely strong electric field imposed and overlapping of electric double layers (EDLs). As will be shown, due to an enhanced

counterions concentration polarization (CP) and an extra friction force stemming from the soft nanopore (Figure 5.1b), we can simultaneously raise DNA capture velocity and reduce its translocation velocity in the nanopore while maintaining the ionic current signatures. Similar to those in solid-state nanopores,[38, 214] our results show that the change in the ionic current due to the translocating DNA depends largely on the level of salt concentration.

5.2. Results and Discussion

5.2.1 Fundamental Theory.

Figure 5.1 shows the problem considered: an uncoiled dsDNA is electrophoretically driven by an applied electric field in the opposite axial direction, **E**, of strength E, translocating from the *cis* compartment along the axis of a cylindrical soft nanopore of length L_N and radius R_N, toward the *trans* compartment. The dsDNA is simulated by a long, rigid nanorod of radius a=1 nm and length L_p=49 nm (ca. 14 helical pitches). Here, L_p is shorter than the persistence length of dsDNA (ca. 50 nm)[150] to ensure that its shape is approximately invariable during the entire translocation process. The soft nanopore is simulated by coating a functionalized soft layer on the wall of a membrane. For simplicity, we assume that the soft layer is ion-penetrable, homogeneously structured, and bears dissociable function groups, which yield a uniform fixed charge density ρ_{fix}.[125] In addition, the possible morphology deformation of the soft layer[119] is neglected. The cylindrical coordinates r, θ, z with the origin at the center of the nanopore are adopted. Because the present problem is θ symmetric, only the (r, z) domain needs be considered. Figure 5.1b summarizes the forces and the mechanisms involved: the electrophoretic force F_E, the hydrodynamic drag F_H, the electroosmotic flow (EOF), the extra friction force stemming from the soft layer $\mathbf{F}_{\mathbf{fric}}$,[124-125] the enhancement of the local electric field $\mathbf{E}_{\mathbf{enhanced}}$ in the nanopore, and the counterions concentration polarization (CP) in the vicinity of the nanopore mouth. A continuum-based model comprising the Poisson-Nernst-Planck (PNP) equations for the ionic transport and modified Stokes equations for the liquid flow is adopted to describe the present problem.[65, 124-125]

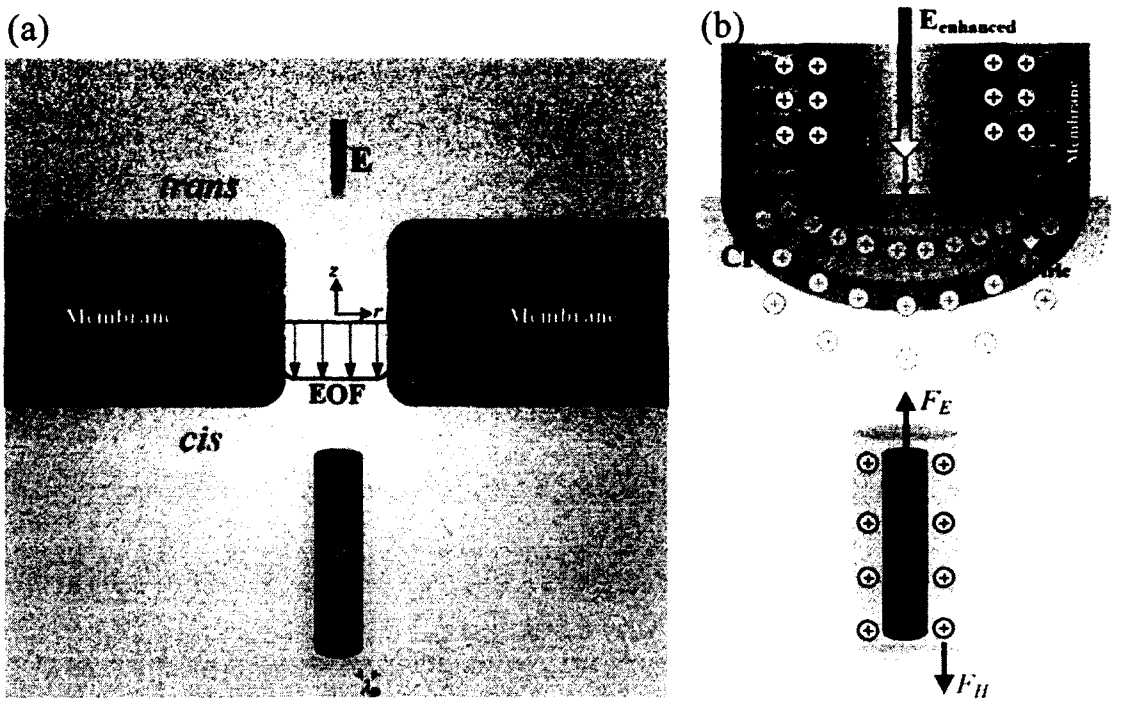

Figure 5.1. (a) The translocation of a double-stranded DNA (dsDNA), simulated by a long, rigid nanorod, along the axis (in the z direction) of a soft nanopore, which is simulated by coating a functionalized soft layer on the wall of a membrane. Due to the imposed electric field **E**, an electroosmotic flow (EOF) is induced in the charged soft nanopore. $\lambda_D = \kappa^{-1}$ and $\lambda^{-1} = \sqrt{\mu/\gamma}$ are the Debye length and the softness degree of the soft layer, respectively, where μ and γ are the fluid viscosity and the hydrodynamic frictional coefficient of the soft layer, respectively. (b) Mechanisms involved in the present problem (not to scale). The soft layer, which is ion-penetrable, homogeneously structured, and bears dissociable functional groups, yields an extra friction force $\mathbf{F}_{fric}$ acting on the liquid flowing through it. The negatively charged DNA experiences an electrophoretic force F_E in the z direction and a hydrodynamic drag F_H in the opposite direction arising from the movement of the counterions inside EDL. Concentration polarization (CP)[123] occurs, where counterions and coions simultaneously gather near the nanopore mouth; the amount of the former is much greater than that of the latter, inducing a significant counterions-enriched electrostatic field facilitating DNA capture. $\mathbf{E}_{enhanced}$ is the enhanced local electric field inside the nanopore.

(1) Poisson-Nernst-Planck equations

$$-\nabla^2\phi = \frac{h\rho_{fix} + \rho_e}{\varepsilon_f} = \frac{h\rho_{fix} + \sum_j Fz_j c_j}{\varepsilon_f}, \tag{5.1}$$

$$\nabla \cdot \mathbf{N}_j = \nabla \cdot (\mathbf{u}c_j - D_j \nabla c_j - z_j \frac{D_j}{RT} F c_j \nabla\phi) = 0. \tag{5.2}$$

ϕ is the electric potential; $\mathbf{u}$ is the fluid velocity; $\rho_e = \sum_j Fz_j c_j$ is the space charge density of the mobile ions; $\mathbf{N}_j$, c_j, D_j, and z_j are the flux, the concentration, the diffusivity, and the valence of the j^{th} ionic species, respectively (j=1 for cations, and 2 for anions). ε_f, F, R, and T are the fluid permittivity, Faraday constant, gas constant, and the absolute temperature, respectively. h is a unit region function (h=0, the region outside the soft layer; h=1, the region inside it). $\rho_{fix} \cong (eZ\sigma_s / R_s)\chi_s$ is the fixed charge density of the soft layer with e, Z, σ_s, R_s, and χ_s being the elementary charge, the valance of the dissociable groups per molecular chain, the molecular chain surface density grafted to solid-state nanopore, the thickness of the soft layer, and the dissociated degree of functional groups in the soft layer, respectively. We assume that Z=−1 and $\sigma_s = 0.6/\text{nm}^2$, which are typical to a lipid bilayer surface.[121]

(2) Modified Stokes equations:[124-125]

$$-\nabla p + \mu\nabla^2\mathbf{u} - (\sum_j Fz_j c_j)\nabla\phi - h\gamma\mathbf{u} = \mathbf{0}, \tag{5.3}$$

$$\nabla \cdot \mathbf{u} = 0, \tag{5.4}$$

where p is the hydrodynamic pressure.

To specify the boundary equations associated with Eqs (5.1), (5.2), (5.3), and (5.4), we assume the following. (i) The rigid surface of the membrane is non-slip ($\mathbf{u} = \mathbf{0}$), ion-impenetrable ($\mathbf{n} \cdot \mathbf{N}_j = 0$) and uncharged ($-\varepsilon_f \mathbf{n} \cdot \nabla V = \sigma_w = 0$), where σ_w is the surface charge density on the membrane wall and $\mathbf{n}$ is the unit outer normal vector. (ii) The ionic concentrations at both ends of the two large reservoirs are maintained at their bulk values, $c_j = C_{j0} = C_0$, and the electric potential there are $V(cathode) = 0$ and $V(anode) = V_0$. A normal flow without external pressure gradient is specified at the ends of the two big reservoirs.[52] (iii) The electric potential and field, ionic concentrations, and flow field are

all continuous on the PE layer/liquid interface.[124-125] (iv), slip boundary condition for the flow field, insulation boundary condition for the potential, and zero normal ionic fluxes are imposed at the side boundaries of the two reservoirs, which are far away from the nanopore. Symmetric boundary condition is specified along the axis of the nanopore. Moreover, the surface of the DNA nanoparticle is non-slip ($\mathbf{u} = U_p\mathbf{e}_z$), ion-impenetrable ($\mathbf{n}\bullet\mathbf{N}_j = \mathbf{n}\bullet(\mathbf{u}c_j)$) and uncharged ($\mathbf{n}\bullet(-\varepsilon_f\nabla V) = \sigma_p$), where σ_p is the surface charge density on the DNA surface and $\mathbf{n}$ is the unit outer normal vector.

Based on a quasi-steady state assumption, the translocation velocity of DNA, U_p, can be determined by a balance of the forces acting on it in the z direction, $F_E + F_H = 0$.[65] The performance of the translocation process can be measured by the ionic current deviation, $(I - I_\infty)/I_\infty$, with I and I_∞ being the ionic current (see Method section) and its value when the DNA is far away from the nanopore. A negative (positive) value of $(I - I_\infty)/I_\infty$ represents a current blockade (enhancement) during the translocation of DNA.[149] A more detailed description of the theoretical part is provided in the Supporting Information.

5.2.2 Numerical Method

The strongly coupled non-linear equations and the associated boundary conditions are numerically solved by the commercial finite element package, COMSOL Multiphysics (version 3.5a, www.comsol.com) operating in a high-performance cluster. The computational domain is discretized into quadratic triangular elements. Nonuniform elements are employed with larger numbers of elements assigned locally as necessary. Typically the total number of elements for system I and II are approximately 210,000 with finer mesh in the PE layer and on the DNA surface to capture the EDL. Lagrange – Quadratic elements are used for solving PNP equations, while Lagrange – P_2P_1 elements are for the Stokes and Brinkman equations. The ionic current through the nanopore is obtained by using the weak constrain in COMSOL specially developed for an accurate calculation of flux. Rigorous mesh-refinement tests have been performed to ensure that the solutions obtained are convergent and grid independent. A maximum tolerance of 0.1% is imposed on the relative difference $|(|I_a| - |I_c|)/|I_a|$, where I_a and I_c are respectively the

current entering (anode) and leaving (cathode) the nanopore. The numerical scheme has been validated to be sufficiently efficient and accurate for solving similar electrokinetic problems, such as the electrokinetic ion transport in a solid-state nanopore[14, 109-113] and the electrokinetic rigid and soft nanoparticle translocation through a nanopore.[52, 115-117, 122, 126]

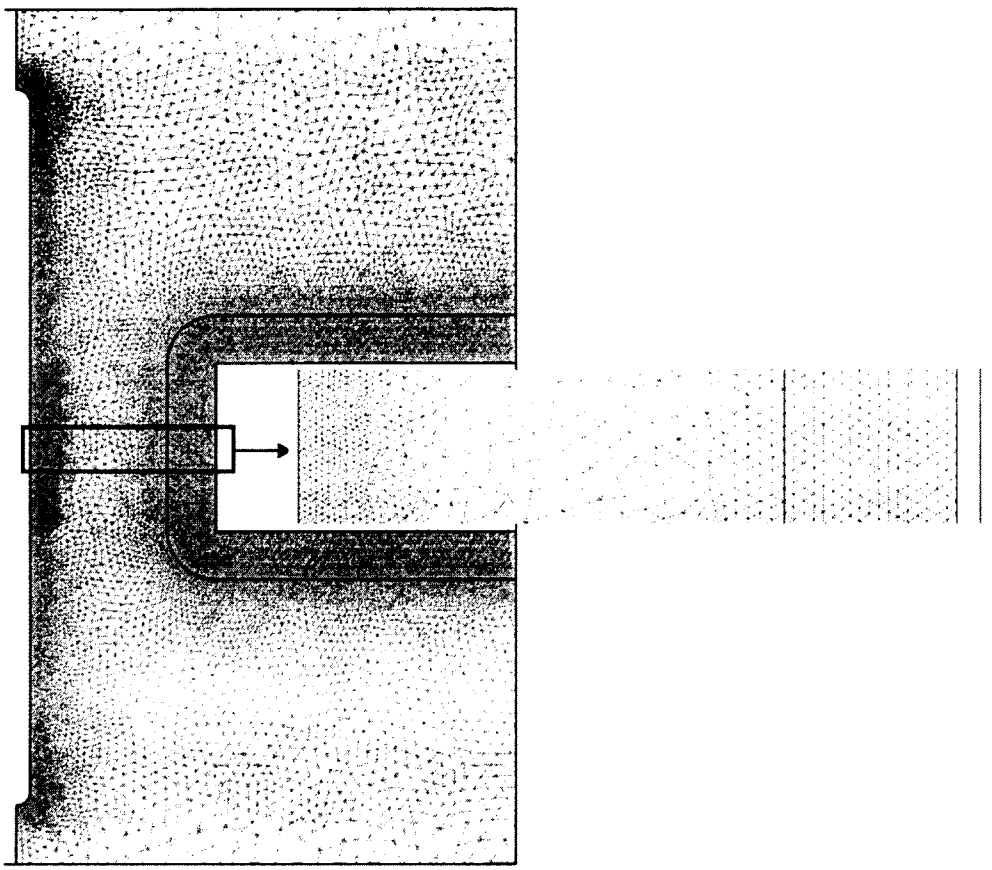

Figure 5.2. The meshes used in the simulation with enlarged finer mesh in the PE layer and on DNA surface

5.2.3 Influence of Soft Layer Properties and Bulk Salt Concentration on DNA Translocation.

Let us first fix the length of a nanopore at 60 nm, which is slightly longer than the DNA considered (49 nm). This is based on the experimental design of the solid-state nanopore used by Chang et al.,[214] where the length of a pore (ca. 50-60 nm) is comparable to that of DNA (ca. 50 nm) so that the possible influence due to the DNA geometry change during its translocation can be avoided. Figure 5.3a-c depicts the normalized translational

velocity of the DNA nanoparticle as a function of its location, z_p, for various fixed charge density ρ_{fix}, (a), softness degree λ^{-1}, (b), and the bulk salt concentration C_0, (c). λ^{-1} is a measure for the shielding length characterizing the extent of the fluid flow penetrating into the soft layer.[125] The smaller the λ^{-1} the more compact (or ordered) the soft layer structure is (e.g., well-ordered lipid bilayer). Figure 5.3a reveals that the velocity of DNA inside a solid-state nanopore is much faster than that in the fluid compartments (discrete symbols), which is consistent with experimental observation.[131] This is because the local electric field in the former is much stronger than that in the latter. To reduce the velocity of DNA inside a nanopore, we propose using a novel soft nanopore. Figure 5.3a-c shows that this is feasible, where DNA translocation velocity is seen to be slower at larger ρ_{fix}, λ^{-1}, and C_0. Note that if these parameters are sufficiently large, then the velocity of DNA is negative in front of the nanopore, implying that it is blocked there. It is expected that the higher the fixed charge density of the soft layer the more significant the EOF inside the nanopore, and therefore, the slower the DNA translocation velocity. Similarly, the friction force stemming from the soft layer decreases with increasing softness degree, thereby strengthening the EOF (inset of Figure 5.3d) and slowing down the DNA translocation velocity. However, the strength of the EOF at the center of the nanopore outside its soft layer ($0 \le r < 3\,\text{nm}$) decreases with increasing bulk salt concentration (Figure 5.3d). This contradicts to the salt concentration dependence of the DNA translocation velocity shown in Figure 5.3c, implying that other mechanisms might be present. In addition, it is known that the electrophoretic force acting on a DNA usually decreases with increasing bulk salt concentration.[215] Therefore, if this factor dominates, then the DNA translocation velocity should decrease with increasing salt concentration. The dependence of the EOF inside the nanopore on the bulk salt concentration and the softness of the soft layer are illustrated in Figure 5.3d, where the axial fluid velocity is plotted against the nanopore radius r over the cross section z=0. It should be pointed out that our analysis is based on a continuum model, which was validated to be sufficient to capture and elucidate the essential physics in 5-10 nm solid-state nanopores.[56-57, 64, 149-150, 216] In addition, the dependence of the velocity of the DNA on its location is examined under various conditions, which can be used to judge whether it is blocked prior to

funneling the nanopore. This was often overlooked in previous theoretical studies, which assumed a DNA nanoparticle was located at the center of a nanopore. Our results show that DNA is unable to enter a nanopore under certain conditions.

Therefore, if the fixed charge density and/or the softness of the soft layer are sufficiently large, the DNA translocation velocity can be effectively reduced and regulated by the proposed novel soft nanopore. In addition, it is interesting to note that the DNA velocity before funneling the nanopore entrance, defined as the DNA capture velocity, significantly increases first as it approaches the nanopore entrance ($-70\,\text{nm} < z_p < -60\,\text{nm}$), and then starts to decrease at $z_p \cong -55\,\text{nm}$, as shown in Figure 5.3c. This phenomenon has not been reported previously in relevant theoretical studies for the case of solid-state nanopores.[57, 59, 65, 149] The enhancement in the capture velocity in our case is attributed to the significant counterions CP effect occurring at the nanopore mouth. To explain this, we plot the axial variation of the normalized difference between the concentration of cations and that of anions, $(c_1 - c_2)/C_0$, in Figure 5.4a,b; both the result for soft nanopore and that for the corresponding solid-state nanopore are shown. This Figure reveals that in the latter case the concentration of counterions (cations) is high in the vicinity of the rigid surface of the solid-state nanopore, but remains high outside the soft layer of the soft nanopore in the former case.

As can be seen in Figure 5.4c, the concentration of counterions near the entrance of the soft nanopore is significantly higher than that of the corresponding solid-state nanopore. This implies that the effect of counterions CP is significantly enhanced by the soft nanopore. The electrostatic interaction between the enriched counterions (cations) at the nanopore mouth and the negatively charged DNA nanoparticle induces an attractive force, yielding an increase in the DNA capture velocity. Similar electrostatic focusing concept was also adopted by Wanunu et al.[41] through applying a salt concentration gradient to create an electrostatically enhanced electric field capable of capturing more DNA molecules into the nanopore. Under the conditions assumed, the ratio V_{cis}/V_0=(voltage drop in the *cis* compartment/overall voltage bias) is 0.0973 for the case of Figure 5.4a (soft nanopore), and 0.0914 for the case of Figure 5.4b (solid-state nanopore). That is, the larger the (V_{cis}/V_0) the higher is the capture rate,[57] which is consistent with our results.

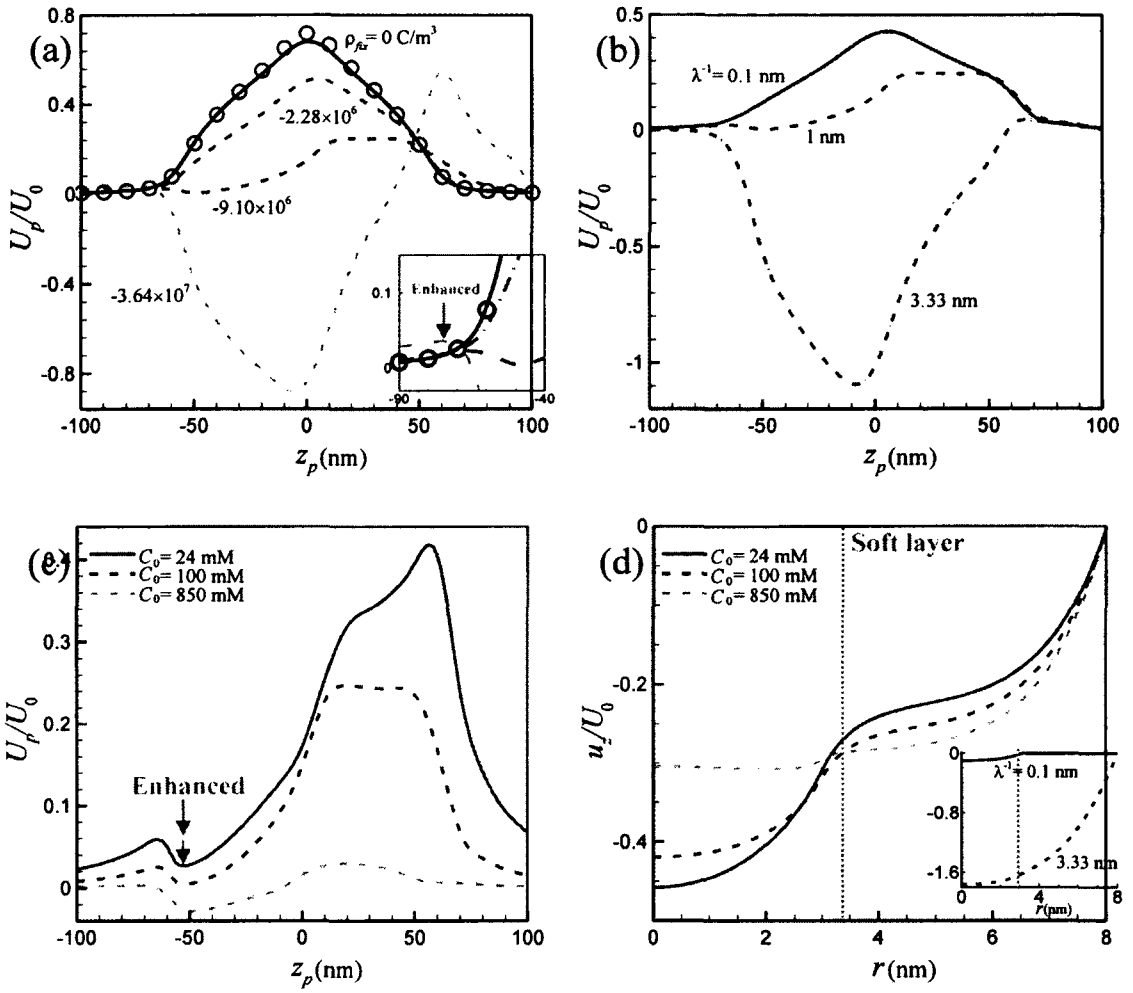

Figure 5.3. Variation of the DNA translational velocity (normalized with the reference Smoluchowski velocity $U_0 = \varepsilon_f R^2 T^2/\mu a F^2$) as a function of the particle position z_p at various fixed charge density ρ_{fix}, (a), the softness degree λ^{-1} of the soft layer, (b), and the bulk salt concentration C_0, (c), for the case where the nanopore radius R_N=8 nm, the nanopore length L_N=60 nm, the thickness of the soft layer R_s=5 nm, and the electric bias V_0=1.12 V. (a): λ^{-1}=1 nm, C_0 =100 mM, open circles denote the corresponding results for a solid-state nanopore (i.e., ρ_{fix}=λ^{-1}=0); (b): ρ_{fix}= -9.1×10^6 C/m^3 and C_0 =100 mM; (c): ρ_{fix}= -9.1×10^6 C/m^3 and λ^{-1}=1 nm; (d): variation of the normalized z component fluid velocity (u_z/U_0) along the nanopore radius r over the cross section z=0 for various bulk salt concentrations, C_0, and soft degrees of the soft layer (inset) in the absence of DNA particle for the cases of (b) and (c).

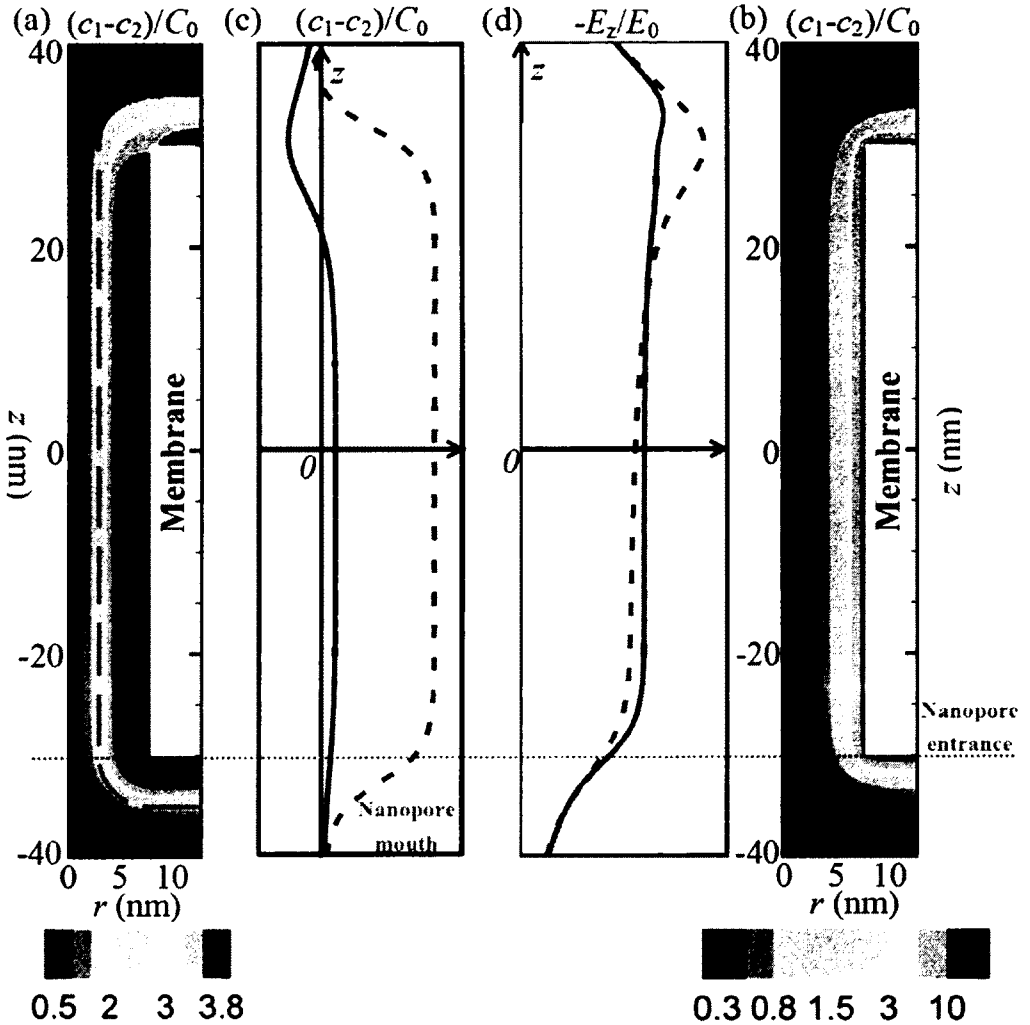

Figure 5.4. Spatial distribution of the normalized net ionic concentration difference, $(c_1-c_2)/C_0$ at bulk salt concentration $C_0 = 24\,\text{mM}$. (a): a soft nanopore with fixed charge density $\rho_{fix} = -9.1\times10^6\ \text{C/m}^3$ and softness degree $\lambda^{-1} = 1\,\text{nm}$; (b): a solid-state nanopore with surface charge density σ_w. Other parameters are the same as those in Figure 5.3.

Figure 5.4d shows the axial variation in the normalized z component of the local electric field for both soft and the corresponding solid-state nanopores. This Figure reveals that, in addition to the typical enhancement of the local electric field inside both nanopores, it is highly asymmetric in the case of the soft nanopore due to the strong CP effect occurring at the nanopore openings. This suggests that the Poisson-Boltzmann

equation usually adopted in the literatures is inapplicable in the present case, and explains that why the DNA velocity in Figure 5.3a-c is highly asymmetric across the soft nanopore. In general, the higher the fixed charge density of the soft layer and/or the lower the bulk salt concentration (thicker double layer) the more significant the enhancement in the capture velocity (Figure 5.3a,c). However, it should be pointed out that if the fixed charge density is too high, then due to a strong opposite EOF inside the nanopore, DNA can be trapped before funneling the nanopore. If the bulk salt concentration is too low, two important outcomes might occur: (i) The DNA translocation velocity is not effectively reduced. (ii) The ionic current signal changes from current blockade to current enhancement, as will be discussed latter.

5.2.4 Influence of Nanopore Length

In nanopore-based biomolecules sensing techniques, the length of a solid-state nanopore plays an important role.[20, 33, 57, 136] To see the influence of the length of a soft nanopore on the DNA translocation, we plot the normalized translational velocity U_p/U_0 and the corresponding relative ionic current deviation $(I-I_\infty)/I_\infty$ against the DNA location z_p for various nanopore length L_N in Figure 5.5. For illustration, we assume that the functional groups in the soft layer are completely dissociated (χ_s = 1), corresponding to $\rho_{fix} = -5.33\times10^7$ C/m^3. Figure 5.5a reveals that if a nanopore is sufficiently long (dashed and dash-double dotted curves), then the DNA is blocked before entering it, and if it is sufficiently short (solid and dash-dotted curves), then the DNA is capable of funneling through it. The latter is because the shorter the nanopore the less the amount of fixed charge in the soft layer of the nanopore, thereby depressing the effect of EOF. Figure 5.5a also shows two important phenomena: (i) Similar to the results seen in Figure 5.3a-c, the velocity of the DNA increases due to the enhanced local electric field during its translocation. (ii) The influence of the aforementioned counterions CP effect on the DNA velocity near the nanopore entrance is insignificant. This is because the bulk salt concentration considered is high (1000 mM, Debye length $\lambda_D \cong 0.3$ nm) and the double layers inside the soft nanopore are not overlapped.

As mentioned previously, a nanopore-based sensing technique is based on the variation in the ionic current through a nanopore due to the presence of a DNA molecule. The influence of the length of a nanopore on the ionic current signature is depicted in Figure 5.5b. This Figure reveals that if the nanopore is sufficiently short, then current blockade occurs (solid curve). If it is sufficiently long, then a momentarily current enhancement occurs as the DNA is about to exit the nanopore. The former can be explained by the current blockage by the DNA nanoparticle, as was verified in many experiments based on solid-state nanopores[33, 38, 41] and functionalized nanopores.[34, 42] The latter was also found in the experiment based on DNA-functionalized nanopore (Figure 5.1c in ref. 23).[43] As pointed out by Chang et al.,[214] although the introduction of a DNA strand into a nanopore results in a decrease in ionic current, the screened counterions (coions) carried by the negatively charged DNA backbone also provides an additional source to increase the ionic current as it enters the nanopore. If the latter dominates, current enhancement occurs. Under the conditions considered, if the nanopore is long, then the amount of fixed charge in the soft layer is large, and therefore, the amount of counterions inside that layer is greater than that outside it. As a result, the excluded volume effect due to the presence of the DNA inside the soft nanopore is less significant than that for the case of a short nanopore, yielding a current enhancement. Our analysis is capable of explaining for the first time that why current blockade occurs only in a short nanopore. Figure 5.5b also shows that the ionic current signal is significantly asymmetric as the DNA translocating through the nanopore. This can be explained by the position dependent and highly asymmetric local electric field and the ionic concentration distributions inside the soft nanopore, as can be seen in Figure 5.4.

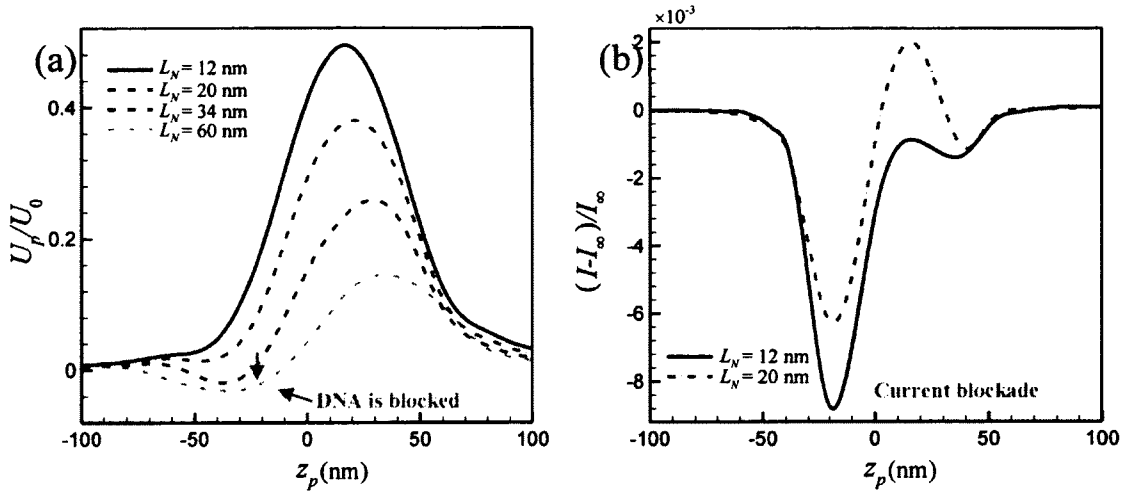

Figure 5.5. Variation of the normalized DNA translational velocity U_p/U_0, (a), and the ionic current deviation $(I-I_\infty)/I_\infty$, (b), as a function of the particle location z_p at various length of the nanopore L_N for the case where the nanopore radius R_N=14 nm, thickness of soft layer R_s=5 nm, bulk salt concentration $C_0 = 1000$ mM, electric bias $V_0 = 1.12$ V, fixed charge density $\rho_{fix} = -5.33\times10^7$ C/m^3, and softness degree $\lambda^{-1} = 1$nm . The arrows in (a) indicate that DNA is blocked before entering the soft nanopore; the curves in (b) show the results for the cases when DNA is able to pass through the nanopore. Under the conditions assumed, current blockade occurs if the nanopore is relatively short.

5.2.5 Other Factors Influencing the Ionic Current Signatures

Figure 5.6 illustrates the influences of the soft layer properties (ρ_{fix} and λ^{-1}) and the bulk salt concentration C_0 on the ionic current deviation during the DNA translocation through the nanopore. The values of the parameters assumed here are the same as those used in the experiment.[42] Figure 5.6a reveals that current blockade might occur at $C_0 = 1000$ mM, which is consistent with the result of Figure 5.5b. This Figure also shows that although the higher the fixed charge density of the soft layer the more significant is the current blockade, the ionic current signatures (current blockade) are almost independent of the soft layer properties. This implies that at a high salt concentration the present soft nanopore is capable of regulating the DNA capture (translocation) velocity

and simultaneously enhancing the magnitude of the resulting current blockade without affecting its basic signatures. Note that although the chemical interaction between the sensing molecule and the soft nanopore is neglected, our results qualitatively agree with the results observed in the experiments[42-43] where fluidic lipid bilayer-[42] and DNA-functionalized[43] nanopores were utilized to strengthen the resolution and selectivity of sensing biomolecules. As seen in Figure 5.6b, the bulk salt concentration C_0 has a significant influence on the ionic current signatures. If C_0 is sufficiently high (1000 mM), only current blockade is observed during the DNA translocation through the nanopore.

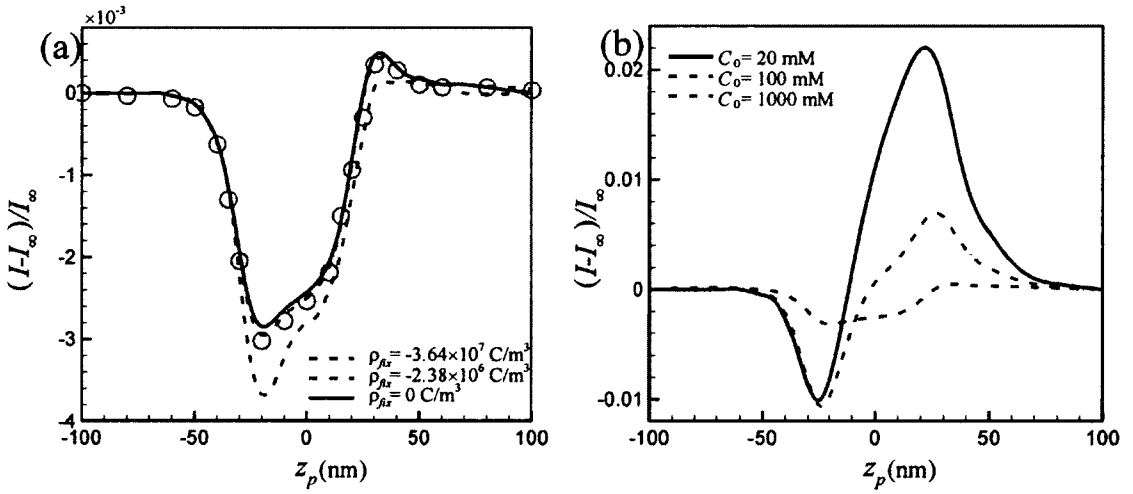

Figure 5.6. Variation of the ionic current deviation, $(I-I_\infty)/I_\infty$, as a function of the particle location z_p for various combinations of ()the fixed charge density ρ_{fix} and (a): the softness degree λ^{-1} at bulk salt concentration $C_0 = 1000$ mM ; (b): various C_0 at $\rho_{fix} = -1.16\times10^7$ C/m^3 and $\lambda^{-1} = 0.3$ nm. The values of the parameters are chosen from those in the experiment:[42] nanopore radius R_N=14 nm, pore length L_N=12 nm, thickness of soft layer R_s=3.4 nm, and electric bias $V_0 = 0.5$ V. Curves in (a): $\lambda^{-1} = 0.3$ nm; open circles: $\lambda^{-1} = 0.5$ nm and $\rho_{fix} = -2.38\times10^6$ C/m^3.

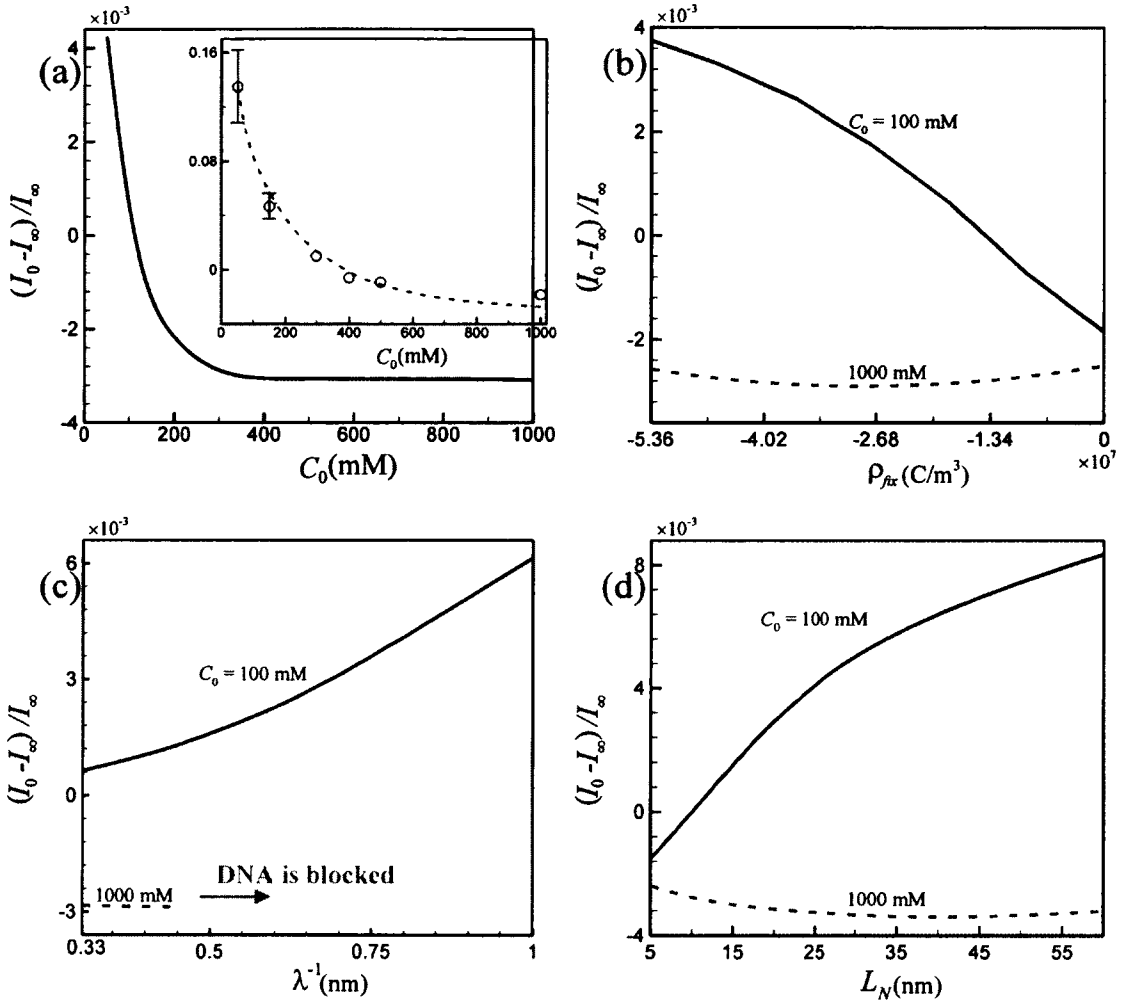

Figure 5.7. Variation of the relative ionic current change $(I_0 - I_\infty)/I_\infty$ due to the presence of a DNA at the center of a soft nanopore as a function of (a): the bulk salt concentration C_0; (b): the fixed charge density ρ_{fix}; (c): the softness degree λ^{-1}; (d): the nanopore length L_N, (d). (a): $\rho_{fix} = -1.81\times10^7$ C/m^3, $\lambda^{-1} = 0.3$ nm, and L_N=12 nm; (b): $\lambda^{-1} = 0.3$ nm and L_N=12 nm; (c): $\rho_{fix} = -1.81\times10^7$ C/m^3 and L_N=12 nm; (d): $\rho_{fix} = -1.81\times10^7$ C/m^3 and $\lambda^{-1} = 0.3$ nm. The other parameters are chosen as those in the experiment:[42] nanopore radius R_N=14 nm, thickness of the soft layer R_s=3.4 nm, and electric bias $V_0 = 0.5$ V.

This is consistent with many experimental results,[34, 38, 42-43] and can be explained by the physical blocking of the DNA strand introduced into the nanopore. However, it is

interesting to note that if C_0 is sufficiently low, current blockade occurs as the DNA enters the nanopore, but current enhancement is observed as it exits the nanopore. As mentioned previously, the current enhancement is mainly due to the increase in the screened counterions brought by the DNA molecule. The increase in the ionic conductance, and therefore, electric current, due to the passage of the DNA through the nanopore is possible to yield a current enhancement when the bulk salt concentration is low. Note that although a long soft nanopore is capable of yielding a momentarily current enhancement signal during DNA translocation (Figure 5.5b), the salt concentration might also influence significantly the ionic current signal, as will be discussed next.

5.2.6 Dependence of Ionic Current on Salt Concentration

To further elaborate the dependence of the ionic current on the bulk salt concentration due to the presence of the DNA, we define a relative ionic current change when the DNA is located at the center of the nanopore, $(I_0 - I_\infty)/I_\infty$,[56] where I_0 is the ionic current at $z_p = 0$. The length of the unlabelled dsDNA in the nanopore-based DNA sequencing experiments typically ranges from hundreds to thousands of base pairs (bps), and therefore, the observed saturated ionic current can reasonably be assumed as that when the DNA strand is located at the center of a nanopore. To verify this, we plot $(I_0 - I_\infty)/I_\infty$ against the bulk salt concentration C_0 for the case of a solid-state nanopore in the inset of Figure 5.7a Assuming $\sigma_w = -60$ mC/m^2 and $V_0 = 0.35$ V, we find that our numerical results agree very well with the experimental findings.[38] We predict that current blockade occurs when C_0 exceeds a critical salt concentration (ca. 390 mM), and current enhancement occurs when C_0 is lower than that concentration. As pointed out by Smeets et al,[38] these phenomena result from two competing effects: (i) The ionic current decreases because the available volume of the ionic transport inside the nanopore is occupied by the dielectric DNA strand. (ii) The screened counterions accompanied with the DNA strand provide a positive contribution to the ionic current. However, the mechanisms involved in the present soft nanopore are far more complicated than those in the corresponding solid-state nanopore because both the ionic concentration and the local

electric field inside the soft nanopore are position dependent, and highly depend on its charged properties, as shown in Figures 5.4 and 5.5b (inset). Using the same values of the parameters as those in the experiment,[42] we illustrate the influences of the bulk salt concentration C_0, the soft layer properties (ρ_{fix} and λ^{-1}), and the length of the nanopore L_N, on the relative ionic current change in Figure 5.7 As seen in Figure 5.7a that, similar to the case of a solid-state nanopore, current enhancement occurs when C_0 is lower than a critical level, ca. 130 mM under the conditions assumed, and current blockade occurs when C_0 exceeds that level. As illustrated in Figure 5.7b-c, if C_0 is sufficiently high (1000 mM), current blockade is always present, regardless of the levels of ρ_{fix}, λ^{-1}, and L_N. On the other hand, if C_0 is sufficiently low (100 mM), current blockade occurs when both ρ_{fix} and L_N are small, and current enhancement occurs when both ρ_{fix} and L_N are large. Assuming that the local electric field inside the soft nanopore is uniform, these behaviors can be explained by the difference in the ionic current due to the presence of the DNA nanoparticle in the soft nanopore, $\Delta I = I_0 - I_\infty$, which can be evaluated by

$$\Delta I = (V_0 / L_N)\left[-\pi a^2(\mu_K + \mu_{Cl})en_{KCl} + \lambda_{DNA}\mu_K^*\right]. \tag{5.5}$$

Here, $\mu_K = 7.616\times10^{-8}$ m^2/Vs and $\mu_{Cl} = 7.909\times10^{-8}$ m^2/Vs are the electrophoretic mobilities of K^+ (cations) and Cl^- (anions),[38] respectively. n_{KCl} is the number density of the K^+ (or Cl^-) inside the soft nanopore excluding the volume occupied by the DNA nanoparticle. λ_{DNA} is the effective line charge density on the DNA. μ_K^* is the effective electrophoretic mobility of K^+ along the DNA nanoparticle. The first term in the square bracket on the right-hand of Eq. (5.5) denotes the reduction of the ionic current due to the decrease in the nanopore space occupied by the DNA, and the second term is the excess current due to the transport of counterions along the DNA nanoparticle surface. Because the n_{KCl} in Eq. (5.5) highly depends upon both the bulk salt concentration and the net charges inside the soft layer, so is ΔI. For example, if the bulk salt concentration is low, n_{KCl} is small, and the second term in the square bracket on the right-hand of Eq. (5.5)

dominates, yielding a positive ΔI, and therefore, a current enhancement. Similarly, if the fixed charged density of the soft layer is high and/or the nanopore is long, n_{KCl} is small, yielding also a current enhancement. Note that because the softness degree mainly affects the hydrodynamic field inside the nanopore, the ionic current deviation in Figure 5.7c does not change appreciably with λ^{-1}.

5.3. Conclusions

For the first time, the electrokinetic translocation of a DNA nanoparticle through a novel soft nanopore comprising a solid-state nanopore and an ion-penetrable polyelectrolyte soft layer is theoretically analyzed. We show that the DNA translocation process can be effectively regulated by the induced counterions concentration polarization (CP) occurring at the mouth of the soft nanopore and an opposite electroosmotic flow (EOF) inside it. These effects simultaneously yield an increase in the DNA capture velocity at the nanopore mouth and a decrease in its translocation velocity within the nanopore. The ionic current signatures of the proposed soft nanopore strongly depend upon its length and the bulk salt concentration. In general, if the salt concentration is high and the nanopore is short, regardless of the levels of the fixed charge density and the softness degree, current blockade always occurs. This implies that the soft nanopore can be applied to regulate the DNA translocation behavior without changing the ionic current signature. Considering recent advances in nanofabrication techniques and continuous growing of the widespread interests in chemically modified nanopores, the present work provides both necessary theoretical background and reasonable interpretations for the experimental observations on DNA translocation through a nanopore.

CHAPTER 6

ELECTROKINETIC PARTICLE TRANSLOCATION THROUGH A NANOPORE CONTAINING A FLOATING ELECTRODE

Abstract

Electrokinetic particle translocation through a nanopore containing a floating electrode is investigated by solving a continuum model composed of the coupled Poisson-Nernst-Planck (PNP) equations for the ionic mass transport and the modified Stokes equations for the flow field. Two effects due to the presence of the floating electrode, the induced-charge electroosmosis (ICEO) and the particle-floating electrode electrostatic interaction, could significantly affect the electrokinetic mobility of DNA nanoparticles. When the electrical double layers (EDLs) of the DNA nanoparticle surface and the floating electrode are not overlapped, the particle-floating electrode electrostatic interaction becomes negligible. As a result, the DNA nanoparticle could be trapped near the floating electrode arising from the ICEO when the applied electric field is relatively high. The presence of the floating electrode attracts more ions inside the nanopore resulting in an increase in the ionic current flowing through the nanopore; however, it has a limited effect on the deviation of the current from its base current when the particle is far from the pore.

6.1. Introduction

With great advances in the nanofabrication technology, nanopore-based sensing has emerged as one of the most promising techniques to accomplish a high-throughput and affordable DNA sequencing.[37, 141-142, 217-221] In this technique, the DNA nanoparticle translocation through a nanopore gives rise to a change in the ionic current through the nanopore. Accordingly, the order of the nucleotide bases in one single DNA nanoparticle can be determined based on the discrimination of the ionic current signals.[40, 214] In order to achieve the goal of high throughput, a relatively high electric field is applied to generate the electrokinetic DNA translocation through the nanopore. However, a very

fast DNA translocation may result in an inaccurate detection of the ionic current.[28] As a result, several methods, including optical tweezers,[70, 211] chemical functionalization of the nanopore,[222] adjustment of the aqueous solution's property,[46-47, 49-50] have been proposed to slow down or actively control the DNA translocation through a nanopore, as reviewed in our previous study.[65] In particular, Ai *et al.* utilized a gate electrode to modify the surface potential of the nanopore, which in turn actively controls the DNA translocation through a nanopore.[65]

Induced-charge electroosmosis (ICEO) at an ideally polarizable surface, introduced first by Squires and Bazant,[76-77] has attracted much attention in the microfluidics community. Compared to the conventional electroosmosis that is linearly related to the electric field imposed, the ICEO is proportional to the square of the electric field strength making it a nonlinear electrokinetic phenomenon. In addition, the induced charge highly depends on the surface geometry, which has been successfully exploited for fluid stirring and mixing.[79-82] Recently, ICEO has been demonstrated to achieve various particle manipulations, such as separation, enrichment and trapping.[83-84, 223] Most existing theoretical analyses and numerical simulations of ICEO are focused on the fluid motion arising from the nonlinear electrokinetic phenomenon[78, 80, 224] however, the use of ICEO to control the electrokinetic particle translocation through a nanopore has never been explored.

In this chapter, we propose to coat a layer of a conductor like metal on the inner surface of a nanopore for the first time, which functions as a floating electrode to control DNA translocation through a nanopore. The floating electrode is not electrically excited which is in contrast to the gate electrode employed in our previous field effect control of DNA translocation through a nanopore. A multi-ion model (MIM) composed of the coupled Poisson-Nernst-Planck (PNP) equations for the ionic mass transport and the modified Stokes equations for the flow field have been employed to study the ionic current rectification in a nanopore.[202, 204, 225] The results show good agreements with the experiment data. In addition, the continuum MIM model has also been successfully used to predict the electrokinetic particle translocation through a dielectric nanopore in the absence of a floating electrode, which also shows excellent agreement with the experimental data.[165, 173] As a result, the MIM model is implemented to investigate the

electrokinetic DNA translocation in a nanopore with a floating electrode. We show that the DNA translocation through a nanopore is governed by three main control factors including the applied electric field across the nanopore, the ratio of the particle radius to the Debye length and the length of the floating electrode. The effects of these parameters are discussed in detail in this chapter.

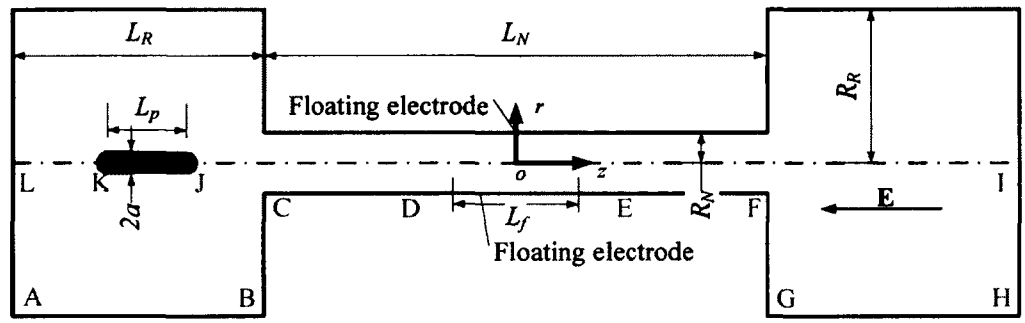

(a)

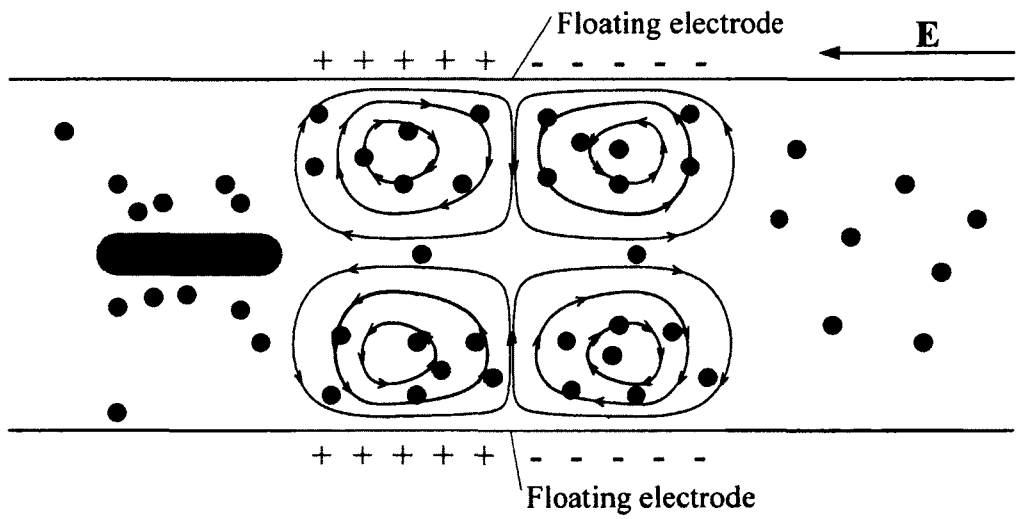

(b)

Figure 6.1. (a): schematic view of particle translocation through a cylindrical nanopore with a floating electrode. (b): charge density distribution on the floating electrode and the ICEO flow pattern in the floating electrode area.

6.2. Mathematical Model

We consider an uncharged nanopore of length L_N and radius R_N connecting two identical reservoirs, whose length and radius are L_R and R_R, respectively, as shown in Figure 6.1a. The nanopore and the reservoirs are filled with KCl aqueous solution of viscosity μ, density ρ, and permittivity ε_f. Since both the geometry and the physical fields are axisymmetric, an axisymmetric model is employed in this chapter. Therefore, a cylindrical coordinate system (r, z) with the origin fixed at the center of the nanopore is used. We assume the reservoirs are large enough to maintain a bulk concentration c_0 far away from the nanopore. In general, a coiled DNA molecule is unzipped and stretched during its translocation through a nanopore [65]. It is thus reasonable to approximate the DNA molecule as a negatively charged cylindrical nanoparticle. As a result, a cylindrical nanoparticle of length L_p capped with two hemispheres of radius a at both ends is used to represent the stretched DNA molecule. A slice of conductor with length L_f is coated on the inner surface of the nanopore as the floating electrode. A negative electric field, **E**, is applied across both the nanopore and the two reservoirs to drive the DNA nanoparticle translocation along the axis of the nanopore and concurrently generate an ionic current through the nanopore. We assume the floating electrode is inherently uncharged and ideally polarizable. A non-uniform surface charge distribution with zero net charge is thus induced along the floating electrode. Basically, the $z < 0$ region of the floating electrode carries an opposite charge to the polarity of the electrode positioned in the left-side reservoir and vice versa. Accordingly, the net charge within the EDL formed adjacent to the floating electrode interacts with the applied electric field, which in turn generates a pair of vortices arising from the induced ICEO, as shown in Figure 6.1b. Obviously, the induced ICEO vortices would significantly affect the DNA translocation through the nanopore.

The numerical simulation of DNA translocation is implemented by solving the electric field, the ionic concentrations and the fluid flow. The electric field and the ionic concentrations within the electrolyte solution are governed by the verified PNP equations [202, 204-205, 225]; while the fluid flow is governed by the modified Stokes equations as the inertial terms are negligible due to a very small Reynolds number in this chapter. The governing equations are normalized based on the bulk concentration c_0 as the ionic

concentration scale, $V_0 = RT/F$ as the potential scale, the particle radius a as the length scale, $u_0 = \varepsilon R^2T^2/(\mu a F^2)$ as the velocity scale, $D_0 = \varepsilon R^2T^2/(\mu F^2)$ as the diffusivity scale of the ionic species, $N_0 = c_0 \varepsilon R^2T^2/(\mu a F^2)$ as the ionic flux scale, $I_0 = c_0 a \varepsilon R^2T^2/(\mu F)$ as the ionic current scale and $p_0 = \mu u_0/a$ as the pressure scale. In the above, R is the universal gas constant, T is the absolute temperature of the electrolyte solution, and F is the Faraday constant. The dimensionless PNP equations and the modified Stokes equations are:

$$-\nabla^{*2}V^* = \frac{1}{2}(\kappa a)^2 (z_1 c_1^* + z_2 c_2^*), \tag{6.1}$$

$$\nabla \bullet \mathbf{N}_i^* = \nabla \bullet \left(\mathbf{u}^* c_i^* - D_i^* \nabla^* c_i^* - z_i D_i^* c_i^* \nabla^* V^*\right) = 0, \; i = 1 \text{ and } 2, \tag{6.2}$$

$$\nabla^* \bullet \mathbf{u}^* = 0 \tag{6.3}$$

$$-\nabla^* p^* + \nabla^{*2}\mathbf{u}^* - \frac{1}{2}(\kappa a)^2 (z_1 c_1^* + z_2 c_2^*)\nabla^* V^* = 0, \tag{6.4}$$

where $\kappa^{-1} = \sqrt{\varepsilon_f RT / \sum_{i=1}^{2} F^2 z_i^2 c_0}$ is the Debye length, c_i^* is the dimensionless concentration of the i^{th} ionic species, z_i are, respectively, the valences of the cations and anions (in present work, $z_1 = 1$ for K^+ and $z_2 = -1$ for Cl^-).

The axial symmetric boundary conditions for the physical fields are applied on the axis of the nanopore. The ionic concentrations at the ends of the two reservoirs are, $c_i^*\left(r^*, \pm\left(L_R^* + L_N^*/2\right)\right) = 1, \;\; i = 1 \text{ and } 2$. Only the convective flux remains in the normal flux on the particle surface, $\mathbf{n}^* \bullet \mathbf{N}_i^* = \mathbf{n}^* \bullet (u^* c_i^*)$, $i = 1$ and 2, where $\mathbf{n}^*$ is the unit normal vector directed from the particle surface into the fluid. The normal ionic fluxes on all the other boundaries are zero.

The applied electric potential at the ends of the two reservoirs are, respectively, $V^*\left(r^*, -\left(L_R^* + L_N^*/2\right)\right) = 0$ and $V^*\left(r^*, -\left(L_R^* + L_N^*/2\right)\right) = V_0^*$. The electric potential on the conducting floating electrode is a constant, $V^* = V_f^*$, which is solved based on the fact that the net induced charge on the floating electrode is zero [77, 226-227],

$$\int_{-L_f^*/2}^{L_f^*/2} \frac{\partial V^*}{\partial \mathbf{n}^*} dz^* = 0. \tag{6.5}$$

A zero normal electric field is applied on the other boundaries.

The non-slip boundary condition is imposed on the boundaries except the two ends of reservoirs and the particle surface. A zero pressure difference is applied between the two ends of reservoirs. The flow boundary condition on the particle surface is $\mathbf{u}^* = u_p^* \mathbf{e}_z^*$, where u_p^* is the axial particle velocity and $\mathbf{e}_z^*$ is the axial unit vector. The axial particle velocity is determined on the basis of the balance of the force in the z^* direction acting on the particle using a quasi-static method [164, 166-167, 197, 228],

$$F_E^* + F_H^* = 0 \tag{6.6}$$

where

$$F_E^* = \int (\frac{\partial \phi^*}{\partial z^*} \frac{\partial \phi^*}{\partial r^*} n_r^* + \frac{1}{2}\left(\frac{\partial \phi^*}{\partial z^*}\right)^2 n_z^* - \frac{1}{2}\left(\frac{\partial \phi^*}{\partial r^*}\right)^2 n_z^*) d\Gamma^*, \tag{6.7}$$

is the axial electrical force derived from the integration of the Maxwell stress tensor over the particle surface and

$$F_H^* = \int (-p^* n_z^* + 2\frac{\partial u_z^*}{\partial z^*} n_z^* + \left(\frac{\partial u_r^*}{\partial z^*} + \frac{\partial u_z^*}{\partial r^*}\right) n_r^*) d\Gamma^*, \tag{6.8}$$

is the axial hydrodynamic force. In the above, n_r^* and n_z^* are, respectively, the r^* and z^* components of the unit vector component $\mathbf{n}^*$. u_r^* and u_z^* are, respectively, the r^* and z^* components of the fluid velocity. Γ^* denotes the surface of the DNA nanoparticle.

The dimensionless ionic current flowing through the nanopore is

$$I^* = \int_{S^*} (z_1 \mathbf{N}_1^* + z_2 \mathbf{N}_2^*) \bullet \mathbf{n} dS^*, \tag{6.9}$$

where S^* denotes either end of the reservoirs because of the current conservation. The particle mobility and ionic current deviation are defined, respectively, as:

$$\eta_p^* = \frac{u_p^*}{E_z^*}, \tag{6.10}$$

and

$$\chi^* = \frac{I^* - I_\infty^*}{I_\infty^*}, \tag{6.11}$$

where E_z^* is the imposed electrical field obtained by dividing the electric potential difference between the two reservoirs over the total length of the computational domain and I_∞^* is the base ionic current when the DNA nanoparticle is far away from the nanopore.

6.3. Results and Discussion

6.3.1 Numerical Method and Code Validation

A commercial finite element package COMSOL (http://www.comsol.com, version 3.5a) operating in a high-performance cluster is chosen to solve the strongly coupled equations. The computational domain is discretized into quadratic triangular elements. Nonuniform elements are employed with larger numbers of elements assigned locally as necessary. Typically the total number of elements is approximately 100,000, with finer mesh on the floating electrode and DNA particle surface to capture the EDL. Lagrange – Quadratic elements are used for solving PNP equations, while Lagrange – P_2P_1 elements are for the Stokes equation. The ionic current through the nanopore is obtained by using the weak constrain in COMSOL specially developed for an accurate calculation of flux. Rigorous mesh-refinement tests have been performed to ensure that the solutions obtained are convergent and grid independent. A maximum tolerance of 0.1% is imposed on the relative difference $(|I_a| - |I_c|)/|I_a|$, where I_a and I_c are respectively the current entering (anode) and leaving (cathode) the nanopore. The numerical scheme has been validated to be sufficiently efficient and accurate for solving similar electrokinetic problems, such as the electrokinetic ion transport in a solid-state nanopore[14, 109-113] and the electrokinetic rigid and soft nanoparticle translocation through a nanopore.[52, 115-117, 122, 126]

We also simulate the electrophoresis of a sphere translocating along the axis of an uncharged dielectric cylindrical nanopore, whose analytical solution is available when the zeta potential of the particle is relatively small and the EDL of the particle is not disturbed by the external electric field, flow field and the solid boundary [161]. Figure 6.2 indicates a good agreement between our numerical results (circles) and the analytical solution (solid line). We further use the present model to predict the induced surface charge along a conducting sphere, which is in quantitative agreement with an existing

analytical solution derived by Bazant and Squires [226] when its EDL thickness is relatively small.

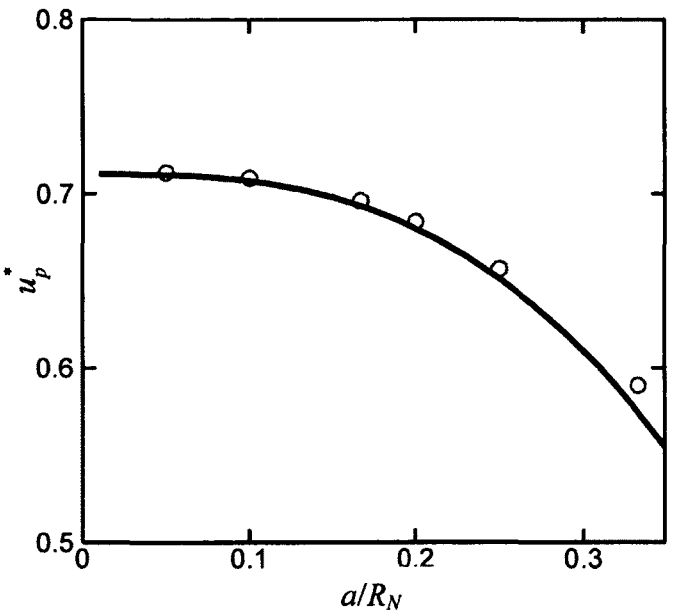

Figure 6.2. Electrophoretic velocity normalized by $\varepsilon\zeta E/\mu$ of a sphere translating along the axis of an uncharged cylindrical nanopore as a function of the ratio of the particle radius to the pore radius, a/R_N. Solid line and circles denote, respectively, the analytical approximation solution and our numerical results. The conditions are a = 1 nm, κa = 2.05, the zeta potential of the particle, ζ = 1 mV, and the axial electric field, E_z = 100 KV/m.

The following parameters, the fluid permittivity, $\varepsilon = 7.08\times10^{-10}$ F/m, the fluid density, $\rho = 1\times10^{3}$ kg/m^3, the fluid viscosity, $\mu = 1\times10^{-3}$ Pa·s, the diffusivity of K^+, $D_1 = 1.95\times10^{-9}$ m^2/s, the diffusivity of Cl^-, $D_2 = 2.03\times10^{-9}$ m^2/s, the temperature of the system, T = 300K, and the surface charge density of the particle, σ_p = –0.01 C/m^2, are used in the numerical simulation. The dimensions of the computational domain are $L_R = L_N$ = 40 nm, R_N = 4 nm and R_R = 40 nm. The floating electrode is always located with respect to z = 0. The radius and the length of the DNA nanoparticle are, respectively, a = 1 nm and L_p = 10 nm. We investigate the effects due to the applied electric field, the ratio of the particle radius to the Debye length, and the length of the floating electrode, on the DNA translocation through a nanopore in this section. Although the surface charge density of

the nanopore plays an important role on the DNA nanoparticle translocation, the nanopore is assumed to be uncharged in present work to emphasize the floating electrode effect.

6.3.2 The Effect of Applied Electric Field

The induced surface charge on the floating electrode highly depends on the externally applied electric field, which accordingly plays a significant role on the control of ICEO inside the nanopore and DNA translocation through the nanopore. Figure 6.3 shows the surface charge density induced on the floating electrode when κa =1 (dashed line: $E_z^* = 3.87 \times 10^{-4}$; circles: $E_z^* = 1.93 \times 10^{-2}$) and κa = 4 (solid line: $E_z^* = 3.87 \times 10^{-4}$; squares: $E_z^* = 1.93 \times 10^{-2}$). It is revealed that the induced surface charge density on the floating electrode exhibits a linear relationship to its local position except the two ends of the floating electrode. The $z^* > 0$ region near the anode is negatively charged, while the $z^* < 0$ region carries an anti-symmetrically positive charge to maintain a zero net charge on the floating electrode. The results denoted by symbols are divided by 50 to obtain a clear comparison for $E_z^* = 3.87 \times 10^{-4}$ and $E_z^* = 1.93 \times 10^{-2}$. The coincidence of the symbols and lines demonstrates that the induced surface charge density is proportional to the external electric field. For a specific external electric field, the induced surface charge density also increases as κa increases.

Figure 6.4 shows the variation of the particle mobility along the axis of the nanopore with a floating electrode when κa = 4, $L_f = L_N/2$ (a) and $L_f = L_N$ (b) under three different electric fields, $E_z^* = 3.87 \times 10^{-4}$ (solid lines), $E_z^* = 3.87 \times 10^{-3}$ (dashed lines) and $E_z^* = 1.93 \times 10^{-2}$ (dash-dotted lines). The particle mobility in the absence of the floating electrode (circles) is also included in Figure 6.4 as a reference mobility, which is independent of the applied electric field and remains a constant inside the nanopore. The particle mobility inside the nanopore is much larger than in the reservoir because of an enhanced electric field inside the nanopore. The variation of the particle mobility inside a nanopore with a floating electrode becomes quite complicated compared to the absence of floating electrode (circles). When the length of the floating electrode is half of the total length of the nanopore, $L_f = L_N/2$, as shown in Figure 6.4a, the particle mobility is nearly

the same as the reference mobility when $E_z^* = 3.87 \times 10^{-4}$. As the external electric field increases to $E_z^* = 3.87 \times 10^{-3}$, the particle mobility follows the reference mobility very well when the particle is away from the floating electrode. As it approaches the floating electrode, the particle mobility begins to decrease and minimizes at $z_p^* = -5$. Subsequently, the particle mobility further increases as the particle moves towards the center of the nanopore. When the particle reaches $z_p^* = 0$, the particle mobility recovers the reference mobility. As the particle moves even further, the particle mobility gradually increases and maximizes at $z_p^* = 5$, which later decreases and recovers the reference mobility as the particle moves out of the floating electrode region. When the external electric field further increases to $E_z^* = 1.93 \times 10^{-2}$, the variation of the particle mobility follows a similar tendency as described for the case of $E_z^* = 3.87 \times 10^{-3}$. However, the deviation from the reference mobility becomes even larger under $E_z^* = 1.93 \times 10^{-2}$, indicating a more significant effect due to the floating electrode. The particle mobility becomes negative when the particle approaches the $z^* < 0$ region of the floating electrode, which implies that the particle is trapped near the floating electrode. The predicted particle trapping phenomenon near a floating electrode has recently been experimentally observed in a microchannel fabricated with a floating electrode [84, 223]. When the nanopore is fully coated with a floating electrode, $L_f = L_N$, as shown in Figure 6.4b, the effect of the external electric field on the particle mobility exhibits a similarity as discussed in Figure 6.4a however, the particle mobility is affected by the floating electrode along the entire nanopore. In addition, it is found that the magnitude of the maximum particle mobility for $L_f = L_N$ is larger than that for $L_f = L_N/2$. Obviously, the effect of the floating electrode on the particle translocation increases as its total length increases. When the external electric field is $E_z^* = 1.93 \times 10^{-2}$, the particle cannot even enter the nanopore and is trapped at the entrance of the nanopore itself.

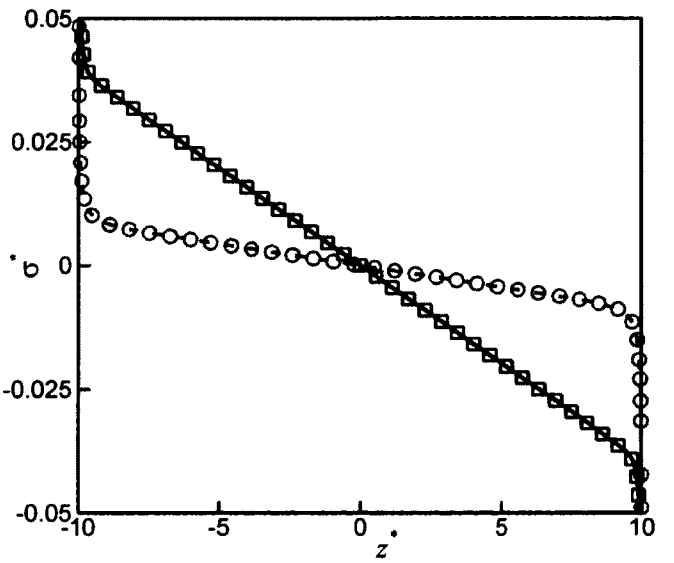

Figure 6.3. Surface charge density induced on the float electrode when κa =1 (dashed line: $E_z^* = 3.87\times10^{-4}$; circles: $E_z^* = 1.93\times10^{-2}$) and κa = 4 (solid line: $E_z^* = 3.87\times10^{-4}$; squares: $E_z^* = 1.93\times10^{-2}$). Symbols are divided by 50 for a clear comparison.

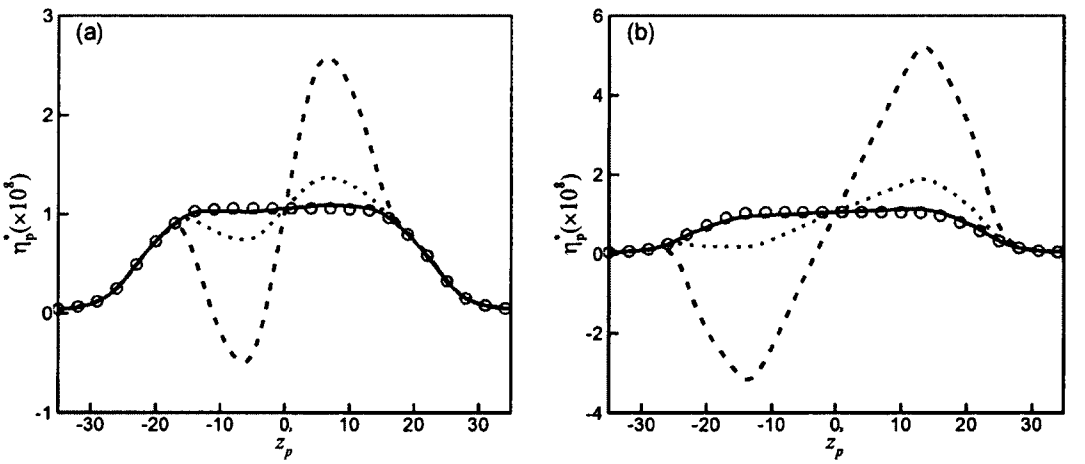

Figure 6.4. Variation of particle mobility along the axis of the nanopore when (a): κa = 4, $L_f = L_N/2$; (b): κa = 4, $L_f = L_n$. Solid line, dashed line and dash-dotted line represent, respectively, $E_z^* = 3.87\times10^{-4}$, 3.87×10^{-3} and 1.93×10^{-2} with floating electrode, while circles represent the mobility for a dielectric nanopore (i.e., L_f=0).

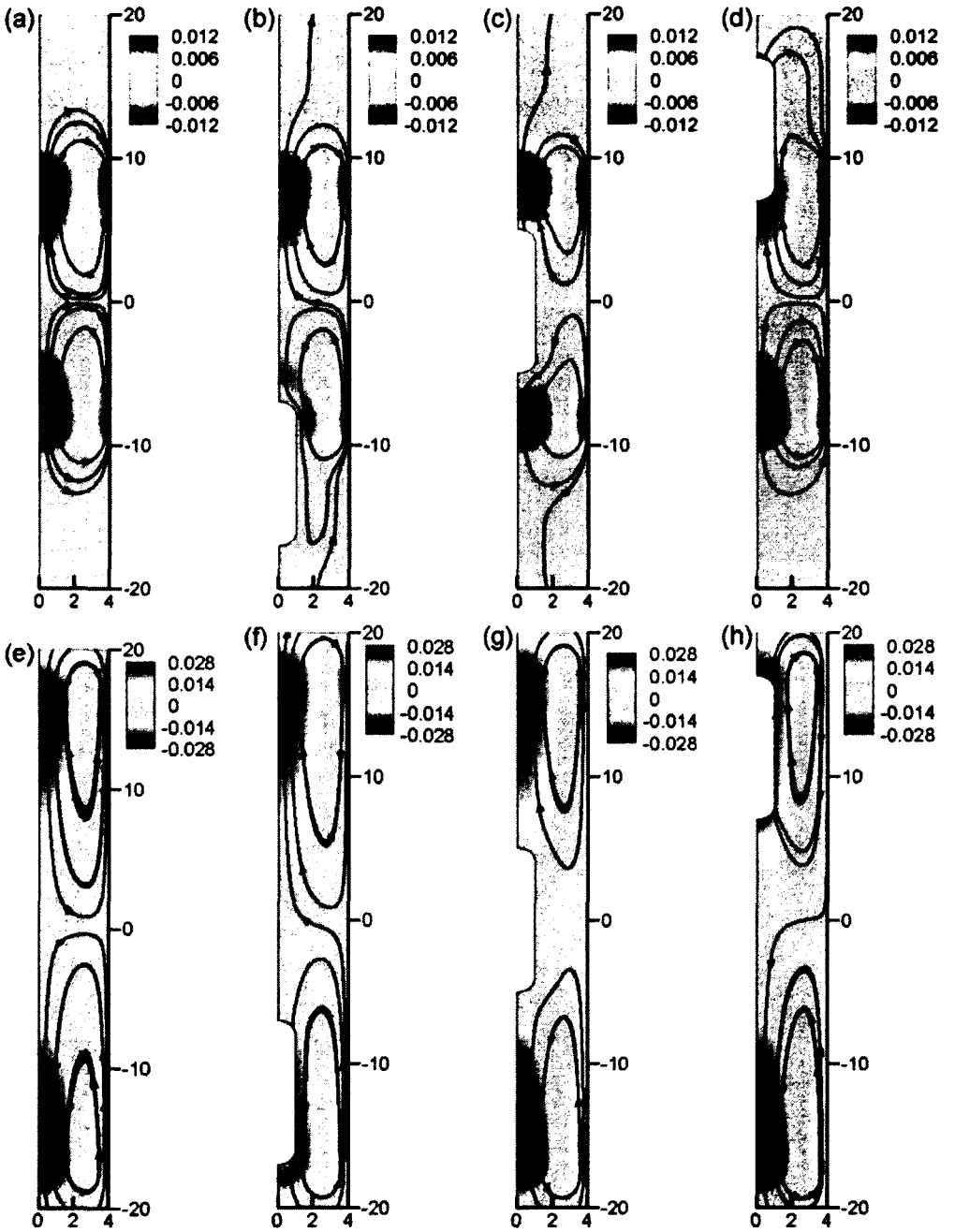

Figure 6.5. Flow field near the floating electrode when κa = 4, $E_z^* = 1.93\times10^{-2}$, (a, e): $z_p^* = -35$; (b, f): $z_p^* = -12$; (c, g): $z_p^* = 0$; (d, h): $z_p^* = 12$. The length of the floating electrode for (a-d) and (e-h) are, respectively, $L_f = L_N/2$ and $L_f = L_N$. Color levels denote the fluid velocity in the z direction and streamlines with arrows denote the fluid velocity vector. The red lines and arrow indicate the location of floating electrode and the direction of particle motion, respectively.

To further explain the aforementioned particle behavior due to the presence of the floating electrode, the flow fields inside the nanopore at four different particle locations are illustrated in Figure 6.5 when κa = 4, $E_z^* = 1.93 \times 10^{-2}$, $L_f = L_N/2$ (a-d) and $L_f = L_N$ (e-h). The induced charge on the floating electrode leads to the formation of EDL, which interacts with the applied electric field and in turn generates the ICEO inside the nanopore. When the particle is still in the reservoir, its presence does not affect the ICEO inside the nanopore. Due to the anti-symmetric distribution of the induced surface charge along the floating electrode, the ICEOs next to the $z^* < 0$ and $z^* > 0$ regions are oppositely facing each other. This in turn generates a pair of vortices symmetric with respect to $z^* = 0$, as shown in Figure 6.5a. It is shown that the ICEO along the axis in the $z^* < 0$ region is opposite to the particle translocation, which obviously retards the particle translocation. On the contrary, the ICEO along the axis in the $z^* > 0$ region is in the same direction of the particle motion and tends to facilitate the particle translocation. When the particle is located at $z_p^* = -12$, as shown in Figure 6.5b, the particle translocation is mainly affected by the ICEO in the $z^* < 0$ region of the floating electrode. As a result, the opposite ICEO resists the particle translocation, as shown in Figure 6.5b, which accordingly decreases the particle mobility as shown in Figure 6.4a. When the particle is located at $z_p^* = 0$, the particle translocation is retarded by the ICEO in the $z^* < 0$ region of the floating electrode, and facilitated by the ICEO in the $z^* > 0$ region of the floating electrode, as shown in Figure 6.5c. Due to the symmetric location of the particle, the retardation and facilitation of the particle translocation cancel each other, which thus recover the particle mobility to the reference mobility indicated in Figure 6.4a. When the particle is located at $z_p^* = 12$, as shown in Figure 6.5d, the particle translocation is mainly affected by the ICEO in the $z^* > 0$ region of the floating electrode, which accordingly facilitates the particle translocation. When the floating electrode covers the entire nanopore ($L_f = L_N$), the effective region of the generated ICEO is accordingly extended to the entire nanopore. The ICEO patterns shown in Figures 6.5e-6.5h exhibit a similarity to those in Figures 6.5a-6.5d, respectively. As discussed in Figure 6.3, the induced surface charge on the floating electrode is linearly proportional to its local position. Thus, a longer floating electrode implies a higher magnitude of the induced surface charge. Comparing the maximum fluid velocity in

Figure 6.5e to that in Figure 6.5a, it is found that the ICEO effect increases as the length of the floating electrode increases. As a result, the ICEO effect on the particle mobility when $L_f = L_N$ is more pronounced than the case when $L_f = L_N/2$, as shown in Figure 6.4b.

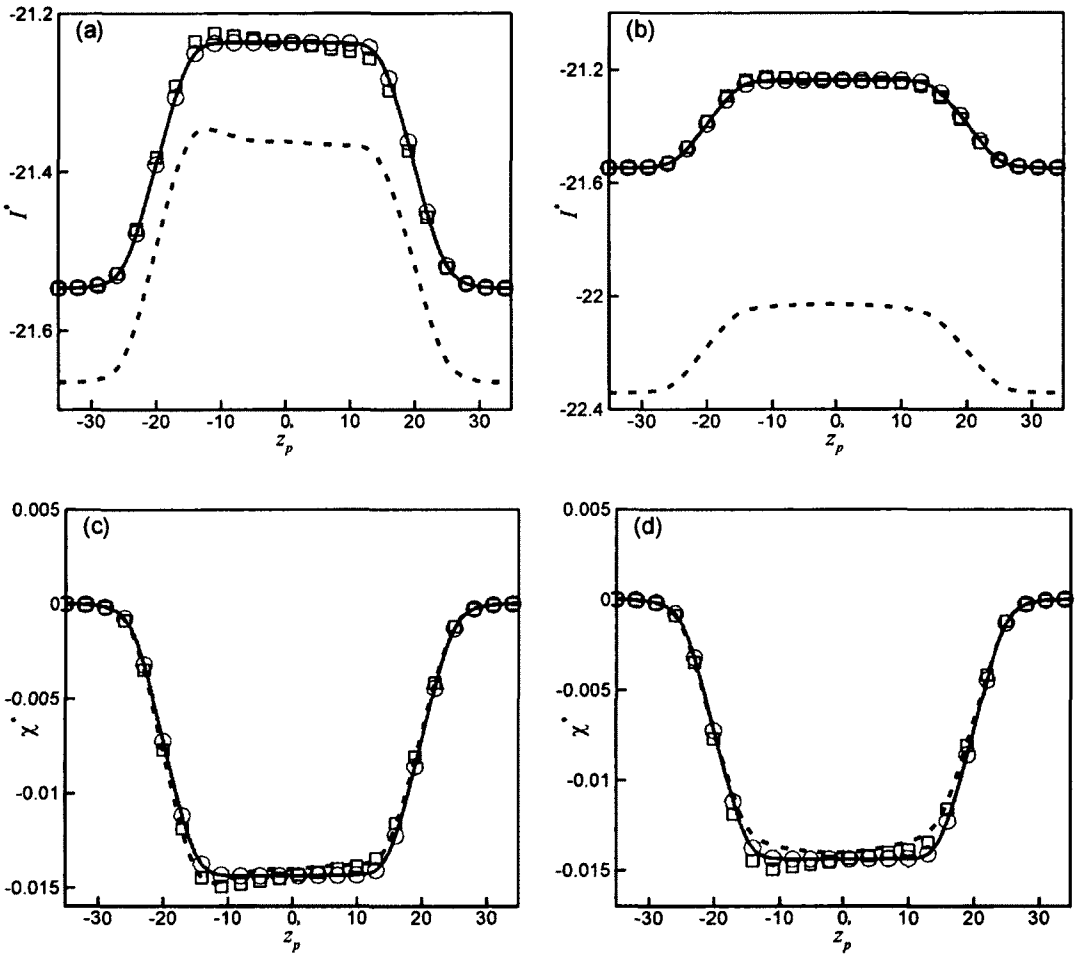

Figure 6.6. Ionic current (a, b) and ionic current deviation (c, d) through the nanopore as a function of the particle position when $\kappa a = 4$ and (a, c): $L_f = L_N/2$; (b, d): $L_f = L_N$ Solid line (circles) and dash-dotted line (squares) represent, respectively, $E_z^* = 3.87 \times 10^{-4}$ and $E_z^* = 1.93 \times 10^{-2}$ with (without) floating electrode. The ionic current for $E_z^* = 3.87 \times 10^{-4}$ is multiplied by 50 for comparison.

Figures 6.6a and 6.6b depict the ionic current through the nanopore as a function of the particle position when $\kappa a = 4$, $L_f = L_N/2$ (a) and $L_f = L_N$ (b). When the applied electric

field is relatively low (solid line and circles), the effect of the floating electrode on the ionic current through the nanopore is negligible. As the applied electric field increases, the induced charge on the floating electrode accordingly increases. As a result, more ions are attracted into the nanopore, which increases the ionic conductivity of the nanopore. Hence, the ionic current increases owing to the presence of the floating electrode when the applied electric field is relatively high. In the nanopore-based sensing of nanoparticles, the relative change in the ionic current is used to characterize the particle. Figures 6.6c and 6.6d show the corresponding ionic current deviation, defined in Eq. (6.11), as a function of the particle's position. When the particle is inside the nanopore, a current blockade is predicted when κa is relatively high, which is in qualitative agreement with the experimental observations [37, 136, 218, 229]. In addition, it is revealed that the presence of the floating electrode has very limited effect on the ionic current deviation.

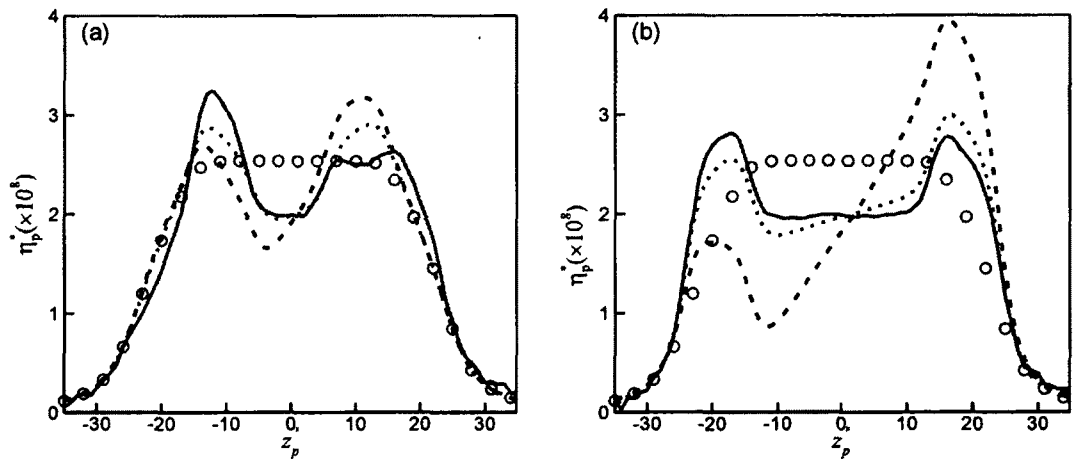

Figure 6.7. Variation of particle mobility along the axis of the nanopore when κa = 1 and (a): $L_f = L_N/2$; (b): $L_f = L_N$. Solid line, dashed line and dash-dotted line represent, respectively, $E_z^* = 3.87\times10^{-4}$, 3.87×10^{-3} and 1.93×10^{-2} with a floating electrode, while circles represent the particle mobility without floating electrode.

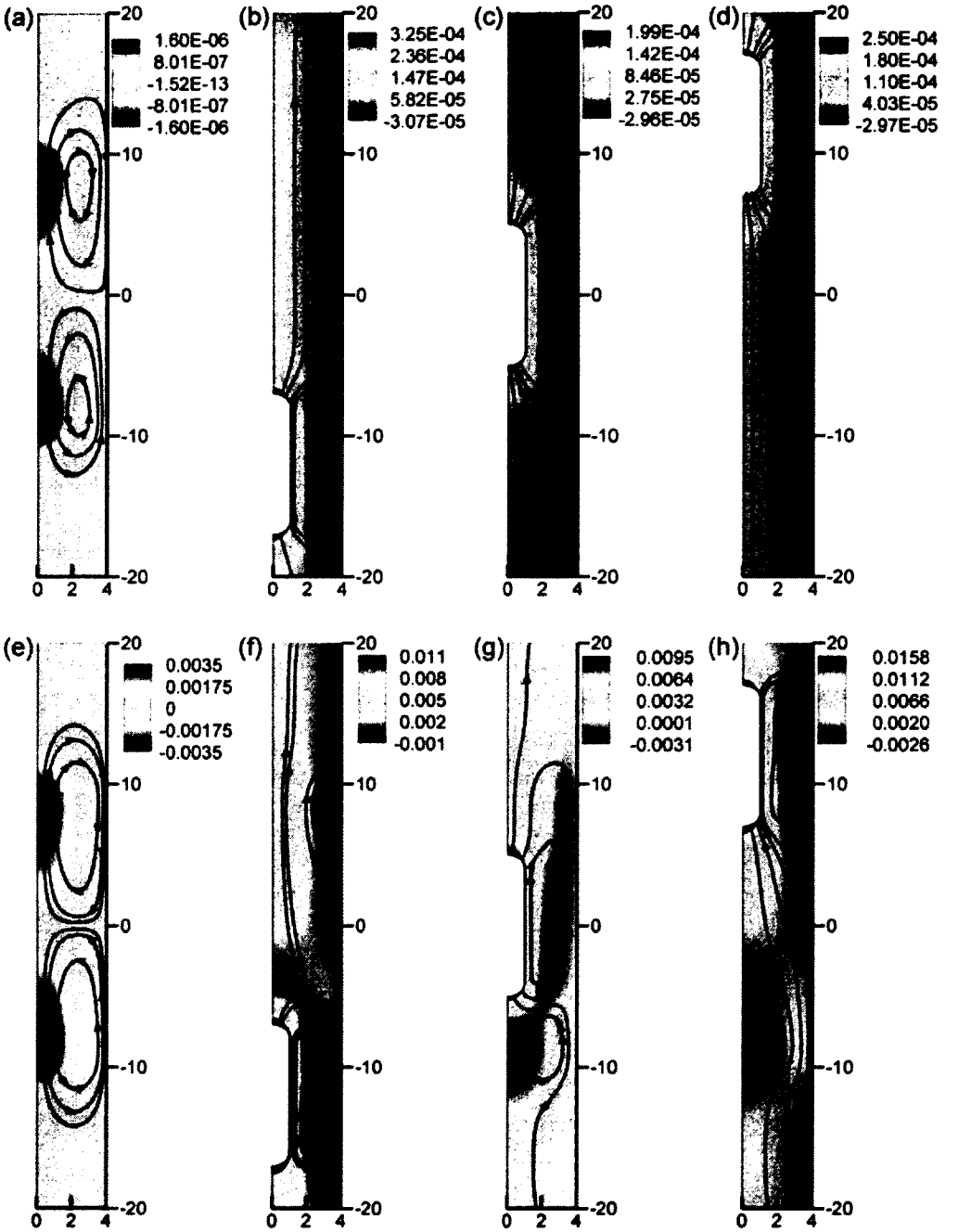

Figure 6.8. Flow field near the floating electrode when κa = 1, L_f = L_N/2 and (a, e): $z_p^* = -35$; (b, f): $z_p^* = -12$; (c, g): $z_p^* = 0$; (d, h): $z_p^* = 12$. The electric fields for (a-d) and (e-h) are, respectively, $E_z^* = 3.87 \times 10^{-4}$ and $E_z^* = 1.93 \times 10^{-2}$. Color levels denote the fluid velocity in the z direction and streamlines with arrows denote the fluid velocity vector. The red lines and arrow indicate the location of floating electrode and the direction of particle motion, respectively.

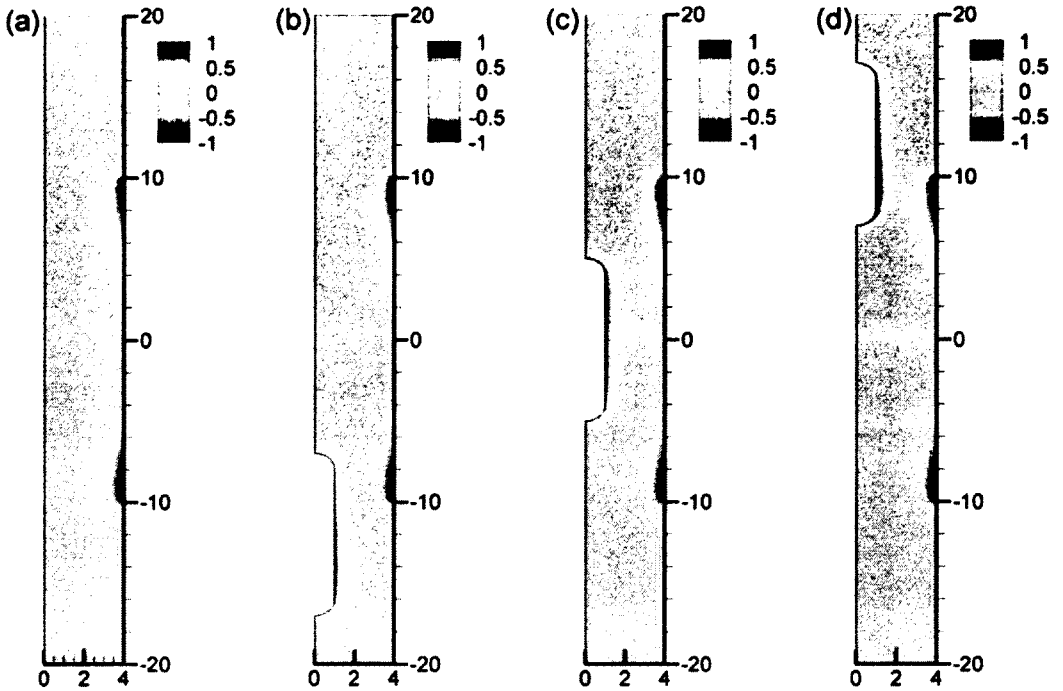

Figure 6.9. Net concentration distribution $c_1^* - c_2^*$ near the floating electrode when κa = 1, $L_f = L_N/2, E_z^* = 1.93\times10^{-2}$ and (a): $z_p^* = -35$; (b): $z_p^* = -12$; (c): $z_p^* = 0$; (d): $z_p^* = 12$. The lines and arrow indicate the location of floating electrode.

6.3.3 The Effect of the Ratio of the Particle Radius to the Debye Length, κa

In Section 4.1, the EDLs of the particle and the floating electrode are not overlapped. As a result, the particle translocation through the nanopore is mainly affected by the ICEO. Here, we increase the EDL thickness to investigate the effect of EDL overlapping on the particle translocation. Figure 6.7 shows the variation of particle mobility along the axis of the nanopore with a floating electrode when κa = 1, $L_f = L_N/2$ (a) and $L_f = L_N$ (b) under three different electric fields, $E_z^* = 3.87\times10^{-4}$ (solid lines), 3.87×10^{-3} (dashed lines) and 1.93×10^{-2} (dash-dotted lines). The particle mobility in the absence of the floating electrode is also included in Figure 6.7 as the reference mobility. As discussed in Figure 6.4, the particle mobility decreases in the $z^* < 0$ region of the floating electrode, and increases in the $z^* > 0$ region of the floating electrode when κa = 4. Apparently, the effect of the floating electrode on the particle mobility under EDL overlapping shown in Figure

6.7 is totally distinct from the cases shown in Figure 6.4. When $L_f = L_N/2$, the particle mobility is nearly identical to the reference mobility when the particle is away from the floating electrode in the reservoir. When the applied electric field is relatively low, $E_z^* = 3.87 \times 10^{-4}$, the particle mobility is enhanced when the particle approaches the $z^* < 0$ region of the floating electrode. The particle mobility is maximized near $z_p^* = -12$ and subsequently decreases below the reference mobility with a minimum value at $z_p^* = 0$. Later, the particle mobility increases again when it moves toward the $z^* > 0$ region of the floating electrode and is maximized near $z_p^* = 12$. Once the particle completely moves out of the floating electrode region, the particle mobility recovers the reference mobility. When the applied electric field increases 10 times to $E_z^* = 3.87 \times 10^{-3}$, the effect of the floating electrode on the particle mobility follows a similar trend as the case when $E_z^* = 3.87 \times 10^{-4}$. However, it is predicted that the enhancement of the particle mobility is reduced in the $z^* < 0$ region of the floating electrode, but the enhancement of the particle mobility in the $z^* > 0$ region of the floating electrode is further increased. When the applied electric field further increases, the decrease (increase) in the enhancement of the particle mobility in the $z^* < 0$ ($z^* > 0$) region of the floating electrode is more significant. When the nanopore is fully coated with a floating electrode, $L_f = L_N$, as shown in Figure 6.7b, the effect of the applied electric field on the particle mobility is very similar as discussed in Figure 6.7a.

Figure 6.8 shows the flow fields inside the nanopore at four different particle locations when $\kappa a = 1$, $L_f = L_N/2$, $E_z^* = 3.87 \times 10^{-4}$ (a-d) and $E_z^* = 1.93 \times 10^{-2}$ (e-h). When the particle is far away from the floating electrode, a pair of ICEO vortices is generated inside the nanopore, as shown in Figures 6.8a and 6.8e. It is found that the magnitude of the maximum fluid velocity in Figure 6.8e is about 2500 times of that in Figure 6.8a, which confirms that the ICEO is proportional to the square of the electric field strength. The ICEO flow is too weak to affect the particle translocation under $E_z^* = 3.87 \times 10^{-4}$, and as a result, the flow inside the nanopore is dominated by the particle electrophoretic velocity when the particle is inside the nanopore, as shown in Figures 6.8b, 6.8c and 6.8d. When the applied electric field is relatively high, $E_z^* = 1.93 \times 10^{-2}$, the ICEO is strong

enough to retard the particle translocation in the $z^* < 0$ region of the floating electrode and enhance the particle translocation in the $z^* > 0$ region of the floating electrode, as shown in Figures 6.8f and 6.8h.

Our previous study found that the electrostatic interaction between the particle and the nanopore wall plays an important role in the particle translocation under the EDL overlapping condition [65]. The electrostatic interaction exerts either attractive or repulsive electrostatic force on the particle, depending on the polarities of the particle and the floating electrode. Figure 6.9 shows the net charge represented by $c_1^* - c_2^*$ near the floating electrode at four different particle locations when κa = 1, L_f = L_N/2 and $E_z^* = 1.93 \times 10^{-2}$. The distributions of the net charge near the floating electrode at the four particle locations when $E_z^* = 3.87 \times 10^{-4}$ are very similar to those shown in Figure 6.9. The $z^* < 0$ and $z^* > 0$ regions of the floating electrode carry, respectively, positive and negative charge, as illustrated in Figure 6.9a. When the particle is located at $z_p^* = -12$, the particle is mainly under the influence of the $z^* < 0$ region of the floating electrode. An attractive force arising from the particle-floating electrode electrostatic interaction facilitates the particle translocation, which thus enhances the particle mobility above the reference mobility, as shown in Figure 6.7a (solid line). When the particle is located at $z_p^* = 0$, the particle translocation is affected by both the $z^* < 0$ and $z^* > 0$ regions of the floating electrode. The electrostatic interaction between the particle and the $z^* < 0$ ($z^* > 0$) region of the floating electrode is an attractive (a repulsive) force. However, both electrostatic interactions retard the particle translocation, which accordingly decrease the particle mobility, as shown in Figure 6.7a (solid line). When the particle is located at $z_p^* = 12$, the particle translocation is mainly affected by the $z^* > 0$ region of the floating electrode. As a result, the particle-floating electrode electrostatic interaction exerts a repulsive force on the particle, which in turn enhances the particle mobility above the reference mobility as shown in Figure 6.7a (solid line). In summary, the particle translocation is mainly affected by the particle-floating electrode electrostatic interaction under EDL overlapping when the applied electric field is relatively low.

When the applied electric field is relatively high, $E_z^* = 1.93 \times 10^{-2}$, both the ICEO and the particle-floating electrode electrostatic interaction affect the particle translocation.

When the particle is located at $z_p^* = -12$, the ICEO retards the particle translocation; while particle-electrode electrostatic interaction facilitates the particle translocation. However, the ICEO is proportional to the square of the electric field strength. By contrast, the particle-floating electrode electrostatic interaction is proportional to the electric field strength. Hence, the ICEO effect dominates over the effect from the particle-floating electrode electrostatic interaction, which in turn decreases the enhancement of the particle mobility, as shown in Figure 6.7a (dash-dotted line). When the particle is located at $z_p^* = 0$, the ICEOs arising from the $z^* < 0$ and $z^* > 0$ regions of the floating electrode almost cancel each other. Accordingly, the particle mobility nearly recovers the mobility under a relatively low electric field, as shown in Figure 6.7a (dash-dotted line). When the particle is located at $z_p^* = 12$, both the ICEO and the particle-electrode electrostatic interaction facilitate the particle translocation. As a result, the enhancement of the particle mobility by ICEO is further enhanced by the particle-floating electrode electrostatic interaction, as shown in Figure 6.7a (dash-dotted line). The effects of the floating electrode on the ionic current and ionic current deviation for $\kappa a = 1$ are very similar to those shown in Figure 6.6. Basically, the magnitude of the ionic current increases as the induced charge on the floating electrode attracts more ions inside the nanopore when the applied electric field is relatively high. However, the floating electrode has very limited effect on the ionic current deviation.

6.4. Conclusions

Effects of the presence of a floating electrode in the form of a conducting metal coating along the inner surface of a nanopore on the DNA translocation through a nanopore have been studied using a continuum model. The model includes coupled PNP equations for the ionic mass transport and the modified Stokes equations for the flow field. The ideally polarizable floating electrode interacting with the applied electric field induces a non-uniform charge density on its surface. Two main factors, ICEO and particle-floating electrode electrostatic interaction, could significantly affect the DNA translocation through a nanopore. The ICEO effect exists under both thin and thick EDLs and is proportional to the square of the applied electric field. As a result, the ICEO is negligible

under a relatively low electric field and becomes significant under a relatively high electric field. The ICEO retards the DNA translocation when it approaches the floating electrode, however, facilitates the DNA translocation when it moves away from the floating electrode. It has been predicted that the particle could be trapped near the floating electrode when the applied electric field is relatively high and the EDLs are relatively thin. On the other hand, the particle-floating electrode electrostatic interaction is only pronounced when the EDLs of the particle and floating electrode are overlapped. An attractive (or repulsive) particle-floating electrode electrostatic interaction is generated when the polarity of the particle's surface charge is opposite (identical) to that of the local floating electrode. In general, the particle-floating electrode electrostatic interaction facilitates the DNA translocation at the two ending regions of the floating electrode and retards the DNA translocation in the middle region of the floating electrode. Thus, the floating electrode technique might be helpful for attracting DNA from the reservoir into the nanopore and slowing down its motion inside the nanopore during sequence sensing. A longer floating electrode implies a higher surface charge is induced on the floating electrode, which in turn induces a more significant effect on the DNA translocation. The present of the floating electrode attracts more ions inside the nanopore resulting in an increase in the ionic current flowing through the nanopore, and exhibits a minor effect on the ionic current deviation.

CHAPTER 7

DNA ELECTROKINETIC TRANSLOCATION THROUGH A NANOPORE: LOCAL PERMITTIVITY ENVIRONMENT EFFECT

Abstract

Many existing studies revealed that counterion condensation and/or the strong hydrogen bonding interactions in the vicinity of a charged DNA nanoparticle significantly reduce the local liquid permittivity surrounding it. However, the existing studies on DNA electrokinetic translocation through a nanopore used a constant instead of varying liquid permittivity. The effect of the local liquid permittivity surrounding the DNA nanoparticle, referred to as the local permittivity environment (LPE) effect, on its electrokinetic translocation through a nanopore is investigated for the first time using a continuum-based model, composed of the coupled Poisson-Nernst-Planck (PNP) equations for the ionic mass transport, and the Stokes and Brinkman equations for the hydrodynamic fields in the region outside of the DNA and within the ion-penetrable layer of the DNA nanoparticle, respectively. The nanoparticle translocation velocity and the resulting current deviation are systematically investigated for both constant and spatially varying permittivities surrounding the DNA nanoparticle under various conditions. The LPE effect in general reduces the particle translocation velocity. The LPE effect on the current deviation is insignificant when the imposed electric field is relatively high. However, when the eclectic field and the bulk electrolyte concentration are relatively low, both current blockade and enhancement are predicted considering the LPE effect, while only current blockade is predicted using a constant liquid permittivity.

7.1. Introduction

Solid-state nanopores[141] have emerged as single-molecule biosensors for detection and characterization of biopolymers such as polypeptide,[138-139] RNA,[20] as well as DNA[20, 136, 142] over the past decade. Electrically driven translocation of charged nanoparticles through a nanopore giving rise to detectable changes in ionic transpore current enables

the sensing of unlabeled single-molecule for various bio-analytical applications. Among these, nanopore-based DNA sequencing technique[29, 35, 230] is one of the most promising applications, which makes it possible to identify nucleotide bases sequence by discriminating the ionic current signals as well as at high speed and low lost.[29]

Despite nanopore-based sensing techniques recent inception, a growing number of experimental studies[33, 35, 37-38, 41, 43, 136, 138-139, 214, 218, 231-234] as well as theoretical ones[39-40, 56-57, 59, 64-65, 149-150, 218, 235-236] on such single-molecule sensors have appeared. Experimental results demonstrated that the ionic current during the DNA translocation depends on the thickness of the membrane,[136, 232] the pore materials and radius,[33, 136, 231-233] the DNA length,[43, 136, 214, 218, 231] the voltage across the nanopore,[37, 233] and the pH[234] and the bulk concentration[38, 41, 214] of the aqueous solution. Among these, when bulk salt concentration is relatively high (i.e. 1 M) the typically current blockade[33, 35, 37, 41, 43, 136, 218, 231-234] is observed during the single-molecule translocation. Chang et al.[214] first found that when the bulk salt concentration is relatively low (i.e. 0.1 M) and the DNA length is comparable to the thickness of the nanopore, the surprising current enhancement is appeared. Later Fan et al.[45] also observed the current blockade to current enhancement phenomenon during DNA translocation through inorganic nanotube on changing the buffer concentration. Dekker's group[38] further demonstrated that the salt concentration dependence of the ionic current by using solid-state nanopores, and very recently it was analyzed numerically by He et al.[56] adopting the Poisson-Boltzmann coupled with Navier-Stokes models. Both the current blockade and current enhancement phenomena during the DNA translocation through nanopores are observed by Timp's[40] and Schulten's groups[39] as well using the molecular dynamics (MD) simulation, and later Liu et al.[149] adopted the coupled Poisson-Nernst-Planck (PNP) with Navier-Stokes (NS) equations to theoretically investigate this similar problem. Liu et al.[149] concluded that their results based on the PNP coupled with NS model are successful in predicting ionic current through a nanopore and in good qualitative agreement with the experimental data and MD's prediction.

To my best understanding, all of these theoretical predictions in ionic current of the electrokinetic DNA translocation through nanopores are based on a general assumption of constant liquid permittivity inside and outside DNA molecules. Many existing studies,

however, indicate that this basic assumption of constant liquid permittivity is unrealistic and incorrect.[237-241] In the vicinity of a charged DNA molecule in water, the local liquid permittivity in fact obviously deviates from its bulk value as a consequence of the significant counterion condensation and the strong hydrogen bonding interactions[237, 240] and consequently, the activity of the water and ions as well as the local liquid permittivity surrounding the DNA are reduced. On the basis of fitting to the local permittivity obtained from the MD simulation, the spatial varying permittivity from the DNA nanoparticle surface ε_r, referred to as the local permittivity environment (LPE) effect, can be described by the empirical Hingerty-Lavery type sigmoidal permittivity function,[238-239]

$$\varepsilon_r = \varepsilon_w - \left[\left(\frac{\varepsilon_w - \varepsilon_i}{2}\right)\left(\alpha^2 + 2\alpha + 2\right)e^{-\alpha}\right] \tag{7.1}$$

Here, $\varepsilon_w = 80$ and $\varepsilon_i = 1.76$ are the relative permittivity of the liquid phase far away (bulk aqueous solution) and on the DNA nanoparticle surface, respectively, and $\alpha = 1.2s$ with s being the normal distance from the DNA surface. As shown in the inset of Figure 7.1, the dependence of the spatial distribution of the local liquid permittivity on the normal distance from the DNA nanoparticle surface within 1 nm is depicted.

Taking the LPE effect into account, the DNA electrokinetic translocation through a nanopore is investigated using a continuum-based model, composed of the coupled Poisson-Nernst-Planck (PNP) equations for the ionic mass transport, and the Stokes and Brinkman equations[124-125, 215, 242] for the hydrodynamic fields in the region outside of the DNA and within the ion-penetrable layer of the DNA nanoparticle, respectively. The nanoparticle translocation velocity and the resulting current deviation for both constant and spatially varying permittivities surrounding the DNA nanoparticle are examined in detail through varying the bulk ionic concentration, the strength of applied electric field, and the nanopore surface charge density. We propose, for the first time, that no matter what is the electric field imposed the predictions in ionic current with considering the LPE effect are in good qualitative agreement with the experimental observations in the literature. This chapter is also aimed to provide theoretical background for elaboration the physical mechanisms of affecting the DNA translocation through a nanopore.

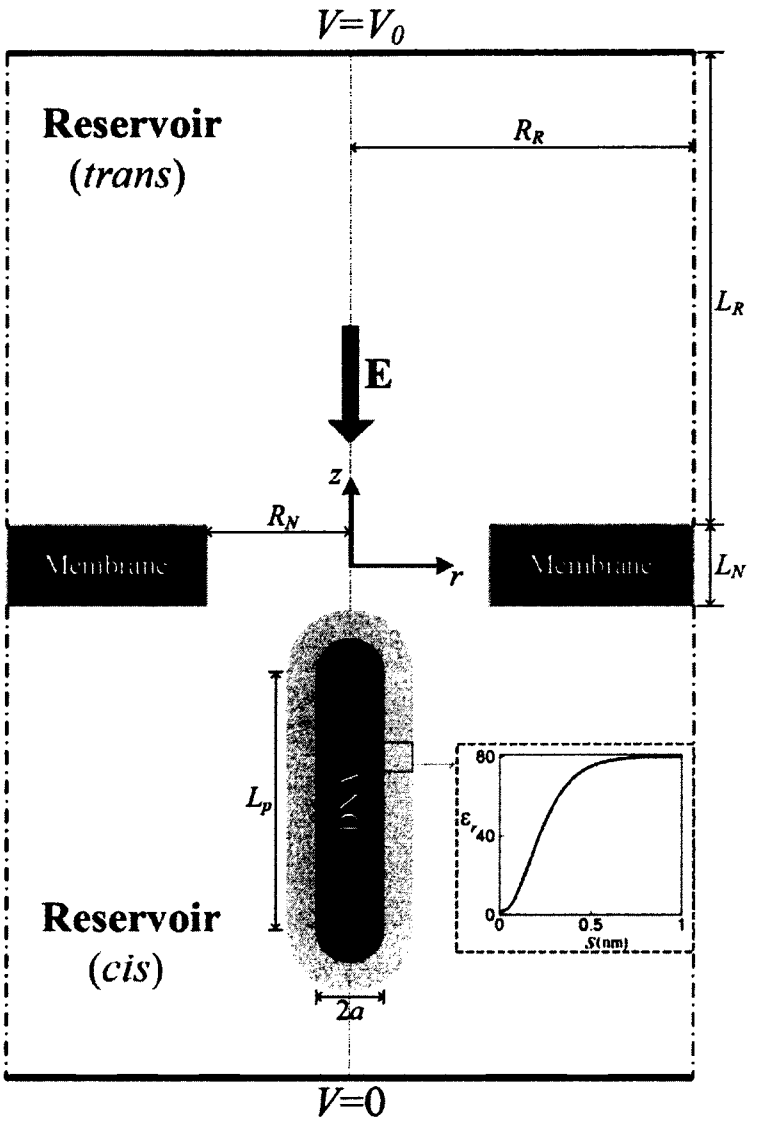

Figure 7.1. Schematic view of a soft DNA translocation through a nanopore. Inset: variation of the local permittivity environment as a function of the normal distance from the DNA surface based on Eq. (7.1).[239]

7.2. Mathematical Model

We consider a nanopore of length L_N and radius R_N connecting two large, identical reservoirs (referred to as *cis* and *trans* reservoirs, respectively) of length L_R and radius R_R

on either side, as schematically shown in Figure 7.1. The nanopore and reservoirs are filled with an aqueous binary electrolyte solution with z_1 and z_2 being the valences of the cations and the anions, respectively. A double-stranded DNA (dsDNA) molecule is initially positioned inside the *cis* reservoir as shown in Figure 7.1. The dsDNA contains a rigid inner core, which is approximated as an uncharged nanorod of length L_p with two hemispheres of radius a on either end, covered by an ion-penetrable soft layer of uniform thickness d.[149, 241] The ion-penetrable soft layer is homogeneously structured and bears dissociable function groups to form the phosphate backbones in DNA, yielding a uniform fixed charge density, ρ_{fix}, and an extra friction force acting on the liquid flowing inside.[125] We further assume that the DNA nanoparticle is initially placed with its axis coinciding with the cylindrical nanopore's axis so that a two dimensional axial symmetric geometry can be used to describe all variables in this chapter. The origin of the cylindrical coordinate (r, z) is fixed at the center of the nanopore. The two reservoirs are assumed large enough for the ionic concentration far away from the nanopore to maintain as its bulk value, C_0. A potential bias V_0 is applied between the two electrodes positioned far away from the nanopore inside the two reservoirs, inducing a negative axial electric field, **E**, to electrophoretically drive the negatively charged DNA from the *cis* reservoir along the axis of the nanopore toward the *trans* reservoir and simultaneously generate a detectable ionic current through the nanopore.

In this chapter, we adopt the verified continuum-based model, composed of the PNP equations for the ionic mass transport and the Stokes equations for the hydrodynamic field,[124-125, 215, 242] to model the DNA electrokinetic translocation through a nanopore with the emphasis on the LPE effect. The ionic mass transport in the electrolyte solution is governed by the PNP equations:[65, 124]

$$-\nabla\cdot(\varepsilon_0\varepsilon_{f,i}\nabla V)=\rho_e+\rho_{fix}\text{, inside the ion-penetrable layer} \tag{7.2}$$

$$-\nabla\cdot(\varepsilon_0\varepsilon_{f,0}\nabla V)=\rho_e\text{, outside the ion-penetrable layer} \tag{7.3}$$

and

$$\nabla\cdot\mathbf{N}_j=\nabla\cdot(\mathbf{u}c_j-D_j\nabla c_j-z_j\frac{D_j}{RT}Fc_j\nabla V)=0\text{, }j\text{=1 and 2.} \tag{7.4}$$

In the above, V is the electric potential; $\mathbf{u}$ is the fluid velocity; $\rho_e = F(z_1c_1 + z_2c_2)$ is the space charge density of mobile ions; $\mathbf{N}_j$, c_j, D_j, and z_j are the ionic flux density, the ionic concentration, the diffusivity, and the valence of the j^{th} ionic species, respectively (j=1 and 2 represent the cations and anions, respectively); ε_0, F, R, and T are the vacuum permittivity, the Faraday constant, the universal gas constant, and the absolute temperature, respectively; $\varepsilon_{f,i}$ and $\varepsilon_{f,o}$ are the relative permitivities of the liquid phase inside and outside the ion-penetrable layer, respectively.

Since the Reynolds number of the electrokinetic flow in nanofluidics is extremely low (i.e. Re<<1), the flow field at quasi–steady state can be described by the modified Stokes equations:[124-125, 215, 242]

$$-\nabla p + \mu\nabla^2\mathbf{u} - F(z_1c_1 + z_2c_2)\nabla V - \gamma(\mathbf{u} - \mathbf{u}_p) = \mathbf{0}, \text{ inside the ion-penetrable layer} \quad (7.5)$$

$$-\nabla p + \mu\nabla^2\mathbf{u} - F(z_1c_1 + z_2c_2)\nabla V = \mathbf{0}, \text{ outside the ion-penetrable layer} \quad (7.6)$$

and

$$\nabla \cdot \mathbf{u} = 0. \quad (7.7)$$

In the above, p and μ are the hydrodynamic pressure and the dynamic viscosity of the fluid, respectively; γ is the hydrodynamic frictional coefficient of the ion-penetrable layer; $\mathbf{u}_p = U_p\mathbf{e}_z$ is the particle translocation velocity along the axis of the nanopore and $\mathbf{e}_z$ is the unit vector in the z-direction.

To solve the above coupled governing equations, Eq. (7.2)-(7.7), appropriated boundary conditions are required. The ionic concentrations at the ends of the two reservoirs are the bulk ionic concentrations, $c_j = C_{j0}$, j=1 and 2. The particle's rigid core is ion-impermeable. Since the particle is translating with a velocity, U_p, along the axis of the nanopore, the normal ionic flux at the surface of the rigid core includes the convective flux, $\mathbf{n} \cdot \mathbf{N}_j = \mathbf{n} \cdot (\mathbf{u}c_j)$, j=1 and 2, where $\mathbf{n}$ is the unit normal vector directed from the corresponding surface into the fluid.[159] At the ion-penetrable layer/liquid interface of the DNA nanoparticle, the concentration and normal flux of each ionic species are continuous. The normal ionic fluxes on all other boundaries are zero.

For the electric field, the electric potential imposed at the ends of the *cis* and *trans* reservoirs are $V = 0$ and $V = V_0$, respectively. The surface of the particle's rigid core is assumed uncharged, $-\mathbf{n} \cdot (\varepsilon_{f,i} \nabla V) = 0$.[125] The surface charge density on the nanopore wall is specified as $-\mathbf{n} \cdot (\varepsilon_{f,o} \nabla V) = \sigma_w$, and all other boundaries use the insulating boundary condition, $-\mathbf{n} \cdot (\varepsilon_{f,o} \nabla V) = 0$. At the ion-penetrable layer/liquid interface of the DNA nanoparticle, continuous boundary condition for the electric potential and the normal electric field is used.

For the flow field, non-slip boundary condition is imposed on the inner surfaces of the nanopore and the membrane. A normal flow with no external pressure gradient (i.e. p=0) is applied at the ends of the two big reservoirs. Since the side boundaries of the two reservoirs are far away from the nanopore, a symmetric slip boundary condition is specified. Along the ion-penetrable layer/liquid interface of the DNA, continuous flow boundary condition, including the flow velocity and both the normal and the tangential viscous stress tensors, is used.[125] As the DNA translocates along the axis of the nanopore, the fluid velocity on the surface of the particle's rigid core is $\mathbf{u} = U_p \mathbf{e}_z$. Under quasi-steady state, the particle translocation velocity, U_p, will be determined by the condition of zero net force acting on the particle,[65, 124]

$$F_E + F_H = 0, \tag{7.8}$$

where F_E and F_H are, respectively, the z-component electrical and hydrodynamic forces acting on the particle, and they are obtained by the integration of the Maxwell stress tensor,[65, 124] and the hydrodynamic stress tensor,[65, 124-125] over the DNA nanoparticle surface Ω_p, respectively,

$$F_E = \int_{\Omega_p} \varepsilon_0 \varepsilon_{f,o} \left[\frac{\partial V}{\partial r} \frac{\partial V}{\partial z} n_r - \frac{1}{2} \left(\left(\frac{\partial V}{\partial r} \right)^2 + \left(\frac{\partial V}{\partial z} \right)^2 \right) n_z \right] d\Omega_p, \tag{7.9}$$

and

$$F_H = \int_{\Omega_p} \left[\mu \left(\frac{\partial u_r}{\partial z} + \frac{\partial u_z}{\partial r} \right) n_r + n_z \left(-p + 2\mu \frac{\partial u_z}{\partial z} \right) \right] d\Omega_p. \tag{7.10}$$

In the above, n_r and n_z are the r- and z-components of the unit normal vector, $\mathbf{n}$, respectively; and u_r and u_z are, respectively, the r- and z-components of the fluid velocity.

In experiments, one typically measures the ionic current flowing through the nanopore as a function of time during the DNA nanoparticle translocation process. The ionic current is evaluated by

$$I = \int_S F(\sum_{j=1}^{2} z_j \mathbf{N}_j) \cdot \mathbf{n} dS, \tag{7.11}$$

where S denotes either end of the reservoirs due to the ionic current conservation. To measure the effect of the translocating DNA nanoparticle on the ionic current through the nanopore, ionic current deviation is defined as

$$\chi = \frac{I - I_\infty}{I_\infty}, \tag{7.12}$$

where I_∞ is the base ionic current when the DNA nanoparticle is far away from the nanopore. $\chi < 0$ represents a current blockade, while $\chi > 0$ implies a current enhancement during the translocation process. In the following we will present many of our results in the form of the particle translocation velocity and χ as a function of the particle's location (i.e. center of mass), z_p.

The dimensionless form of the above mathematical model can be easily derived using the bulk concentration C_0 as the ionic concentration scale, the radius of the dsDNA nanoparticle a as the length scale, RT/F as the potential scale, $U_0 = \varepsilon_0 \varepsilon_w R^2 T^2 / (\mu a F^2)$ as the velocity scale, and $\mu U_0 / a$ as the pressure scale. ε_w is the relative permittivity of water.

7.3. Results and Discussion

7.3.1 Numerical Method and Code Validation

The strongly coupled non-linear equations and the associated boundary conditions are numerically solved by the commercial finite element package, COMSOL Multiphysics (version 3.5a, www.comsol.com) operating in a high-performance cluster. The computational domain is discretized into quadratic triangular elements. Nonuniform

elements are employed with larger numbers of elements assigned locally as necessary. Typically the total number of elements is approximately 170,000 with finer mesh on the DNA surface to capture the LPE effect as shown in Figure 7.2. Lagrange – Quadratic elements are used for solving PNP equations, while Lagrange – P_2P_1 elements are for the Stokes and Brinkman equations. The ionic current through the nanopore is obtained by using the weak constrain in COMSOL specially developed for an accurate calculation of flux. Rigorous mesh-refinement tests have been performed to ensure that the solutions obtained are convergent and grid independent. A maximum tolerance of 0.1% is imposed on the relative difference $(|I_a| - |I_c|)/|I_a|$, where I_a and I_c are respectively the current entering (anode) and leaving (cathode) the nanopore. The numerical scheme has been validated to be sufficiently efficient and accurate for solving similar electrokinetic problems, such as the electrokinetic ion transport in a solid-state nanopore[14, 109-113] and the electrokinetic rigid and soft nanoparticle translocation through a nanopore.[52, 115-117, 122, 126]

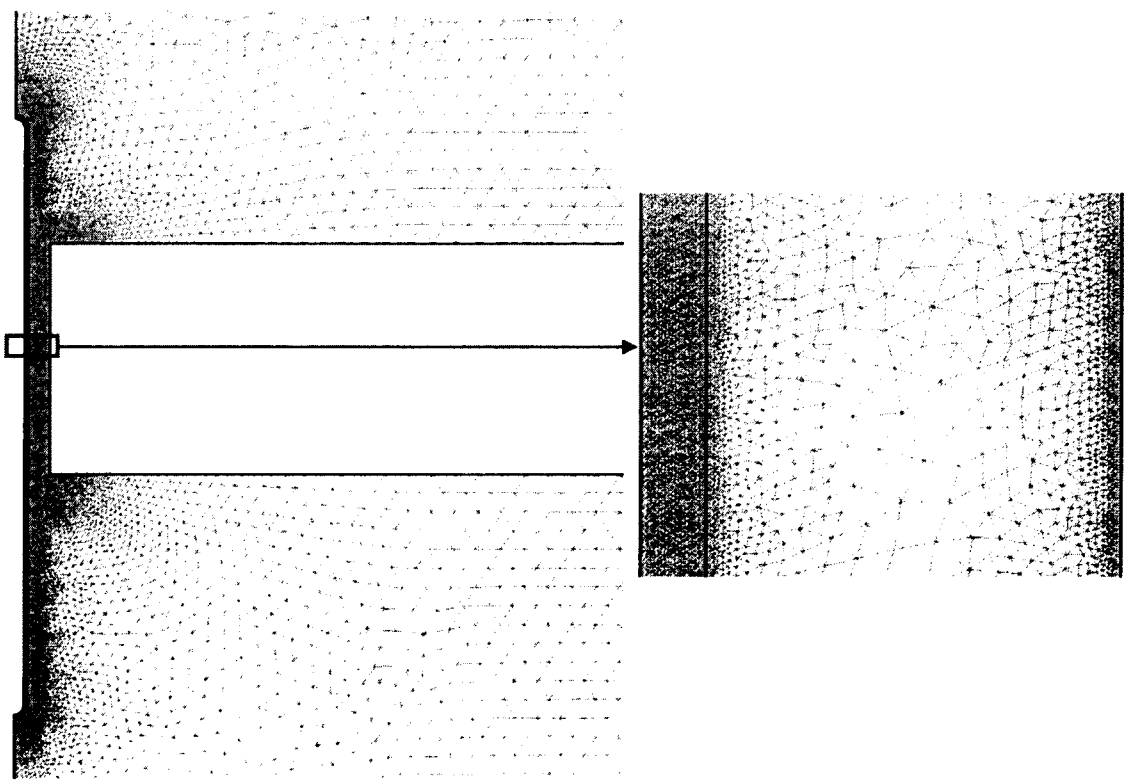

Figure 7.2. The meshes used in the simulation with enlarged finer mesh on the DNA surface.

To further validate our code in the present study, we first simulate electrophoresis of a long, rigid cylindrical particle along the axis of a very long cylindrical pore, whose approximate solution is available under the conditions of assuming the particle's length is much larger than its radius (i.e. $a/L_p<<1$), the nanopore's length is much larger than the particle's length ($L_N/L_p>>1$), relatively low surface potentials on the particle and the pore wall, and weak electric field imposed.[243] To simulate this rigid particle, the ion-penetrable layer is assumed to be uncharged and has a very small frictional coefficient, and the zeta potential on the surface of the particle's rigid core is the thermal potential. Figure 7.3. shows Normalized axial electrophoretic velocity, $u_p^* = U_p / U_{ref}$ with $U_{ref} = \varepsilon_0 \varepsilon_w \zeta_p E / \mu$ being the reference Smoluchowski velocity, of a long cylindrical particle of radius a translating along the axis of an infinitely long, uncharged cylindrical pore of radius b as a function of scaled double layer thickness, κa with $\kappa^{-1} = (\varepsilon_0 \varepsilon_w RT / \sum_{i=1}^{2} F^2 z_i^2 c_0)^{1/2}$ being the Debye length, (a), and as a function of relative permittivity of the aqueous solution $\varepsilon_{f,i} = \varepsilon_{f,o} = \varepsilon_f$ at $\kappa a = 2$, (b), for the case where a/b=0.5, $\zeta_p = RT / F$, and E=20 kV/m. Here the LPE effect is not considered. Our numerical results (circles) are in good agreement with the approximation results (solid line) of Liu et al.[243] expect when κa is small. Double layer polarization (DLP) becomes significant when the double layer is thick, and the DLP effect reduces the particle velocity. The approximate model did not consider the DLP effect. Thus, our result is a little bit lower than the approximate result for κa <1. Figure 7.3 (b) indicates that the particle electrophoretic velocity increases with increasing ${}_f\sum$ and approaches to the result of Liu et al.[243] when ε_f =80 (relative permittivity of water), which also validates our numerical code.

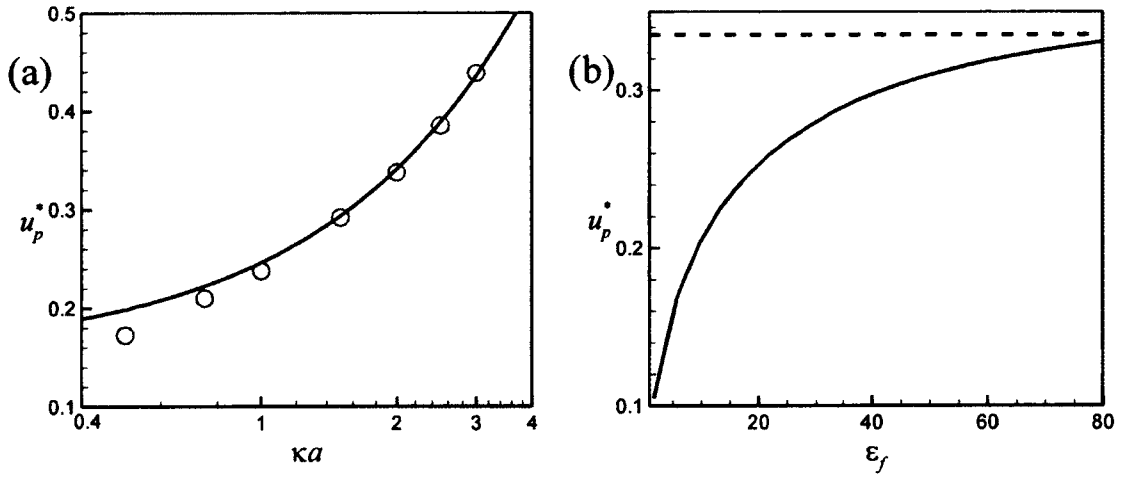

Figure 7.3. Normalized axial electrophoretic velocity, $u_p^* = U_p / U_{ref}$ with $U_{ref} = \varepsilon_0 \varepsilon_w \zeta_p E / \mu$ being the reference Smoluchowski velocity, of a long cylindrical particle of radius a translating along the axis of an infinitely long, uncharged cylindrical pore of radius b (a): as a function of scaled double layer thickness, κa with $\kappa^{-1} = (\varepsilon_0 \varepsilon_w RT / \sum_{i=1}^{2} F^2 z_i^2 c_0)^{1/2}$ being the Debye length; (b): as a function of relative permittivity of the aqueous solution $\varepsilon_{f,i} = \varepsilon_{f,o} = \varepsilon_f$ at $\kappa a = 2$, for the case where a/b=0.5, $\zeta_p = RT / F$, and E=20 kV/m. Solid line: present numerical result; discrete symbols and dashed curve: analytical results of Liu et al.[243]

In this chapter, we assume the radius of the dsDNA nanoparticle is a=1.1 nm[214] and the thickness of its ion-penetrable layer is 0.3 nm, which corresponds to the hydrodynamic diameter of the water molecule.[244] Because one helical pitch of the dsDNA has about 10.5 base pairs (bp)[245] and one bp carries two elementary charges and has a length of 0.334 nm,[246] the fixed charge density of the DNA nanoparticle ρ_{fix} is estimated as -6×10^7 C/m^3 by dividing the bare charge density of $\rho_{fix,b} = -2.53 \times 10^8$ C/m^3 by the Manning factor of 4.2.[216, 247] The bare fixed charge density corresponds to the typical value of the linear charge density on the DNA (c.a. 6 elementary charges/nm). The total length of the DNA nanoparticle L_p is assumed to be 49 nm (c.a.14 helical pitch), which is less than the persistence length of the dsDNA (c.a. 50 nm)[216] to ensure it is a

reasonable approximation by a cylindrical nanorod with two hemispheres on both ends. Since the DNA can be viewed as a highly charged polyelectrolyte, the counterion condensation occurs, resulting in lots of counterions accumulated in the vicinity of the DNA.[216, 240, 247] The counterion condensation effect strongly reduces the activity of the ions near the DNA and accordingly decreases the local liquid permittivity surrounding the DNA,[240, 248] which is referred to as the local permittivity environment (LPE) effect in this chapter. Similarly, counterion condensation also occurs in the vicinity of the charged nanopore wall, inducing LPE effect near the charged nanopore wall. We focus on the LPE effect only arising from the counterion condensation of the DNA, and assume that the LPE effect stemming from the charged nanopore wall is neglected in this chapter. Without considering the LPE effect, the relative permittivity of the liquid within the soft layer and outside of the DNA is a constant, $\varepsilon_{f,i} = \varepsilon_{f,o} = \varepsilon_w = 80$. When the LPE effect arising from the charged DNA is considered, spatially varying relative permittivity is used, $\varepsilon_{f,i} = \varepsilon_i$ and $\varepsilon_{f,o} = \varepsilon_r$. We assume the system is filled with KCl aqueous solution. The physical parameters used in this chapter are summarized in Table 7.1.

7.3.2 Effect of the Bulk Ionic Concentration

Figure 7.4 depicts the normalized translational velocity of the DNA nanoparticle (Figure 7.4a) and the resulting ionic current deviation (Figure 7.4b) as a function of the particle's location, z_p, for various bulk ionic concentrations. Solid lines with symbols represent the results without considering the LPE effect ($\varepsilon_{f,i} = \varepsilon_{f,o} = \varepsilon_w = 80$), while lines without symbols represent the results with the LPE effect ($\varepsilon_{f,i} = \varepsilon_i$ and $\varepsilon_{f,o} = \varepsilon_r$). Since the electric field inside the nanopore is higher than that in the fluid reservoirs, as expected the particle velocity within the nanopore is higher than that inside the fluid reservoirs. This phenomenon is consistent with many theoretical and experimental observations in the literature.[59, 65, 131, 149, 236] Under the other same conditions, the particle velocities with the LPE effect are lower than those without considering the LPE effect. Comparing to the case of without LPE effect, more counterions are confined near the DNA surface in the presence of the LPE effect, resulting in lower effective charge

density, $\rho_e + \rho_{fix}$, accumulated within the soft layer of the DNA particle and accordingly lower particle electrophoretic velocity. It is interesting to note that the maximum particle translational velocity does not occur when the particle is at the center of the nanopore, and the particle velocity peaks at about z_p=±15.6nm, at which the front (rear) end of the DNA nanoparticle reaches the edge of the nanopore at the trans (cis) reservoir. When the particle is completely inside the nanopore, the particle velocity decreases in the range of $-15.6\text{ nm} < z_p < 0$ and increases in the range of $0 < z_p < 15.6\text{ nm}$. Without considering the LPE effect, the first peak particle velocity occurring at about $z_p = -15.6\text{ nm}$ is lower than the second peak particle velocity occurring at $z_p = 15.6\text{ nm}$ when the bulk ionic concentration is relatively low (i.e. C_0 = 10 mM), and the particle velocity is almost symmetric with respect to z_p=0 when the bulk ionic concentration is relatively high (i.e. C_0=100 mM and 1000 mM). However, for the case of considering the LPE effect, the first peak particle velocity is always higher than the second peak particle velocity, and the particle velocity is not symmetric with respect to z_p=0. The asymmetric particle velocity profile can be attributed to the competitive effects of the enhanced local electric field inside the nanopore[57, 86] and the induced concentration polarization (CP), as schematically illustrated in Figure 7.5. The enhancement of the local electric field inside the nanopore arises from the large mismatch of the cross-sectional areas of the fluid reservoirs and the nanopore,[86] resulting in higher particle velocity inside the nanopore. The CP effect is induced by the flow in the gap between the particle and the nanopore wall and DNA-nanopore wall interactions, which include overlapping of the EDLs of the DNA nanoparticle and the charged nanopore wall, and compression of the EDL of the DNA nanoparticle by the nearby (un)charged nanopore wall. The CP effect results in more counterions accumulated near the entrance of the nanopore inside the *cis* reservoir. Figure 7.6 depicts the normalized ionic concentration difference between the cations and the anions, $c_1^* - c_2^* = (c_1 - c_2)/C_0$, when z_p=−15.6 nm (a, d), 0 (b, e), and 15.6 nm (c, f) in the absence (a-c) and presence (d-f) of the LPE effect. As expected, the spatial distribution of the net charge within the liquid, which is proportional to $c_1^* - c_2^*$, varies with the position of the nanoparticle. During the DNA translocation through the nanopore,

the electroosmotic flow (EOF) in the gap between the particle and the nanopore wall, the direction of which is opposite to the particle electrophoretic motion, drives counterions from the nanopore toward the *cis* reservoir, leading to more counterions accumulated near the *cis* reservoir of the nanopore and resulting in a concentration gradient across the nanopore. Figure 7.6 also shows that CP with the LPE effect (Figure 7.6d-f) is more significant than that without considering the LPE effect as shown in Figure 7.6a-c. This is because the LPE effect leads to more counterions confined in the vicinity of the DNA surface, which reduces the electrostatic interaction between the DNA surface and the counterions flowing in the gap between the particle and the nanopore wall toward the *cis* reservoir. Therefore, counterions with the LPE effect are easier to pass through the nanopore toward the rear of the DNA nanoparticle, leading to more significant CP effect than the case without the LPE effect. The induced CP effect generates an electric field, the direction of which is opposite to the externally imposed one, resulting in a decrease in the particle velocity. The local minimum of the particle translocation velocity occurring in the range of $-15.6\,\text{nm} < z_p < 15.6\,\text{nm}$ is mainly attributed to the CP effect. Since the CP effect becomes more significant when the LPE effect is considered, the particle velocity with the LPE effect has a more pronounced local minimum than that without considering the LPE effect, as shown in Figure 7.4a. Without considering the LPE effect, the presence of the two peak particle velocities at z_p=±15.6nm is mainly due to the CP effect, which is more significant when the particle is completely inside the nanopore, since the axial electric field inside the nanopore is almost independent of the particle's location, as shown in Figure 7.7a and b. When the LPE effect is considered, the axial electric field inside the nanopore depends on the particle's location, as shown in Figure 7.7c and d. The average axial electric field inside the nanopore decreases as the particle translocates through the nanopore, which explains why the first peak particle velocity occurring when the particle completely enters the nanopore is higher than the second peak particle velocity when the rear end of the particle exits from the nanopore. In addition, the magnitude of the axial electric field in the presence of the LPE effect is much higher than that without the LPE effect. The significantly enhanced local electric field increases the flow inside the nanopore and accordingly brings more counterions toward the *cis* reservoir near the nanopore, resulting in more significant CP as shown in

Figure 7.6. With the LPE effect, the asymmetric particle velocity profile in the range of $-15.6\,\text{nm} < z_p < 15.6\,\text{nm}$ is due to the combined competitive effects of the enhanced local electric field and the CP effect, as schematically shown in Figure 7.5b. Note that the mechanisms schematically shown in Figure 7.5 highly depend on the Debye length (EDL thickness). CP decreases as the bulk ionic concentration C_0 increases. Therefore, without the LPE effect the particle velocity inside the nanopore is nearly a constant when the bulk concentration is relatively high (i.e. C_0=1000 mM in Figure 7.4a). With the LPE effect, the particle velocity inside the nanopore is not a constant even when the bulk ionic concentration is relatively high, and this is due to the dependence of the axial electric field on the particle position, as shown in Figure 7.7.

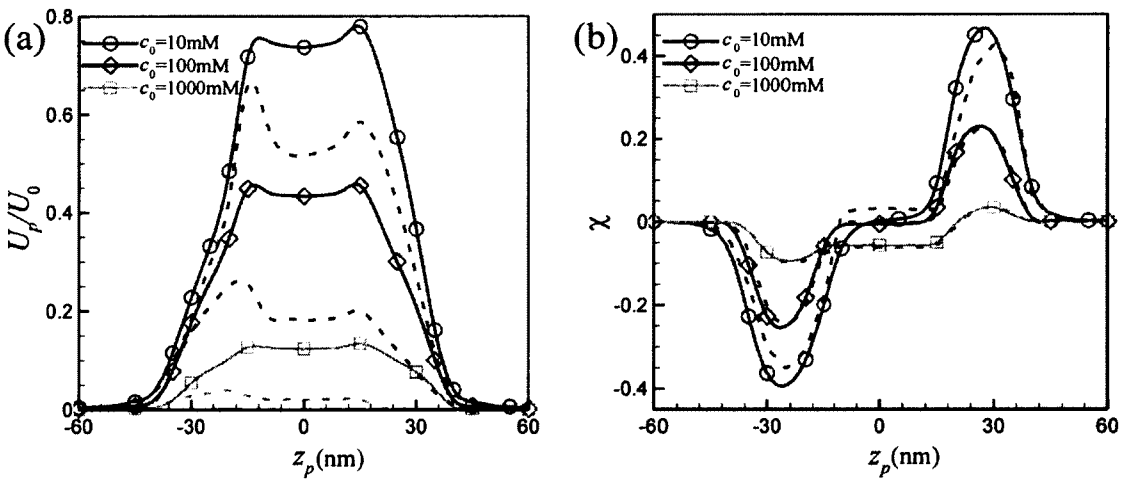

Figure 7.4. Normalized particle translation velocity (a) and ionic current deviation (b) as a function of the particle's location at various bulk ionic concentrations when $\rho_{fix} = -6\times10^7\ \text{C/m}^3$, $\gamma = 1.32\times10^{18}\ \text{kg/sm}^3$, $\sigma_w = 0\ \text{C/m}^2$, and E=2000 kV/m. Solid lines with circles, diamonds, and squares represent the results of $\varepsilon_{f,i} = \varepsilon_{f,o} = \varepsilon_w = 80$ at $c_0 = 10\,\text{mM}$, 100 mM, and 1000 mM, respectively. Dashed, dash-double dotted, and dash-dotted lines represent the results with the LPE effect for $c_0 = 10\,\text{mM}$, 100 mM, and 1000 mM, respectively.

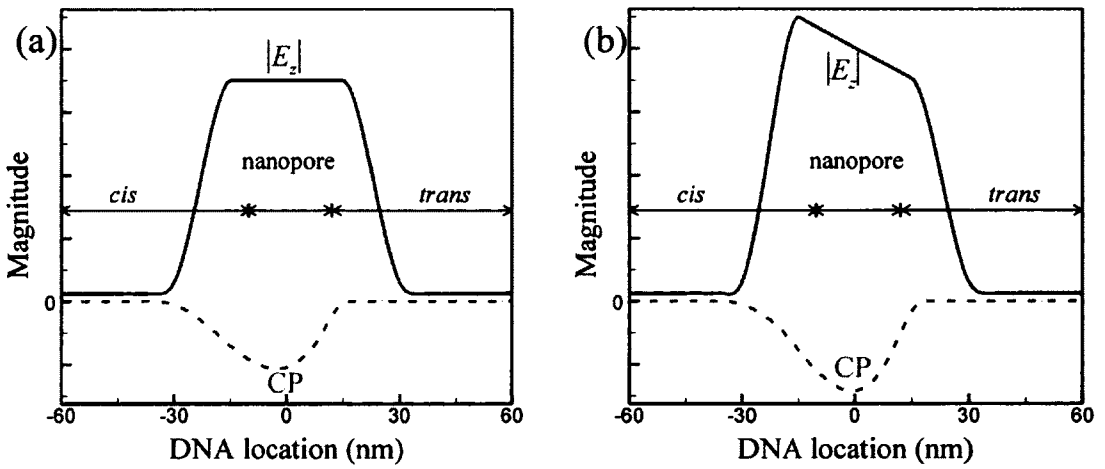

Figure 7.5. Qualitative description of the physical mechanisms of affecting the DNA translocation through a nanopore (not to actual scale). (a) $\varepsilon_{f,i} = \varepsilon_{f,o} = \varepsilon_w = 80$; (b) $\varepsilon_{f,i} = \varepsilon_i$ and $\varepsilon_{f,o} = \varepsilon_r$. $|E_z|$: local enhanced electric field; CP: concentration polarization.

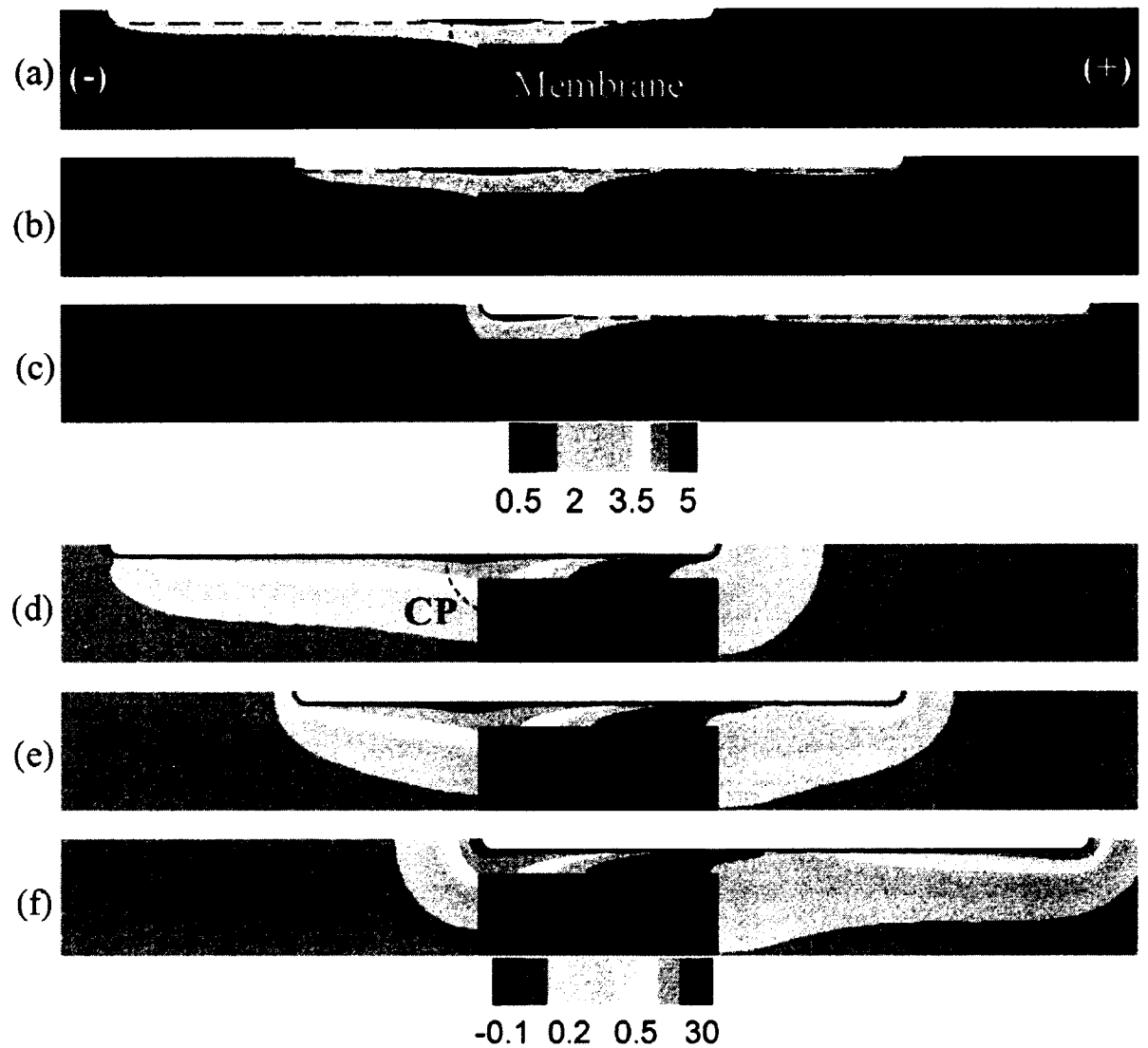

Figure 7.6. Spatial distribution of the normalized net ionic concentration difference, $(c_1 - c_2)/c_0$ at various particle's locations in the absence (a-c) and presence (d-f) of the LPE effect for $c_0 = 10\,\text{mM}$ and (a and d): $z_p = -15.6\,\text{nm}$; (b and e): 0 nm ; (c and f): 15.6 nm .

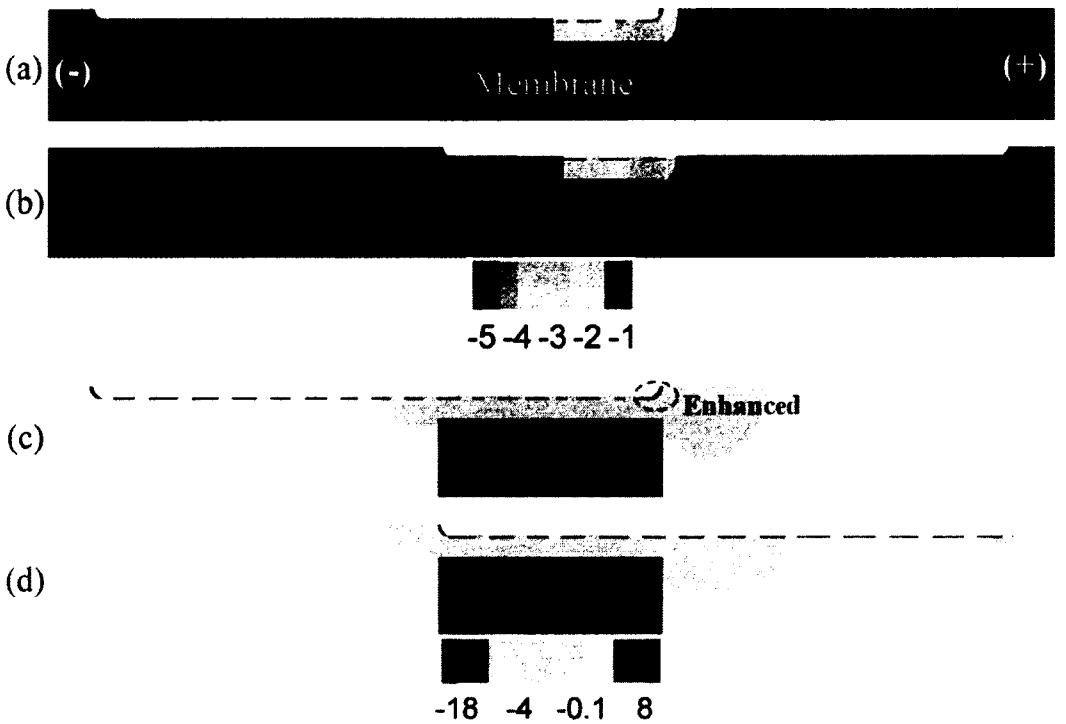

Figure 7.7. Spatial distribution of the normalized local axial electric field, $E_z^* = E_z / E_{ref}$ with $E_z = -dV/dz$ and $E_{ref} = RT/Fa$, at various particle's locations in the absence (a and b) and presence (c and d) of the LPE effect for $c_0 = 10$ mM and (a and c): $z_p = -15.6$ nm ; (b and d): $z_p = 15.6$ nm .

In general, the nanopore-based sensing technique is based on the variation of the ionic current through the nanopore due to the presence of the particle. The influence of the DNA nanoparticle's location on the ionic current deviation through the nanopore is shown in Figure 7.4b. The current deviations in the absences (solid lines with symbols) and presence (lines without symbols) of the LPE effect are almost identical for C_0=100 mM and 1000 mM, and their trends are very similar when C_0=10 mM, implying that the LPE effect on the ionic current deviation is insignificant under the conditions considered. Figure 7.4b also reveals that current blockade is observed as the DNA enters the nanopore, and current enhancement occurs as the DNA starts to exit the nanopore. It is

generally accepted that the former arises from the physical blocking by the DNA nanoparticle, which is consistent with many experimental results in the literature.[20, 33, 41, 142, 231-233] The later was also observed by many groups.[19, 38-40, 45, 56, 149, 214] For example, Chang et al.[214] experimentally studied electrokinetic translocation of a 200-bp dsDNA through a silica nanopore of 2.2 nm in radius and 50 nm in length, and its geometry is very similar to our simulation. They found that if the DNA molecule is about the same length of the nanopore, current enhancement occurs and is attributed to additional counterions (cations) carried by the negatively charged DNA into the nanopore. Liu et al.[149] attributes the current enhancement to the positive diffusive current and this occurs only under the conditions of a thick EDL and a high electric field externally imposed. We find the behavior that current blockade and enhancement during the whole translocation process the competition of the moving gated electric field transistor (FET) concept from the charged DNA, proposed by Chang et al.,[214] and the CP effect aforementioned. The current blockade as the DNA initial enters the nanopore is mainly dominated by the mechanical blocking because much amount of counterions could be retarded accumulated in the *cis* reservoir near the nanopore. Then, the current enhancement appears as the DNA completely enters the nanopore and attains the maximum as the DNA initially leaves the nanopore. This is because with the DNA entering the nanopore the moving FET effect[214] becomes significant while the CP declines with it initial leaving the nanopore.

7.3.3 Effect of the Strength of the Applied Electric Field

Figure 7.8 depicts the translational velocity and the ionic current deviation as a function of the particle's location at various bulk ionic concentrations when the applied electric field is E=20 kV/m, which is 1/100 times of that in Figure 7.4. In order to compare the results for both E=20 kV/m and 20000 kV/m, the y-axis in Figure 7.8a is multiplied by 100. Comparison between Figure 7.4a and 6a reveal that under the same other conditions the particle translocation velocity for E=2000 kV/m is nearly 100 times of that for E=20 kV/m. Without considering the LPE effect, the particle velocity profile for E=20 kV/m is very similar to that for E=2000 kV/m shown in Figure 7.4a. However, with the LPE effect, the particle velocity when the rear end of the particle just exits the nanopore (i.e. $z_p = 15.6\,\text{nm}$) is higher than that when the front end of the DNA just enters the nanopore

($z_p = -15.6$ nm), which is different from the results shown in Figure 7.4a. Figure 7.8a also reveals that the higher the bulk ionic concentration the lower is the particle translocation velocity, which is consistent with the results in Figure 7.4a. However, when the bulk ionic concentration is sufficiently low (i.e. C_0=10 mM) and E=20 kV/m, the particle velocity becomes negative prior to entering the nanopore, implying that the DNA is trapped near the entrance of the nanopore, which has also been found in some experimental results.[249-250] Since the particle could not translocate through the nanopore, we did not plot the results for C_0=10 mM in Figure 7.8. The particle trapping is because the electrophoretic driving force is not high enough to overcome the net effects of the entropic costs of squeezing a coil polyelectrolyte into a narrow pore,[142] and the opposite electroosmotic flow coming from the charged particle.[59, 236]

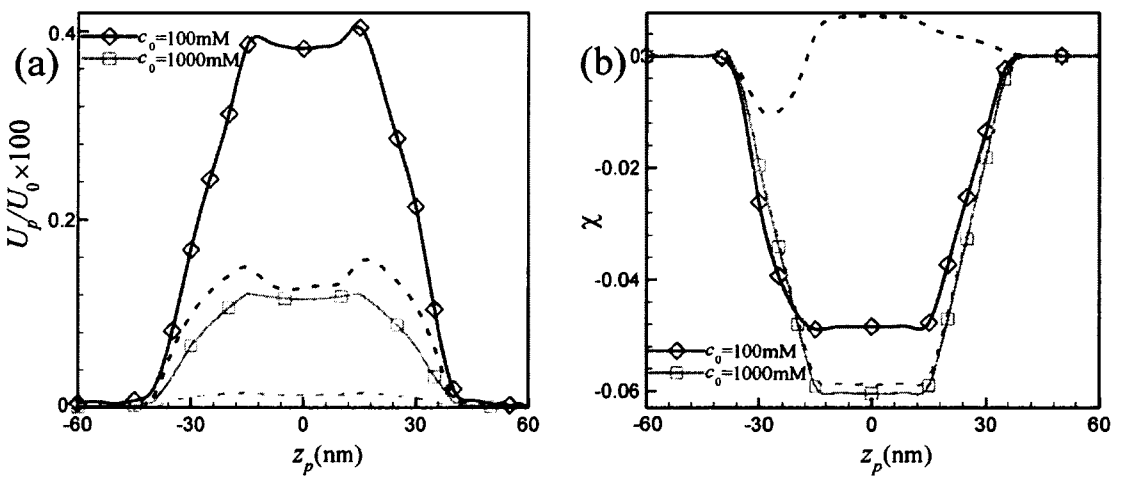

Figure 7.8. Normalized particle translation velocity (a) and ionic current deviation (b) as a function of the particle's location when $\rho_{fix} = -6\times10^7$ C/m^3, $\gamma = 1.32\times10^{18}$ kg/sm^3, $\sigma_w = 0$ C/m^2, and E=20 kV/m. Solid lines with diamonds and squares represent the results without considering the LPE effect at c_0= 100 mM and 1000 mM, respectively. Dash-double dotted and dash-dotted lines represent the results with the LPE effect at c_0= 100 mM and 1000 mM, respectively.

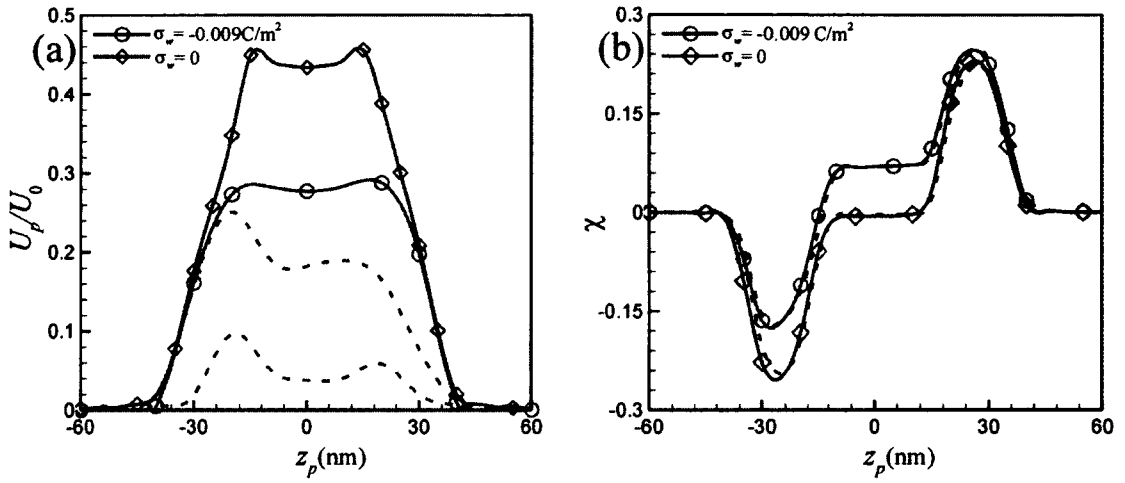

Figure 7.9. The influence of the nanopore surface charge density σ_w on the normalized particle translation velocity (a) and ionic current deviation (b) when $c_0 = 100$ mM, $\rho_{fix} = -6\times10^7$ C/m^3, $\gamma = 1.32\times10^{18}$ kg/sm^3, and E=2000 kV/m. Solid lines with circles and diamonds represent the reference results without the LPE effect at $\sigma_w = -0.009$ C/m^2 and $\sigma_w = 0$ C/m^2, respectively. Dashed and dash-double dotted lines represent the results with the LPE effect at $\sigma_w = -0.009$ C/m^2 and $\sigma_w = 0$ C/m^2, respectively.

Figure 7.8b depicts the ionic current deviation during the particle translocation process when E=20 kV/m. When the bulk ionic concentration is sufficiently high (i.e. 1000 mM), current blockade happens during the entire translocation process for both absence and presence of the LPE effect, and the LPE effect on the current deviation is insignificant. However, for the bulk concentration C_0=10 mM, current blockade is observed when the LPE effect is not considered, while both current blockade and enhancement are found when the LPE effect is taking into account. The current blockade and enhancement behavior at relatively low electric field can be attributed to more counterions, which are accumulated surrounding the DNA surface due to the counterion condensation, are carried into the nanopore.

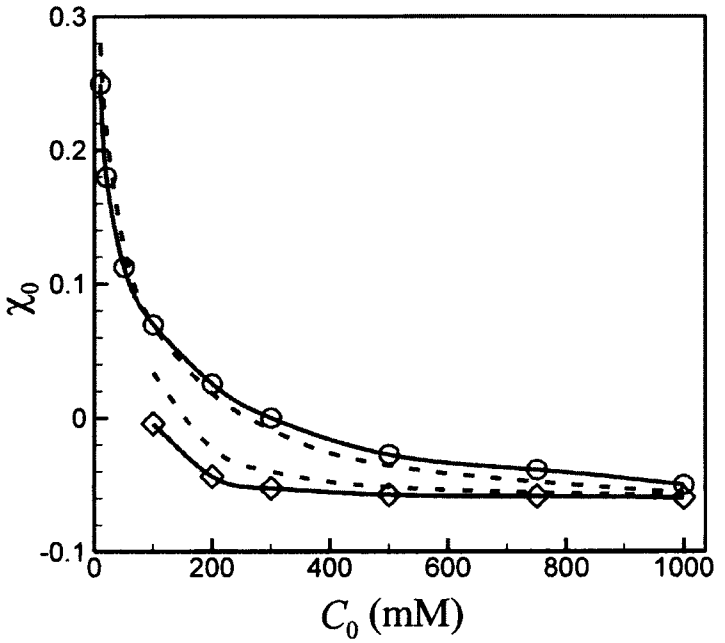

Figure 7.10. The dependence of the relative ionic current due to the DNA translocation in the nanopore on the bulk ionic concentration when $\rho_{fix} = -6 \times 10^7$ C/m^3, $\gamma = 1.32 \times 10^{18}$ kg/sm^3, and $\sigma_w = -0.009$ C/m^2. Solid lines with circles and diamonds represent the reference results without the LPE effect at E=2000 kV/m and E=200 kV/m, respectively. Dashed and dash-double dotted lines represent the results with the LPE effect at E=2000 kV/m and E=200 kV/m, respectively.

7.3.4 Effect of the Surface Charge of the Nanopore

In practical applications, the nanopore wall usually carries a negative surface charge arising from the dissociation of functional groups on it, such as the negatively charged groups, $Si-O^-$, dissociated from the silanol groups on silica nanopore wall. Consequently, an extra electroosmotic flow (EOF) will be induced near the charged nanopore wall, which in turn affects both the ionic current and the particle translocation through the nanopore.[8] Figure 7.9a shows the influence of the nanopore surface charge density, σ_w, on the translational velocity of the DNA. In this case, σ_w is assumed to be –0.009 C/m^2.[149] As expected, the negatively charged nanopore induces an EOF, the direction of which is opposite to that of the DNA electrophoretic motion. Therefore, the

DNA translational velocity for σ_w=–0.009 C/m^2 is lower than that in an uncharged nanopore. The LPE effects in both charged and uncharged nanopores are similar, as shown in Figure 7.9a. We further examine the influence of the nanopore surface charge density on the ionic current deviation, as shown in Figure 7.9b. The same as that in an uncharged nanopore, the LPE effect is not significant in a charged nanopore. Both current blockade and enhancement are observed in both uncharged and charged nanopores. However, the current enhancement phenomenon in a charged nanopore becomes more significant than that in an uncharged nanopore, and this is because there are more counterions in the negatively charged nanopore, yielding an increase in the ionic current. Note that the predicted behaviors of the ionic current are quite consistent with the experiments of sensing single molecule by nanopores,[38] where both current blockade and enhancement behaviors have been observed: the typical phenomenon of the former often appears in high salt concentration, while the later is usually observed under the conditions of relatively low salt concentration.[19, 38, 56, 214]

To further understand the dependence of the salt concentration on the ionic current during the DNA translocation process, we define the relative ionic current due to the DNA translocation in the nanopore, $\chi_0 = (I_0 - I_\infty)/I_\infty$,[56] where I_0 and I_∞ are the ionic current in the presence and absence of the DNA in the nanopore, respectively (i.e. $z_p = 0$ and $z_p = -60$ nm). Figure 7.10 shows the influence of the applied electric field on the relative ionic current. Here, we only present the results of E=200 (blue lines) and 2000 kV/m (red lines). This is because the nanopore considered here is charged, if the electric field imposed is too weak and/or the bulk salt concentration is too low, the particle does not pass through the nanopore. Not that at E=200 kV/m, the particle will be trapped before entering the nanopore when $C_0 < 100$ mM. Figure 7.10 indicates that when the applied electric field is large, the relative ionic current is very similar in the absence and presence of the LPE effect: the current enhancement occurs when the salt concentration is relatively low and the current blockade when it is relatively high, which is qualitatively agrees well with the experimental observation.[38] However, when the applied electric field is low, both the current blockade and enhancement are observed when the LPE effect is considered, while only the current blockade is observed when the LPE effect is not

considered. The former is qualitatively consistent with the theoretical result of the higher electric field and the experimental observation,[38] but the later is not. It can be pointed out that the LPE effect considered here is very important in the DNA translocation through the nanopore, especially when the electric field imposed is relatively weak.

7.4. Conclusions

In summary, we have theoretically investigated for the first time the influence of the liquid permittivity distribution, namely, both constant and spatially varying permittivities surrounding the DNA nanoparticle, on the DNA translocation through a nanopore. Instead of the typical assumption in the former, the later is a more realistic one, referred to as the local permittivity environment (LPE) effect, because if counterion condensation and/or the strong hydrogen bonding interactions in the vicinity of a DNA molecule. We propose two important mechanisms, local enhanced electric field and concentration polarization acting on the DNA translocation process, to explain why the DNA translocation velocity profile is distinctly different for these two models. In addition, we have found that the LPE effect in general has a significant effect reducing the particle translocation velocity; however, it on the ionic current deviation becomes insignificant when the applied electric field is relatively strong. When the applied electric field is relatively weak, both the current blockade and enhancement are predicted at lower bulk salt concentration and with considering the LPE effect, while only the current blockade is found on the other conditions. Taking the LPE effect into account, we stress that the salt concentration dependence of the ionic current phenomena is more qualitatively consistent with the experiment observations in the literature.

Table 7.1. The values or range of the parameters used in this chapter.

Parameters	**value or range**
a (*DNA radius*)	1.1 (nm)
L_p (*DNA length*)	49 (nm)
R_N (*nanopore radius*)	3 (nm)
L_N (*nanopore length*)	20 (nm)
R_R (*reservoir radius*)	260 (nm)
L_R (*reservoir length*)	250 (nm)
d (*thickness of ion-penetrable layer of DNA*)	0.3 (nm)
ε_w (*relative permittivity of water*)	80
ε_i (*relative permittivity of liquid on DNA surface*)	1.76
ε_0 (*vacuum permittivity*)	8.854×10^{-12} (C/Vm)
μ (*dynamic viscosity*)	0.001(kg/sm)
ρ (*fluid density*)	1000 (kg/m^3)
F (*Faraday constant*)	96490 (C/ mol)
c_0 (*bulk ionic concentration*)	10~1000 (mM)
γ (*friction coefficient of ion-penetrable layer*)	1.32×10^{18} (kg/sm^3)
ρ_{fix} (*fixed charge density of ion-penetrable layer*)	-6×10^{7} (C/m^3)
D_1 (*diffusion coefficient of cations*)	1.957×10^{-9} (m^2/s)
D_2 (*diffusion coefficient of anions*)	2.032×10^{-9} (m^2/s)
T (*absolute temperature*)	300 (K)
R (*universal gas constant*)	8.31(1/mol K)
E (*strength of applied electric field*)	20 or 2000(kV/m)
σ_w (*charge density on nanopore wall*)	0 or -0.009 (C/m^2)

CHAPTER 8

REGULATING TRANSLOCATION OF A SOFT CHARGE-REGULATED NANOPARTICLE THROUGH FUNCTIONALIZED SOFT NANOPORES

Abstract

Many existing investigations revealed that the surface charge density of a soft biocolloidal nanoparticle varies with the pH and background salt concentration. However, the existing studies on electrokinetic translocation of a soft biocolloidal nanoparticle through a nanopore used a pre-specified, constant fixed surface charge density, regardless of the pH and salt concentration. This study investigated translocation of a charge-regulated soft biocolloidal nanoparticle such as protein through a polyelectrolyte-modified nanopore and considered charge regulation for the first time. We focused on the effects of two main factors, pH and background salt concentration, on the nanoparticle surface charge density, translocation speed, and the resulting ionic current during the translocation process. The nanoparticle translocation velocity increases with increasing pH and background ionic strength. The resulting current signal also highly depends on pH and ionic strength. Current blockade (enhancement) occurs at relatively low (high) salt concentration. As pH increases, the magnitude of the resulting current deviation increases.

8.1. Introduction

Recently, nanopore is emerging as a promising single-molecule sensor for the detection and characterization of biocolloidal nanoparticles such as proteins and DNAs. [21, 209,20, 29, 141-142] A DC voltage bias is imposed across a nanopore merged in an aqueous electrolyte solution, as schematically shown in Figure 8.1. The imposed electric field generates an ionic current flowing through the nanopore, which can be measured using the electrophysiological techniques. In addition, biocolloidal nanoparticles become charged when they are in contact with an aqueous solution, and their charges depend on the electrolyte solution properties such as pH and ionic strength. In response to the

imposed electric field, negatively charged biocolloidal nanoparticles electrophoretically translocate from the cathode reservoir through the nanopore towards the anode reservoir. Since the current flowing through the nanopore is very sensitive to the size and shape of the nanopore, the ionic current is reduced, referred to as current blockade, when the nanoparticle is inside the nanopore due to the displacement of the electrolyte by the nanoparticle, and returns to the baseline current after the particle exits the nanopore. The nanopore-based biosensors characterize the electrophoretic translocating nanoparticle based on the ionic current change during the nanoparticle translocation process.[40, 214]

Although nanopore-based biosensors have a promising future, most study and research conducted are still at the proof-of-principle stage and many technology related challenges must be resolved before it can be successfully implemented. Two primary challenges include reducing the capture time of the nanopore to increase the through-put and increasing the translocation time within the nanopore to enhance signal read-out accuracy. The capture time or rate of the nanopore depends on the particle motion from the reservoir towards the nanopore entrance, while the translocation time depends on the particle electrokinetic motion inside the nanopore. Chapter 4 proposed to slow down nanoparticle translocation and simultaneously enhance capture rate by using polyelectrolyte-modified nanopores. That study as well as other previous studies[124, 251-256] assumed that the surface charge density of the translocating biocolloidal nanoparticle is uniformly distributed and remains a constant, which is independent of the solution properties including pH and ionic strength. However, the charge of biopolymers is governed by the dissociation/association of the ionizable functional groups, [152] and the surface reactions highly depend on pH and salt concentration. In other words, the biopolymers of the biocolloidal nanopoarticles are charge-regulated, and their charges depend on pH and salt concentration. Very recently, Hsu and Tai,[257] and Hsu et al.[147] studied electrophoresis of a spherical charge-regulated polyelectrolyte in an infinite cylindrical pore, and found that the charge of the polyelectrolyte is spatially dependent and can be regulated by pH and background salt concentration.

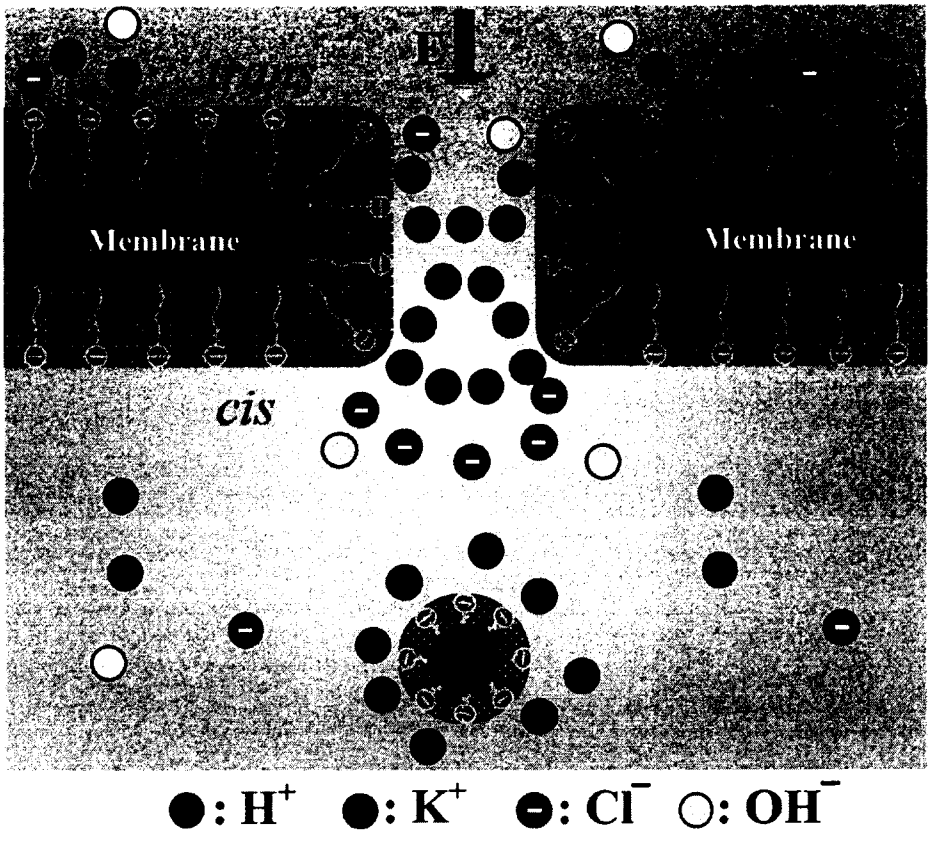

Figure 8.1. Schematic view a soft charge-regulated nanoparticle translocation through a soft nanopore.

In this chapter, electric-field induced translocation of a biocolloidal particle through a polyelectrolyte-modified nanopore is numerically studied using a continuum-based model, which is comprised of the Poisson-Nernst-Planck (PNP) equations for the ionic transport, the modified Stokes equations for the fluid flow outside the polyelectrolyte layers, the modified Brinkman equations for the flow field inside the polyelectrode layers, and the charge regulation model for the charge of the biopolymers on the nanoparticle. In the current study, we only considered charge regulation on the biopolymers of the nanoparticle, and assumed that the polyelectrolytes on the nanopore are highly charged and are not charge regulated. We comprehensively investigated the nanoparticle translocation speed and the resulting ionic current signal as functions of pH, background concentration, and the friction coefficient of the polyelectrode grafted on the nanopore.

8.2. Mathematic Model

We consider a cylindrical soft nanopore of length L_N and radius R_N connected two large, identical fluid reservoirs (referred to as *cis* and *trans* reservoirs, respectively) filled with an electrolyte solution containing N types of ionic species, as schematically shown in Figure 8.1. The soft nanopore contains a functionalized soft layer of thickness L_S on the wall of the membrane. For simplicity, we assume that the soft layer is ion-penetrable, homogeneously structured, and bears dissociable functional groups, yielding a uniform fixed charge density $\rho_{fix,w}$. The axial length, L_R, and radius, R_R, of the reservoirs are large enough so that the concentration of each ionic species at places far away from the nanopore maintains its bulk ionic concentration, C_{j0} (j=1,..., N). A charge-regulated spherical soft nanoparticle is initially positioned inside the *cis* reservoir as shown in Figure 8.1. The soft nanoparticle contains an uncharged spherical rigid inner core of radius a-d, covered by an ion-penetrable soft layer of uniform thickness d. The ion-penetrable soft layer on the soft particle is homogeneously structured, and bears a charge density, $\rho_{fix,p}$, and an extra friction force acting on the liquid flowing inside.[125] We further assume that the nanoparticle is initially placed with its axis coinciding with the cylindrical nanopore's axis so that a two dimensional axial symmetric geometry can be used to describe all variables in the present study. The origin of the cylindrical coordinate (r, z) is fixed at the center of the nanopore. A potential bias V_0 is applied between two electrodes positioned far away from the nanopore inside the two fluid reservoirs, resulting in a negative axial electric field, **E**, to electrophoretically drive the negatively charged nanoparticle from the *cis* reservoir along the axis of the nanopore toward the *trans* reservoir and simultaneously generate a detectable ionic current through the nanopore.

In this chapter, we adopt the verified continuum-based model, composed of the PNP equations for the ionic mass transport, the modified Stokes equations for the hydrodynamic field outside of the soft layers, and the modified Brinkman equations for the flow field inside the soft layers,[124-125, 215, 242] to describe electrokinetic translocation of

a charge-regulated soft particle through a soft nanopore. The ionic mass transport in the electrolyte solution is governed by the PNP equations:[65, 124]

$$-\nabla^2 V = \frac{\rho_e}{\varepsilon_f} + \rho_{fix,\mathrm{w}}, \text{ inside the ion-penetrable layer of the soft nanopore} \tag{8.1}$$

$$-\nabla^2 V = \frac{\rho_e}{\varepsilon_f} + \rho_{fix,\mathrm{p}}, \text{ inside the ion-penetrable layer of the soft nanoparticle} \tag{8.2}$$

$$-\nabla^2 V = \frac{\rho_e}{\varepsilon_f}, \text{ outside the ion-penetrable layers} \tag{8.3}$$

$$\nabla \cdot \mathbf{N}_j = \nabla \cdot \left(\mathbf{u}c_j - D_j \nabla c_j - z_j \frac{D_j}{RT} F c_j \nabla V \right) = 0. \tag{8.4}$$

In the above, V is the electric potential; $\mathbf{u} = u\mathbf{e}_r + v\mathbf{e}_z$ is the fluid velocity with $\mathbf{e}_r$ and $\mathbf{e}_z$ being, respectively, the unit vectors in the r- and z-directions; $\rho_e = \sum_{j=1}^{N} F z_j c_j$ is the space charge density of mobile ions; $\mathbf{N}_j$, c_j, D_j, and z_j are the flux density, concentration, diffusivity, and valence of the j^{th} ionic species, respectively; ε_f, F, R, and T are the fluid permittivity, the Faraday constant, the universal gas constant, and the absolute temperature, respectively. Note that the first, second, and third terms on the right-hand side of Eq. (8.4) denote contributions from the convective, diffusive, and migrative fluxes, respectively.

In this chapter, we only consider charge regulation on the soft layer of the nanoparticle, and neglect charge regulation on the soft layer of the nanopore. The soft layer of the nanoparticle contains both dissociable acidic and basic functional groups, AH and BH^+, respectively. Suppose that the following dissociation/association reactions occur:

$$\mathrm{AH} \leftrightarrow \mathrm{A}^- + \mathrm{H}^+, \tag{8.5}$$

$$\mathrm{BH}^+ \leftrightarrow \mathrm{B} + \mathrm{H}^+. \tag{8.6}$$

If we let K_A and K_B be the corresponding equilibrium constants, $K_\mathrm{A} = [\mathrm{A}^-][\mathrm{H}^+]/[\mathrm{AH}]$ and $K_\mathrm{B} = [\mathrm{B}][\mathrm{H}^+]/[\mathrm{BH}^+]$, where a symbol with square brackets denotes the molar concentration of that symbol. Let N_A and N_B be the total concentration of the acidic and basic functional groups, respectively, that is, $N_\mathrm{A} = [\mathrm{A}^-] + [\mathrm{AH}]$ and $N_\mathrm{B} = [\mathrm{B}] + [\mathrm{BH}^+]$.

Due to the reactions expressed in Eq. (8.5) and (8.6), the ion-penetrable layer of the soft particle bears charge of density $\rho_{fix,p}$. Therefore, it can be shown that

$$\rho_{fix,p} = -1000F\left(\left[A^-\right]-\left[BH^+\right]\right) = -1000F\left[\frac{N_A}{1+\frac{\left[H^+\right]}{K_A}} - \frac{N_B\frac{\left[H^+\right]}{K_B}}{1+\frac{\left[H^+\right]}{K_B}}\right]. \tag{8.7}$$

Since the Reynolds number of the electrokinetic flow in nanopores is extremely small (i.e. Re<<1), the steady-state flow field can be described by the continuity and the modified Stokes and Brinkman equations:[52, 149]

$$\nabla\cdot\mathbf{u} = 0, \tag{8.8}$$

$$-\nabla p + \mu\nabla^2\mathbf{u} - \rho_e\nabla V - \gamma_w\mathbf{u} = \mathbf{0}, \text{ inside the ion-penetrable layer of the soft nanopore} \tag{8.9}$$

$$-\nabla p + \mu\nabla^2\mathbf{u} - \rho_e\nabla V - \gamma_p(\mathbf{u}-\mathbf{u}_p) = \mathbf{0}, \text{ inside the soft layer of the soft nanoparticle} \tag{8.10}$$

$$-\nabla p + \mu\nabla^2\mathbf{u} - \rho_e\nabla V = \mathbf{0}, \text{ outside the ion-penetrable soft layers.} \tag{8.11}$$

In the above, p and μ are the hydrodynamic pressure and the fluid viscosity, respectively; γ_w and γ_p are the hydrodynamic frictional coefficient of the ion-penetrable layers of the nanopore and the nanoparticle, respectively; $\mathbf{u_p} = u_p\mathbf{e_z}$ is the particle translation velocity along the axis of the nanopore and $\mathbf{e_z}$ is the unit vector in the z-direction. We define the softness degree of the ion-penetrable layer of the soft nanopore and nanoparticle as $\lambda_w^{-1} = \sqrt{\mu/\gamma_w}$ and $\lambda_p^{-1} = \sqrt{\mu/\gamma_p}$, respectively.

To solve the above coupled governing Eq. (8.1)-(8.11), appropriated boundary conditions are required. We assume that the ionic concentrations at the ends of the two reservoirs are maintained at their bulk values, $c_j = C_{j0}$. The particle's rigid core is ion-impermeable. Since the particle is translating with a velocity, u_p, along the axis of the nanopore, the normal ionic flux at the surface of the rigid core includes the convective flux, $\mathbf{n}\cdot\mathbf{N}_j = \mathbf{n}\cdot(\mathbf{u}c_j)$, where $\mathbf{n}$ is the unit normal vector directed from the corresponding surface into the fluid.[159] At the ion-penetrable layer/liquid interfaces of the nanoparticle and the membrane, the concentration and normal flux of each ionic species are continuous. The normal ionic fluxes on all other boundaries are zero.

For the electric field, the electric potential imposed at the ends of the cis and trans reservoirs are $V = 0$ and $V = V_0$, respectively. The surface of the particle's rigid core is assumed uncharged, $-\mathbf{n} \cdot \nabla V = 0$. The surface charge density on the membrane rigid wall is zero, $-\mathbf{n} \cdot \nabla V = 0$, and all other boundaries have the insulating boundary condition, $-\mathbf{n} \cdot \nabla V = 0$. At the ion-penetrable layer/liquid interfaces of the nanoparticle and membrane, continuous boundary condition for the electric potential and the normal electric field are used.

For the flow field, non-slip boundary condition is imposed on the inner surfaces of the membrane and the nanoparticle. A normal flow with no external pressure gradient (i.e. p=0) is applied at the ends of the two big reservoirs. Since the side boundaries of the two reservoirs are far away from the nanopore, a symmetric slip boundary condition is specified. Along the ion-penetrable layer/liquid interfaces of the nanoparticle and membrane, continuous flow boundary condition, including the flow velocity and both the normal and the tangential viscous stress tensors, is used.[125] As the nanoparticle translates along the axis of the nanopore, the fluid velocity on the surface of the particle's rigid core is $\mathbf{u}_p = u_p \mathbf{e}_z$. Under quasi-steady state, the particle translation velocity, u_p, will be determined by the condition of zero net force acting on the particle,[65, 124]

$$F_E + F_H = 0, \tag{8.12}$$

where F_E and F_H are, respectively, the z-component electrical and hydrodynamic forces acting on the particle. F_E and F_H can be obtained by the integration of the Maxwell stress tensor,[65, 124] and the hydrodynamic stress tensor,[65, 124-125] respectively, over the outer surface of the soft nanoparticle Ω_p,

$$F_E = \int_{\Omega_p} \varepsilon_f \left[\frac{\partial V}{\partial r} \frac{\partial V}{\partial z} n_r + \frac{1}{2} \left[\left(\frac{\partial V}{\partial z} \right)^2 - \left(\frac{\partial V}{\partial r} \right)^2 \right] n_z \right] d\Omega_p, \tag{8.13}$$

and

$$F_H = \int_{\Omega_p} \left[\mu \left(\frac{\partial u_r}{\partial z} + \frac{\partial u_z}{\partial r} \right) n_r + n_z \left(-p + 2\mu \frac{\partial u_z}{\partial z} \right) \right] d\Omega_p. \tag{8.14}$$

In the above, n_r and n_z are the r- and z-components of the unit normal vector, $\mathbf{n}$, respectively; and u_r and u_z are, respectively, the r- and z-components of the fluid velocity.

In experiments, one typically measures the ionic current flowing through the nanopore as a function of time during the nanoparticle translocation process. The ionic current is evaluated by

$$I = \int_S F(\sum_{j=1}^{N} z_j \mathbf{N}_j) \cdot \mathbf{n} dS, \tag{8.15}$$

where S denotes either end of the reservoirs due to the ionic current conservation. To measure the effect of the translocating nanoparticle on the ionic current through the nanopore, ionic current deviation is defined as

$$\chi = \frac{I - I_\infty}{I_\infty}, \tag{8.16}$$

where I_∞ is the base ionic current when the nanoparticle is far away from the nanopore. $\chi < 0$ represents a current blockade, while $\chi > 0$ implies a current enhancement during the translocation process. In the following we will present our results in the form of the particle translocation velocity and χ as a function of the particle's location (i.e. center of mass), z_p.

8.3. Results and Discussion

8.3.1 Numerical Method and Code Validation

The strongly coupled non-linear equations and the associated boundary conditions are numerically solved by the commercial finite element package, COMSOL Multiphysics (version 3.5a, www.comsol.com) operating in a high-performance cluster. The computational domain is discretized into quadratic triangular elements. Nonuniform elements are employed with larger numbers of elements assigned locally as necessary. Typically the total number of elements is approximately 120,000 with finer mesh in the PE layer to capture the EDL. Lagrange – Quadratic elements are used for solving PNP equations, while Lagrange – P_2P_1 elements are for the Stokes and Brinkman equations. The ionic current through the nanopore is obtained by using the weak constrain in

COMSOL specially developed for an accurate calculation of flux. Rigorous mesh-refinement tests have been performed to ensure that the solutions obtained are convergent and grid independent. A maximum tolerance of 0.1% is imposed on the relative difference ($|I_a|$ - $|I_c|$)/$|I_a|$, where I_a and I_c are respectively the current entering (anode) and leaving (cathode) the nanopore. The numerical scheme has been validated to be sufficiently efficient and accurate for solving similar electrokinetic problems, such as the electrokinetic ion transport in a solid-state nanopore[14, 109-113] and the electrokinetic rigid and soft nanoparticle translocation through a nanopore.[52, 115-117, 122, 126]

We assume that the background electrolyte is made of KCl with concentration C_{KCl}, and the solution's pH is adjusted by KOH and HCl. Therefore, four major ionic species (i.e., N=4), H^+, K^+, Cl^-, and OH^-, are considered, and their bulk concentrations are, respectively, C_{10}, C_{20}, C_{30}, and C_{40} (in the unit of mM). Due to electroneutrality, the bulk concentrations are $C_{10}=10^{(-pH+3)}$, $C_{20}=C_{KCl}$, $C_{30}=C_{KCl}+10^{(-pH+3)}-10^{-(pK_w-pH)+3}$, and $C_{40}=10^{-(pK_w-pH)+3}$ if $pH \le pK_w/2$; and $C_{10}=10^{-pH+3}$, $C_{20}=C_{KCl}-10^{-pH+3}+10^{-(pK_w-pH)+3}$, $C_{30}=C_{KCl}$, and $C_{40}=10^{-(pK_w-pH)+3}$ if $pH > pK_w/2$.[147-148] Here, $pH=-\log([H^+]_0)=-\log(C_{10}/1000)$ and $pK_w=-\log(K_w)=14$ with $[H^+]_0$ and K_w being the bulk molar concentration of H^+ ions (in the unit of M) and the dissociation constant of water, respectively. The physical parameters used in the present study are summarized in Table 8.1. Unless otherwise specified, physical parameters are fixed at the values listed in Table 8.1.

To validate the applicability of the present numerical model, we compared our numerical results of the electrophoretic mobility of a soft nanoparticle in a uncharged solid-state nanopore with the corresponding approximate solution: [187]

$$\frac{u_p^*}{E^*}=\frac{\overline{Q}}{(\lambda a)^2}\left[1+\frac{2}{3}\left(\frac{\lambda}{\kappa}\right)^2\left(\frac{1+\lambda/2\kappa}{1+\lambda/\kappa}\right)\left(1+\frac{a^3}{2(a+d)^3}\right)\right], \tag{8.17}$$

where $E^*=EFa/RT$, $u_p^*=u_p\,\mu aF^2/\varepsilon_f R^2T^2$ and $\overline{Q}=\overline{\rho}_{fix,p}a^2F/(\varepsilon RT)$ represent the dimensionless electric field, particle velocity of the nanoparticle, and the average fixed

charge inside the soft layer of the nanoparticle, respectively. $\kappa^{-1} = \left(\varepsilon_f RT \Big/ F^2 \sum_{i=1}^{N} z_j^2 C_{j0} \right)^{\frac{1}{2}}$ denotes the Debye length. The average fixed charge is defined as $\overline{\rho}_{fix,p} = \int_{\Gamma} \rho_{fix,p} d\Gamma \Big/ \Gamma$, where Γ is the volume of the ion-penetrable layer of the nanoparticle. Figure 8.2b depicts the dimensionless electrophoretic mobility as a function of κa when $\lambda_p a = 8.7$, $d/a = 1$, and $R_N/a = 20$. The solid line and circles represent the approximation solution from Ohshima using corresponding $\overline{Q}$ in Figure 8.2a and the numerical results in present work. Our numerical results (circles) are in good agreement with the approximation solution (solid line).

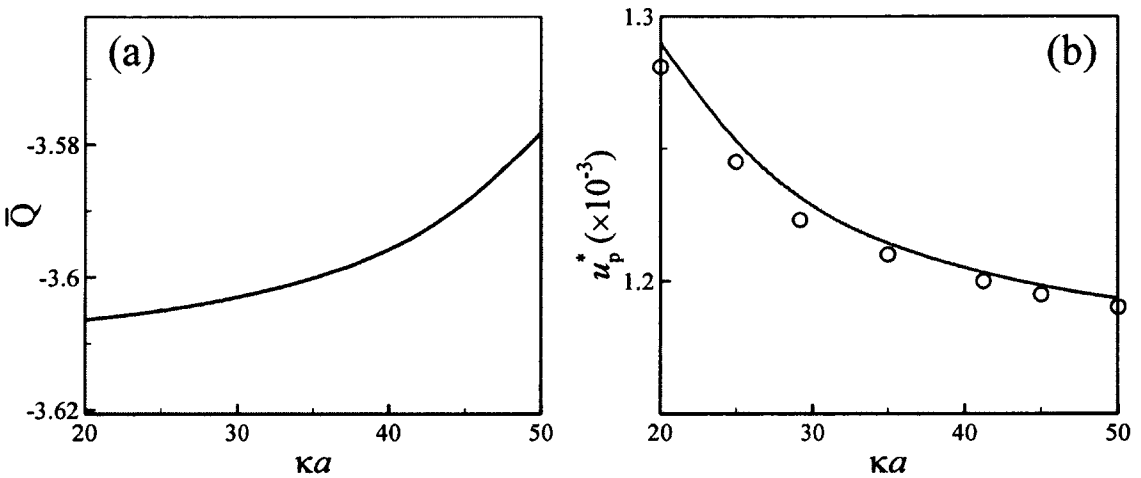

Figure 8.2. Normalized volume-averaged charged density of the ion-penetrable layer of the soft nanoparticle (a) and its normalized particle mobility (b) as a function of κa when $\lambda_p a = 8.7$, $d/a = 1$, and $R_N/a = 20$. Circles and line in Fig.8.2b represent, respectively, the present numerical results and approximation solution from Ohshima. [187]

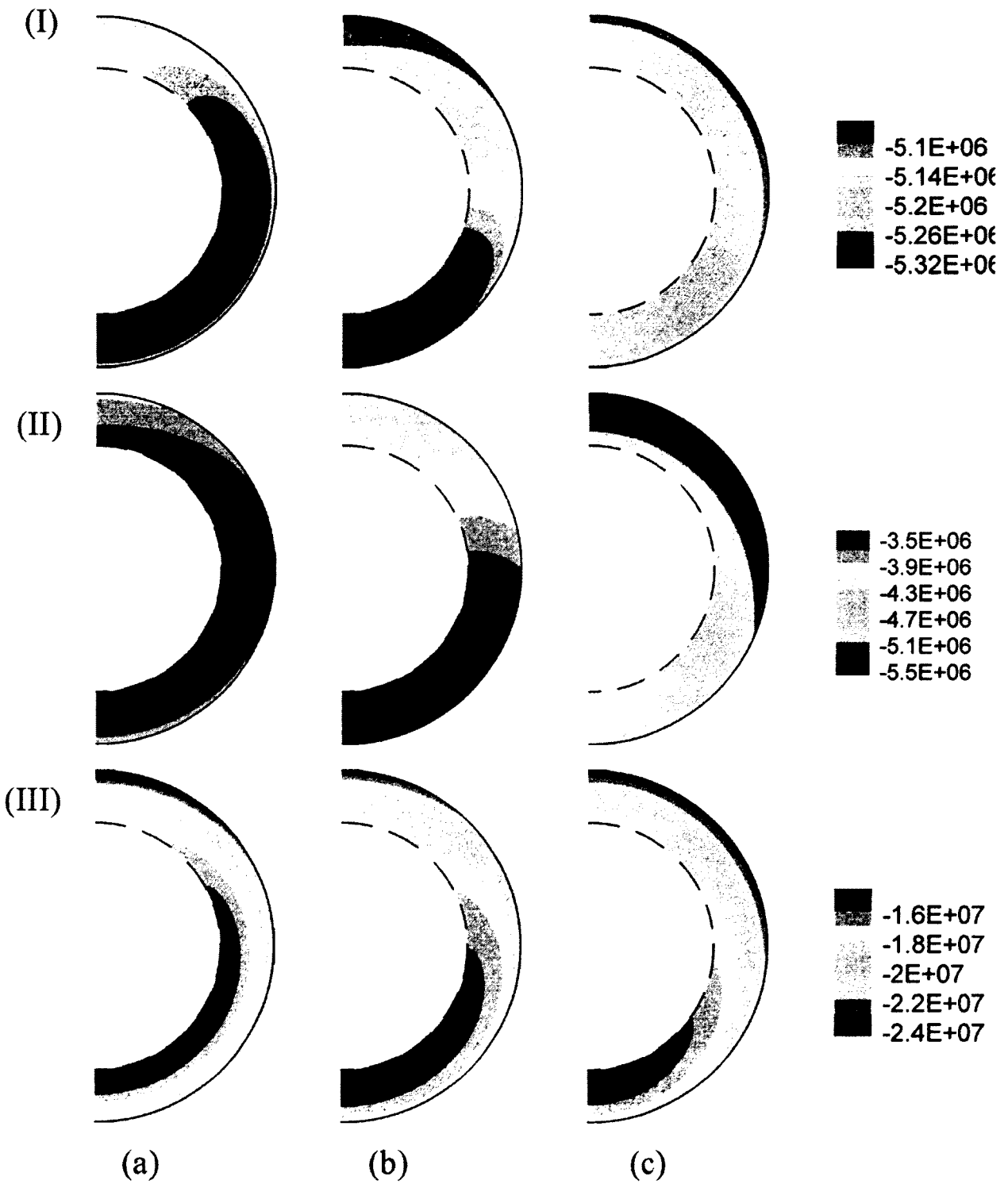

Figure 8.3. Spatial distribution of charge density inside the soft layer of the nanoparticle located at (a): z_p = -15 nm; (b): 0 nm; (c): 15 nm when λ_w^{-1} = 0.3 nm. (I): CKCl = 100 mM and pH=7.5; (II): C_{KCl} = 50 mM and pH=7.5; (III): C_{KCl} = 50 mM and pH=8.5.

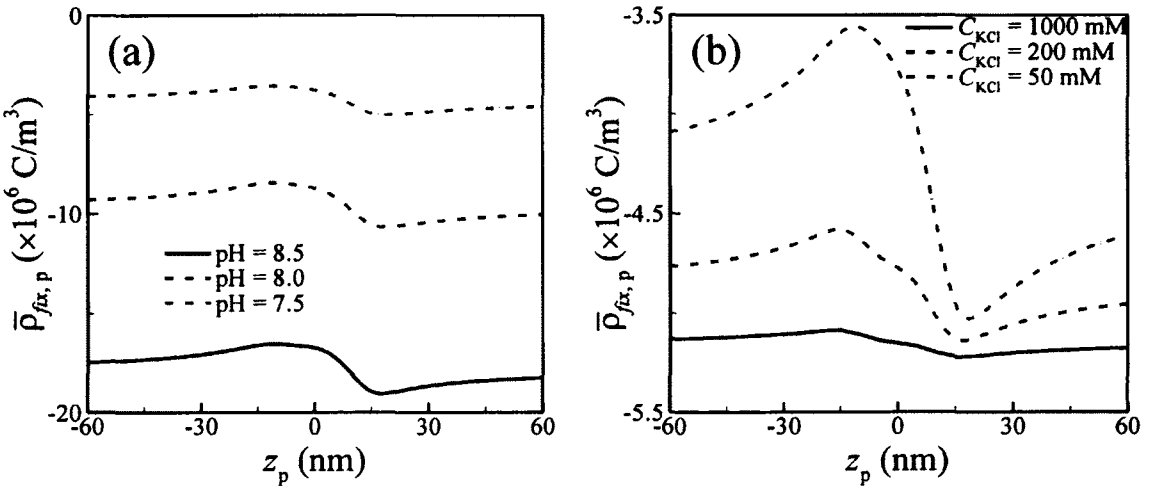

Figure 8.4. Volume-averaged charge in the soft layer of the nanoparticle as a function of its position z_p for (a): various pH values at C_{KCl} = 50 mM; (b): for various C_{KCl} at pH =7.5 when λ_w^{-1} = 0.3 nm.

8.3.2 Effect of Solution Properties on Charge Density of the Nanoparticle

In contrast to the soft particle bearing a uniformly distributed charge density, the charge density inside the charge-regulated soft particle is heterogeneously distributed and depends on the local fluid environment. Figure 8.3 depicts the spatial distribution of the charge density inside the soft nanoparticle when the particle is located at z_p= −15nm (a), 0 (b), and 15 nm (c) for C_{KCl}=1 M and pH=7.5 (I), C_{KCl}=50 mM and pH=7.5 (II), and C_{KCl}=50 mM and pH=8.5 (III). The magnitude of the charge density in the front end of the soft particle is higher than that in the rear end of the particle. Comparisons between the corresponding figures in the first and second rows show that, at fixed pH, the spatial variation of the charge density increases as the background salt concentration decreases. At fixed background ionic concentration, the spatial variation of the charge density inside the soft layer of the nanoparticle also increases with the increase in pH. The magnitude of the charge density increases with increasing the ionic strength and pH.

Figure 8.4 depicts the volume-averaged charge density of the soft particle as a function of the particle's location under various background concentrations (Figure 8.4a) and pH (Figure 8.4b). The volume-averaged charge density varies with the change in the particle position and the solution properties including pH and ionic strength. In general, as pH

increases, the concentration of H^+ decreases, resulting in an increase in the surface reaction (8.5) and thus an increase in the negative charge density. As the background salt concentration increases, the volume-averaged charge density of the soft nanoparticle also increases. The averaged charge density of the particle located in the cis reservoir is significantly lower than that in the trans reservoir when the salt concentration is relatively low and pH is relatively high. As the particle moves toward the nanopore entrance, the charge density decreases and attains the minimum at the nanopore entrance. The charge density increases after the particle enters the nanopore, and attains the maximum at the nanopore exit. The charge density decreases as the particle further moves inside the trans reservoir. The dependence of the averaged charge density of the particle on the particle's location is attributed to the induced concentration polarization phenomenon occurring at both ends of the nanopore. Figure 8.5 depicts the spatial distributions of the ionic concentrations of c_1 (a), c_2 (b), c_3 (c), and c_4 (d) near the soft nanopore without nanoparticle when C_{KCl} = 50mM, pH = 8 and λ_w^{-1} = 0.3 nm. These Figures reveal that the concentrations of counterions (H^+ and K^+) and coions (Cl^- and OH^-) near the nanopore entrance located in the cis reservoir are significantly enhanced, while both counterions and coions are depleted at the other end of the nanopore. Due to the enrichment of H^+ ions at the nanopore entrance, the association reaction of Eq. (8.5) increases resulting in a decrease in the available negative sites A^- and accordingly a decrease in the charge density. Due to the depletion of H^+ ions at the other end of the nanopore, the dissociation reaction of Eq. (8.5) increases, leading to an increase in the charge density. The concentration polarization becomes more significant when the degree of the double layer overlap and the charge density of the nanoparticle increase, leading to more significant spatial variation of the charge density for higher pH due to higher charge density and lower salt concentration due to thicker double layers.

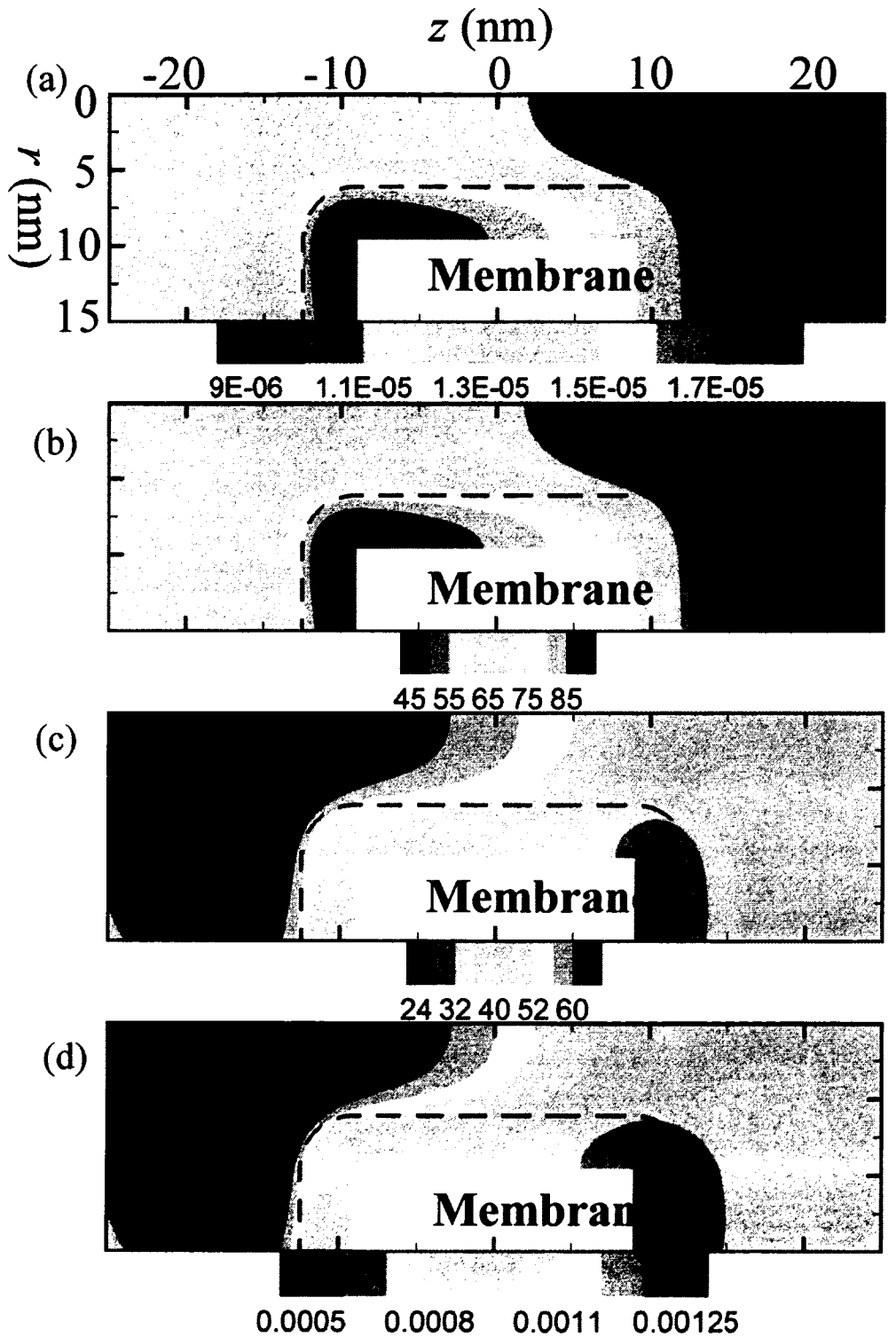

Figure 8.5. Spatial distributions of the ionic concentrations, (a): c_1; (b): c_2; (c): c_3; (d): c_4, in the soft nanopore in the absence of the nanoparticle when C_{KCl} = 50 mM, pH = 8 and λ_w^{-1} = 0.3 nm.

8.3.3 Effect of Solution Properties on Translocation Velocity

Figure 8.6 depicts the particle translocation velocity as a function of particle position z_p at various pH values with C_{KCl} = 50mM (a) and various background concentration C_{KCl} with pH =7.5 (b) when λ_w^{-1} = 0.3nm, which corresponds to the hydrodynamic diameter of the water molecule.[244] Since the electric field inside the nanopore is much higher than that in the fluid reservoirs, as expected the particle velocity within the nanopore is higher than that inside the fluid reservoirs when the particle can translocate through the nanopore. This phenomenon is consistent with many theoretical and experimental observations in the literature.[59, 65, 131, 149, 236] Under the other same conditions, the particle velocity increases with increasing pH due to the increase in the charge density as shown in Figure 8.4a. The increase in charge density with the increasing pH leads to an increase in the electrostatic driving force acting on the particle and an increase in the particle phoretic velocity. In addition, it is interesting to note that the nanoparticle velocity before funneling the nanopore entrance, defined as the nanoparticle capture velocity, significantly increases as it approaches the nanopore entrance (-30 nm < z_p < -20 nm), and then starts to decrease at about z_p = -15 nm, as shown in Figure 8.6a. This phenomenon is different from the results in the solid-state nanopores.[57, 59, 65, 149] The electrostatic interaction between the enriched counterions (cations) at the nanopore mouth and the negatively charged soft nanoparticle induces an attractive force, yielding an increase in the nanoparticle capture velocity. Since the CP is stronger at lower background concentration and higher charge density, the nanoparticle capture velocity increases as C_{KCl} decreases due to the increase in the double layers overlap and as pH increases due to the increase in the charge density of the nanoparticle. Figure 8.6a also shows that the maximum particle translocation velocity occurs at about z_p= 15 nm instead of the center of the nanopore, which is attributed to the maximum charge density of the soft particle occurring at about z_p= 15 nm, as shown in Figure 8.4.

If pH is relatively low, the particle velocity at the nanopore mouth becomes negative, implying that the particle is trapped there and could not translocate through the nanopore. This is attributed to low charge density on the particle at low pH, as shown in Figure 8.4a, and the electrophoretic driving force is lower than the opposite hydrodynamic force arising from the opposite electroosmotic flow of the nanopore. Therefore, one can control

nanoparticle separation or trapping by regulating pH of the solution, which significantly affects the particle charge density. When pH is relatively low, particles are focus or trapped at the nanopore entrance in the cis reservoir. However, particles electrophoretically translocate from the *cis* reservoir into the *trans* reservoir when pH of the solution is relatively high.

Figure 8.6b shows that the particle velocity is also very sensitive to the background salt concentration. The electrophoretic velocity of the charge regulated soft particle inside the reservoirs decreases as the salt concentration increases, which is attributed to the decrease in the degree of concentration polarization and accordingly the induced electrostatic force arising from the interaction between the enriched counterions at the nanopore entrance and the negatively charge nanoparticle. When the salt concentration is relatively low (i.e., C_{KCl}=50 mM), as the particle further moves toward the nanopore entrance, the particle velocity becomes negative implying that the nanoparticle is trapped at the entrance of the nanopore. This is attributed to the decrease in the charge density of the particle arising from the enriched ionic concentrations, as shown by the dash-dotted line in Figure 8.4b. When the salt concentration is relatively high, particle can enter and translocate through the nanopore due to relatively high charge density of the nanoparticle, as shown in Figure 8.4b. The particle velocity in the trans reservoir is a little bit higher than that in the cis reservoir since the charge density of the particle in the trans reservoir is a little bit higher than that in the cis reservoir, as shown in Figure 8.4b.

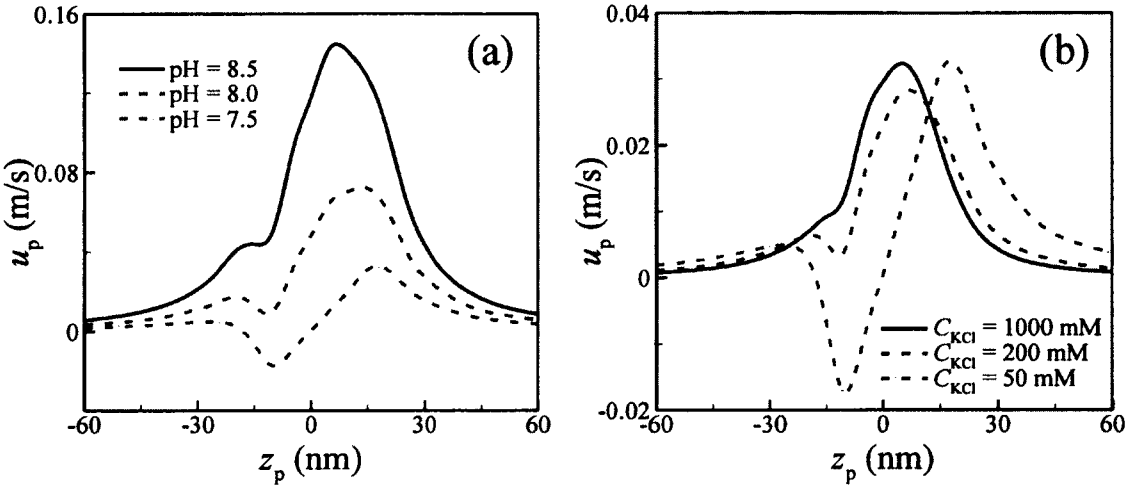

Figure 8.6. Particle translational velocity as a function of its position z_p (a): for various pH values when C_{KCl} = 50 mM; (b): for various C_{KCl} at pH =7.5 when λ_w^{-1} = 0.3 nm.

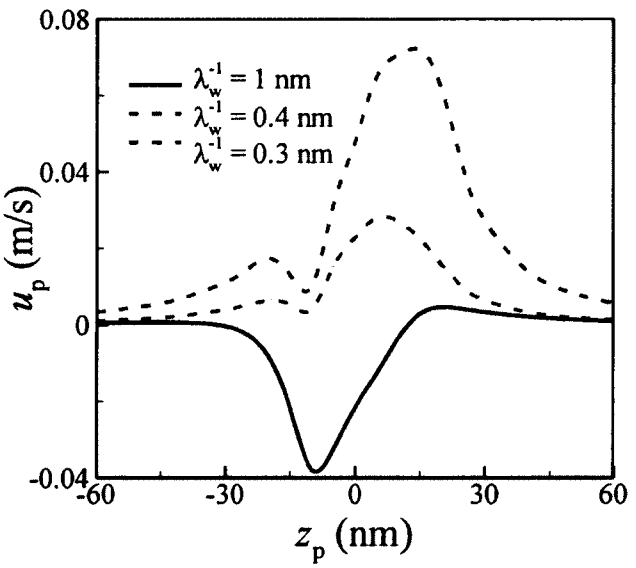

Figure 8.7. Particle translational velocity as a function of its position z_p at various values of λ_w^{-1} when C_{KCl} = 200 mM and pH=7.5.

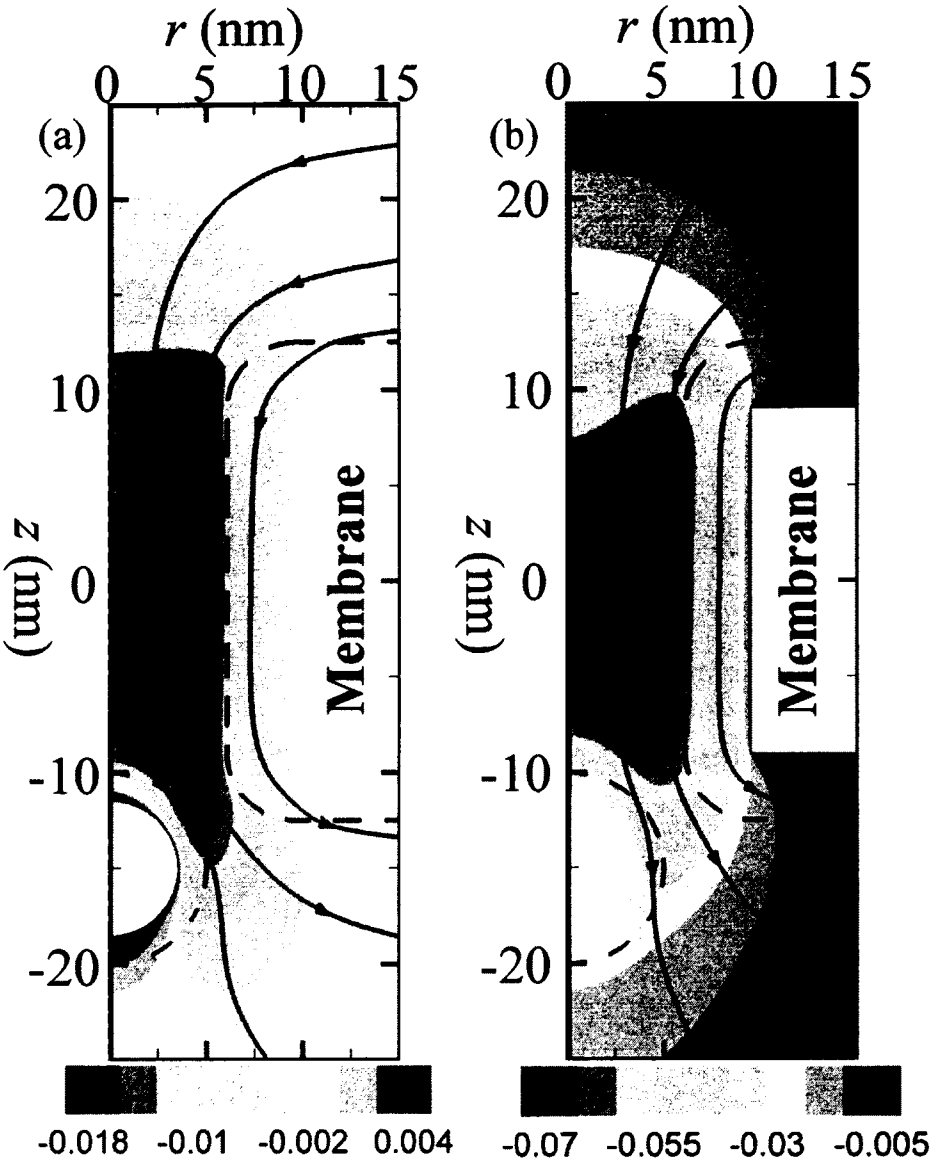

Figure 8.8. Flow field near the nanopore when λ_w^{-1} = 0.3 nm (a) and 1 nm (b) at pH =7.5, C_{KCl} = 200 mM and z_p = -15 nm. Color bars and streamlines with arrows denote the z-component fluid velocity and the fluid velocity vector, respectively.

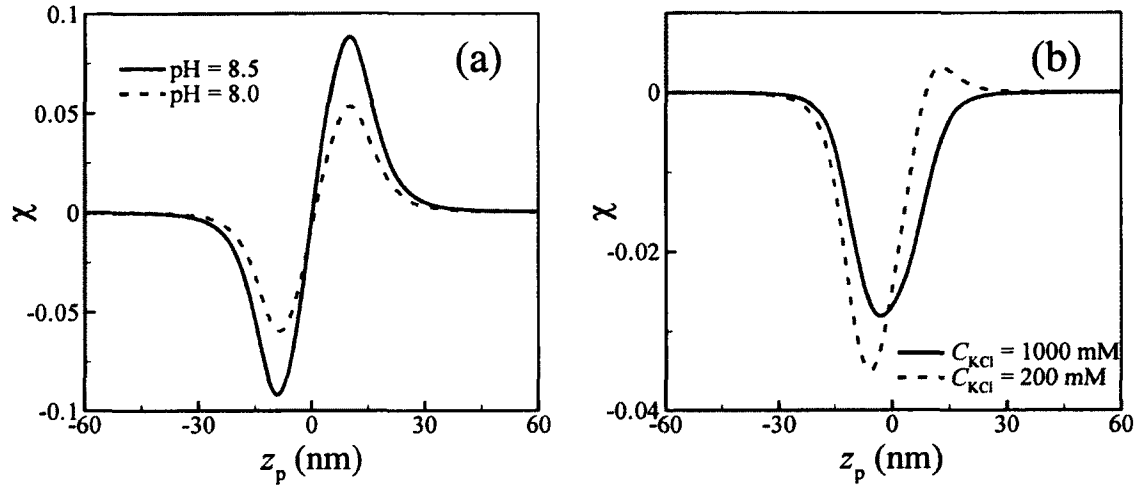

Figure 8.9. Current deviation as a function of the particle position z_p (a): for various pH values at C_{KCl} = 50 mM; (b): for various C_{KCl} at pH =7.5. Other conditions are the same as those in Figure 8.6.

8.3.4 Effect of Softness Degree of the Soft Nanopore on Translocation Velocity

Figure 8.7 depicts the Particle translocation velocity as a function of particle position z_p at various values of λ_w^{-1} when pH =7.5 and C_{KCl} = 200 mM. It is expected that the friction force stemming from the soft layer of the nanopore decreases with increasing its softness degree, thereby strengthening the opposite electroosmotic flow and slowing down the nanoparticle translocation velocity. It is interesting to find that when λ_w^{-1} = 1 nm, corresponding to a very soft nanopore, the nanoparticle is also trapped near the nanopore entrance due to very strong EOF. To further confirm that the particle is trapped by the opposite EOF, Figure 8.8 shows the flow field near the nanopore for λ_w^{-1} = 0.3 nm (a) and 1 nm (b) when pH =7.5, C_{KCl} = 200 mM and z_p = −15 nm, and the color bars denote the z-component fluid velocity and streamlines with arrows denote the fluid velocity vector. Since the nanopore is also negatively charged, the direction of induced EOF is opposite to that of the particle electrophoretic motion. Therefore, the EOF retards particle motion. The EOF for λ_w^{-1} = 0.3 nm is much weaker than that for λ_w^{-1} = 1 nm. Therefore, as λ_w^{-1} increases, the EOF increases, yielding lower particle translocation velocity. If the polyelectrolyte layer of the nanopore is very soft and bears very high fixed charge, the particle will be trapped near the nanopore entrance by the strong opposite EOF.

8.3.5 Effect of Solution Properties on the Ionic Current Signals

As mentioned previously, a nanopore-based sensing technique is based on the variation in the ionic current through the nanopore due to the nanoparticle translocation. Figure 8.9 shows the current deviation as a function of particle position z_p at various pH values with C_{KCl} = 50 mM (a) and as a function of various background concentration C_{KCl} with pH =7.5 (b) when λ_w^{-1} = 0.3nm. Since the particle is trapped prior to entering the nanopore at C_{KCl} = 50 mM and pH = 7.5, only the ionic current deviation for pH = 8.5 and 8 in Figure 8.9a, and C_{KCl} = 200 mM and 1000 mM in Figure 8.9b are presented. Figure 8.9a indicates that when C_{KCl} = 50 mM, current blockade occurs as the nanoparticle enters the nanopore, but current enhancement is observed as it exits the nanopore, which is consistent with the results in the literature.[258] The former arises from the physical blockade of the nanoparticle, and the ionic current decreases due to the displacement of electrolyte by the dielectric particle. This has been verified in many experiments in solid-state nanopores[33, 38, 41] and functionalized soft nanopores.[34, 42] The current enhancement was also found in many experiments.[43,214] As pointed out by Chang et al.,[214] although the introduction of a nanoparticle into a nanopore results in a decrease in the ionic concentration current, the screened counterions carried by the negatively charged nanoparticle also provide an additional source to increase the ionic current as it enters the nanopore. The contribution of the extra counterions carried by the particle becomes important only when the double layers of the particle and the nanopore are overlapped and the charge density of the particle is relatively high. Figure 8.9a also shows that the signals of both blockade and enhancement increase as pH increases. As pH increases, the charge density in the soft layer of the nanoparticle increases, which carries more counterions into the nanopore and accordingly an increase in the current enhancement signal.

Figure 8.9b shows the influence of the background concentration on the ionic current signatures. When C_{KCl} = 200 mM, current blockade occurs as the nanoparticle enters the nanopore, but current enhancement is observed as it exits the nanopore. The current enhancement arises from the higher charge density of the soft particle, as shown in the dashed line in Figure 8.4b. However, when C_{KCl} = 1000 mM, only blockade happens due to thin Debye length.

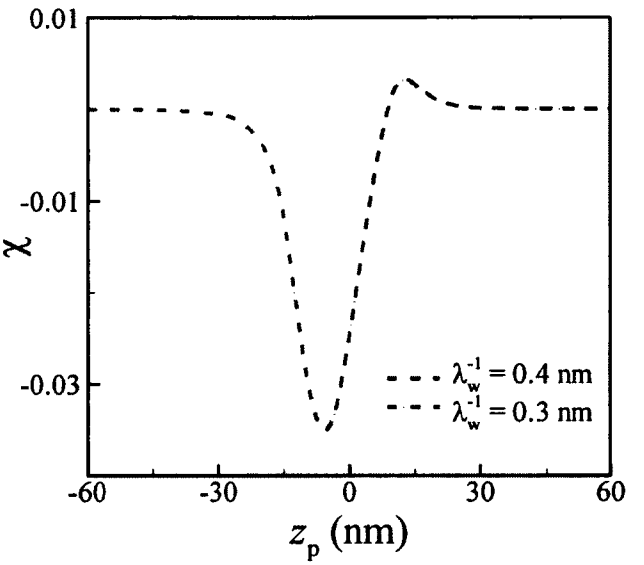

Figure 8.10. Current deviation as a function of the particle position z_p for λ_w^{-1}=0.3 and 0.4. The conditions are the same as those in Figure 8.7.

8.3.6 Effect of Softness Degree on the Ionic Current Signals

Figure 8.10 depicts the current deviation as a function of particle position z_p at various values of λ_w^{-1} when pH =7.5, C_{KCl} = 200 mM and λ_w^{-1} = 0.3 nm. Since the particle could not enter the nanopore due to very strong EOF when λ_w^{-1} = 1 nm, only the ionic current deviation for λ_w^{-1} = 0.3 nm and 0.4 nm are presented in Figure 8.10, and they are identical, which implies that the softness degree of the soft nanopore mainly affects the hydrodynamic field inside the nanopore and has negligible effect on the ionic current signal. Therefore, one might adjust the soft degree of the polyelectrolyte layer grafted on the membrane to regulate the electroosmotic flow and accordingly regulate the particle translocation process without affecting the ionic current signal.

8.4. Conclusions

The electrokinetic translocation of a charge-regulated soft biocolloidal nanoparticle through a functionalized soft nanopore is theoretically analyzed for the first time. In contrast to the existing studies using a pre-specified constant charge density on the

nanoparticle, charge regulation model is used for the first time to determine the charge density of the soft layer in the biocolloidal nanoparticle, which highly depends on the local liquid environment such as the salt concentration and pH surrounding the nanoparticle. The obtained results show that the charge density of the soft particle is spatially nonuniform, and its magnitude in the front end is higher than that in the rear end, and the volume-averaged charge density increases as the salt concentration and pH increases. The charge density of the soft particle also depends on the position of the particle during the translocation process. Due to the induced concentration polarization occurring at both ends of the nanopore, the charge density of the particle located at the nanopore entrance, where both counterions and coions are enriched, is lower than that when the particle is located at the exit of the nanopore where ions are depleted. Due to the dependence of the charge density of the soft particle on pH, salt concentration, and particle's position, nanoparticles could be trapped or focus at the nanopore entrance when pH and salt concentration are relatively low due to low charge density of the soft particle and high soft degree of the polyelectrolyte layer of the nanopore due to strong opposite electroosmotic flow. Otherwise, the particles translocate through the nanopore resulting in current block if the salt concentration is relative high and both current blockade and enhancement if the salt concentration is relatively low. The softness degree of the polyelectrolyte layer grafted on the membrane mainly affects the electroosmotic flow inside the nanopore, which retards the particle electrophoretic motion, and has negligible effects on the current signal during the nanoparticle translocation process. One can regulate the nanoparticle translocation process by tuning pH, salt concentration, charge density and softness degree of the polyelectrolyte layer on the membrane.

Table 8.1. The values or range of physical parameters used in the simulation.

Parameters	**value or range**
a (soft nanoparticle radius)	5 (nm)
d (thickness of ion-penetrable layer of soft nanoparticle)	1.5 (nm)
R_N (nanopore radius)	9.6 (nm)
L_S (thickness of ion-penetrable layer of soft nanopore)	3.5 (nm)
L_N (nanopore length)	18 (nm)
R_R (reservoir radius)	200 (nm)
L_R (reservoir length)	200 (nm)
ε_f (*permittivity of water*)	7.08×10^{-10} (C/Vm)
μ (*dynamic viscosity*)	0.001(kg/sm)
F (*Faraday constant*)	96490 (C/ mol)
C_{KCl} (*background salt concentration*)	50~1000 (mM)
λ_w^{-1} (*soft degree of ion-penetrable layer of soft nanopore*)	0.3-1 (nm)
λ_p^{-1} (*soft degree of ion-penetrable layer of soft nanoparticle*)	1 (nm)
$\rho_{fix,w}$ (*fixed charge density of ion-penetrable layer of nanopore*)	-4.57×10^{-6} (C/m^3)
D_1 (*diffusion coefficient of* H^+)	9.31×10^{-9} (m^2/s)
D_2 (*diffusion coefficient of* K^+)	1.96×10^{-9} (m^2/s)
D_3 (*diffusion coefficient of* Cl^-)	2.03×10^{-9} (m^2/s)
D_4 (*diffusion coefficient of* OH^-)	5.30×10^{-9} (m^2/s)
T (*absolute temperature*)	300 (K)
R (*universal gas constant*)	8.31(1/mol K)
V_0 (*electric potential on trans*)	0.5 (V)
K_w (*dissociation constant of water*)	10^{-14}
K_A (*equilibrium constant of reaction Eq.* (8.5))	$10^{-2.5}$
K_B (*equilibrium constant of reaction Eq.* (8.6))	$10^{-8.5}$
N_A (*total number density of acidic functional groups in soft nanoparticle*)	600 (mol/m^3)
N_B (*total number density of basic functional groups in soft nanoparticle*)	600 (mol/m^3)

CHAPTER 9

CONCLUSIONS AND FUTURE WORK

9.1. Conclusions and Contributions

The success of the next generation nanopore-based DNA sequencing and single molecules detection technology requires comprehensive understand the fundamentals of the electric field induced electrokinetic ion, fluid and particle transport in nanofluidics, which is the objective of this thesis. This dissertation can be divided into three parts.

9.1.1 Electrokinetic Ions and Fluid Transport in Nanopores

Electrokinetic ion and fluid transport in two types of nanopores, solid-state and polyelectrolyte (PE)-modified soft nanopores, have been investigated in this dissertation.

(1) Chapter 2 investigated the electric field induced ion transport and the resulting conductance in a polyelectrolyte (PE)-modified soft nanopore for the first time using a continuum-based model, composed of the coupled Poisson-Nernst-Planck (PNP) equations for the ionic mass transport, and Stokes and Brinkman equations for the flow field. In contrast to the solid-state nanopores in which ions are enriched (depleted) at the opening of nanopore in the cathode (anode) reservoir, two distinct counterions-rich concentration polarization occurring at either end of the nanopore, which significantly depends on the bulk ionic concentration and electric field strength, have been reported. If the bulk ionic concentration is extremely low, the counterions-rich CP occurs at the cathode side of the nanopore. If the bulk ionic concentration is relatively high, the counterions-rich CP occurs at the anode (cathode) side of the nanopore as the electric field is relatively weak (high). The induced CP significantly affects the nanopore conductance.

(2) In contrast to the extensive studies of electrokinetic ion and fluid transport in a solid-state nanopore, whose surface charge density is pre-specified and is assumed to be independent of the solution properties, Chapter 3 investigated electrokinetic ion and fluid transport in a charge-regulated solid-state nanopore and considered

the charge regulation occurring in a typical silica nanopore for the first time. Different from the existing studies using a pre-specified constant surface charge density, the surface charge density is a part of the solution in the proposed model and highly depends on both pH and the background salt concentration. The model taking into account the charge regulation successfully captures the physics of the dependence of the nanopore conductance on the salt concentration and favorably agrees with the experimental data obtained from the literature. The results show that both pH and ionic strength dramatically affect the nanopore surface charge density, which governs the electrokinetic ion, fluid transport and the concentration polarization at the opening of the cathode (anode) side of the nanopore, especially when the double layers overlap. The induced concentration polarization creates a concentration gradient across the nanopore, which induces an electric field opposite to the externally imposed one, and accordingly reduces the electric field inside the nanopore. Therefore, one can control pH and/or salt concentration to tune the surface charge density of the nanopore wall, which in turn controls the nanopore conductance and electroosmotic flow. The induced concentration polarization also can be controlled by tuning pH and/or ionic strength to reduce the electric field inside the nanopore, which can be used to slow down DNA translocation in the next generation nanopore-based DNA sequencing technology.

9.1.2 Nanoparticle Translocation through Nanopores

Based on the obtained knowledge on electrokinetic ion and fluid transport in both solid-state and soft nanopores, electrokinetic motion of various nanoparticles, including highly charged nanoparticles such as DNA and soft nanoparticles without considering charge regulation, and charge-regulated biocolloidal nanoparticles such as proteins, in both solid-state and soft nanopores are comprehensively investigated to elucidate the mechanisms of nanoparticle translocation.

(1) Electrophoretic motion of a soft spherical particle consisting of a rigid core covered by a charged soft layer along the axis of a solid-state nanopore was numerically investigated in Chapter 4. The nanoparticle phoretic velocity decreases as the bulk ionic concentration and the softness degree of the soft nanoparticle increase. At

relatively low bulk concentration, the particle phoretic velocity nonlinearly increases with the fixed charge of the particle arising from the significant double layer polarization effect.

(2) Regulating DNA translocation by using a soft nanopore containing highly charged polyelectrolyte layer grafted on the membrane wall has been proposed and invested for the first time. The results described in Chapter 5 show that the nanopore capture rate is enhanced due to the significant concentration polarization occurring at the entrance of the soft nanopore and the DNA translocation velocity inside the nanopore is reduced due to the enhanced opposite electroosmotic flow inside the soft nanopore. The polyelectrolyte layer mainly affects the fluid and particle motion, and has negligible effect on the ionic current signal. Therefore, soft nanopore is proposed to regulate the DNA translocation behavior without changing the ionic current signature.

(3) Instead of using a dielectric solid-state nanopore, a solid-state nanopore with a floating electrode coated along the inner surface of the nanopore was proposed and theoretically investigated to slow down DNA translocation process. The ideally polarizable floating electrode interacting with the applied electric field induces a non-uniform surface charge density on the floating electrode and generates induced-charge electro-osmotic (ICEO) flow inside the nanopore. The ICEO and particle-floating electrode electrostatic interaction are the two primary factors affecting the DNA translocation through the nanopore. The ICEO effect exists under both thin and thick EDLs and is proportional to the square of the applied electric field, which retards the DNA translocation when it approaches the floating electrode, however, facilitates the DNA translocation when it passes the floating electrode. The particle could be trapped near the floating electrode when the applied electric field is relatively high and the EDLs are relatively thin. The floating electrode technique might be helpful for attracting DNA from the reservoir into the nanopore and slowing down its motion inside the nanopore.

(4) Due to significant counterions condensation on the DNA surface, the liquid permittivity surrounding the DNA nanoparticle becomes spatially dependent. The effects of the local permittivity environment (LPE) on the DNA translocation speed

and the resulting ionic current signal in a solid-state nanopore are numerically investigated. The LPE effect reduces the particle translocation velocity. The LPE effect has significant effect on the ionic current signal only when the applied electric field is relatively strong.

(5) Electrokinetic translocation of a charge-regulated soft biocolloidal nanoparticle (i.e., protein) through a functionalized soft nanopore was numerically analyzed for the first time. The results described in Chapter 8 show that the charge density of the soft nanoparticle is spatially nonuniform and its magnitude depends on pH, salt concentration, and the particle's position inside the nanopore device. One can tune pH and/or ionic strength to control the charge density of the soft particle, and accordingly regulate its motion. One can achieve particle trapping, focusing, and pre-concentration at the nanopore entrance by lowing pH and salt concentration. The softness degree of the soft layer of the nanopore mainly affects the hydrodynamic field and has negligible effect on the resulting ionic current signal.

9.2. Future work

Based on the research work described in this dissertation, some recommendations for further research are briefly described in the following.

9.2.1 Ionic Current Rectification (ICR) in Conical Nanopores

Synthetic solid-state nanopores are attractive materials to mimetic biological ion channels. Study on the ion transport in synthetic nanopores provides an essential way to understand the real process in living organisms. When the EDL thickness is comparable to the characteristic size of the nanopores, some interesting features, such as ion concentration polarization[123, 259] and ion selectivity,[87-88] can be observed. Among various applications, ionic current rectification (ICR), referring to an asymmetric diode-like current-voltage behavior, has attracted considerable attention over the past decades. [86, 123, 260] To produce the ICR phenomenon, two important key factors are required:[261] (i) the overlapping of EDL inside the nanopore, and (ii) an asymmetry in the distributions of ions along the axis of the nanopore. To study the ICR phenomenon in nanopores, several

mechanisms, such as electric potential barrier inside the pore,[92] electrochemical prosperities of the nanopore tip,[262-263] and enrichment and depletion of ions, have been proposed, as summarized by Siwy.[264] Despite the differences among these mechanisms, it is generally accepted that the ICR in nanofluidics depends highly on the surface charge property of the nanopore or the nanochannel wall, which is in contact with the aqueous solution. Several studies have been proposed to study the ICR in nanopores based on the assumption of constant surface charge density of the nanopore.[202, 265] However, the materials of the nanopore in contact with aqueous solution are charge-regulated, and their charge densities depend on both pH and background ionic concentration, as shown in Chapter 3. The work described in Chapter 3 can be extended to explore the ICR phenomenon in a charged-regulated conical solid-state nanopore. In addition, the work described in Chapter 2 can be extended to investigate ICR phenomenon in a conical soft nanopore. The proposed two works have not been reported in the literature.

9.2.2 Field Effect Control of Electrokinetic Transport in Charge-Regulated Nanopores

Since the electrokinectic ion, fluid, and particle transport in nanofluidics is governed by the charge of the nanopore wall, one can regulate the electrokinetic transport phenomena in nanofluidics by active control of the charge of the nanochannel. Recently, analogous to the metal-oxide-semiconductor field effect transistors (MOSFETs), nanofluidic field effect transistor (FET) with an electrically addressable gate electrode has been fabricated using the state-of-the-art nanofabrication technologies.[15, 266-269] The gate electrode can effectively control the surface potential of the nanopore wall,[270] which is consequently employed to regulate the electroosmotic flow (EOF) in ionic transport, and ionic conductance in nanofluidic devices.[9, 87, 266-267, 269] The gate electrode offers a more flexible and electrically compatible approach for the control of the surface potential than the chemical functionalization method. Oh et al.[145, 271] experimentally demonstrated the feasibility to regulate the electrokinetic transport of charged dye nanoparticles using the field effect control. The gate electrode and the liquid inside the micro/nanochannel are separated by an electrically insulating layer, which is made of dielectric material such as silicon dioxide (SiO_2).[145, 271] The SiO_2 is a charge regulated material and its charge property depends on the local fluid environment, as described in Chapter 3. However, the

existing studies on nanofluidic FET did not consider the charge regulation. [56-57, 272,59, 65, 111, 145, 273] The work described in Chapter 3 can be extended to analyze electrokinetic transport phenomena in a nanofluidic FET.

APPENDIX

The variables and parameters in this dissertation are shown in the Table A.1, while the acronyms in the dissertation are listed in the Table A.2.

Table A.1. The variables and parameters used in this dissertation.

Variables/Parameters (Description)
a (radius of the particle rigid spherical core or DNA particle)
C_{0j} (bulk concentration of jth ion)
C_{KCl} (background concentration of KCl)
c_j (concentrations of jth ion)
d (thickness of ion-penetrable porous membrane layer of particle)
D_j (diffusion coefficients of jth ion)
e (elementary charge)
$\mathbf{E}$, E_z (electric field and z direction electric field)
E_∞ (electric field imposed far away from the particle)
$\mathbf{e}_r$, $\mathbf{e}_z$ (the unit vectors in the r- and z-directions)
F (Faraday constant)
F_E, F_D, (electric and hydrodynamic force in the z direction on the particle surface)
G (conductance)
$[H^+]_S$ (molar concentration of H^+ ions at that membrane wall/liquid interface)
I (ionic current, ionic current scale and ionic current without DNA)
I_∞ (base ionic current when the DNA nanoparticle is far away from the nanopore)
K_A, K_B (equilibrium constants of dissociation and association reactions)
K_w (dissociation constant of water)
L_f (floating electrode length)
L_N (nanopore length)
L_p (DNA length)
L_R (reservoir length)
$\mathbf{n}$ (unit outer normal vector)
N_j (flux densities jth ions)

Table A.1. (continued)

N_A (*total number density of acidic functional groups in soft nanoparticle*)
N_B (*total number density of basic functional groups in soft nanoparticle*)
N_{total} (total surface site density on the nanopore/liquid interface)
p (hydrodynamic pressure)
pH (pH value)
Q (dimensionless fixed charge in the soft membrane layer)
Q_{flow} (volumetric flow rate)
R (universal gas constant)
R_N (nanopore radius)
R_R (reservoir radius)
R_s(thickness of ion-penetrable layer of soft nanopore)
T (absolute temperature)
u (fluid velocity)
u, v (fluid velocity in r and z direction)
$\mathbf{U}_p$, u_p (particle velocity and particle velocity in z direction)
V (potential)
V_0 (electric potential on trans)
Z (valance of the dissociable groups per molecular chain)
z_j (valences of jth ion)
γ (frictional coefficient of ion-penetrable layer)
γ_w, γ_p (frictional coefficient of ion-penetrable layer of nanopore and particle in chapter 8)
ε_0 (vacuum permittivity)
ε_i (relative permittivity of liquid on DNA surface)
ε_f (permittivity of water)
$\varepsilon_{f,i}$, $\varepsilon_{f,0}$ (permittivity of water inside and outside of ion-penetrable layer near DNA)
ε_w (relative permittivity of water)
η, η_p (mobilities of soft particle and DNA particle)
ρ (fluid density)

Table A.1. (continued)

ρ_e (space charge density of the mobile ions)
ρ_{fix} (fixed charge density of ion-penetrable layer)
$\rho_{fix,w}$, $\rho_{fix,p}$ (fixed charge density of ion-penetrable layer of nanopore and particle in chapter 8)
ζ (zeta potential on the particle surface)
μ (dynamic viscosity of fluid)
σ_w, σ_p (surface charge density on the nanopore and particle)
σ_s (molecular chain surface density grafted to solid-state nanopore)
κ^{-1} (dimensional EDL thickness)
χ (ionic deviation)
χ_s (dissociated degree of functional groups in the soft layer)
λ (softness degree)
λ_D (Debye length)
λ_w, λ_p (softness degree of nanopore and particle in chapter 8)

Table A.2. The acronyms used in this dissertation.

Acronyms	Full Forms
PE	polyelectrolyte
PNP	Poisson-Nernst-Planck
DC	direct-current
EDL	electrical double layer
PB	Poisson-Boltzmann
EOF	eletroosmosis flow
NS	Navier-Stokes
ICEK	induced-charged electrokinetics
CP	ion concentration polarization
ICR	ionic current rectification
RHS	right-hand side
ICEO	induced-charged eletroosmosis
DLP	double layer polarization
ssDNA	single-stranded DNA
ssRNA	single-stranded RNA
FET	field effect transistors
dsDNA	double-stranded DNA
HPL	hairpin-loop
MIM	multi-ion model
LPE	local permittivity environment
MD	molecular dynamics

LITERATURE CITED

1. C. Vieu, F. Carcenac, A. Pepin, Y. Chen, M. Mejias, A. Lebib, L. Manin-Ferlazzo, L. Couraud and H. Launois, *Appl. Surf. Sci.*, 2000, **164**, 111-117.
2. S. Y. Chou, P. R. Krauss and P. J. Renstrom, *J. Vac. Sci. Technol. B*, 1996, **14**, 4129-4133.
3. L. J. Guo, *Adv. Mater.*, 2007, **19**, 495-513.
4. G. Karniadakis, B. A. and N. Aluru, *Microflows and nanoflows: fundamentals and simulation*, Springer, New York, 2005.
5. J. Edel and A. deMello, *Nanofluidics: Nanoscience and Nanotechnology*, Royal Society of Chemistry, London, 2009.
6. A. T. Conlisk, J. McFerran, Z. Zheng and D. Hansford, *Anal. Chem.*, 2002, **74**, 2139-2150.
7. Y. He, D. Gillespie, D. Boda, I. Vlassiouk, R. S. Eisenberg and Z. S. Siwy, *J. Am. Chem. Soc.*, 2009, **131**, 5194-5202.
8. D. Stein, M. Kruithof and C. Dekker, *Phys. Rev. Lett.*, 2004, **93**.
9. R. Karnik, K. Castelino, R. Fan, P. Yang and A. Majumdar, *Nano Lett.*, 2005, **5**, 1638-1642.
10. R. B. Schoch, L. F. Cheow and J. Han, *Nano Lett.*, 2007, **7**, 3895-3900.
11. H. Daiguji, Y. Oka and K. Shirono, *Nano Lett.*, 2005, **5**, 2274-2280.
12. I. Vlassiouk and Z. S. Siwy, *Nano Lett.*, 2007, **7**, 552-556.
13. A. Alcaraz, P. Ramirez, E. Garcia-Gimenez, M. L. Lopez, A. Andrio and V. M. Aguilella, *J. Phys. Chem. B*, 2006, **110**, 21205-21209.
14. H. Daiguji, P. D. Yang and A. Majumdar, *Nano Lett.*, 2004, **4**, 137-142.
15. R. Karnik, R. Fan, M. Yue, D. Y. Li, P. D. Yang and A. Majumdar, *Nano Lett.*, 2005, **5**, 943-948.
16. N. Savage and M. S. Diallo, *Journal of Nanoparticle Research*, 2005, **7**, 331-342.
17. P. Jovancic and M. Radetic, in *Handbook of Environmental Chemistry*, ed. D. P. M. Barcelo, 2008, vol. 5, pp. 239-264.
18. J. Clarke, H. C. Wu, L. Jayasinghe, A. Patel, S. Reid and H. Bayley, *Nat. Nanotechnol.*, 2009, **4**, 265-270.
19. A. Aksimentiev, *Nanoscale*, 2010, **2**, 468-483.
20. B. M. Venkatesan and R. Bashir, *Nat. Nanotechnol.*, 2011, **6**, 615-624.
21. J. J. Kasianowicz, E. Brandin, D. Branton and D. W. Deamer, *Proc. Natl. Acad. Sci. U. S. A.*, 1996, **93**, 13770-13773.
22. M. Wanunu, J. Sutin, B. McNally, A. Chow and A. Meller, *Biophys. J.*, 2008, **95**, 4716-4725.
23. G. M. Skinner, M. van den Hout, O. Broekmans, C. Dekker and N. H. Dekker, *Nano Lett.*, 2009, **9**, 2953-2960.
24. A. Singer, M. Wanunu, W. Morrison, H. Kuhn, M. Frank-Kamenetskii and A. Meller, *Nano Lett.*, 2010, **10**, 738-742.
25. T. Z. Butler, M. Pavlenok, I. M. Derrington, M. Niederweis and J. H. Gundlach, *Proc. Natl. Acad. Sci. U. S. A.*, 2008, **105**, 20647-20652.
26. V. Mussi, P. Fanzio, L. Repetto, G. Firpo, P. Scaruffi, S. Stigliani, M. Menotta, M. Magnani, G. P. Tonini and U. Valbusa, *Journal of Physics-Condensed Matter*, 2010, **22**.
27. K. K. Saha, M. Drndic and B. K. Nikolic, *Nano Lett.*, 2012, **12**, 50-55.
28. H. Bayley, *Curr. Opin. Chem. Biol.*, 2006, **10**, 628-637.
29. D. Branton, D. W. Deamer, A. Marziali, H. Bayley, S. A. Benner, T. Butler, M. Di Ventra, S. Garaj, A. Hibbs, X. H. Huang, S. B. Jovanovich, P. S. Krstic, S. Lindsay, X. S. S. Ling, C. H. Mastrangelo, A. Meller, J. S. Oliver, Y. V. Pershin, J. M. Ramsey, R.

Riehn, G. V. Soni, V. Tabard-Cossa, M. Wanunu, M. Wiggin and J. A. Schloss, *Nat. Biotechnol.*, 2008, **26**, 1146-1153.
30. C. S. Pareek, R. Smoczynski and A. Tretyn, *J. Appl. Genetics*, 2011, **52**, 413-435.
31. S. W. Kowalczyk, A. R. Hall and C. Dekker, *Nano Lett.*, 2010, **10**, 324-328.
32. S. W. Kowalczyk, M. W. Tuijtel, S. P. Donkers and C. Dekker, *Nano Lett.*, 2010, **10**, 1414-1420.
33. S. K. Min, W. Y. Kim, Y. Cho and K. S. Kim, *Nat. Nanotechnol.*, 2011, **6**, 162-165.
34. V. Mussi, P. Fanzio, L. Repetto, G. Firpo, S. Stigliani, G. P. Tonini and U. Valbusa, *Biosens. Bioelectron.*, 2011, **29**, 125-131.
35. M. Tsutsui, M. Taniguchi, K. Yokota and T. Kawai, *Nat. Nanotechnol.*, 2010, **5**, 286-290.
36. A. Meller and D. Branton, *Electrophoresis*, 2002, **23**, 2583-2591.
37. A. Meller, L. Nivon and D. Branton, *Phys. Rev. Lett.*, 2001, **86**, 3435-3438.
38. R. M. M. Smeets, U. F. Keyser, D. Krapf, M. Y. Wu, N. H. Dekker and C. Dekker, *Nano Lett.*, 2006, **6**, 89-95.
39. A. Aksimentiev, J. B. Heng, G. Timp and K. Schulten, *Biophys. J.*, 2004, **87**, 2086-2097.
40. J. B. Heng, C. Ho, T. Kim, R. Timp, A. Aksimentiev, Y. V. Grinkova, S. Sligar, K. Schulten and G. Timp, *Biophys. J.*, 2004, **87**, 2905-2911.
41. M. Wanunu, W. Morrison, Y. Rabin, A. Y. Grosberg and A. Meller, *Nat. Nanotechnol.*, 2010, **5**, 160-165.
42. E. C. Yusko, J. M. Johnson, S. Majd, P. Prangkio, R. C. Rollings, J. L. Li, J. Yang and M. Mayer, *Nat. Nanotechnol.*, 2011, **6**, 253-260.
43. S. M. Iqbal, D. Akin and R. Bashir, *Nat. Nanotechnol.*, 2007, **2**, 243-248.
44. J. Comer, V. Dimitrov, Q. Zhao, G. Timp and A. Aksimentiev, *Biophys. J.*, 2009, **96**, 593-608.
45. R. Fan, R. Karnik, M. Yue, D. Y. Li, A. Majumdar and P. D. Yang, *Nano Lett.*, 2005, **5**, 1633-1637.
46. D. Fologea, J. Uplinger, B. Thomas, D. S. McNabb and J. L. Li, *Nano Lett.*, 2005, **5**, 1734-1737.
47. S. Ghosal, *Phys. Rev. Lett.*, 2007, **98**, 238104.
48. T. Chou, *J. Chem. Phys.*, 2009, **131**, 034703.
49. R. S. S. de Zoysa, D. A. Jayawardhana, Q. T. Zhao, D. Q. Wang, D. W. Armstrong and X. Y. Guan, *J. Phys. Chem. B*, 2009, **113**, 13332-13336.
50. R. Kawano, A. E. P. Schibel, C. Cauley and H. S. White, *Langmuir*, 2009, **25**, 1233-1237.
51. S. Y. Lee, S. E. Yalcin, S. W. Joo, A. Sharma, O. Baysal and S. Z. Qian, *Microgravity Sci. Technol.*, 2010, **22**, 329-338.
52. Y. Ai, J. Liu, B. K. Zhang and S. Qian, *Anal. Chem.*, 2010, **82**, 8217-8225.
53. S. E. Yalcin, S. Y. Lee, S. W. Joo, O. Baysal and S. Qian, *J. Phys. Chem. B*, 2010, **114**, 4082-4093.
54. S. W. Joo and S. Z. Qian, *Journal of Colloid and Interface Science*, 2011, **356**, 331-340.
55. M. Rincon-Restrepo, E. Milthallova, H. Bayley and G. Maglia, *Nano Lett.*, 2011, **11**, 746-750.
56. Y. H. He, M. Tsutsui, C. Fan, M. Taniguchi and T. Kawai, *ACS Nano*, 2011, **5**, 5509-5518.
57. Y. H. He, M. Tsutsui, C. Fan, M. Taniguchi and T. Kawai, *ACS Nano*, 2011, **5**, 8391-8397.
58. U. F. Keyser, *J. R. Soc. Interface*, 2011, **8**, 1369-1378.
59. M. K. Zhang, Y. Ai, A. Sharma, S. W. Joo, D. S. Kim and S. Z. Qian, *Electrophoresis*, 2011, **32**, 1864-1874.
60. B. Luan, G. Stolovitzky and G. Martyna, *Nanoscale*, 2012, **4**, 1068-1077.
61. S. W. Kowalczyk, D. B. Wells, A. Aksimentiev and C. Dekker, *Nano Lett.*, 2012, **12**, 1038-1044.

62. R. I. Stefureac, A. Kachayev and J. S. Lee, *Chem. Commun.*, 2012, **48**, 1928-1930.
63. S. W. Kowalczyk, D. B. Wells, A. Aksimentiev and C. Dekker, *Nano Lett.*, 2012, **12**, 1038-1044.
64. S. Ghosal, *Phys. Rev. Lett.*, 2007, **98**.
65. Y. Ai, J. Liu, B. K. Zhang and S. Qian, *Anal. Chem.*, 2010, **82**, 8217-8225.
66. B. Q. Luan, G. Martyna and G. Stolovitzky, *Biophys. J.*, 2011, **101**, 2214-2222.
67. T. Chou, *THE JOURNAL OF CHEMICAL PHYSICS*, 2009, **131**, 034703.
68. S. Y. Lee, S. E. Yalcin, S. W. Joo, A. Sharma, O. Baysal and S. Qian, *Microgravity Science and Technology*, 2010, **22**, 329-338.
69. Y. He, M. Tsutsui, C. Fan, M. Taniguchi and T. Kawai, *ACS Nano*, 2011, **5**, 8391-8397.
70. E. H. Trepagnier, A. Radenovic, D. Sivak, P. Geissler and J. Liphardt, *Nano Lett.*, 2007, **7**, 2824-2830.
71. R. J. Hunter, *Foundations of Colloid Science*, Oxford Univ. Press, New York, 2001.
72. D. Q. Li, *Electrokinetics in Microfluidics*, Elsevier Academic Press, New York, 2004.
73. J. H. Masliyah and S. Bhattacharjee, *Electrokinetic and Colloid Transport Phenomena*, John Wiley & Sons Inc, New York, 2006.
74. M. von Smoluchowski, *Naturwissenschaften*, 1918, **6**, 253-263.
75. D. C. Henry, *Proc. R. soc. Lond. Ser. A-Contain. Pap. Math. Phys. Character*, 1931, **133**, 106-129.
76. M. Z. Bazant and T. M. Squires, *Phys. Rev. Lett.*, 2004, **92**, 066101.
77. T. M. Squires and M. Z. Bazant, *J. Fluid Mech.*, 2004, **509**, 217-252.
78. M. Z. Bazant and T. M. Squires, *Curr. Opin. Colloid Interface Sci.*, 2010, **15**, 203-213.
79. H. Zhao and H. H. Bau, *Phys. Rev. E*, 2007, **75**, 066217.
80. Z. M. Wu and D. Q. Li, *Microfluid. Nanofluid.*, 2008, **5**, 65-76.
81. Z. M. Wu and D. Q. Li, *Electrochimica Acta*, 2008, **53**, 5827-5835.
82. M. Jain, A. Yeung and K. Nandakumar, *J. Microelectromech. Syst.*, 2009, **18**, 376-384.
83. R. Dhopeshwarkar, D. Hlushkou, M. Nguyen, U. Tallarek and R. M. Crooks, *J. Am. Chem. Soc.*, 2008, **130**, 10480-+.
84. S. E. Yalcin, A. Sharma, S. Qian, S. W. Joo and O. Baysal, *Electrophoresis*, 2010, **31**, 3711-3718.
85. S. E. Yalcin, A. Sharma, S. Qian, S. W. Joo and O. Baysal, *Sens. Actuator B-Chem.*, 2011, **153**, 277-283.
86. L. J. Cheng and L. J. Guo, *Chem. Soc. Rev.*, 2010, **39**, 923-938.
87. H. Daiguji, *Chem. Soc. Rev.*, 2010, **39**, 901-911.
88. P. Pang, J. He, J. H. Park, P. S. Krstic and S. Lindsay, *ACS Nano*, 2011, **5**, 7277-7283.
89. S. J. Kim, Y. C. Wang, J. H. Lee, H. Jang and J. Han, *Phys. Rev. Lett.*, 2007, **99**, 044501.
90. J. Y. Jung, P. Joshi, L. Petrossian, T. J. Thornton and J. D. Posner, *Anal. Chem.*, 2009, **81**, 3128-3133.
91. C. Wei, A. J. Bard and S. W. Feldberg, *Anal. Chem.*, 1997, **69**, 4627-4633.
92. Z. Siwy, Y. Gu, H. A. Spohr, D. Baur, A. Wolf-Reber, R. Spohr, P. Apel and Y. E. Korchev, *Europhys. Lett.*, 2002, **60**, 349-355.
93. Z. J. Guo, J. H. Wang, J. T. Ren and E. K. Wang, *Nanoscale*, 2011, **3**, 3767-3773.
94. F. H. J. van der Heyden, D. J. Bonthuis, D. Stein, C. Meyer and C. Dekker, *Nano Lett.*, 2007, **7**, 1022-1025.
95. S. J. Kim, S. H. Ko, K. H. Kang and J. Han, *Nat. Nanotechnol.*, 2010, **5**, 297-301.
96. R. Kwak, S. J. Kim and J. Han, *Anal. Chem.*, 2011, **83**, 7348-7355.
97. M. Ali, P. Ramirez, S. Mafe, R. Neumann and W. Ensinger, *ACS Nano*, 2009, **3**, 603-608.
98. M. Ali, B. Yameen, J. Cervera, P. Ramirez, R. Neumann, W. Ensinger, W. Knoll and O. Azzaroni, *J. Am. Chem. Soc.*, 2010, **132**, 8338-8348.
99. X. Hou, F. Yang, L. Li, Y. L. Song, L. Jiang and D. B. Zhu, *J. Am. Chem. Soc.*, 2010, **132**, 11736-11742.

100. X. Hou, Y. J. Liu, H. Dong, F. Yang, L. Li and L. Jiang, *Adv. Mater.*, 2010, **22**, 2440-2443.
101. W. Guo, H. W. Xia, L. X. Cao, F. Xia, S. T. Wang, G. Z. Zhang, Y. L. Song, Y. G. Wang, L. Jiang and D. B. Zhu, *Adv. Funct. Mater.*, 2010, **20**, 3561-3567.
102. P. Actis, B. Vilozny, R. A. Seger, X. Li, O. Jejelowo, M. Rinaudo and N. Pourmand, *Langmuir*, 2011, **27**, 6528-6533.
103. M. Ali, R. Neumann and W. Ensinger, *ACS Nano*, 2010, **4**, 7267-7274.
104. L. X. Zhang, X. H. Cao, Y. B. Zheng and Y. Q. Li, *Electrochem. Commun.*, 2010, **12**, 1249-1252.
105. P. Kohli, C. C. Harrell, Z. H. Cao, R. Gasparac, W. H. Tan and C. R. Martin, *Science*, 2004, **305**, 984-986.
106. R. Zimmermann, D. Kuckling, M. Kaufmann, C. Werner and J. F. L. Duval, *Langmuir*, 2010, **26**, 18169-18181.
107. L. H. Yeh, S. Xue, S. W. Joo, S. Qian and J. P. Hsu, *J. Phys. Chem. C*, 2012, **116**, 4209-4216.
108. R. J. Hunter, *Zeta Potential in Colloid Science*, Academic Press, New York, 1981.
109. I. Vlassiouk, S. Smirnov and Z. Siwy, *Nano Lett.*, 2008, **8**, 1978-1985.
110. Y. Ai, M. K. Zhang, S. W. Joo, M. A. Cheney and S. Z. Qian, *J. Phys. Chem. C*, 2010, **114**, 3883-3890.
111. Y. Ai, J. Liu, B. K. Zhang and S. Z. Qian, *Sens. Actuator B-Chem.*, 2011, **157**, 742-751.
112. S. Movahed and D. Q. Li, *Electrophoresis*, 2011, **32**, 1259-1267.
113. B. K. Zhang, Y. Ai, J. Liu, S. W. Joo and S. Z. Qian, *J. Phys. Chem. C*, 2011, **115**, 24951-24959.
114. Y. S. Choi and S. J. Kim, *Journal of Colloid and Interface Science*, 2009, **333**, 672-678.
115. W. J. Lan, D. A. Holden, J. Liu and H. S. White, *J. Phys. Chem. C*, 2011, **115**, 18445-18452.
116. W. J. Lan, D. A. Holden and H. S. White, *J. Am. Chem. Soc.*, 2011, **133**, 13300-13303.
117. L. H. Yeh, M. K. Zhang, S. Qian and J. P. Hsu, *Nanoscale*, 2012, doi: 10.1039/C1032NR30102D.
118. B. Corry, S. Kuyucak and S. H. Chung, *Biophys. J.*, 2000, **78**, 2364-2381.
119. O. Peleg, M. Tagliazucchi, M. Kroger, Y. Rabin and I. Szleifer, *ACS Nano*, 2011, **5**, 4737-4747.
120. M. Tagliazucchi, Y. Rabin and I. Szleifer, *J. Am. Chem. Soc.*, 2011, **133**, 17753-17763.
121. D. Marsh, R. Bartucci and L. Sportelli, *Biochim. Biophys. Acta-Biomembr.*, 2003, **1615**, 33-59.
122. M. K. Zhang, L. H. Yeh, S. Qian, J. P. Hsu and S. W. Joo, *J. Phys. Chem. C*, 2012, **116**, 4793-4801.
123. R. B. Schoch, J. Y. Han and P. Renaud, *Rev. Mod. Phys.*, 2008, **80**, 839-883.
124. L. H. Yeh and J. P. Hsu, *Soft Matter*, 2011, **7**, 396-411.
125. H. Ohshima, *Adv. Colloid Interface Sci.*, 1995, **62**, 189-235.
126. W. J. Lan, D. A. Holden, B. Zhang and H. S. White, *Anal. Chem.*, 2011, **83**, 3840-3847.
127. D. Stein, M. Kruithof and C. Dekker, *Phys. Rev. Lett.*, 2004, **93**, 035901.
128. L. H. Yeh, K. L. Liu and J. P. Hsu, *J. Phys. Chem. C*, 2012, **116**, 363-373.
129. J. F. L. Duval and F. Gaboriaud, *Curr. Opin. Colloid Interface Sci.*, 2010, **15**, 184-195.
130. S. J. Kim, L. D. Li and J. Han, *Langmuir*, 2009, **25**, 7759-7765.
131. D. Stein, Z. Deurvorst, F. H. J. van der Heyden, W. J. A. Koopmans, A. Gabel and C. Dekker, *Nano Lett.*, 2010, **10**, 765-772.
132. F. H. J. van der Heyden, D. Stein and C. Dekker, *Phys. Rev. Lett.*, 2005, **95**.
133. M. R. Wang and Q. J. Kang, *Microfluid. Nanofluid.*, 2010, **9**, 181-190.
134. M. Wang, Q. J. Kang and E. Ben-Naim, *Anal. Chim. Acta*, 2010, **664**, 158-164.

135. M. Akeson, D. Branton, J. J. Kasianowicz, E. Brandin and D. W. Deamer, *Biophys. J.*, 1999, **77**, 3227-3233.
136. J. L. Li, M. Gershow, D. Stein, E. Brandin and J. A. Golovchenko, *Nat. Mater.*, 2003, **2**, 611-615.
137. P. Chen, J. J. Gu, E. Brandin, Y. R. Kim, Q. Wang and D. Branton, *Nano Lett.*, 2004, **4**, 2293-2298.
138. A. Han, M. Creus, G. Schurmann, V. Linder, T. R. Ward, N. F. de Rooij and U. Staufer, *Anal. Chem.*, 2008, **80**, 4651-4658.
139. D. S. Talaga and J. L. Li, *J. Am. Chem. Soc.*, 2009, **131**, 9287-9297.
140. A. R. Hall, J. M. Keegstra, M. C. Duch, M. C. Hersam and C. Dekker, *Nano Lett.*, 2011, **11**, 2446-2450.
141. C. Dekker, *Nat. Nanotechnol.*, 2007, **2**, 209-215.
142. S. Howorka and Z. Siwy, *Chem. Soc. Rev.*, 2009, **38**, 2360-2384.
143. X. Hou, Y. J. Liu, H. Dong, F. Yang, L. Li and L. Jiang, *Adv. Mater.*, 2010, **22**, 2440-+.
144. B. Yameen, M. Ali, R. Neumann, W. Ensinger, W. Knoll and O. Azzaroni, *J. Am. Chem. Soc.*, 2009, **131**, 2070-+.
145. Y. J. Oh, A. L. Garcia, D. N. Petsev, G. P. Lopez, S. R. J. Brueck, C. F. Ivory and S. M. Han, *Lab Chip*, 2009, **9**, 1601-1608.
146. J. P. Hsu and Y. H. Tai, *Langmuir*, 2010, **26**, 16857-16864.
147. J. P. Hsu, Y. H. Tai, L. H. Yeh and S. Tseng, *J. Phys. Chem. B*, 2011, **115**, 3972-3980.
148. J. P. Hsu, Y. H. Tai, L. H. Yeh and S. J. Tseng, *Langmuir*, 2012, **28**, 1013-1019.
149. H. Liu, S. Z. Qian and H. H. Bau, *Biophys. J.*, 2007, **92**, 1164-1177.
150. S. van Dorp, U. F. Keyser, N. H. Dekker, C. Dekker and S. G. Lemay, *Nat. Phys.*, 2009, **5**, 347-351.
151. M. B. Andersen, J. Frey, S. Pennathur and H. Bruus, *Journal of Colloid and Interface Science*, 2011, **353**, 301-310.
152. L. H. Yeh, S. Xue, S. W. Joo, Q. S. and J. P. Hsu, *J. Phys. Chem. C*, 2012, **116**, 8.
153. L. Liang, Y. Ai, J. Zhu, S. Qian and X. C. Xuan, *J. Colloid Interface Sci.*, 2010, **347**, 142-146.
154. Y. Ai, S. Park, J. Zhu, X. C. Xuan, A. Beskok and S. Qian, *Langmuir*, 2010, **26**, 2937-2944.
155. Y. Ai, A. Beskok, D. T. Gauthier, S. W. Joo and S. Qian, *Biomicrofluidics*, 2009, **3**, 044110.
156. Y. Ai, S. W. Joo, Y. T. Jiang, X. C. Xuan and S. Qian, *Electrophoresis*, 2009, **30**, 2499-2506.
157. X. C. Xuan, S. Raghibizadeh and D. Q. Li, *J. Colloid Interface Sci.*, 2006, **296**, 743-748.
158. X. C. Xuan and D. Q. Li, *Electrophoresis*, 2005, **26**, 3552-3560.
159. H. J. Keh and J. L. Anderson, *J. Fluid Mech.*, 1985, **153**, 417-439.
160. H. J. Keh and J. Y. Chiou, *Aiche J.*, 1996, **42**, 1397-1406.
161. J. Ennis and J. L. Anderson, *J. Colloid Interface Sci.*, 1997, **185**, 497-514.
162. J. P. Hsu and C. Y. Kao, *J. Phys. Chem. B*, 2002, **106**, 10605-10609.
163. J. P. Hsu, M. H. Ku and C. Y. Kao, *J. Colloid Interface Sci.*, 2004, **276**, 248-254.
164. S. Qian, A. H. Wang and J. K. Afonien, *J. Colloid Interface Sci.*, 2006, **303**, 579-592.
165. H. Liu, S. Qian and H. H. Bau, *Biophys. J.*, 2007, **92**, 1164-1177.
166. S. Qian and S. W. Joo, *Langmuir*, 2008, **24**, 4778-4784.
167. S. Qian, S. W. Joo, W. S. Hou and X. X. Zhao, *Langmuir*, 2008, **24**, 5332-5340.
168. J. P. Hsu, Z. S. Chen, D. J. Lee, S. Tseng and A. Su, *Chem. Eng. Sci.*, 2008, **63**, 4561-4569.
169. L. J. Wang and H. J. Keh, *J. Phys. Chem. C*, 2009, **113**, 12790-12798.
170. H. J. Keh and T. H. Hsieh, *Langmuir*, 2008, **24**, 390-398.
171. H. Ohshima, *J. Colloid Interface Sci.*, 1995, **171**, 525-527.

172. A. L. Zydney, *J. Colloid Interface Sci.*, 1995, **169**, 476-485.
173. Y. Ai and S. Qian, *Phys. Chem. Chem. Phys.*, 2011, **DOI: 10.1039/c0cp02267e**.
174. K. Makino, J. Tabata, T. Yoshioka, M. Fukuda, M. Ikekita, H. Ohshima and H. Terada, *Colloid Surf. B-Biointerfaces*, 2003, **29**, 277-284.
175. R. Bos, H. C. van der Mei and H. J. Busscher, *Biophys. Chem.*, 1998, **74**, 251-255.
176. A. J. de Kerchove and M. Elimelech, *Abstr. Pap. Am. Chem. Soc.*, 2004, **228**, U633.
177. J. F. L. Duval, K. J. Wilkinson, H. P. Van Leeuwen and J. Buffle, *Environ. Sci. Technol.*, 2005, **39**, 6435-6445.
178. V. M. Starov and Y. E. Solomentsev, *J. Colloid Interface Sci.*, 1993, **158**, 166-170.
179. M. Rasmusson, B. Vincent and N. Marston, *Colloid Polym. Sci.*, 2000, **278**, 253-258.
180. J. F. L. Duval and H. P. van Leeuwen, *Langmuir*, 2004, **20**, 10324-10336.
181. J. F. L. Duval, *Langmuir*, 2005, **21**, 3247-3258.
182. A. Vonarbourg, P. Saulnier, C. Passirani and J. P. Benoit, *Electrophoresis*, 2005, **26**, 2066-2075.
183. J. F. L. Duval, H. J. Busscher, B. van de Belt-Gritter, H. C. van der Mei and W. Norde, *Langmuir*, 2005, **21**, 11268-11282.
184. H. Ohshima, *J. Colloid Interface Sci.*, 1994, **163**, 474-483.
185. H. Ohshima, *J. Colloid Interface Sci.*, 2000, **228**, 190-193.
186. H. Ohshima, *Colloid Polym. Sci.*, 2005, **283**, 819-825.
187. H. Ohshima, *Electrophoresis*, 2006, **27**, 526-533.
188. J. F. L. Duval and H. Ohshima, *Langmuir*, 2006, **22**, 3533-3546.
189. L. P. Yezek, J. F. L. Duval and H. P. van Leeuwen, *Langmuir*, 2005, **21**, 6220-6227.
190. J. F. L. Duval, R. Zimmermann, A. L. Cordeiro, N. Rein and C. Werner, *Langmuir*, 2009, **25**, 10691-10703.
191. J. Lyklema and J. F. L. Duval, *Adv. Colloid Interface Sci.*, 2005, **114**, 27-45.
192. D. A. Saville, *J. Colloid Interface Sci.*, 2000, **222**, 137-145.
193. R. J. Hill, D. A. Saville and W. B. Russel, *J. Colloid Interface Sci.*, 2003, **258**, 56-74.
194. R. J. Hill, *Phys. Rev. E*, 2004, **70**, 051406.
195. R. J. Hill and D. A. Saville, *Colloid Surf. A-Physicochem. Eng. Asp.*, 2005, **267**, 31-49.
196. J. J. Lopez-Garcia, C. Grosse and J. Horno, *J. Colloid Interface Sci.*, 2003, **265**, 327-340.
197. J. P. Hsu, Z. S. Chen and S. Tseng, *J. Phys. Chem. B*, 2009, **113**, 7701-7708.
198. X. G. Zhang, J. P. Hsu, Z. S. Chen, L. H. Yeh, M. H. Ku and S. Tseng, *J. Phys. Chem. B*, 2010, **114**, 1621-1631.
199. E. Lee, Y. P. Tang and J. P. Hsu, *Langmuir*, 2004, **20**, 9415-9421.
200. C. H. Huang, W. L. Cheng, Y. Y. He and E. Lee, *J. Phys. Chem. B*, 2010, **114**, 10114-10125.
201. W. L. Cheng, Y. Y. He and E. Lee, *J. Colloid Interface Sci.*, 2009, **335**, 130-139.
202. Y. Ai, M. K. Zhang, S. W. Joo, M. A. Cheney and S. Qian, *J. Phys. Chem. C*, 2010, **114**, 3883-3890.
203. S. Y. Lee, S. E. Yalcin, S. W. Joo, O. Baysal and S. Qian, *J. Phys. Chem. B*, 2010, **114**, 6437-6446.
204. S. Qian, S. W. Joo, Y. Ai, M. A. Cheney and W. S. Hou, *J. Colloid Interface Sci.*, 2009, **329**, 376-383.
205. S. Qian, B. Das and X. B. Luo, *J. Colloid Interface Sci.*, 2007, **315**, 721-730.
206. G. S. Beavers and D. D. Joseph, *J. Fluid Mech.*, 1967, **30**, 197-&.
207. J. A. Ochoatapia and S. Whitaker, *International Journal of Heat and Mass Transfer*, 1995, **38**, 2647-2655.
208. J. A. Ochoatapia and S. Whitaker, *International Journal of Heat and Mass Transfer*, 1995, **38**, 2635-2646.
209. L. Z. Song, M. R. Hobaugh, C. Shustak, S. Cheley, H. Bayley and J. E. Gouaux, *Science*, 1996, **274**, 1859-1866.

210. Y. H. He, R. H. Scheicher, A. Grigoriev, R. Ahuja, S. B. Long, Z. L. Huo and M. Liu, *Adv. Funct. Mater.*, 2011, **21**, 2674-2679.
211. U. F. Keyser, B. N. Koeleman, S. Van Dorp, D. Krapf, R. M. M. Smeets, S. G. Lemay, N. H. Dekker and C. Dekker, *Nat. Phys.*, 2006, **2**, 473-477.
212. M. van den Hout, I. D. Vilfan, S. Hage and N. H. Dekker, *Nano Lett.*, 2010, **10**, 701-707.
213. K. Kececi, L. T. Sexton, F. Buyukserin and C. R. Martin, *Nanomedicine*, 2008, **3**, 787-796.
214. H. Chang, F. Kosari, G. Andreadakis, M. A. Alam, G. Vasmatzis and R. Bashir, *Nano Lett.*, 2004, **4**, 1551-1556.
215. L. H. Yeh, J. P. Hsu and S. Tseng, *J. Phys. Chem. C*, 2010, **114**, 16576-16587.
216. U. F. Keyser, S. van Dorp and S. G. Lemay, *Chem. Soc. Rev.*, 2010, **39**, 939-947.
217. O. A. Saleh and L. L. Sohn, *Nano Lett.*, 2003, **3**, 37-38.
218. A. J. Storm, C. Storm, J. H. Chen, H. Zandbergen, J. F. Joanny and C. Dekker, *Nano Lett.*, 2005, **5**, 1193-1197.
219. M. Rhee and M. A. Burns, *Trends Biotechnol.*, 2006, **24**, 580-586.
220. J. Griffiths, *Anal. Chem.*, 2008, **80**, 23-27.
221. K. Healy, B. Schiedt and A. P. Morrison, *Nanomedicine*, 2007, **2**, 875-897.
222. Y. R. Kim, J. Min, I. H. Lee, S. Kim, A. G. Kim, K. Kim, K. Namkoong and C. Ko, *Biosens. Bioelectron.*, 2007, **22**, 2926-2931.
223. S. E. Yalcin, A. Sharma, S. Qian, S. W. Joo and O. Baysal, *Sens. Actuator B-Chem.*, **doi:10.1016/j.snb.2010.10.025**.
224. C. L. Zhao and C. Yang, *Phys. Rev. E*, 2009, **80**.
225. H. S. White and A. Bund, *Langmuir*, 2008, **24**, 2212-2218.
226. M. Z. Bazant and T. M. Squires, *Phys. Rev. Lett.*, 2004, **92**.
227. T. M. Squires and M. Z. Bazant, *J. Fluid Mech.*, 2006, **560**, 65-101.
228. J. P. Hsu, W. L. Hsu and K. L. Liu, *Langmuir*, 2010, **26**, 8648-8658.
229. A. J. Storm, J. H. Chen, H. W. Zandbergen and C. Dekker, *Phys. Rev. E*, 2005, **71**, 051903.
230. A. Meller, L. Nivon, E. Brandin, J. Golovchenko and D. Branton, *Proc. Natl. Acad. Sci. U. S. A.*, 2000, **97**, 1079-1084.
231. Z. Chen, Y. B. Jiang, D. R. Dunphy, D. P. Adams, C. Hodges, N. G. Liu, N. Zhang, G. Xomeritakis, X. Z. Jin, N. R. Aluru, S. J. Gaik, H. W. Hillhouse and C. J. Brinker, *Nat. Mater.*, 2010, **9**, 667-675.
232. G. F. Schneider, S. W. Kowalczyk, V. E. Calado, G. Pandraud, H. W. Zandbergen, L. M. K. Vandersypen and C. Dekker, *Nano Lett.*, 2010, **10**, 3163-3167.
233. B. M. Venkatesan, A. B. Shah, J. M. Zuo and R. Bashir, *Adv. Funct. Mater.*, 2010, **20**, 1266-1275.
234. M. Firnkes, D. Pedone, J. Knezevic, M. Doblinger and U. Rant, *Nano Lett.*, 2010, **10**, 2162-2167.
235. M. Muthukumar and C. Y. Kong, *Proc. Natl. Acad. Sci. U. S. A.*, 2006, **103**, 5273-5278.
236. Y. Ai and S. Z. Qian, *Phys. Chem. Chem. Phys.*, 2011, **13**, 4060-4071.
237. B. Honig and A. Nicholls, *Science*, 1995, **268**, 1144-1149.
238. J. Ramstein and R. Lavery, *Proc. Natl. Acad. Sci. U. S. A.*, 1988, **85**, 7231-7235.
239. M. A. Young, B. Jayaram and D. L. Beveridge, *J. Phys. Chem. B*, 1998, **102**, 7666-7669.
240. O. Malysheva, T. Tang and P. Schiavone, *J. Phys. Chem. C*, 2010, **114**, 3781-3790.
241. S. T. Cui, *J. Phys. Chem. B*, 2011, **115**, 10699-10706.
242. M. K. Zhang, Y. Ai, D. S. Kim, J. H. Jeong, S. W. Joo and S. Z. Qian, *Colloid Surf. B-Biointerfaces*, 2011, **88**, 165-174.
243. H. Liu, H. H. Bau and H. H. Hu, *Langmuir*, 2004, **20**, 2628-2639.
244. J. K. Holt, H. G. Park, Y. M. Wang, M. Stadermann, A. B. Artyukhin, C. P. Grigoropoulos, A. Noy and O. Bakajin, *Science*, 2006, **312**, 1034-1037.

245. E. N. Trifonov and J. L. Sussman, *Proceedings of the National Academy of Sciences of the United States of America-Biological Sciences*, 1980, **77**, 3816-3820.
246. A. Spiering, S. Getfert, A. Sischka, P. Reimann and D. Anselmetti, *Nano Lett.*, 2011, **11**, 2978-2982.
247. G. S. Manning, *J. Chem. Phys.*, 1969, **51**, 924-&.
248. M. Muthukumar, *J. Chem. Phys.*, 2004, **120**, 9343-9350.
249. A. Plecis, R. B. Schoch and P. Renaud, *Nano Lett.*, 2005, **5**, 1147-1155.
250. Y. C. Wang, A. L. Stevens and J. Y. Han, *Anal. Chem.*, 2005, 77, 4293-4299.
251. G. S. Manning, *J. Chem. Phys.*, 1969, **51**, 924-933.
252. M. Deserno, C. Holm and S. May, *Macromolecules*, 2000, **33**, 199-206.
253. A. R. Denton, *Phys. Rev. E*, 2003, **67**.
254. K. Grass and C. Holm, *Soft Matter*, 2009, **5**, 2079-2092.
255. M. Lebret and B. H. Zimm, *Biopolymers*, 1984, **23**, 287-312.
256. H. P. Hsu and E. Lee, *Electrochem. Commun.*, 2012, **15**, 59-62.
257. J.-P. Hsu and Y.-H. Tai, *Langmuir*, 2010, **26**, 16857-16864.
258. L. H. Yeh, M. K. zhang, Q. S. and J. P. hsu, *Nanoscale*, 2012.
259. T. A. Zangle, A. Mani and J. G. Santiago, *Chem. Soc. Rev.*, 2010, **39**, 1014-1035.
260. X. Hou, W. Guo and L. Jiang, *Chem. Soc. Rev.*, 2011, **40**, 2385-2401.
261. M. L. Kovarik, K. M. Zhou and S. C. Jacobson, *J. Phys. Chem. B*, 2009, **113**, 15960-15966.
262. D. Woermann, *Physical Chemistry Chemical Physics*, 2004, **6**, 3130-3132.
263. D. Woermann, *Physical Chemistry Chemical Physics*, 2003, **5**, 1853-1858.
264. Z. S. Siwy, *Adv. Funct. Mater.*, 2006, **16**, 735-746.
265. D. Constantin and Z. S. Siwy, *Phys. Rev. E*, 2007, **76**.
266. E. B. Kalman, O. Sudre, I. Vlassiouk and Z. S. Siwy, *Anal. Bioanal. Chem.*, 2009, **394**, 413-419.
267. S. W. Nam, M. J. Rooks, K. B. Kim and S. M. Rossnagel, *Nano Lett.*, 2009, **9**, 2044-2048.
268. M. Taniguchi, M. Tsutsui, K. Yokota and T. Kawai, *Appl. Phys. Lett.*, 2009, **95**.
269. P. Joshi, A. Smolyanitsky, L. Petrossian, M. Goryll, M. Saraniti and T. J. Thornton, *J. Appl. Phys.*, 2010, **107**.
270. R. B. M. Schasfoort, S. Schlautmann, L. Hendrikse and A. van den Berg, *Science*, 1999, **286**, 942-945.
271. Y. J. Oh, T. C. Gamble, D. Leonhardt, C. H. Chung, S. R. J. Brueck, C. F. Ivory, G. P. Lopez, D. N. Petsev and S. M. Han, *Lab Chip*, 2008, **8**, 251-258.
272. X. Z. Jin and N. R. Aluru, *Microfluid. Nanofluid.*, 2011, **11**, 297-306.
273. S. Xue, N. Hu and S. Qian, *Journal of Colloid and Interface Science*, 2012, **365**, 326-328.

VITA

EDUCATION

- **Ph.D.** in Aerospace Engineering *May 2012*
  Old Dominion University, Norfolk, VA, USA;
- **Ph.D.** in Fluid Mechanics *June 2008*
  Zhejiang University, Hangzhou, Zhejiang, China;
- **B.S.** in Engineering Mechanics *June 2003*
  Zhejiang University, Hangzhou, Zhejiang, China;

SELECTED PUBLICATIONS

1. Ye Ai, Mingkan Zhang, Sang W. Joo, Marcos A. Cheney and Shizhi Qian, Effects of Electroosmotic Flow on Ionic Current Rectification in Conical Nanopores, J. Phys. Chem. C., 2010, 114 (9), 3883–3890.

2. Mingkan Zhang, Ye Ai, Ashutosh Sharma, Sang W. Joo, Dong-Soo Kim, Shizhi Qian, Electrokinetic particle translocation through a nanopore containing a floating electrode, Electrophoresis, 2011, 32(14), 1864-1874

3. Mingkan Zhang, Ye Ai, Dong-Soo Kim, Jun-Ho Jeong, Sang W. Joo, Shizhi Qian, Electrophoretic motion of a soft spherical particle in a nanopore, Colloids and Surfaces B: Biointerfaces, 2011, 88 (1), 165-174.

4. Mingkan Zhang, Li-Hsien Yeh, Shizhi Qian, Jyh-Ping Hsu, and Sang W. Joo, DNA Electrokinetic Translocation through a Nanopore: Local Permittivity Environment Effect, J. Phys. Chem. C, 2012, 116(7), 4793-4801

5. Li-Hsien Yeh, Mingkan Zhang, Shizhi Qian, Jyh-Ping Hsu, Regulating DNA Translocation through Functionalized Soft Nanopores, Nanoscale, 2012, 4. 2685-2693.

6. Li-Hsien Yeh, Mingkan Zhang, Shizhi Qian, Jyh-Ping Hsu, shiojenn Tseng, Ion Concentration Polarization in Polyelectrolyte-Modified Nanopores, accepted to J. Phys. Chem. C.

7. Li-Hsien Yeh, Mingkan Zhang, Sang W. Joo, Shizhi Qian, Slowing Down DNA Translocation through a Nanopore by Lowering Fluid Temperature, submitted to Electrophoresis. (Under review)